ASME
SETTING THE STANDARD

Transactions of the ASME, Journal of Fluids Engineering
(ISSN 0098-2202) is published monthly by
The American Society of Mechanical Engineers,
Three Park Avenue, New York, NY 10016.
Periodicals postage paid at New York, NY
and additional mailing offices.
POSTMASTER: Send address changes to Transactions of the
ASME, Journal of Fluids Engineering, c/o THE AMERICAN
SOCIETY OF MECHANICAL ENGINEERS,
22 Law Drive, Box 2300, Fairfield, NJ 07007-2300.
CHANGES OF ADDRESS must be received at Society
headquarters seven weeks before they are to be effective.
Please send old label and new address.
STATEMENT from By-Laws. The Society shall not be
responsible for statements or opinions advanced in papers
or ... printed in its publications (B7.1, Par. 3).

Journal of Fluids Engineering

Published Monthly by ASME

VOLUME 131 • NUMBER 12 • DECEMBER 2009

RESEARCH PAPERS

Flows in Complex Systems

Fundamental Issues and Canonical Flows

Techniques and Procedures

(Contents continued on inside back cover)

This journal is printed on acid-free paper, which exceeds the ANSI Z39.48-1992 specification for permanence of paper and library materials. ∞™
♻ 85% recycled content, including 10% post-consumer fibers.

Journal of Fluids Engineering Volume 131, Number 12 DECEMBER 2009

TECHNICAL BRIEFS

The ASME Journal of Fluids Engineering is abstracted and indexed in the following:

Applied Science & Technology Index, Chemical Abstracts, Chemical Engineering and Biotechnology Abstracts (Electronic equivalent of Process and Chemical Engineering), Civil Engineering Abstracts, Computer & Information Systems Abstracts, Corrosion Abstracts, Current Contents, Ei EncompassLit, Electronics & Communications Abstracts, Engineered Materials Abstracts, Engineering Index, Environmental Engineering Abstracts, Environmental Science and Pollution Management, Excerpta Medica, Fluidex, Index to Scientific Reviews, INSPEC, International Building Services Abstracts, Mechanical & Transportation Engineering Abstracts, Mechanical Engineering Abstracts, METADEX (The electronic equivalent of Metals Abstracts and Alloys Index), Petroleum Abstracts, Process and Chemical Engineering, Referativnyi Zhurnal, Science Citation Index, SciSearch (The electronic equivalent of Science Citation Index), Shock and Vibration Digest, Solid State and Superconductivity Abstracts, Theoretical Chemical Engineering

An Experimental and Analytical Investigation of Rectangular Synthetic Jets

Gopi Krishnan

Kamran Mohseni[1]
e-mail: mohseni@colorado.edu

Department of Aerospace Sciences,
University of Colorado,
Boulder, CO 80309-429

In this paper the flow field of a rectangular synthetic jet driven by a piezoelectric membrane issuing into a quiescent environment is studied. The similarities exhibited by synthetic and continuous turbulent jets lead to the hypothesis that a rectangular synthetic jet within a limited region downstream of the orifice be modeled using similarity analysis just as a continuous planar jet. Accordingly, the jet is modeled using the classic two-dimensional solution to a continuous jet, where the virtual viscosity coefficient of the continuous turbulent jet is replaced with that measured for a synthetic jet. The virtual viscosity of the synthetic jet at a particular axial location is related to the spreading rate and velocity decay rate of the jet. Hot-wire anemometry is used to characterize the flow downstream of the orifice. The flow field of rectangular synthetic jets is thought to consist of four regions as distinguished by the centerline velocity decay. The regions are the developing, the quasi-two-dimensional, the transitional, and the axisymmetric regions. It is in the quasi-two-dimensional region that the planar model applies, and where indeed the jet exhibits self-similar behavior as distinguished by the collapse of the lateral time average velocity profiles when scaled. Furthermore, within this region the spanwise velocity profiles display a saddleback profile that is attributed to the secondary flow generated at the smaller edges of the rectangular orifice. The scaled spreading and decay rates are seen to increase with stroke ratio and be independent of Reynolds number. However, the geometry of the actuator is seen to additionally affect the external characteristics of the jet. The eddy viscosities of the synthetic jets under consideration are shown to be larger than equivalent continuous turbulent jets. This enhanced eddy viscosity is attributed to the additional mixing brought about by the introduction of the periodic vortical structures in synthetic jets and their ensuing break down and transition to turbulence. Further, a semi-empirical modeling approach is proposed, the final objective of which is to obtain a functional relationship between the parameters that describe the external flow field of the synthetic jet and the input operational parameters to the system.
[DOI: 10.1115/1.4000422]

1 Introduction

A synthetic jet is a type of pulsatile jet that results from the formation and interaction of vortex rings or pairs [1]. A common method of generating a synthetic jet employs a cavity-diaphragm setup and is the method used in this experiment. The setup consists of a sealed cavity with a flexible vibrating diaphragm on one end and an orifice on the other. As shown in Fig. 1, the synthesis is comprised of a cycle with two strokes, suction, and ejection. During the suction stroke the diaphragm moves away from the orifice increasing the volume of the cavity and subsequently decreasing the pressure within, resulting in the entrainment of low momentum fluid into the cavity. During the ejection stroke the diaphragm moves toward the orifice, resulting in the expulsion of fluid through the orifice. If a formation criteria is met [2,3], the shear layer formed at the edge of the orifice rolls up to form a vortical structure that travels downstream due to its self-induced velocity. A series of such suction-ejection strokes results in the formation of a train of vortical structures moving away from the orifice. These coherent structures may then form a laminar jet, or interact and break down in a transition toward a turbulent jet that is directed downstream.

This operational principle allows for the synthetic jet to be synthesized entirely from the surrounding medium. This implies a zero net mass flux across the actuator boundary. However, on account of the asymmetry of the system a net momentum flux is imparted to the external flow. The lack of plumbing provides added benefits of reduced size, weight, and fabrication complexity. Additionally, the periodic vortical structures introduced into the flow exhibit an ability to influence the environment at a variety of length scales. All these properties make synthetic jets attractive in a number of applications that include active flow control [4–6], electronics cooling [7,8], fluid mixing [9], as well as both aerial [10–13] and underwater propulsion [14,15].

Synthetic jet actuators occur primarily in axisymmetric [16–18] and rectangular [19–21] configurations, where the latter is studied in this paper. Rectangular synthetic jets differ from circular ones in terms of the vortex dynamics involved in the evolution of the jet and the time average and fluctuating velocity characteristics in the far field [22,23]. The primary mechanism accountable for jet entrainment in the near field of continuous circular jets is known to be vortex ring formation and merging. In continuous rectangular jets an additional mode of axis switching of the vortical structures is understood to enhance entrainment. Synthetic rectangular jets have been shown to engage in behavior similar to continuous rectangular jets in terms of the complex evolution that the coherent vortical structures undergo as they switch axis, interact, and break down [24,25]. At the same time it is known that the primary mechanism for the generation of large-scale coherent structures is different in both continuous and synthetic jets.

A schematic of a rectangular synthetic jet is shown in Fig. 2. A single rectangular shaped vortical structure is shown in the near

[1]Corresponding author.
Contributed by the Fluids Engineering Division of ASME for publication in the JOURNAL OF FLUIDS ENGINEERING. Manuscript received November 29, 2008; final manuscript received September 25, 2009; published online November 10, 2009. Editor: Joseph Katz.

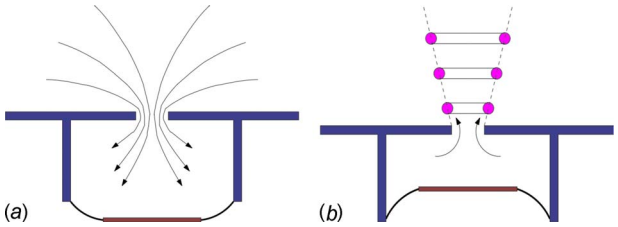

Fig. 1 Schematic of synthetic jet operation

field, while the time average velocity profiles are shown in far field. The x, y, and z coordinates may hereafter be referred to as the streamwise, transverse, and spanwise directions as well. During the expulsion stroke the shear layer formed at the orifice rolls up to form a rectangular shaped vortical structure, in contrast to the counter-rotating roller vortices present in an idealized two-dimensional jet. The differential, self-induced velocity on account of the variation in curvature along the vortical structure results in the section of the vortex structure parallel to the major axis, moving faster than that along the minor axis causing the structure to deform [8]. As the vortex structure moves downstream, the continued self-induced deformation under certain conditions leads to axis switching, reconnection, and bifurcation [25,26]. Simultaneously, azimuthal instabilities start to develop and add further complexity to structures topology [19,25,27]. The interactions between such successively deformed coherent structures results in the formation of braid or rib vortices. This in turn induces further deformation and elicits instabilities leading to the breakdown of the vortical structures. Due to the unstable large-scale coherent structures and the enhanced small-scale mixing, rectangular nozzles serve as a passive method of enhancing mixing in a synthetic jet. This rapid breakdown results in rectangular synthetic jets exhibiting a quicker transition to turbulence and increased entrainment in comparison with round synthetic jets [26].

The far field of synthetic and continuous jets exhibit similarities as well. The transverse time average and fluctuating velocity profiles in synthetic jets exhibit self-similarity as distinguished by the collapse of the profiles when normalized by appropriate variables [19]. At low Reynolds numbers, synthetic jets show some deviation from planar continuous jets in terms of the centerline velocity decay not exhibiting $x^{-1/2}$ behavior, and the jet width not showing linear growth. This deviation was attributed to the presence of a pressure gradient formed due to the periodic suction strokes [8,19]. However, at higher Reynolds numbers synthetic jets exhibit both decay and spreading behavior characteristic of planar continuous jets [20]. Thus suggesting that perhaps there is some threshold value to Reynolds number at a given Strouhal number. The synthetic jets do however develop more quickly, with both the centerline velocity decay and jet spread increasing more rapidly than equivalent planar turbulent continuous jets.

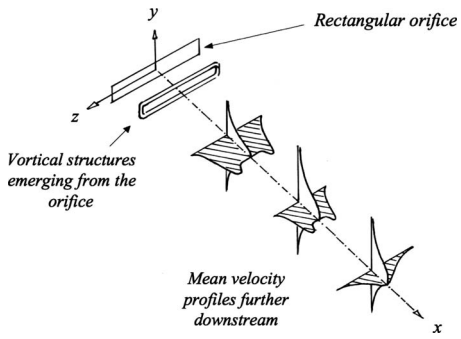

Fig. 2 Schematic of the evolution of a rectangular synthetic jet

It should be noted however that the exact nature of the evolution of both the near and far field of the synthetic jet are sensitive to initial conditions that include nozzle geometry [8] and actuator parameters. Two nondimensional variables, namely, the stroke ratio and Reynolds number have been identified as the primary factors that influence synthetic jets [19]. The stroke ratio is representative of a length of the slug of fluid ejected from the orifice during the ejection stroke. The Reynolds number embodies the velocity of this ejected slug. The explicit definitions are given later in the paper.

In order to design rectangular synthetic jets for various applications, a model of the evolution of the external jet at least in the time average sense is required. The external flow field of rectangular synthetic jets may be modeled using either numerical [21,24,25,28–30] or semi-analytical [19–21] techniques, where each has its own advantages and disadvantages. The numerical approach provides detailed information of the flow at the expense of computational time. The semi-analytical methods on the other hand are simpler but require experimental investment to extract empirical parameters. This paper builds upon the latter semi-analytical method to suggest a modeling approach that circumvents the computational cost of a detailed numerical analysis, while at the same time captures the essential physics required for further optimization studies.

The semi-analytical approach is built upon the previously mentioned facts that the far fields of synthetic jets resemble that of turbulent continuous jets in their self-similarity, with the synthetic jet spreading and decaying more rapidly [19,20]. This then suggests that the turbulent planar jet model may be extended to a synthetic jet by taking into account the increased spreading rate through an enhanced turbulent mixing coefficient associated with the synthetic jet. The previous semi-analytical descriptions of the external flow field employed velocity profiles identical to that of planar turbulent jets to just fit the synthetic jet velocity profiles. The present work goes further in suggesting that the external flow field of the synthetic jet may be characterized and systematically modeled based on the classical planar jet derivation. Additionally, the differences in the far field between synthetic and continuous jets are ascribed to an eddy viscosity coefficient that encompasses the magnitude of momentum transfer in the flow. This study is the first step in developing and obtaining a functional, semi-empirical relationship between the characteristics of the external jet and the critical input parameters of the actuator. The framework may be used in the future as a universal guideline for designing synthetic jet actuators during a first design iteration.

This paper is outlined as follows. Section 2 lays out the theoretical models of the external flow field of the synthetic jet, followed by a model of the actuator. The experimental setup for the measurement of the velocity field and diaphragm deflection is then described in Sec. 3. After which the results are presented and discussed in Sec. 4. In Sec. 5, the conclusions and future work are summarized.

2 Theoretical Modeling

A complete model for a rectangular synthetic jet must detail the relationship between the input driving parameters and geometry of the actuator, to the external characteristics of the ensuing jet. In this paper, the geometry of the actuator is not studied and is the topic of future work addressed in Sec. 5. With this said, in using a piezoelectrically driven actuator the driving parameters are frequency (f) and Voltage (V_d) in the case of a sinusoidal driving function. This input translates to a deflection of the membrane that depends on the system dynamics of the actuator cavity and diaphragm. This deflection and frequency may then be expressed as nondimensional actuator related parameters $(L/h, \mathrm{Re}_{U_o})$. The actuator parameters subsequently influence the far field of the issuing synthetic jet that may be characterized by a decay rate (K_u) and spreading rate (K_b). This framework relating the identified input variables to the output variables is the basis of the semi-

analytical modeling approach mentioned in Sec. 1. In Sec. 2.1 a model for the external flow field in terms of velocity profiles, spreading rates, and decay rates are outlined first. Following which a model relating the amplitude of deflection and frequency of the driving diaphragm to the nondimensional actuator parameters is presented.

2.1 Time Average Flow Field. Consider the region of the synthetic jet flow where the periodically formed vortical structures cease to be coherent and a turbulent jet directed downstream exists (Fig. 2). In this regime, the influence of the edge has not completely permeated the flow and the transverse velocity profiles may be thought to be independent of the spanwise coordinate. The jet may be viewed to issue from a long, narrow slot (momentum source) into the external quiescent environment where it may be admissible to describe the time average velocities in the jet by boundary layer equations. The basic premise in this section is that the observed far field properties of a synthetic jet allow one to follow the classic modeling approach for turbulent continuous jets [31], with the key addition being the replacement of the eddy viscosity of the continuous turbulent jet with that of the synthetic jet. Following the classic derivation of the jet [31], the boundary layer equations with no pressure gradient may be expressed as

$$u\frac{\partial u}{\partial x}+v\frac{\partial u}{\partial y}=\frac{1}{\rho}\frac{\partial \tau}{\partial y}, \quad \text{and} \quad \frac{\partial u}{\partial x}+\frac{\partial v}{\partial y}=0 \tag{1}$$

where τ is the turbulent shear stress and ρ is the fluid density. The turbulent shear stress may be related to the time average velocity by an eddy viscosity approximation given as $\tau=\rho\varepsilon\frac{\partial u}{\partial y}$, where ε is a coefficient of eddy viscosity or virtual viscosity. The eddy viscosity hypothesis assumes that the momentum transfer in a turbulent flow is due to eddies in turbulence, in contrast to laminar flow where molecular diffusion is responsible for momentum transport. With the eddy viscosity characterizing the time average momentum transfer due to turbulent fluctuations, previous observations of the enhanced spreading rate immediately suggest that a synthetic jet has a higher eddy viscosity than a continuous jet. Then based on the similarity between synthetic rectangular and continuous jets, and the enhanced spreading rates of the former over the latter, it is hypothesized here that synthetic jets may be modeled as continuous planar jets with the replacement of the eddy viscosity of the continuous turbulent jet with the enhanced value associated with a synthetic jet.

Assuming that the evolution of the jet is dependent only on local length and velocity scales, and lacks memory of the slot dimensions itself, the streamwise time average velocity profiles may be considered self-similar. From the mixing length hypothesis and conservation of streamwise momentum it may be shown that the characteristic length and velocity of the jet scale as $b\propto x$ and $u\propto x^{1/2}$, respectively. The self-similar assumption then leads to a streamwise velocity profile of the form $u=x^{1/2}g(y/x)$. The similarity variable is written as $\eta=\sigma y/x$, where σ is a free constant. As a consequence of the form of self-similarity assumed, the eddy viscosity is proportional to the distance downstream of the momentum source and centerline velocity, $\varepsilon\propto xu_c$. This assumption implies that the eddy viscosity varies only in the streamwise direction and is constant in the lateral direction.

The governing equations along with the self-similar velocity profile assumption, the eddy viscosity model, and boundary conditions result in the reduction in the boundary layer equations to an ordinary differential equation, $\varphi^2+\varphi'=1$. This is the same equation obtained for a two-dimensional laminar jet where $\varphi=\tanh(\eta)$ is a solution. From the conservation of momentum and the assumed form of the velocity distribution, the solutions for the velocity components are then written as

$$u=\frac{\sqrt{3}}{2}\sqrt{\frac{K\sigma}{x}}(1-\tanh^2\,\eta), \quad \text{and}$$
$$v=\frac{\sqrt{3}}{4}\sqrt{\frac{K}{x\sigma}}(2\eta(1-\tanh^2\,\eta)-\tanh\,\eta) \tag{2}$$

where K is the kinematic momentum per unit length and is a measure of the strength of the jet, and may be obtained from $\rho K=J=\rho\int_{-\infty}^{+\infty}u^2dy$. It is important to note here that the above analysis assumes a constant momentum flux in the streamwise direction. While this is readily applicable to continuous jets, in synthetic jets it has been reported that the momentum flux at the orifice is higher than that in the far field [19,21]. The momentum flux was shown to decrease in the near field of the jet due to an adverse pressure gradient, and then asymptote in the far field to some fraction of the exit momentum flux. It is this reduced asymptotic value of the momentum flux that should serve as the magnitude of the driving momentum flux in the above similarity analysis for the synthetic jet, and not the exit momentum flux at the orifice of the actuator. However if it is assumed that the asymptotic value applies to all synthetic jets equally, then the use of the exit momentum flux as a scale is permissible, with the added benefit that it may be obtained from an actuator model.

The centerline streamwise velocity may be expressed as

$$U_c=\frac{\sqrt{3}}{2}\sqrt{\frac{K\sigma}{x}}=S_u\frac{1}{\sqrt{x}} \tag{3}$$

where S_u is the centerline velocity jet decay rate. In scaling this equation, the centerline velocity decay may be expressed as

$$\left(\frac{U_o}{U_c}\right)^2=K_u\left(\frac{x-x_{o,u}}{h}\right) \tag{4}$$

where U_o is an average velocity associated with the actuator, h is the width of the rectangular slot, K_u is a scaled decay rate of the jet, and $x_{o,u}$ is the axial location of the virtual origin based on the centerline velocity. The location of the virtual origin is obtained from the intersection of the line asymptote of $1/U_c$ and the abscissa (x), and may be thought of as the self-similarity origin of the jet.

The width of the jet at a particular axial station may be characterized by a half width $b_{1/2}$ defined as the lateral distance from the centerline at which the streamwise velocity drops to half the centerline velocity. The axial variation in the jet width may be expressed either as $b_{1/2}=S_bx$ or identically as

$$\frac{b_{1/2}}{h}=K_b\left(\frac{x-x_{o,b}}{h}\right) \tag{5}$$

where S_b and K_b are the spreading rates, and $x_{o,b}$ is the axial location of the virtual origin based on the jet width. From Eqs. (2)–(4) the free constant σ in the similarity variable is related to the spreading rate as $\sigma\approx 0.88/S_b$. From Prandtl's second hypothesis for eddy viscosity [32], the eddy viscosity may expressed as

$$\varepsilon\approx\frac{0.28U_cb_{1/2}}{\sigma}\approx 0.32S_uS_b^2\sqrt{x}\approx\frac{0.32U_o\sqrt{hx}K_b^2}{\sqrt{K_u}} \tag{6}$$

From Eq. (6) it is seen that the eddy viscosity (i) varies in the axial direction as $\sqrt{x}$, (ii) depends on the both the dimensions of the orifice and the exit velocity of the jet, and (iii) increases with the square of the spreading rate.

In summary, Eqs. (2), (4), and (5) describe the velocity profiles, jet decay, and spreading rate, and are used to characterize the external flow field of the synthetic jet. The inputs required are U_o,h,K_u,K_b. The averaged exit velocity is obtained from an incompressible model described in Sec. 2.2, the orifice width is

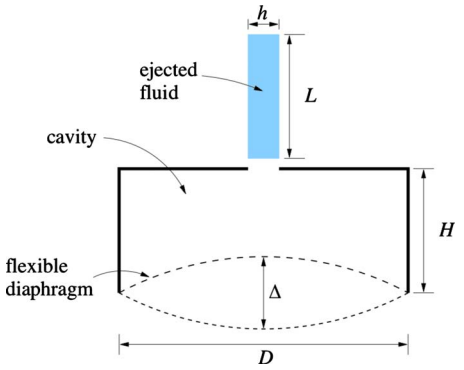

Fig. 3 Schematic of an incompressible actuator model, where the volume of fluid displaced by the diaphragm is ejected through the orifice in the form of a slug

know beforehand, while the decay and spreading rates are obtained from measurements of the external flow field described in Sec. 3.

2.2 Actuator Model. In a quiescent environment the evolution of a synthetic jet depends on several parameters that include (i) the actuator geometry, (ii) the properties of the working fluid, and (iii) the actuation parameters. Ignoring the explicit nondimensional geometric parameters, two nondimensional actuation-related variables have been proposed and established as key parameters governing the evolution and development of synthetic jets [19]. They are the stroke ratio (L/h) and Reynolds number (Re_{U_o}) based on the ejection cycle.

It has been shown that the flow in the actuator may be considered incompressible if the frequency of actuation is far less than the Helmholtz frequency [33]. This will later be shown to be the case which permits the use of an incompressible model to estimate the exit jet velocities. Figure 3 shows a schematic representation of the model, where it is assumed that the volume displaced by the membrane is equal to the volume ejected from the orifice. The length of the slot (w) is not shown in the figure. The stroke ratio is defined as the ratio of the stroke length (L) to the orifice width (h), where the stroke length may be thought of as the length of a hypothetical slug of fluid that is ejected from the orifice during the expulsion stroke [34].

To obtain the volume displaced by the membrane, the shape of the deflected membrane and the central amplitude are required. It is assumed that the shape of the membrane may be modeled as the static deflection of the circular membrane clamped at the edges subject to a uniform load. The deflection profile yields [35]

$$\delta(r) = \frac{\Delta}{2}\left[1 - \frac{r^2}{R^2} + \frac{2r^2}{R^2} ln\left(\frac{r}{R}\right)\right] \tag{7}$$

where r is the radial coordinate and R is the radius of the membrane. The total volume displaced by the membrane during the expulsion stroke from the trough to the crest is $Q = 2\int_0^R \delta(r) 2\pi r dr$, and is equal to 0.25 for the deflection profile considered.

With the ejected volume approximated as a rectangular slug of fluid with the same cross section as the exit orifice $(w \times h)$ and equating the volume of the displaced fluid to that of the slug, the stroke ratio is determined to be

$$\frac{L}{h} = \frac{0.25\pi D^2 \Delta}{4wh^2} \tag{8}$$

The periodic nature of synthetic jets allows for the velocity scales to be defined based on either volume or momentum flux [36]. If based on volume flux the velocity scale is given as $U_o = L/T = fL$, and if based on momentum flux it is given as $U_o = \sqrt{2}L/T = \sqrt{2}fL$. It is more appropriate to use the velocity scale based on momentum flux here, as the self-similar jet solutions employed in this study define equivalent jets based on the same momentum flux and not mass flux. Consequently, the Reynolds number is defined as

$$\mathrm{Re}_{U_o} = \frac{\sqrt{2}Lfh}{\nu} \tag{9}$$

The Reynolds number is explicitly seen to vary with both membrane driving frequency and amplitude, with the stroke ratio appearing to be independent of frequency. This independence of stroke ratio on frequency is not entirely accurate as the use of a piezoelectric diaphragm as a driver gives rise to the coupling between frequency and deflection, and consequently stroke ratio. However, for purposes of calculating the jet parameters the model is seen to serve the purpose. Equations (8) and (9) now relate the input driving deflection amplitude (Δ) and frequency (f) to the nondimensional actuator parameters $(L/h, \mathrm{Re}_{U_o})$.

In summary, Secs. 2.1 and 2.2 yield the following methodology that may be used in modeling synthetic jets. (i) Given a known input driving frequency (f) and voltage (V_d) the centerline deflection (Δ) is either determined from a model of the system [33] or measured experimentally (as was done in this study). (ii) The actuator parameters $(L/h, \mathrm{Re}_{U_o})$ are calculated from Eqs. (8) and (9). (iii) The spreading rate (K_b) and velocity decay rate (K_u) are experimentally determined from the flow field. (iv) The eddy viscosity is calculated from Eq. (6). (v) The analytical velocity profiles are then modeled using Eq. (2). (vi) Steps (i) through (v) are repeated for the same actuator at different operating conditions so that a relationship between the actuator parameters output (K_b, K_u) and actuator parameters $(L/h, \mathrm{Re}_{U_o})$ may be determined.

It is apparent that the above methodology is appropriate for a single actuator. A more universal model requires a design of experiments that may isolate the effect of individual geometric parameters of the output. In this paper, steps (i)–(vi) are carried out over a limited input range. Next, the experimental setup used to determine the parameters are described.

3 Experimental Setup

From Sec. 2 the inputs to the model include (i) the spreading rate of the jet (K_b), (ii) the centerline velocity decay of the jet (K_u), (iii) the central deflection of the membrane (Δ), and (iv) the frequency of oscillation (f). In this section the experimental setup to measure the parameters are described.

3.1 External Flow Field. The experimental setup to measure the external flow field is shown in Fig. 4 and consisted of a synthetic jet actuator, computer controlled stages, and a hot-wire probe, all of which are placed in a large Plexiglas enclosure to isolate the jet from external disturbances. To evaluate the effect of the size of the Plexiglas enclosure on the flow field, initial experiments were conducted with the setup placed in a small box (1

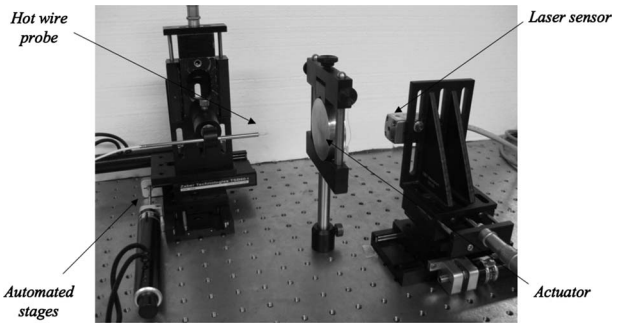

Fig. 4 Experimental setup

Fig. 5 Actuator with a rectangular slot orifice along side a dime provided for scale

$\times 0.5 \times 0.5$ m^3) and a large box ($1.5 \times 1 \times 1$ m^3). The results were then compared with the setup located in the ambient laboratory environment, with the doors closed and ventilation systems turned off. With the jets operating for 5 min in the enclosure to establish a stationary flow state, no significant differences were observed in the time average and rms velocity profiles. Thus, the smallest enclosure was used to isolate the jet flow field from the ambient conditions.

The actuator used was a piezoelectrically driven apparatus that consists of a circular piezomembrane and an aluminum housing. The piezoelectric element was sandwiched between the two circular aluminum elements, which when screwed together form a cavity with a rectangular orifice on one end and a flexible membrane on the other (Fig. 5). The piezo element was connected to a power amplifier (fixed gain of 10×) driven by a sinusoidal signal from a function generator. Two actuators were tested for this study. The dimensions common to both included nozzle length $w = 38.6$ mm, nozzle depth $t = 0.5$ mm, cavity diameter $D = 44.5$ mm, and cavity height $H = 2$ mm, with the difference being the slot width $h = 0.5$ mm and 0.85 mm. This translated to aspect ratios (w/h) of 77:1 (Actuator 1) and 45:1 (Actuator 2). It was observed that at aspect ratios less than 20:1, a jet with a measurable quasiplanar region was not present and hence not considered in this study.

The velocity measurements were made using a single normal hotwire probe operating in constant temperature anemometry (CTA) mode. The probe wire was 1.25 mm long and 5 μm in diameter and aligned such that the prongs were parallel to the streamwise axis or the plane jet. The signal obtained at a sampling rate of 50 kHz was fed through a low pass filter with a cutoff frequency of 10 kHz. The hot-wire was calibrated in an iterative procedure [37] with a fourth order polynomial curve used to convert voltage to velocity. The uncertainty in the time average velocity measurements were estimated to be ±2% for velocities greater than 1.75 m/s and ±10% for velocities less at 0.75 m/s, with the largest contribution to the uncertainty arising from the calibration process. It should be noted that quantifying the uncertainty associated with single hot-wire measurements in regions where the fluid velocity is both low and contains a significant radial component was not assessed.

It should be noted that the issues arising from the use of single hot-wire probes is that associated with directional ambiguity and measurements of very low velocities. While oscillatory flow and low velocities are encountered in the near field and outer edges of the flow, respectively, neither are expected to adversely change the conclusions drawn in the study as the purpose of the experiment is not so much as quantify the velocity components themselves but to verify a modeling method and qualitatively evaluate the effect of actuator parameters on the jet parameters.

The hot-wire probe was affixed to a holder positioned on two computer controlled stages capable of traversing the horizontal plane. In order to characterize the flow field the probe was moved in the horizontal plane of the orifice in discrete intervals, where at each location the flow was sampled for 5 s. The extent over which the measurements were made was dependent on the actuator. For actuator 1, the centerline velocity measurements were made at axial locations ranging from $6x/h$ to $65x/h$. Upon identifying the quasi-two-dimensional region, velocity profiles were obtained at axial positions ranging from $12x/h$ to $32x/h$ in intervals of $4x/h$. The spanwise and lateral extent of measurements about the central axis of the jet were $\pm 45z/h$ and $\pm 12y/h$. The velocity profile, half width of the jet, centerline velocity, and the location of virtual origin were then obtained from the flow measurements. K_u and K_b were subsequently calculated based on these data.

3.2 Diaphragm Deflection. The setup to measure the centerline deflection of the piezoelectric membrane consisted of a laser nanosensor, a movable stage, and a small sliver of silicon (not shown) affixed to the center of the piezoelectric membrane while it was housed in the actuator (Fig. 4).

The principle of operation of the laser sensor is as follows. A laser beam generated by the sensor is incident upon a reflective surface (the piece of silicon serves this purpose) on the diaphragm. The reflected beam returns through the same sensor opening, whereupon it passes through an optical system and is projected on photodiodes. As the target moves back and forth, the position of the reflected beam translates on the photodiode surface where this translation is correlated with the motion of the target through calibration. The sensor acquired data at 25 kHz. The calibration of the sensor was conducted as such: with the sensor attached to a movable automated stage and the diaphragm fixed in a particular location, the laser was moved in increments of 1 μm toward the diaphragm with the signal response measured at each location. This nonlinear displacement-response curve then served as the calibration curve.

To make measurements, the laser was positioned at the location that allowed for the largest sensitivity over the measurable range. The diaphragm was then operated where the resulting dynamic signal response from the laser was translated to a deflection through the calibration curve. To estimate the overall measurement accuracy of the laser, the uncertainties associated with stage position, sensor resolution, calibration, and experimental repeatability were taken into account. For a typical value the total combined uncertainty was estimated by the root sum square to be ±1 μm. The measurements of the dynamic response of the diaphragm result in the central deflection of the membrane (Δ), and the frequency of diaphragm oscillation (f).

4 Results and Discussion

In this section results of the dynamic response of the piezoelectric membrane are presented first, following which the external flow field is characterized.

A synthetic jet with a cavity-diaphragm setup is a coupled system consisting of an electromechanical domain in the form of the diaphragm, and a fluidic/acoustic domain in the form of the resonant cavity. The system may be thought to possess two fundamental frequencies; one associated with the resonant frequency of the diaphragm and the other with the Helmholtz frequency of the cavity. In order to determine (i) the approximate frequency at which to operate the actuator, and (ii) to check for the validity of the incompressible actuator model, the frequency response of the diaphragm was determined. With the driving voltage fixed at 3 V, the driving frequency was swept in intervals of 20 Hz over a range of 0–3000 Hz with the laser sensor measuring the central dynamic response of the membrane. Figure 6 shows the resulting deflection

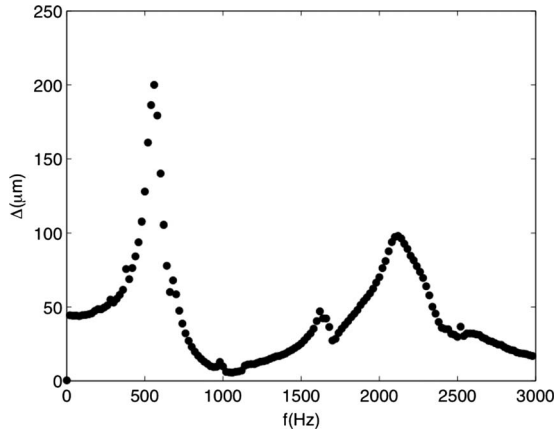

Fig. 6 The dynamic deflection response of the center of the piezoelectric diaphragm to the variation in driving frequency. Actuator 1, V_d=30 V.

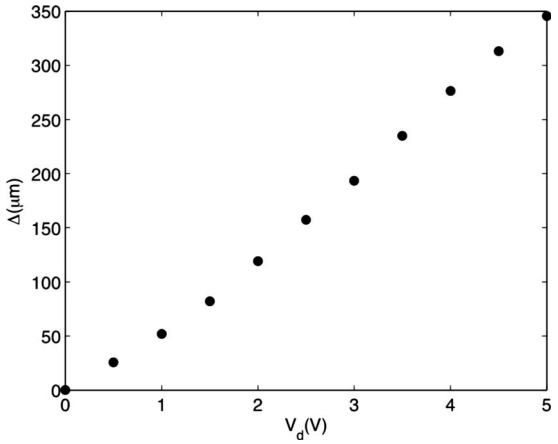

Fig. 7 The dynamic deflection response of the piezoelectric membrane at the center to the variation in driving voltage. Actuator 1, f=560 Hz.

frequency response of the diaphragm where three peaks are observed. The following expression presents a simple formula for the fundamental frequency of a clamped circular membrane [38]

$$f_d = 0.4705 \frac{p}{R^2} \sqrt{\frac{E}{\rho(1-\nu^2)}} \tag{10}$$

where p is the thickness, R is the radius, and E, ρ, and ν are the modulus of elasticity, density, and Poisson's ratio of the membrane, respectively. Using the above formula, the peaks at 560 Hz and 2120 Hz may be associated with the natural resonant frequency of the membrane in modes (0,1) and (0,2). Furthermore, an expression for the Helmholtz frequency of a cavity is [38]

$$f_h = \frac{c}{2\pi} \sqrt{\frac{A}{(H+0.85h)V}} \tag{11}$$

where c is the speed of sound, A is the area of the orifice, and V is the volume of the cavity. While it is recognized that the occurrence of a rectangular slot as opposed to a circular orifice complicates determining the Helmholtz frequency, using both (i) Eq. (11) along with a calculated effective diameter, and (ii) an expression for a Helmholtz frequency of a slot resonator [39], the Helmholtz frequency was calculated to be greater than 4000 Hz. The location of the small peak at 1620 Hz may be a result of the coupled nature of the diaphragm-cavity system and could not be correlated with the Helmholtz frequency from the simple analytical expressions. In spite of this, it is evident that the first mode of the membrane is less than the Helmholtz frequency, allowing for flow in the actuator to be considered incompressible [33]. This gives support to the actuator model considered in Sec. 2.2. From Fig. 6, 560 Hz was selected as the frequency to subsequently operate the actuator as it maximized both the membrane deflection and exit velocity.

Next, the effect of the driving voltage at a fixed frequency was studied. With the frequency fixed at 560 Hz, the driving voltage was swept over a range of 0–5 V in intervals of 0.5 V. The dynamic response is seen to increase with driving voltage (Fig. 7). The slight nonlinear response may be attributed to the dynamics of the actuator at the particular operating frequency. With actuator 2 similar trends in the frequency and amplitude response were observed as well. Now, the deflection results provide the centerline deflection of the membrane (Δ), which serves as an input to the actuator model described in Sec. 2.2. For example for actuator 1, the linear increase in displacement with voltage (Fig. 7) corresponds directly to a stroke ratio range of $0 < L/h < 14$ and Reynolds number range of $0 < \mathrm{Re}_{U_o} < 260$. As seen from the frequency response curve (Fig. 6) the amplitude of vibration and frequency are tied together, and thus do not permit the study of the effect of frequency independently of amplitude over a wide range. With this constraint in mind experiments with varying driving parameters were conducted, where the test matrix for actuators 1 and 2 are summarized in Tables 1 and 2, respectively.

Measurements of the external flow field are now addressed and presented. They are the result of the average of three runs. First, the different regions that comprise the synthetic jet are identified. Figure 8 shows the axial progression of the streamwise time average velocity (U_c) along the centerline axis of the jet for actuator 2 for the four cases in Table 2. The flow field may be thought to be comprised of four regions. The first region, referred to as a developing region ($0 < x/h < 3$), is not captured in this experiment due to the limitations associated with the hot-wire mentioned in Sec. 3.1. However, it has been shown that in this region the velocity increases, reaches a maximum, and then starts to decrease [19]. The second region, referred to as a quasi-two-dimensional region ($3 < x/h < 25$), is where the velocity decays like a planar jet or as $x^{1/2}$. The third region, referred to as a transition region ($25 < x/h < 35$), is where the jet once again deviates from planar jet behavior, while further downstream the fourth region is where the jet starts to exhibit axisymmetric behavior. Results for actuator 2 are presented in Fig. 8 as three of the latter regions were clearly distinguishable. In actuator 1 the axisymmetric region was not observed as the jet decayed to such a point it could not be measured using the hot-wire, before the axisymmetric regime occurred.

Table 1 Test matrix for actuator 1 with w/h=77

Case no.	f (Hz)	V_d (V)	L/h	Re
1a	560	3	7.5	141
1b	560	3.5	9.3	173
1c	560	4	10.9	203
1d	560	4.5	12.3	230
1e	560	5	13.6	254

Table 2 Test matrix for actuator 2 with w/h=45

Case no.	f (Hz)	V_d (V)	L/h	Re
2a	560	1.5	2.5	137
2b	560	2	4.2	228
2c	560	2.5	5.1	275
2d	560	3	5.8	311

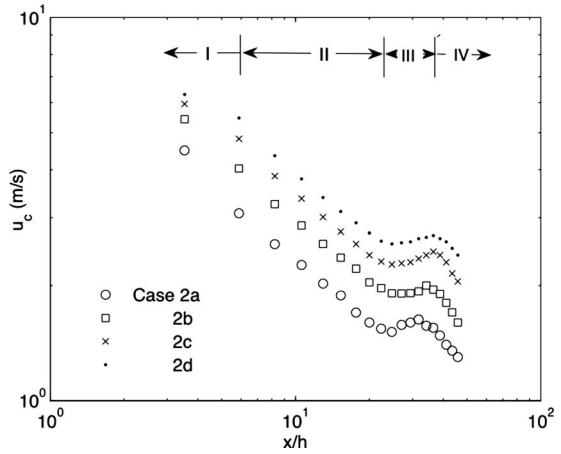

Fig. 8 Variation in the time average centerline velocity with axial distance, displaying the I: developing, II: quasi-two-dimensional, III: transition, and IV: axisymmetric regions (Actuator 2, see Table 2 for details of cases)

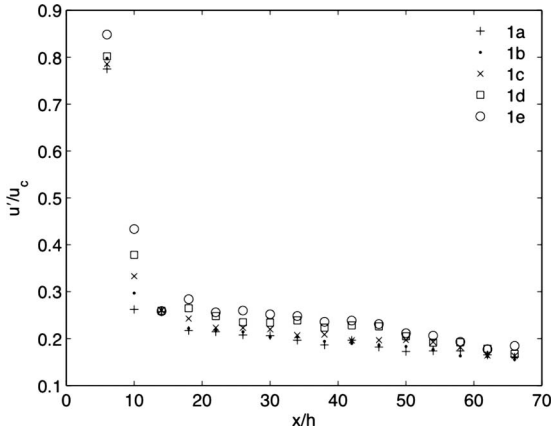

Fig. 10 Streamwise evolution of turbulence intensity at the centerline (Actuator 1, see Table 1 for details of cases))

While the details of the developing region are not captured in this study, the region is known to be characterized by the periodic formation and advection of coherent vortical structures. As the stroke length increases it has been observed that both the extent of, and the peak velocity in this developing region increase [21]. This may be attributed to the increased slug length and momentum accompanying an increase in stroke ratio, and the resulting increased distance over which the initial development of the jet takes place. This being said, Fig. 8 clearly shows the velocity in a synthetic jet at an axial station increases with stroke ratio.

The quasi-two-dimensional region follows the developing region and extends to about 25 x/h from the orifice for all cases. In this region the central portion of jet may be approximated as a planar turbulent jet as the edge effects are not perceived here, as they continue to penetrate toward the center of the flow. It is this regime that the planar jet model applies to. With the centerline velocity decay expressed by Eq. (4), the variation in the decay constant K_u with an increase in displacement amplitude for both actuators is shown in Fig. 9. It is seen that in both cases that the velocity decay rate when plotted against the stroke ratio increase. However, the rate of increase is different suggesting that the actuator geometry plays a role in rectangular jet characteristics. The error associated with the decay rate is estimated to be 2%.

As seen from Fig. 6, due to the rather sharp deflection response it was not possible to study the effect of frequency over a large range on account of a lack of a measurable issuing jet beyond a certain limited window. However, in order to evaluate solely the effect of frequency, the driving voltage was fixed at 3 V while two frequencies (f=480 Hz and f=620 Hz) that yield approximately the same deflection (105 μm) and consequently stroke ratios were selected. It was seen that there was no significant difference in spreading rate and velocity decay rate for both cases. While the frequency range was limited, the results do support other workers data [18], suggesting that jet spreading and velocity decay are independent of Reynolds number, which is connected to the frequency via Eq. (9). The exact nature of the relationship between the velocity decay, spreading rate, and stroke ratio is however seen to be dependent on the geometry of the actuator.

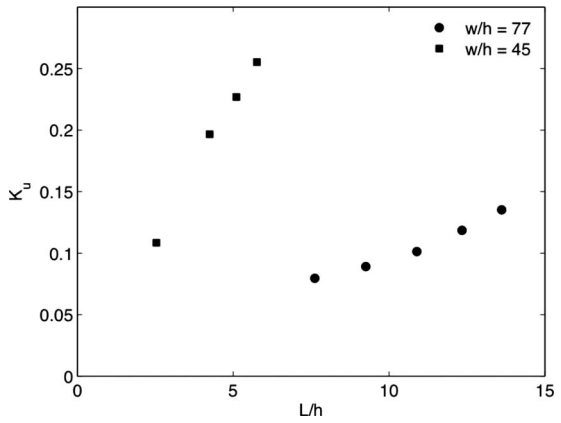

Fig. 9 Dependence of centerline decay rate on stroke ratio for both actuators

The transition region is quite indicative of the influence of the finite slot width and is a result of the complex interaction of the periodic vortex structures emerging form the slot. The time average centerline velocity reached a local minimum then increases momentarily, and then starts to decay. This increase is thought to be due to the effect of the meeting and interaction of the off-center velocity peaks (Fig. 13) at the centerline. The jet starts to decay once again at a more rapid rate than in the quasiplanar regime, suggesting that the jet is transitioning to an axisymmetric jet, as is seen in continuous rectangular jets in the far field [40].

The axial variation in streamwise turbulent intensity is show in Fig. 10. In the developed region large intensities are shown to be present. It should be noted that on account of the very high turbulent intensities in this region the time average velocities in the developing region should be interpreted qualitatively, as a single hot-wire introduces large errors either by overestimating the time average flow, or underestimating the rms velocity [41]. In this region the axial development of the turbulence intensity is thought to be the result of the manner in which (i) the initial turbulence at the orifice decays, and (ii) the coherent structures breakdown toward to a turbulent flow. The increase in turbulence intensity with L/h may once again be attributed to the increase in the vigorous mixing that is brought about by the increase in both momentum and volume associated with the periodically formed vortical structures.

Figure 11 shows the transverse time average velocity profiles in the quasi-two-dimensional region at different streamwise stations. The streamwise velocity and lateral distance are normalized by the centerline velocity and streamwise distance from the velocity virtual origin, respectively. From Fig. 8 it is observed that as the jet moves downstream it slows down, and from Fig. 11 it may be deduced that the jet widens due to the entrainment of the surrounding fluid. The profiles collapse reasonably well in the central region, and appear to be self-similar and Gaussian in nature. Error bars are selectively shown in two locations, at $y-y_o/x$=0.1 and 0.5 for representative purposes. Toward the periphery of the jet

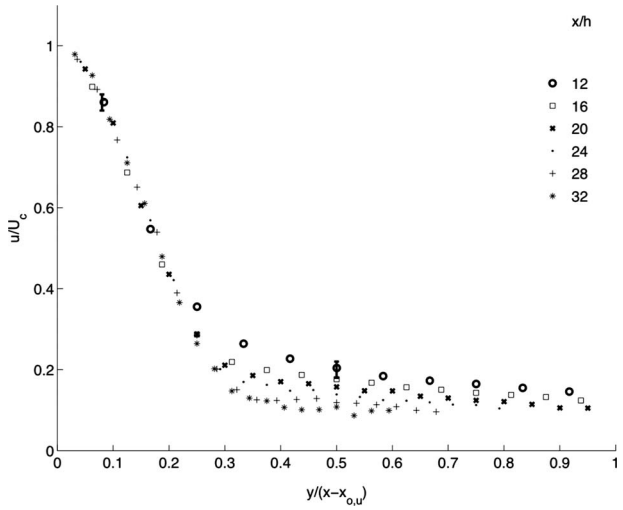

Fig. 11 Normalized time average streamwise velocity profile (Case 1a)

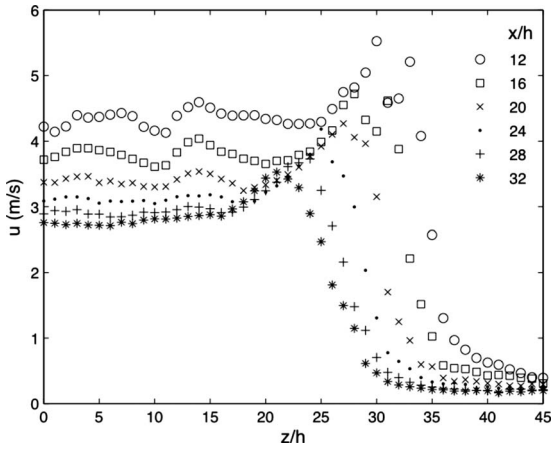

Fig. 13 Time average velocity profile along the major axis at different axial locations (Case 1a)

$(y-y_o/x>0.5)$ the velocity is both low and contains a significant radial component. In this region the limitations of using a single normal hot-wire arises. As mentioned previously, the uncertainty due to this limitation was not quantified in this study.

Figure 12 shows the streamwise turbulent intensity profiles along the minor plane, with the turbulent fluctuation and lateral distance normalized by the centerline velocity and streamwise distance from the virtual origin, respectively. As the jet moves downstream the profile moves from a Gaussian shape to one that shows a distinct noncentral peak and the profiles appear to continue to develop. The turbulence intensity as with any shear flow tends to become self-similar further downstream in comparison to the time average flow, as the turbulence reacts slower to local conditions. Since the turbulence intensity profiles have not yet achieved self-similarity it would not be possible to say if the synthetic jet is less or more turbulent than an equivalent continuous jet.

The streamwise time average velocity profiles in the major plane are shown in Fig. 13. A distinct peak is noticed away from the center, the location of which moves toward the centerline line in the downstream direction and disappears far downstream (not seen in the graph). This saddle back profile has been observed both in synthetic [8] and continuous rectangular jets as well [42–44]. While reflective of the finite nature of the rectangular slot, several explanations have been offered to interpret the phenomena that include the interaction of streamwise [42] and circumferential vortices [43] with the time average flow, resulting in a secondary flow that cause the peaks. It has also been suggested that the centrifugal forces developed result in a pressure distribution that cause fluid to move away from the center of the jet and toward the peaks [44]. In synthetic jets it has been observed that the edge induced counter-rotating vortex structures migrate inwards on account of their mutual attraction [8]. It is plausible that the time average flow on account of the vortex rotation may result in fluid moving toward the location of the observed peaks. The vortex pairs move inwards on account of mutual interaction, which is consistent with the movement of the peaks inwards. The central portion of the region however appears relatively flat suggesting that approximating the lateral velocity profile in the central region to be two-dimensional is feasible. The streamwise turbulent intensity profiles in the major plane (not shown) exhibit this saddle back profile as well, where the off-center peaks moved closer to the centerline as the flow moved downstream. The maximum streamwise turbulence intensity in the central major plane was observed to be higher than that in the central minor plane due to steep velocity gradients accompanying the saddle shape time average velocity profiles.

The axial variation in lateral width of the jet $(b_{1/2})$ within the quasi-two-dimensional region is shown in Fig. 14. Initially the jet width increases slowly, however beyond $x/h \approx 15$ the growth is more rapid and linear, further reinforcing the planar jet behavior.

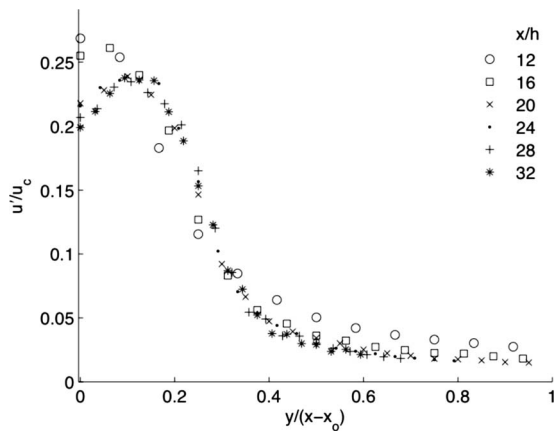

Fig. 12 Normalized fluctuating streamwise velocity profile (Case 1a)

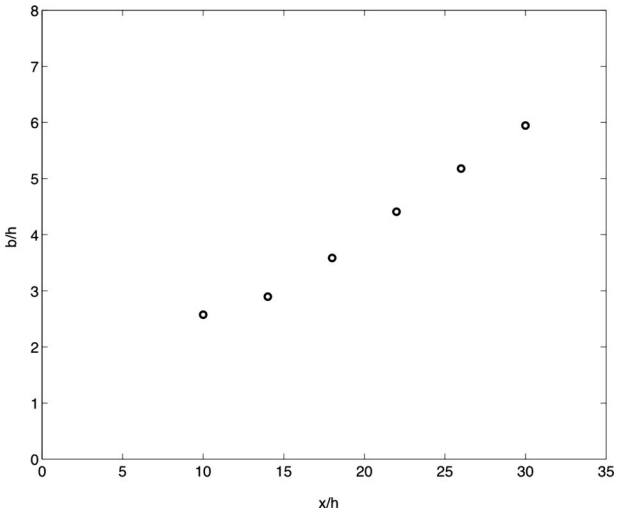

Fig. 14 Variation in jet half width with axial distance (Case 1a)

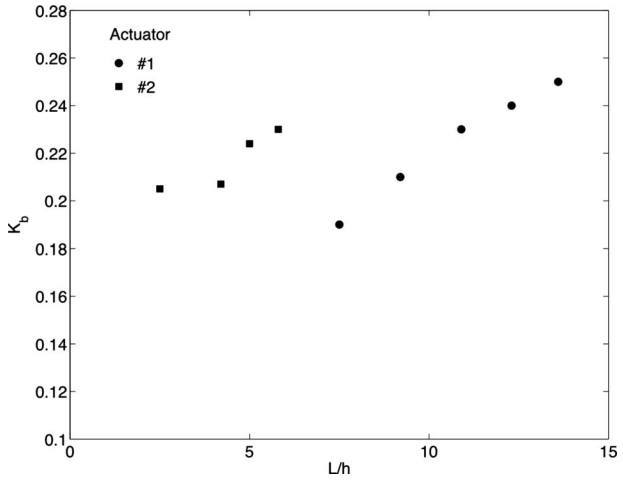

Fig. 15 Variation in spreading rate with increasing stroke ratio for both actuators

The lateral spreading rate for case 1a was calculated to be 0.19, which is greater than the spreading rate of a turbulent continuous jet of 0.11. Consequently for the synthetic jet $\sigma=4.6$, in comparison to 7.67 for a continuous jet. With the plane jet spreading rate expressed as Eq. (5), an increase in the driving voltage was observed to increase the lateral spreading rate (K_b) as shown in Fig. 15 for both actuators. As mentioned earlier the spreading rates show dependence on the geometry of the actuator. The error based on the uncertainty in velocity measurements, stage position, and curve fitting are estimated to be between 3% and 7%.

Figure 16 presents the variation in the eddy viscosity (Eq. (6)) with stroke ratio for the two actuators. The eddy viscosity of an equivalent continuous jet is also shown for comparison. Synthetic and continuous jets of the same orifice width (h) are considered equivalent in this investigation based on momentum flux, or otherwise if the steady bulk exit velocity of a continuous jet is equal to the time average velocity of a synthetic jet as calculated from $U_o=\sqrt{2}fL$. The eddy viscosity of the synthetic jet is seen to far exceed that of the equivalent continuous jet. The effect of employing a velocity scaling based on mass flux is to reduce the eddy viscosity as reported in Fig. 16 by a factor of $\sqrt{2}$. With the eddy

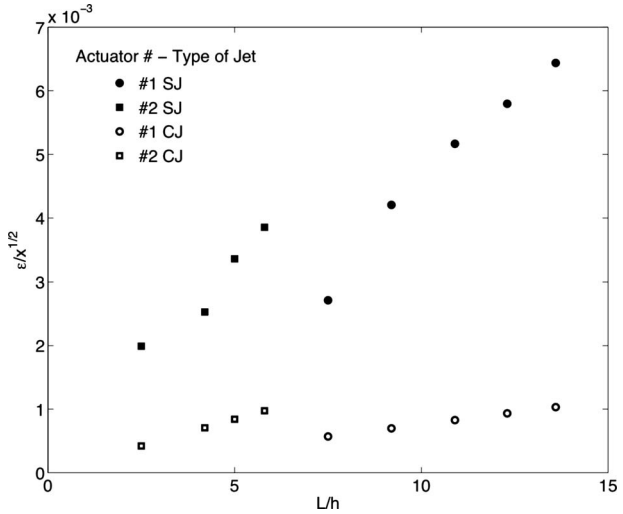

Fig. 16 Dependence of eddy viscosity (ε) on stroke ratio for the two synthetic jet actuators. The eddy viscosity of equivalent turbulent continuous jets are shown for comparison: CJ-continuous jet and SJ-synthetic jet.

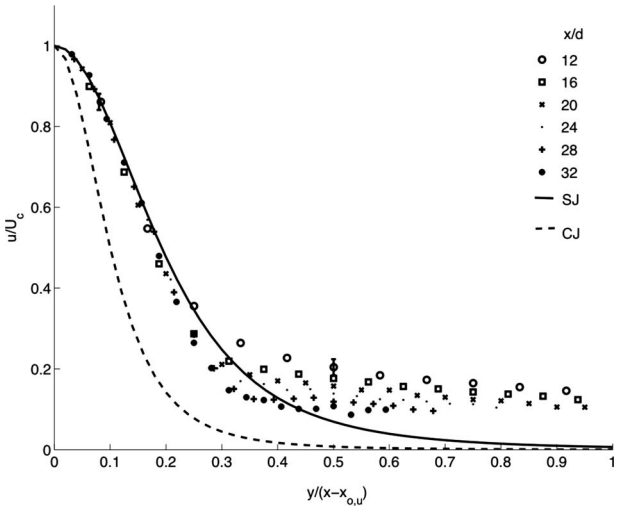

Fig. 17 Comparison of the analytical model and experimental data of a synthetic jet (Case 1a)

viscosity encompassing the capacity to transfer momentum to the surrounding fluid, it appears that the periodic nature of a synthetic jet greatly enhances the momentum transfer in comparison to continuous jets. The observed increase in the spreading rate, velocity decay rate, and eddy viscosity with stroke ratio may be explained as follows. It is known that the interactions of the large-scale coherent vortical structures in a jet are primarily responsible for mixing and spreading. An increase in excitation amplitude or otherwise stroke ratio results in an increase in the size of the slug (and subsequent vortical structure) issuing from the orifice. This slug additionally has an increased impulse and energy associated with it. This increased volume, impulse, and energy result in enhanced interactions further downstream, resulting in increased spreading and more rapid decay [2,19]. This higher eddy viscosity of the synthetic jet makes it appropriate for applications where changes in the surrounding fluid are desired as in fluid mixing or flow control.

Figure 17 compares the analytical time average velocity profiles of the jet obtained from Eq. (2) with the experimental data. A profile of an equivalent continuous turbulent jet with a spreading rate of 0.1 is presented for comparison. Error bars are selectively shown in two locations at $y-y_o/x=0.1$ and 0.5 for representative purposes. Other points in the bell part of the plot have error bars with similar magnitude. The enhanced mixing present in the synthetic jet in comparison to the continuous jet is clearly seen. The model approximates the data well toward the center of the jet thereby validating the eddy viscosity replacement hypothesis. However, progressing away from the center there is some deviation where the model underpredicts the flow. This discrepancy between the self-similar solution and the experimental data has also been observed in turbulent jets; see page 119 of Ref. [45]. This has been attributed to the constant eddy viscosity assumption in the self-similar solution. Here, we observe similar discrepancy for a synthetic jet. It is also plausible that toward the edges the flow is not predominantly in the streamwise direction, and thus the hot-wire measurement are less accurate [30,46]. Additional velocity components in the cross-stream or spanwise direction would results in the hot-wire measurements being higher than the true value which may explain why the model under predicts the velocity there [46].

5 Conclusions

The external flow field of a rectangular synthetic jet was studied using hot-wire anemometry. Four regions as distinguished by the centerline velocity were recognized. (i) An initial developing re-

gion where the coherent periodic vortical structures exist and interact, (ii) a quasi-two-dimensional region where the jet exhibits characteristics similar to a planar continuous jet, (iii) a transition region where the jet once again deviates from planar jet behavior on account of the spreading influence of the narrow edges, and (iv) an axisymmetric region where the jet starts to decay like a round jet. In the quasi-two-dimensional region the time average velocity profiles in the lateral direction exhibit self-similar behavior. The centerline velocity decay and jet width growth show trends similar to a continuous turbulent jet. This similitude leads to the hypothesis that the synthetic jet may be modeled as a continuous turbulent jet with the replacement of the eddy viscosity of a turbulent jet with that of a synthetic jet. The systematic modeling of the synthetic jet is carried out to show that similar to a continuous turbulent jet, the eddy viscosity of a synthetic jet can be obtained from the spreading and decay rates of the jet. The experiments on the flow field validate this hypothesis, further showing the eddy viscosity of the synthetic jet is larger than an equivalent continuous turbulent jet. This enhanced eddy viscosity is attributed to the additional mixing brought about initially by the introduction of the periodic vortical structures and their ensuing break down and transition to turbulence. Therefore by using the adjusted value of the eddy viscosity, the theoretical models of a continuous turbulent jet may still be used to model a synthetic jet. Within the small range tested, the velocity decay rate and spreading rate were insensitive to Reynolds number. However, both parameters increase with an increase in stroke ratio. The study shows a semi-analytical method in modeling synthetic jets that connects (i) the external flow field as characterized by the spreading rate (K_b) and velocity decay rate (K_u) to the actuator parameters ($L/h, \mathrm{Re}_{U_o}$), and (ii) the actuator parameters to the input driving function (Δ, f).

While the above analysis and method provided useful tools for modeling the synthetic jet, there is still work that needs to be addressed. First an extensive parametric study is needed to assess the effects of the geometry and actuation parameters on the issuing synthetic jet. A thorough study characterizing the variable space may lend itself to a functional relationship between the spreading/decay rates to the geometric and operational parameters as represented below.

$$K_u, K_b = f\left(\frac{L}{h}, \mathrm{Re}_{U_o}, \frac{h}{H}, \ldots\right) \tag{12}$$

This study may then show that certain variables are not critical, thus reducing the number of variables resulting in some simplification. Second, at a fundamental level, the classic similarity analysis employed in this study assumes that the jet originates from a constant source of momentum. Even though the far field of a synthetic jet may be approximated by the results of the classic analysis, the constant momentum efflux is clearly not realized in a synthetic jet. Thus the next step in terms of analysis would be to seek a connection between an oscillatory transient point source of momentum and the ensuing steady flow that develops far from the source. This may further yield a clearer description of the evolution particular to a synthetic jet. Both these areas are topics of future work.

Acknowledgment

The authors thank Mr. Yunfei Wang for his initial contribution to the experiment, and the reviewers for their insightful comments that added clarity to the paper.

Nomenclature

- K = kinematic momentum flux per unit length (m^3/s)
- L = length of slug (m)
- Re_{U_o} = Reynolds number
- T = time period of oscillation (s)
- f = frequency of oscillation (Hz)
- h = width of orifice (m)
- r = radial coordinate on membrane
- u = time average streamwise velocity (m/s)
- v = time average transverse velocity (m/s)
- w = spanwise length of orifice (m)
- x = streamwise coordinate
- y = transverse coordinate
- z = spanwise coordinate
- ε = eddy viscosity (m^2/s)
- η = self-similar variable
- ρ = density of fluid (kg/m^3)
- τ = turbulent shear stress (Pa)
- Δ = centerline peak to peak deflection of membrane (m)
- $b_{1/2}$ = jet half width (m)
- K_b = spreading rate
- K_u = scaled velocity decay constant
- U_c = centerline streamwise velocity (m/s)
- U_o = average actuator exit velocity (m/s)
- V_d = driving voltage (V)
- $x_{o,u}$ = axial location of virtual origin based on velocity (m)
- $x_{o,b}$ = axial location of virtual origin based on width (m)

References

[1] Glezer, A., and Amitay, M., 2002, "Synthetic Jets," Annu. Rev. Fluid Mech., **34**, pp. 503–529.
[2] Utturkar, Y., Holman, R., Mittal, R., Carroll, R., Sheplak, B., and Cattafesta, L., 2003, "A Jet Formation Criterion for Synthetic Jet Actuators," 41st Aerospace Sciences Meeting and Exhibit, Reno, NV, AIAA Paper No. 2003-0636.
[3] Holman, R., Utturkar, Y., Mittal, R., Smith, B., and Cattafesta, L., 2005, "Formation Criterion for Synthetic Jets," AIAA J., **43**(10), pp. 2110–2116.
[4] Amitay, M., Smith, B., and Glezer, A., 1998, "Aerodynamic Flow Control Using Synthetic Jet Technology," 36th Aerospace Sciences Meeting and Exhibit, Paper No. 98-0208.
[5] Seifert, A., Eliahu, S., Greenblatt, D., and Wygnanski, I., 1998, "Use of Piezoelectric Actuators for Airfoil Separation Control," AIAA J., **36**(8), pp. 1535–1537.
[6] Rathnasingham, R., and Breuer, K., 2003, "Active Control of Turbulent Boundary Layers," J. Fluid Mech., **495**, pp. 209–233.
[7] Mahalingam, R., and Glezer, A., 2005, "Design and Thermal Characteristics of a Synthetic Jet Ejector Heat Sink," ASME J. Electron. Packag., **127**(2), pp. 172–177.
[8] Pavlova, A., and Amitay, M., 2006, "Electronic Cooling Using Synthetic Jet Impingement," ASME J. Heat Transfer, **128**(9), pp. 897–907.
[9] Davis, S. A., and Glezer, A., 1999, "Mixing Control of Fuel Jets Using Synthetic Jet Technology," AIAA Paper No. 99-0447.
[10] Parviz, B., Najafi, K., Muller, M., Bernal, L., and Washabaugh, P., 2005, "Electrostatically Driven Synthetic Microjet Arrays as a Propulsion Method for Micro Flight—Part I: Principles of Operation, Modelling, and Simulation," Microsyst. Technol., **11**(11), pp. 1214–1222.
[11] Finley, T., and Mohseni, K., 2004, "Micro Pulsatile Jets for Thrust Optimization," 2004 ASME International Mechanical Engineering Congress and RD&D Expo, Anaheim, CA, Paper No. IMECE 2004-62042.
[12] Vargas, Y., Finley, T., Mohseni, K., and Hertzberg, J., 2006, "Flow Characterization of a Synthetic Jet," 44th AIAA Aerospace Sciences Meeting and Exhibit, Reno, NV, AIAA Paper No. 2006-1422,.
[13] Krishnan, G., and Mohseni, K., 2007, "On the Modeling of a Synthetic jet as a Spherical Jet," Fifth Joint ASME/JSME Fluids Engineering Conference, San Diego, CA, Paper No. FEDSM2007 2007-37306.
[14] Mohseni, K., 2006, "Pulsatile Vortex Generators for Low-Speed Maneuvering of Small Underwater Vehicles," Ocean Eng., **33**(16), pp. 2209–2223.
[15] Krieg, M., and Mohseni, K., 2008, "Thrust Characterization of Pulsatile Vortex Ring Generators for Locomotion of Underwater Robots," IEEE J. Ocean. Eng., **33**(2), pp. 123–132.
[16] Mallinson, S., Hong, G., and Reizes, J., 1999, "Some Characteristics of Synthetic Jets," *Proceedings of the 30th AIAA Fluid Dynamics Conference*, Norfolk, VA, AIAA Paper No. 1999-3651.
[17] Cater, J., and Soria, J., 2002, "The Evolution of Round Zero-Net-Mass-Flux Jets," J. Fluid Mech., **472**, pp. 167–200.
[18] Shuster, J. and Smith, D., 2007, "Experimental Study of the Formation and Scaling of a Round Synthetic Jet," Phys. Fluids, **19**(4), p. 045109.
[19] Smith, B., and Glezer, A., 1998, "The Formation and Evolution of Synthetic Jets," Phys. Fluids, **10**(9), pp. 2281–2297.
[20] Smith, B., and Swift, G., 2003, "A Comparison Between Synthetic Jets and Continuous Jets," Exp. Fluids, **34**(4), pp. 467–72.

[21] Fugal, S. R., Smith, B. L., and Spall, R. E., 2005, "Displacement Amplitude Scaling of a Two-Dimensional Synthetic Jet," Phys. Fluids, **17**(4), p. 045103.
[22] Gutmark, E., and Grinstein, F., 1999, "Flow Control With Noncircular Jets," Annu. Rev. Fluid Mech., **31**, pp. 239–272.
[23] Grinstein, F., 2001, "Vortex Dynamics and Entrainment in Rectangular Free Jets," J. Fluid Mech., **437**, pp. 69–101.
[24] Rizetta, D. P., Visbal, M. R., and Stanek, M. J., 1998, "Numerical Investigation of Synthetic Jet Flowfields," AIAA Paper No. 98-2910.
[25] Menon, S., and Soo, J.-H., 2004, "Simulation of Vortex Dynamics in Three-Dimensional Synthetic and Free Jets Using the Large-Eddy Lattice Boltzmann Method," J. Turbul., 5, Art. No. 32.10.1088/1468-5248/5/1/032
[26] Zhong, S., Garcillan, L., Pokusevski, Z., and Wood, N., 2004, "A PIV Study of Synthetic Jets With Different Orifice Shape and Orientation," AIAA Paper No. 2004-2213.
[27] Amitay, M. and Cannelle, F., 2006, "Evolution of Finite Span Synthetic Jets," Phys. Fluids, **18**(5), p. 054101.
[28] Ravi, B., 2006, "Numerical Study of Large Aspect-Ratio Synthetic Jets," AIAA Paper No. 2006-315.
[29] Mittal, R., Rampunggoon, P., and Udaykumar, H. S., 2001, "Interaction of a Synthetic Jet With a Flat Plate Boundary Layer," AIAA Paper No. 2001-2773.
[30] Kotapati, R. B., Mittal, R., and Cattafesta, L. N., III, 2007, "Numerical Study of a Transitional Synthetic Jet in Quiescent External Flow," J. Fluid Mech., **581**, pp. 287–321.
[31] Schlichting, H., 1933, "Laminare strahlausbreitung," J. Appl. Math. Mech., **13**, pp. 260–263.
[32] Schlichting, H., 1979, *Boundary-Layer Theory*, McGraw-Hill, New York.
[33] Gallas, Q., Holman, R., Nishida, T., Carroll, B., Sheplak, M., and Cattafesta, L., 2003, "Lumped Element Modeling of Piezoelectric-Driven Synthetic Jet Actuators," AIAA J., **41**(2), pp. 240–247.
[34] Glezer, A., 1988, "The Formation of Vortex Rings," Phys. Fluids, **31**(12), pp. 3532–3542.
[35] Timoshenko, S., 1999, *Theory of Plates and Shells*, McGraw-Hill, New York.
[36] Smith, B., and Swift, G., 2001, "Synthetic Jets at Larger Reynolds Number and Comparison to Continuous Jets," 31st AIAA Fluid Dynamics Conference and Exhibit, Anaheim, CA, AIAA Paper No. 2001-3030.
[37] Johnstone, A., Uddin, M., and Pollard, A., 2005, "Calibration of Hot-Wire Probes Using Non-Uniform Mean Velocity Profiles," Exp. Fluids, **39**(3), pp. 527–534.
[38] Blevins, R. D., 1995, *Formulas for Natural Frequency and Mode Shape*, Krieger, Malabar, FL.
[39] Everest, F., 2000, *The Master Handbook of Acoustics*, McGraw-Hill, New York.
[40] Krothapalli, A., Baganoff, D., and Karamcheti, K., 1981, "On the Mixing of a Rectangular Jet," J. Fluid Mech., **107**, pp. 201–220.
[41] Tavoularis, S., 2005, *Measurement in Fluid Mechanics*, Cambridge University Press, Cambridge, UK.
[42] Marsters, G. F., 1981, "Spanwise Velocity Distributions in Jets From Rectangular Slots," AIAA J., **19**(2), pp. 148–152.
[43] Van Der Hegge Zijnen, B., 1958, "Measurements of Velocity Distribution in Plane Turbulent Jet of Air," Appl. Sci. Res., Sect. A, **7**(4), pp. 256–276.
[44] Quinn, W., Pollard, A., and Marsters, G., 1983, "On "Saddle-Backed" Velocity Distributions in Three-Dimensional Turbulent Free Jets," AIAA Paper No. 83-1677.
[45] Pope, S., 2000, *Turbulent Flows*, Cambridge University Press, New York.
[46] Rumsey, C., Gatski, T., Sellers, W., Vatsa, V., and Viken, S., 2006, "Summary of the 2004 Computational Fluid Dynamics Validation Workshop on Synthetic Jets," AIAA J., **44**(2), pp. 194–207.

Flow Separation Control on a Race Car Wing With Vortex Generators in Ground Effect

Yuichi Kuya
e-mail: yuichi@soton.ac.uk

Kenji Takeda
Senior Lecturer
e-mail: ktakeda@soton.ac.uk

Xin Zhang
Professor
e-mail: x.zhang1@soton.ac.uk

Scott Beeton[1]

Ted Pandaleon[2]

School of Engineering Sciences,
University of Southampton,
Southampton SO17 1BJ, UK

Flow separation control using vortex generators on an inverted wing in ground effect is experimentally investigated, and its performance is characterized in terms of forces and pressure distributions over a range of incidence and ride height. Counter-rotating and co-rotating rectangular-vane type vortex generators are tested on the suction surface of the wing. The effect of device height and spacing is investigated. The counter-rotating sub-boundary layer vortex generators and counter-rotating large-scale vortex generators on the wing deliver 23% and 10% improvements in the maximum downforce, respectively, compared with the clean wing, at an incidence of one degree, and delay the onset of the downforce reduction phenomenon. The counter-rotating sub-boundary layer vortex generators exhibit up to 26% improvement in downforce and 10% improvement in aerodynamic efficiency at low ride heights. Chordwise pressure measurement confirms that both counter-rotating vortex generator configurations suppress flow separation, while the co-rotating vortex generators exhibit negligible effectiveness. This work shows that a use of vortex generators, notably of the counter-rotating sub-boundary layer vortex generator type, can be effective at controlling flow separation, with a resultant improvement in downforce for relatively low drag penalty. [DOI: 10.1115/1.4000420]

1 Introduction

In open-wheel racing series, such as Formula 1 and Indy Racing, both a front wing and rear wing are inverted to produce downforce, that is, negative lift, leading to an enhancement of acceleration and cornering performance of the cars. The aerodynamic performance plays a significant role in open-wheel race cars and is one of the most important factors to be developed [1,2]. The performance of aerodynamic devices is altered when operating in close proximity to a solid boundary, known as the ground effect regime, and different flow features are exhibited compared with the freestream condition. This study attempts to improve aerodynamic performance of a generic single-element inverted wing, modeling a race car front wing, in ground effect via vortex generator (VG) attachment. VGs are known to be capable of controlling flow separation in adverse pressure gradient flows [3,4].

A number of experimentally investigated studies for the front wing have been previously carried out [5–11]. Typical features of a single-element wing in ground effect are described by Zerihan and Zhang [5] and Zhang and Zerihan [6] using a moving ground. In wind tunnel testing, use of a moving ground rig, which runs at the same speed as the freestream in order to control the boundary layer on the ground, is necessary for race car aerodynamics in ground effect to properly simulate the real conditions on a race track. Zerihan and Zhang [5] showed not only an increase of downforce as the ride height is reduced but also captured the downforce reduction phenomenon, when the wing is mounted below the height where the maximum downforce is generated. The results of surface flow visualization revealed the downforce reduction phenomenon by showing a breakdown of edge vortices at the end plates and flow separation on the suction surface of the wing. Flow separation is induced by the large adverse pressure gradient, where the streamwise momentum of the flow is reduced, and the flow separates from the wall [3,4]. At a moderate ride height, flow separation was observed near the trailing edge of the wing, and as the wing is brought close to the ground through the ride height of the maximum downforce, the region of the flow separation increases, resulting in the loss of the downforce. Zhang and Zerihan [6] studied characteristics of the edge vortices with respect to the ride height. It was shown that the edge vortices break down when the wing reaches maximum downforce height. The investigations suggest that separation control on the suction surface of a wing and a development of end plates could improve the aerodynamic performance of the wing, controlling the flow and edge vortices, leading to higher downforce or more efficient downforce-to-drag ratio. In general, flow separation is generated downstream of maximum suction point, and even though the effect of the separation on lift or downforce of a wing is not significant, a thicker turbulent boundary layer, yielded by the separation, induces a significant increase in drag, thus, adversely affects the performance of the wing [12].

A number of separation control methods exists. Lin [12,13] suggested that effective devices for separation control are those that generate streamwise vortices such as those produced by VGs. The VGs commonly used for aeronautical applications are attached upstream of the separation line and generate streamwise vortices, which accelerate mixing of streamwise momentum of the freestream and the flow in a boundary layer in order to overcome the large adverse pressure gradient. Sub-boundary layer vortex generators (SVGs) have a device height between 10% and 50% of the boundary layer thickness according to the classification of Lin [12], and are more advantageous in terms of effectiveness and less drag penalty compared with large-scale vortex generators (LVGs), whose device height is of the same order as the boundary layer thickness [12–14]. Several experimental investigations of VGs have been performed to improve wing performance in freestream [13,15–17]. Garcia and Katz [18] and Katz and Morey [19] investigated LVGs attached to a flat plate in ground effect, simulating an application of VGs on lower surface of race cars. There is, however, a lack of investigation of an inverted wing with VGs for separation control in ground effect. There have been computational studies regarding VG applications; a flat plate [20,21],

[1]Present address: Williams F1.
[2]Present address: TotalSim LLC.

Contributed by the Fluids Engineering Division of ASME for publication in the JOURNAL OF FLUIDS ENGINEERING. Manuscript received March 20, 2009; final manuscript received October 1, 2009; published online November 19, 2009. Editor: Joseph Katz.

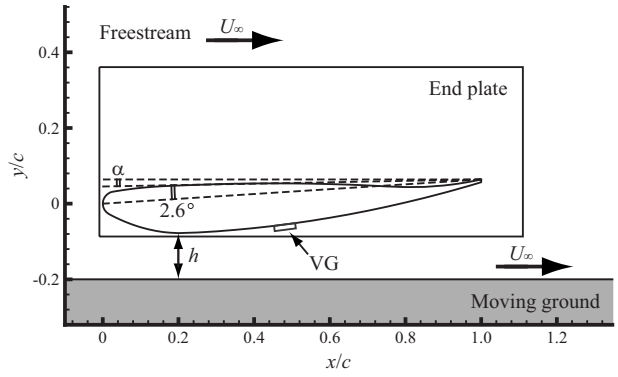

Fig. 1 Schematic of single-element wing, end plate, and VG

wings [22], and source term models [22–24]. An application of VGs to an inverted wing in ground effect was computationally studied by Kuya et al. [25].

This paper investigates contribution of VGs on aerodynamic performance of an inverted wing in ground effect, describing time-averaged force and pressure characteristics. The experimental testing is performed in a wind tunnel equipped with a moving belt rig. Rectangular vane type SVGs and LVGs are used and attached on the suction surface of the wing in counter-rotating and co-rotating configurations. Different device spacings are also studied with the SVGs. Kuya et al. [26] described the detailed flow characteristics of an inverted wing with VGs in ground effect, using surface flow visualization and particle image velocimetry.

2 Experimental Setup

2.1 Test Facility. The experiments described here are performed in the 2.1m × 1.5m closed section wind tunnel at the University of Southampton. This wind tunnel has been used for a number of ground effect aerodynamics studies, including Zerihan and Zhang [5,9], Zhang and Zerihan [6–8], Senior and Zhang [27], Ruhrmann and Zhang [28], and Zhang et al. [29]. The tunnel is of conventional return circuit design and is equipped with a moving belt rig and a three-component overhead balance system. The 3.2m × 1.5m moving belt is controlled by slots and suction system for boundary layer removal, which gives 99.8% of the freestream velocity at 2 mm above the belt. The turbulence intensity of the freestream is about 0.3%. Further descriptions of the wind tunnel are given by Burgin et al. [30]. For the experiments presented here, the freestream velocity U_∞ and moving belt speed are set at 30 m/s, corresponding to Reynolds number Re of 450,000 based on the wing chord c.

2.2 Experimental Models. Figure 1 shows a schematic of the single-element wing geometry and installation used. The model used is an 80% scale model of the main element of the 1998 Tyrrell 026 F1 car front wing, which is based on a NASA GA(W) profile, type LS(1)-0413, and is manufactured by carbon fiber composite. The model has a span of 1100 mm, constant chord c of 223.4 mm, and finite trailing edge of 1.65 mm and is the same model used by Zerihan and Zhang [5,9] and Zhang and Zerihan [6]. The origin of the coordinate system is set at the leading edge of the wing. Generic end plates of 250mm × 100mm × 4mm are attached on both ends of the wing throughout the experiment. The incidence α is measured relative to a line from the trailing edge to the most swelled point on the pressure surface which corresponds to 2.6 deg relative to the chord line. The true incidence is therefore equal to the measured incidence plus 2.6 deg. When the incidence is 1 deg, corresponding to the true incidence of 3.6 deg, the upper and lower edges of the end plates are parallel to the ground. The incidence is varied by rotating about the quarter chord position. The ride height h is defined by the distance from the lowest point on the suction surface of the wing to the moving ground as the incidence is fixed at 1 deg.

Rectangular vane type VGs are employed here comprising three configurations, which are counter-rotating sub-boundary layer vortex generators (CtSVGs), counter-rotating large-scale vortex generators (CtLVGs), and co-rotating sub-boundary layer vortex generators (CoSVGs). The SVG and LVG have a device height of 2 mm ($(h_{VG}/c)=0.009$) and 6 mm ($(h_{VG}/c)=0.027$), respectively. The VGs are made of aluminum plate with 0.6 mm thickness and built in pairs separated by $4h_{VG}$ at the trailing edge of the VGs. Although carbon fiber may be used in race car applications, effects due to the difference of VG material are deemed negligible. The vanes are oriented at ±15 deg relative to the streamwise direction, comprising the counter-rotating or co-rotating VG configuration. Pairs of VGs are put side by side along the span of the wing, as shown in Fig. 2. The VGs are attached on the suction surface of the wing such that the trailing edge of the VGs is fixed at $(x/c)=0.537$. The height to length ratio of the vanes is fixed at 1:4. For the CtLVG and CoSVG configurations, the device spacing d_{VG} between each device pair of the VGs is fixed at $4h_{VG}$, while close- and wide-spacings of $2h_{VG}$ and $8h_{VG}$ are also examined with the CtSVG configuration in addition to the reference-spacing of $4h_{VG}$. Unless there is a particular notation, "CtSVG" represents a CtSVG configuration with the reference-spacing of $4h_{VG}$, which is the same device spacing as the other VG configurations.

2.3 Experimental Methods. The time-averaged downforce and drag are measured by a three-component overhead balance system. The coefficients of downforce and drag are calculated by using the corrected force values, taking into account variances of air density because of changes in the freestream temperature and pressure during the tests. The C_L quoted in the investigation represents the downforce coefficient. The ride height of the wing is altered between $0.045c$ and $0.448c$. The incidence is swept from 1 deg to 17 deg.

A pressure tapped wing model is employed for the surface pressure measurement on the wing in the chordwise direction. The tapped wing has the same geometry as the wing used in the force measurement. The pressure tapped array has an orientational angle of 22.5 deg regarding the streamwise direction. Twenty-five and 23 pressure taps are, respectively, mounted on the suction surface and pressure surface around the center portion of the wing. An

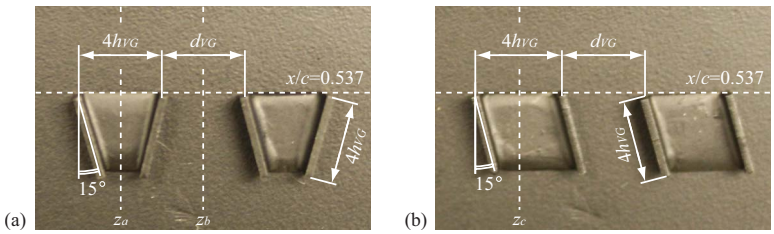

Fig. 2 Configuration of VGs on wing: (*a*) counter-rotating VGs and (*b*) co-rotating VGs. Flow is from bottom to top.

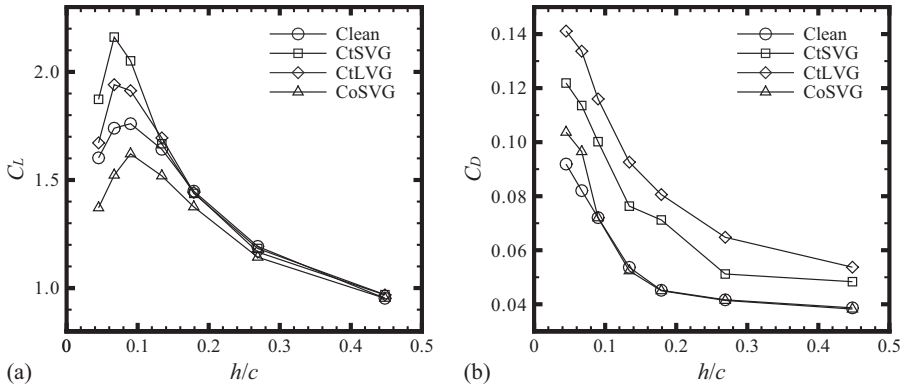

Fig. 3 Force characteristics at various ride heights at $\alpha=1$ deg: (*a*) downforce and (*b*) drag

average in the spanwise direction is taken for the measurement of the VG configurations since the flow of the VG configurations is not two-dimensional and is described in detail in the Appendix. The ride height and incidence are fixed at $0.090c$ and 1 deg, respectively.

2.4 Repeatability and Uncertainty. The repeatability and uncertainties are estimated for the force and pressure measurements using procedures described in Refs. [31,32]. The repeatability of the measurements is categorized into short, medium, and long-term repeatability. In the short term repeatability test, data are continuously taken during a single wind tunnel run without turning the wind tunnel off. The medium-term repeatability is tested by starting from scratch settings of experimental parameters such as the incidence and ride height of the wing. The test is conducted with several wind tunnel runs over a couple of hours. For the long-term repeatability test, a set of data is taken in an interval of more than 1 month. The standard error for the short, medium, and long terms is given as 0.0016, 0.0018, and 0.043 for the downforce coefficient, 0.00019, 0.00028, and 0.0064 for the drag coefficient, respectively, while for the pressure coefficient, the standard error for each term is, respectively, given as 0.035, 0.034, and 0.067. The uncertainty of the downforce, drag, and pressure coefficients for the medium-term are, respectively, given as 0.0035, 0.0006, and 0.068 with the 95% confidence, where the coverage factor of 2 is used.

3 Results

3.1 Force Characteristics. Figure 3 shows the downforce and drag coefficients of the four different configurations examined here at various ride heights at $\alpha=1$ deg.

All the configurations show a downforce enhancement regime and reach the maximum downforce, followed by a downforce reduction regime as the wing is moved closer to the ground. Of interest here is that both counter-rotating VG configurations exhibit higher downforce below $(h/c)=0.134$ compared with the clean wing, meanwhile the CoSVG configuration exhibits a deterioration of performance at almost all ride heights. For ride heights above $(h/c)=0.134$, both the counter-rotating VG configurations show very similar downforce to that yielded by the clean wing. At $(h/c)=0.134$, Zerihan and Zhang [5] discussed small regions of flow separation on the suction surface of the clean wing at 95% chord that appears to grow as the ride height is decreased. The higher downforce of the counter-rotating VG configurations could be due to the suppression of the flow separation below $(h/c)=0.134$ [26]. Further evidence for this are presented in the pressure distributions discussed as follows. In addition, although it may be inferred that the downforce increase is due to the increased suction by the VG-generated vortices, the evidence that both the counter-rotating VG configurations produce very similar downforce to the clean wing for ride heights above $(h/c)=0.134$ indicate that the effect of the increased suction due to the VG-generated vortices is not significant; the downforce enhancement due to the VGs attachment could be mainly led by the suppression of flow separation rather than the increased suction due to the VG-generated vortices. The use of CtSVGs and CtLVGs on the wing delivers 23% and 10% improvements in the maximum downforce, respectively. Additionally, the counter-rotating VG configurations show a delay of the downforce reduction phenomenon; while, for the clean wing, the downforce reaches a maximum at $(h/c)=0.090$ and drops below this ride height, both the counter-rotating VG configurations reach the maximum value at $(h/c)=0.067$ and the downforce reduction phenomenon are observed below this height. The downforce of the counter-rotating VG configurations show almost the same values above $(h/c)=0.134$, and the CtSVG configuration generates higher downforce than the CtLVG configuration below $(h/c)=0.134$. The downforce of the CoSVG configuration reaches the maximum values at $(h/c)=0.090$, the same as the clean wing but with lower magnitude.

The drag indicates an increase of value as the wing is moved closer to the ground. The gradient of the curves becomes steeper as the wing is mounted below $(h/c)=0.134$. For the clean wing, the increase of drag is due to an enhancement of the pressure drag; the streamwise component of the force generated by the pressure on the wing. As the wing moves closer to the ground the force enhancement phenomenon and flow separation on the suction surface lead to enhancement of the pressure drag. All of the VG configurations generate higher drag than the clean wing at all the ride heights. For the CoSVG configuration, since the CoSVGs exhibits a deterioration in performance of the wing as shown in the downforce, the increase in the pressure drag should be relatively small. Therefore, the contribution of the drag increase in the CoSVG configuration is led by the device drag, which is composed of the pressure drag and skin friction drag of the VGs. The CtLVG configuration generates higher total drag than the CtSVG configuration. By the comparison between the CtSVG and CtLVG configurations, it can be deduced that the contribution of the device drag of the counter-rotating VGs to the total drag enhancement is higher than that of the pressure drag. The CtSVG configuration generates a higher pressure difference between the pressure and suction surfaces than the CtLVG configuration, and hence the pressure drag of the CtSVG configuration should be higher than that of the CtLVG configuration. The total drag is, however, higher for the CtLVG configuration compared with the CtSVG configuration at all the ride heights examined here.

Figure 4 shows contour maps of downforce with respect to the incidence and ride height of the four configurations. The downforce contours show that both the counter-rotating VG configura-

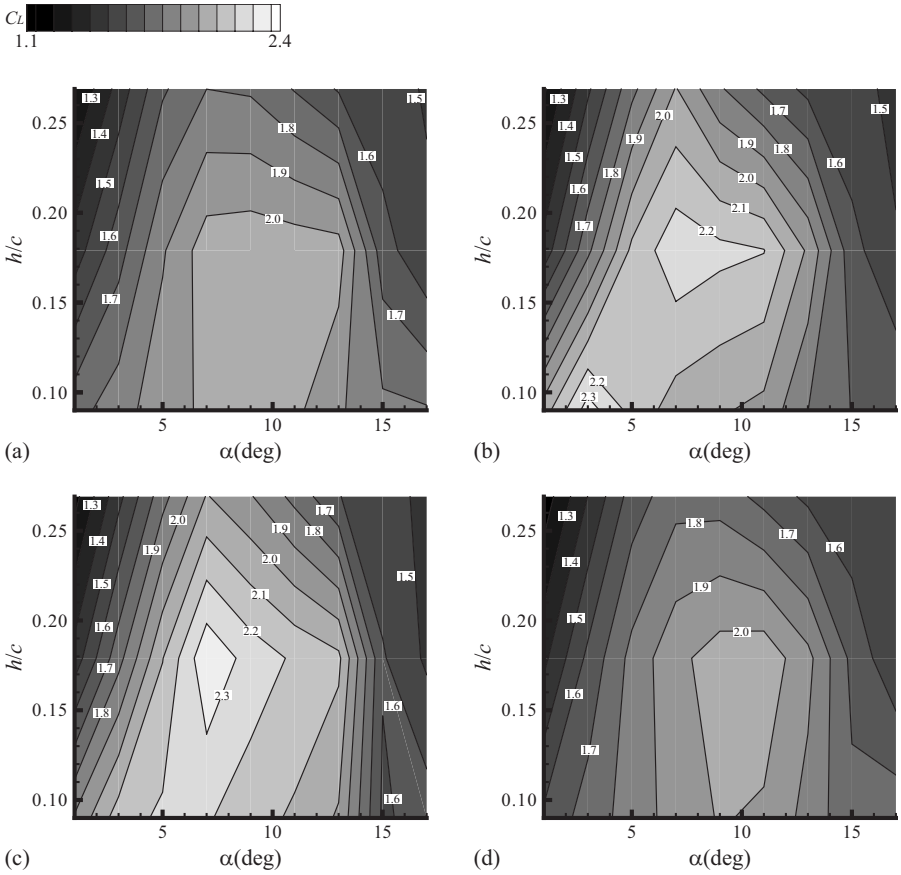

Fig. 4 Downforce characteristics with respect to incidence and ride height: (*a*) clean, (*b*) CtSVG, (*c*) CtLVG, and (*d*) CoSVG

tions produce higher downforce, showing steep gradient of contour lines at low incidences, and reaching the maximum downforce region distributing relatively lower incidences compared with the clean wing. The CtSVG configuration also indicates another high downforce region around $(h/c)=0.090$ and $\alpha=3$ deg addition to the region around the center of the plot. The CoSVG configuration shows the similar degree of the downforce but a smaller high downforce region than clean wing, indicating the CoSVG configuration deteriorates the performance. Table 1 lists increases in the maximum downforce via the attachment of the VGs against the clean wing at $(h/c)=0.090$, 0.179, and 0.269. The counter-rotating VG configurations apparently exhibit better improvements in the maximum downforce than the co-rotating VG configurations. The CoSVG configuration reduces the maximum downforce at all the three ride heights.

For the counter-rotating configurations which exhibit higher downforce than the clean wing, downforce and downforce-to-drag ratio improvements relative to the clean wing are shown in Fig. 5. Both the counter-rotating configurations show an improvement in the downforce. The CtSVG configuration shows a higher downforce region at $1\leq\alpha\leq12$ deg at all the ride heights, and 26% maximum improvement is obtained at $\alpha=3$ deg and $(h/c)=0.090$. Meanwhile, the CtLVG configuration indicates a wider region of improvement at $1\leq\alpha\leq14$ deg than the CtSVG configuration, and 16% maximum improvement is achieved at $\alpha=3$ deg and $(h/c)=0.090$, and at $\alpha=7$ deg and $(h/c)=0.179$. Of note here is that the CtSVG configuration exhibits regions of higher efficiency with respect to the clean wing with improvement of the downforce, obtaining 10% maximum improvement at $\alpha=7$ deg and $(h/c)=0.269$, while the CtLVG configuration shows entirely lower efficiency. The effective region of the CtSVG configuration is observed at $2\leq\alpha\leq6$ deg when the ride height is low and at $5\leq\alpha\leq8$ deg when the ride height is high. This is as the strength of adverse pressure gradient on the suction surface is similar between the conditions at low ride height with low incidence and at high ride height with relatively high incidence. In general it is known that adverse pressure gradient, which leads to flow separation, is induced when a wing is operated close to a ground or at high incidence. This suggests that a use of the CtSVGs has advantages both in the downforce and efficiency against certain level of the adverse pressure gradient.

Table 1 Increase in maximum downforce relative to clean wing (%)

h/c	CtSVG	CtLVG	CoSVG
0.090	15.0	8.7	−1.6
0.179	9.6	15.0	−0.1
0.269	11.5	11.5	−1.9

The close- and wide-spacings ($d_{VG}=2h_{VG}$ and $8h_{VG}$) are examined in addition to the reference-spacing ($d_{VG}=4h_{VG}$) in the CtSVG configuration. Figure 6 shows the effect of the device spacing on improvements of downforce and downforce-to-drag relative to the clean wing. The close-spacing CtSVG configuration shows a similar distribution of the improved region of the downforce to the reference-spacing CtSVG configuration; however, higher improvement is observed in most of region. A 24% maximum improvement is obtained at $\alpha=3$ deg and $(h/c)=0.090$, which is slightly less than that of the reference-spacing CtSVG configuration. The distribution of the efficiency is rather different between the close- and reference-spacing CtSVG configuration;

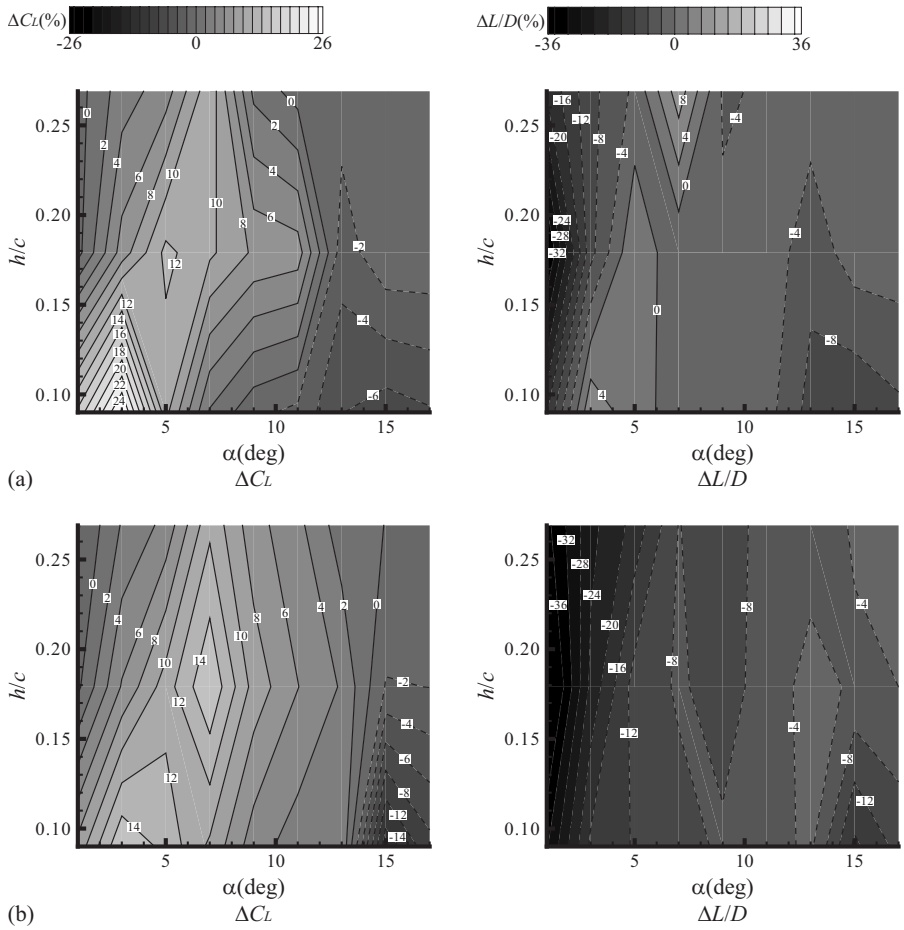

Fig. 5 Effect of counter-rotating VGs on downforce and downforce-to-drag ratio improvements relative to clean wing: (*a*) CtSVG and (*b*) CtLVG

however, the effective region is similar with a 10% maximum improvement at $\alpha=7$ deg and $(h/c)=0.269$. Meanwhile, the wide-spacing CtSVG configuration shows less improvement in downforce and similar or less efficiency compared with the improvements of the close- and reference-spacing CtSVG configurations.

3.2 Averaged-Chordwise Surface Pressure Distributions. Results of the pressure measurement with the pressure tapped wing are presented here. Figure 7 shows distributions of the averaged-chordwise surface pressure on the wing at $\alpha=1$ deg, and $(h/c)=0.090$ corresponding to the clean wing reaches the maximum downforce at $\alpha=1$ deg (Fig. 3(*a*)). The vertical lines in the figure represent the leading and trailing edges of the VGs. The pressure distributions of the VG configurations takes the average in the spanwise direction, since the flows are not two-dimensional, as revealed by surface flow visualization [26]. While the current method does not represent the pure chordwise pressure distributions, it provides a representative measurement to determine the trend characteristics.

All the configurations produce apparently similar pressure distributions on the pressure surface, while both the counter-rotating VG configurations show slightly higher pressure around the trailing edge. Evidence of a short reattachment bubble can be seen at about 30% chord on the suction surface in all of the configurations and is captured by the surface flow visualization in Ref. [26]. For the counter-rotating VG configurations, the VGs enhance the suction compared with the clean wing. The CtSVG configuration shows higher suction on the suction surface than the CtLVG configuration, leading to the higher value of downforce, as shown in the force characteristics. A similar effect can be seen when a Gurney flap is fitted at the trailing edge of a wing, which can enhance the suction over the entire suction surface. The Gurney flap, however, also increases pressure on the pressure surface because the presence of the flap at the trailing edge decelerates the velocity on the pressure surface [9]. The CoSVG configuration shows very similar distribution to that of the clean wing and produces less suction at some points than the clean wing. The gradient of the pressure on the suction surface of the clean wing suddenly changes at about 75% chord, showing a constant value region near the trailing edge. Both the counter-rotating VG configurations, however, show the pressure recovery at an almost constant gradient toward the trailing edge and eliminate the constant value region, indicating that flow separation is suppressed by the VGs. The pressure recovery of the CoSVG configuration indicates a significantly small or negligible effect of the CoSVGs regarding the separation control.

4 Discussion

The experimental result of the force characteristics at $\alpha=1$ deg suggests that both the counter-rotating configurations can increase downforce compared with the clean wing when the wing is operated in the ground effect regime. Meanwhile, the VGs also increase both the pressure and device drag. The results of downforce and downforce-to-drag ratio improvements relative to the clean wing suggest that a use of the CtSVGs has advantages both in downforce and efficiency under some conditions, but the CtLVG configuration indicates less efficiency than the clean wing and CtSVG configuration. For race car applications, tracks require

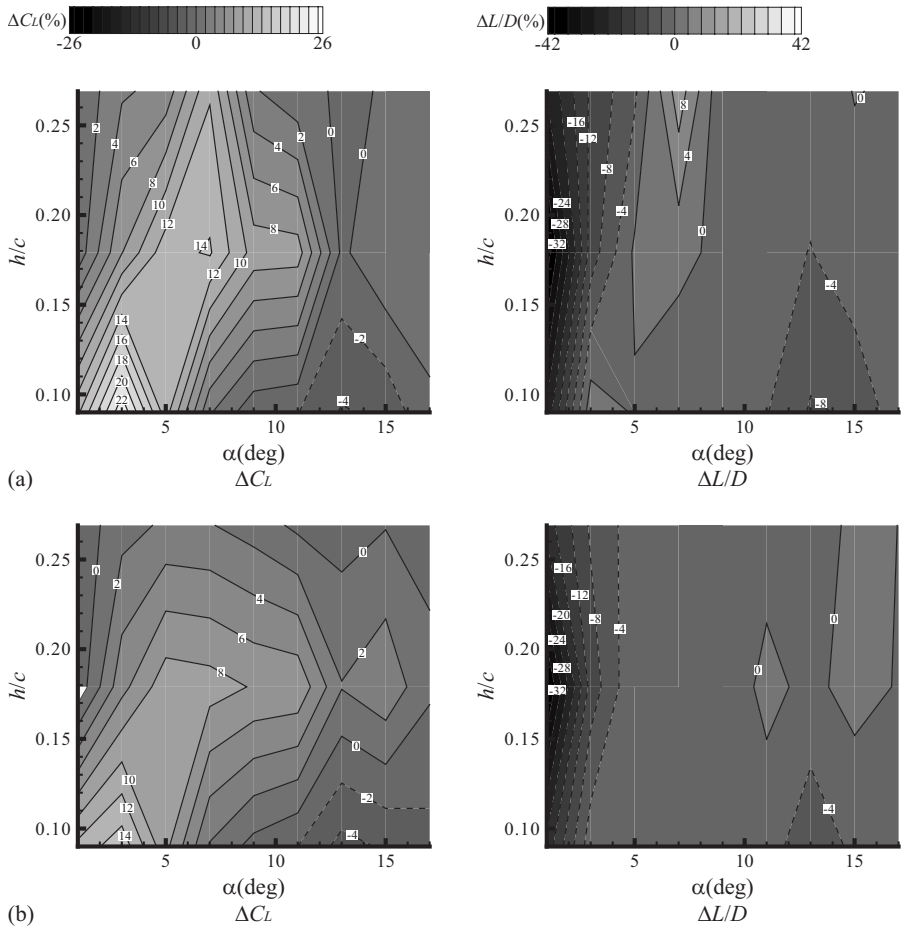

Fig. 6 Effect of VG device spacing on downforce and downforce-to-drag ratio improvements relative to clean wing: (*a*) close-spacing CtSVG and (*b*) wide-spacing CtSVG

different levels of downforce and downforce-to-drag ratio. The use of the VGs may have more favorable effects in a scenario where high downforce is demanded. In this research, the CtSVG configuration shows best performance in terms of the separation control due to the high downforce increase and relatively low drag penalty, meanwhile the CoSVG configuration deteriorates the wing performance.

The close- and wide-spacings ($d_{VG}=2h_{VG}$ and $8h_{VG}$) are examined in addition to the reference-spacing ($d_{VG}=4h_{VG}$) in the CtSVG configuration. The close-spacing CtSVG configuration shows similar level of improvement to the reference-spacing CtSVG configuration in downforce and efficiency relative to the clean wing. Meanwhile, the wide-spacing CtSVG configuration shows less improvement in downforce and similar or less efficiency compared with that of the close- and reference-spacing CtSVG configurations.

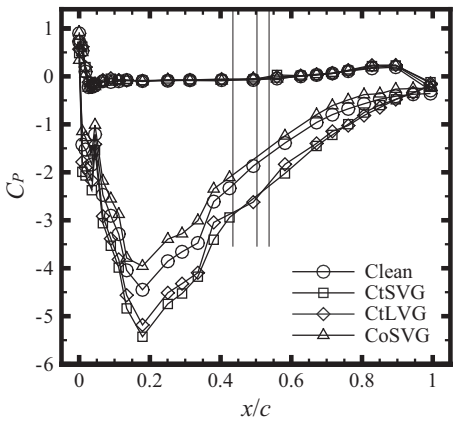

Fig. 7 Averaged-chordwise surface pressure distributions on wing at $\alpha=1$ deg and $(h/c)=0.090$

The suppression of flow separation due to the counter-rotating VGs can be seen in the chordwise pressure distributions. When flow separation has occurred, the pressure distribution plateaus, as the clean wing shows in this investigation. Meanwhile, both the counter-rotating VG configurations show moderate pressure recoveries, indicating a reduced or an absence of flow separation. The CoSVG configuration exhibits a lesser effect of the vortices on separation control, exhibiting a similar pressure recovery trend to that of the clean wing.

The detailed flow characteristics studied by Kuya et al. [26] explains the above features. The vortices generated by the VGs induce the downwash and upwash to the suction surface, which mixes the outer flow and boundary layer flow. The downwash generated at the center of each device pair pumps the high momentum of the outer flow into the boundary layer flow leading to the suppression of flow separation. The co-rotating vortices, however, cancel the downwash and upwash having opposite flow directions to each other at the center between each vane, leading to a more rapid decay of the vortices and thus the negligibly small effect on the separation control.

A further possible advantage of the application of VGs to a race car front wing is that VGs could eliminate hysteresis of the downforce curve with varying ride height. Storms and Ross [17] observed an elimination of hysteresis of lift via wishbone type VGs

performed in a freestream condition. On a race track, a race car is in an unsteady flow condition and the distance between the wing and ground continuously varies. VGs may also be beneficial in cases where active incidence changes are initiated on a wing. These dynamic changes make the hysteresis in force and sometimes make the wing impossible to recover flow condition [11]. The VGs, therefore, could help the wing to produce much more stable characteristics. An application of VGs with a Gurney flap is also of great interest. Zerihan and Zhang [9] showed earlier stall of a Gurney flap fitted wing compared with a clean wing due to its larger adverse pressure gradient on the suction surface. In addition, although an inverted single-element wing is employed and operated in ground effect, in the current investigation, an application of VGs to a multi-element wing is also of great interest and should have some advantages, as indicated in freestream tests [13,15,17]. For the global aerodynamic characteristics of a race car, a front wing with VGs could potentially help to improve the performance of components downstream such as a diffuser and radiator.

5 Concluding Remarks

Contribution of VGs on aerodynamic performance of an inverted wing in ground effect is experimentally examined regarding force and pressure characteristics, and the following conclusions are drawn.

- VGs have an effect on flow separation control in an adverse pressure gradient, particularly at low incidence ($\alpha \leq 5$ deg) and low ride height ($h/c \leq 0.12$), and medium incidence ($5 \leq \alpha \leq 10$ deg) and medium ride height ($0.15 \leq h/c \leq 0.20$) examined here, leading to the improvement of the downforce.
- The attachment of CtSVGs and CtLVGs on the wing respectively delivers 23% and 10% improvements in the maximum downforce relative to the clean wing at $\alpha=1$ deg. The CtSVG configuration shows best performance in terms of the separation control due to the its high downforce increase and relatively low drag penalty, meanwhile the CoSVG configuration deteriorates the wing aerodynamic performance.
- The results of downforce and downforce-to-drag ratio improvements relative to the clean wing suggest that a use of the CtSVGs has advantages both in the downforce and efficiency under several conditions, indicating a 26% and a 10% maximum improvement of the downforce and efficiency. Meanwhile, the CtLVG configuration indicates less efficiency than the clean wing and CtSVG configuration.
- The close- and wide-spacings ($d_{VG}=2h_{VG}$ and $8h_{VG}$) are examined in addition to the reference-spacing ($d_{VG}=4h_{VG}$) in the CtSVG configuration. The close-spacing CtSVG configuration shows a similar level of improvement of downforce and efficiency relative to the clean wing to the reference-spacing CtSVG configuration. Meanwhile, the wide-spacing CtSVG configuration shows less improvement in downforce, and similar or less efficiency compared with that of the close- and reference-spacing CtSVG configurations.
- The chordwise pressure distribution features flow separation on the suction surface of the clean wing where the pressure curve shows a plateau. The counter-rotating VG configurations show a moderate slope of the pressure recovery toward the trailing edge and eliminate the constant value region, indicating no or less separation. Meanwhile, the CoSVG configuration exhibits a similar pressure recovery trend to that of the clean wing.
- VGs may help to reduce hysteresis effect due to flow separation. Combinational application of VGs and a Gurney flap, or a multi-element wing may also improve performance.

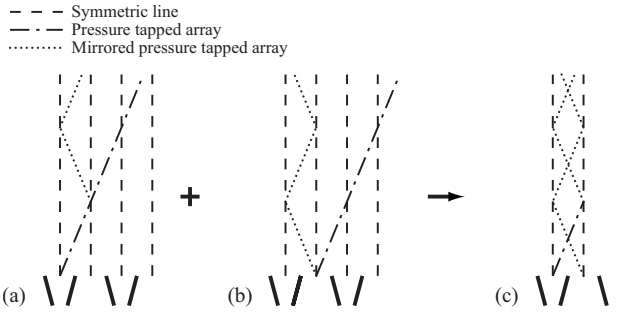

Fig. 8 Schematic of pressure tapped array and mirrored pressure tapped array of counter-rotating VG configuration

Acknowledgment

Y.Kuya gratefully acknowledge the financial support of the Ministry of Education, Culture, Sports, Science and Technology of Japan and the School of Engineering Sciences, University of Southampton. The authors would like to thank Mr. Mike Tudor-Pole for his assistance through the experiments.

Nomenclature

Roman Symbols

c = wing chord
C_D = drag coefficient ($=2D/\rho U_\infty^2 S$)
C_L = downforce coefficient ($=2L/\rho U_\infty^2 S$)
C_P = pressure coefficient ($=2(p-p_\infty)/\rho U_\infty^2$)
D = drag
d_{VG} = device spacing of vortex generator
h_{VG} = device height of vortex generator
h = wing ride height
L = downforce
p = pressure
p_∞ = freestream static pressure
Re = Reynolds number ($=\rho U_\infty c/\mu$)
S = wing planform area
U_∞ = freestream velocity
x,y,z = Cartesian tensor system; streamwise, lateral, and spanwise directions

Greek Symbols

α = wing incidence
μ = dynamic viscosity
ρ = density

Appendix: Surface Pressure Measurement

An average in the spanwise direction is taken for the measurement of the VG configurations since the flow of the VG configurations is not two-dimensional. Additionally, the pressure tapped array orients at 22.5 deg with respect to the streamwise direction for ease of manufacture and to work more pressure taps on the surface. Figures 8 and 9 respectively, illustrate the feature of the pressure measurement undertaken in the investigation for counter-rotating and co-rotating VG configurations.

For the counter-rotating VG configurations, the pressure tapped array passes through center of each device pair or between each device pair, as shown in Figs. 8(*a*) and 8(*b*), respectively. Figure 8 also illustrates the symmetric lines between each vane and a mirrored pressure tapped array, which is a mirror image of the pressure tapped array with respect to the symmetric lines. When a consideration regarding the mirrored pressure tapped array is taken and the average is taken between the two arrangements of the pressure tapped array, the process can provide an averagely interpolated pressure distribution along the center of a single vane, as shown in Fig. 8(*c*).

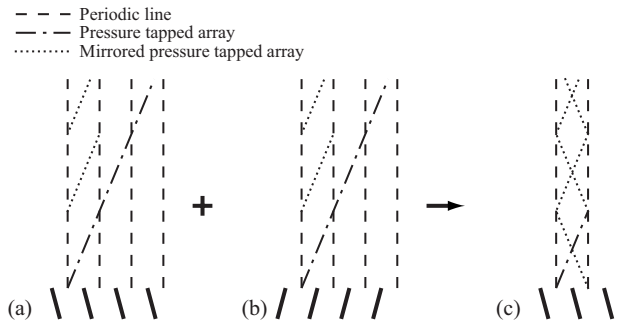

Fig. 9 Schematic of pressure tapped array and mirrored pressure tapped array of co-rotating VG configuration

Similarly, for the co-rotating VG configuration, the pressure measurement is taken with two co-rotating VG configurations, which compose mirroring configurations of each other, as illustrated in Figs. 9(*a*) and 9(*b*), and the periodic lines are considered instead of the symmetric lines. An image of the mirrored pressure tapped array in the co-rotating VG configuration given in Fig. 9(*c*) shows the absolutely same as that of the counter-rotating VG configuration given in Fig. 8(*c*). Therefore, the procedure also can provide the averagely interpolated pressure distribution along the center of a single vane.

References

[1] Zhang, X., Toet, W., and Zerihan, J., 2006, "Ground Effect Aerodynamics of Race Cars," Appl. Mech. Rev., **59**, pp. 33–49.

[2] Katz, J., 2006, "Aerodynamics of Race Cars," Annu. Rev. Fluid Mech., **38**, pp. 27–63.

[3] Gad-el-Hak, M., 1990, "Control of Low-Speed Airfoil Aerodynamics," AIAA J., **28**(9), pp. 1537–1552.

[4] Gad-el-Hak, M., and Bushnell, D. M., 1991, "Separation Control: Review," ASME J. Fluids Eng., **113**, pp. 5–30.

[5] Zerihan, J., and Zhang, X., 2000, "Aerodynamics of a Single Element Wing in Ground Effect," J. Aircr., **37**(6), pp. 1058–1064.

[6] Zhang, X., and Zerihan, J., 2003, "Off-Surface Aerodynamic Measurements of a Wing in Ground Effect," J. Aircr., **40**(4), pp. 716–725.

[7] Zhang, X., and Zerihan, J., 2003, "Aerodynamics of a Double-Element Wing in Ground Effect," AIAA J., **41**(6), pp. 1007–1016.

[8] Zhang, X., and Zerihan, J., 2004, "Edge Vortices of a Double-Element Wing in Ground Effect," J. Aircr., **41**(5), pp. 1127–1137.

[9] Zerihan, J., and Zhang, X., 2001, "Aerodynamics of Gurney Flaps on a Wing in Ground Effect," AIAA J., **39**(5), pp. 772–780.

[10] Soso, M. D., and Wilson, P. A., 2006, "Aerodynamics of a Wing in Ground Effect in Generic Racing Car Wake Flows," Proc. Inst. Mech. Eng., Part D (J. Automob. Eng.), **220**(1), pp. 1–13.

[11] Coe, D., Chipperfield, A., and Williams, C., 2006, "Transient Wing in Ground Effect Aerodynamics: Comparisons of Static and Dynamic Testing," Sixth MIRA International Vehicle Aerodynamics Conference, pp. 404–410.

[12] Lin, J. C., 2002, "Review of Research on Low-Profile Vortex Generators to Control Boundary-Layer Separation," Prog. Aerosp. Sci., **38**(4–5), pp. 389–420.

[13] Lin, J. C., 1999, "Control of Turbulent Boundary-Layer Separation Using Micro-Vortex Generators," AIAA Paper No. 1999-3404.

[14] Lin, J. C., Howard, F. G., and Selby, G. V., 1990, "Small Submerged Vortex Generators for Turbulent Flow Separation Control," J. Spacecr. Rockets, **27**(5), pp. 503–507.

[15] Lin, J. C., Robinson, S. K., McGhee, R. J., and Valarezo, W. O., 1994, "Separation Control on High-Lift Airfoils Via Micro-Vortex Generators," J. Aircr., **31**(6), pp. 1317–1323.

[16] Storms, B. L., and Jang, C. S., 1994, "Lift Enhancement of an Airfoil Using a Gurney Flap and Vortex Generators," J. Aircr., **31**(3), pp. 542–547.

[17] Storms, B. L., and Ross, J. C., 1995, "Experimental Study of Lift-Enhancing Tabs on a Two-Element Airfoil," J. Aircr., **32**(5), pp. 1072–1078.

[18] Garcia, D. L., and Katz, J., 2003, "Trapped Vortex in Ground Effect," AIAA J., **41**(4), pp. 674–678.

[19] Katz, J. and Morey, F., 2008, "Aerodynamics of Large-Scale Vortex Generator in Ground Effect," ASME J. Fluids Eng., **130**(7), p. 071101.

[20] Allan, B. G., Yao, C.-S., and Lin, J. C., 2002, "Numerical Simulations of Vortex Gner-ator Vanes and Jets on a Flat Plate," AIAA Paper No. 2002–3160.

[21] Allan, B. G., Yao, C.-S., and Lin, J. C., 2002, "Simulation of Embedded Streamwise Vortices on a Flat Plate," NASA/CR-2002-211654, ICASE Report No. 2002-14.

[22] Brunet, V., Francois, C., Garnier, E., and Pruvost, M., 2006, "Experimental and Numerical Investigations of Vortex Generators Effects," AIAA Paper No. 2006–3027.

[23] Bender, E. E., Anderson, B. H., and Yagle, P. J., 1999, "Vortex Generator Modeling for Navier-Stokes Codes," Paper No. FEDSM99-6919.

[24] May, N. E., 2001, "A New Vortex Generator Model for Use in Complex Configuration CFD Solvers," AIAA Paper No. 2001–2434.

[25] Kuya, Y., Takeda, K., and Zhang, X., "Computational Investigation of a Race Car Wing with Vortex Generators in Ground Effect," ASME J. Fluids Eng., submitted.

[26] Kuya, Y., Takeda, K., Zhang, X., Beeton S., and Pandaleon, T., 2009, "Flow Physics of a Race Car Wing with Vortex Generators in Ground Effect," ASME J. Fluids Eng., **131**, p. 121103.

[27] Senior, A. E., and Zhang, X., 2001, "The Force and Pressure of a Diffuser-Equipped Bluff Body in Ground Effect," ASME J. Fluids Eng., **123**, pp. 105–111.

[28] Ruhrmann, A., and Zhang, X., 2003, "Influence of Diffuser Angle on a Bluff Body in Ground Effect," ASME J. Fluids Eng., **125**, pp. 332–338.

[29] Zhang, X., Senior, A., and Ruhrmann, A., 2004, "Vortices Behind a Bluff Body With an Upswept Aft Section in Ground Effect," Int. J. Heat Fluid Flow, **25**, pp. 1–9.

[30] Burgin, K., Adey, P. C., and Beatham, J. P., 1986, "Wind Tunnel Tests on Road Vehicle Models Using a Moving Belt Simulation of Ground Effect," J. Wind Eng. Ind. Aerodyn., **22**, pp. 227–236.

[31] Abernethy, R. B., Benedict, R. P., and Dowdell, R. B., 1985, "ASME Measurement Uncertainty," ASME J. Fluids Eng., **107**, pp. 161–164.

[32] Bell, S., 1999, "A Beginner's Guide to Uncertainty of Measurement," Measurement Good Practice Guide, **11**(2), pp. 1–33.

Flow Physics of a Race Car Wing With Vortex Generators in Ground Effect

Yuichi Kuya
e-mail: yuichi@soton.ac.uk

Kenji Takeda
Senior Lecturer
e-mail: ktakeda@soton.ac.uk

Xin Zhang
Professor
e-mail: x.zhang1@soton.ac.uk

Scott Beeton[1]

Ted Pandaleon[2]

School of Engineering Sciences,
University of Southampton,
Southampton, Hampshire SO17 1BJ, UK

This paper experimentally investigates the use of vortex generators for separation control on an inverted wing in ground effect using off-surface flow measurements and surface flow visualization. A typical racing car wing geometry is tested in a rolling road wind tunnel over a wide range of incidences and ride heights. Rectangular vane type of sub-boundary layer and large-scale vortex generators are attached to the suction surface, comprising counter-rotating and corotating configurations. The effects of both device height and spacing are examined. The counter-rotating sub-boundary layer vortex generators and counter-rotating large-scale vortex generators suppress the flow separation at the center of each device pair, while the counter-rotating large-scale vortex generators induce horseshoe vortices between each device where the flow is separated. The corotating sub-boundary layer vortex generators tested here show little evidence of separation control. Increasing the spacing of the counter-rotating sublayer vortex generator induces significant horseshoe vortices, comparable to those seen in the counter-rotating large-scale vortex generator case. Wake surveys show significant spanwise variance behind the wing equipped with the counter-rotating large-scale vortex generators, while the counter-rotating sub-boundary layer vortex generator configuration shows a relatively small variance in the spanwise direction. The flow characteristics revealed here suggest that counter-rotating sub-boundary layer vortex generators can provide effective separation control for race car wings in ground effect. [DOI: 10.1115/1.4000423]

1 Introduction

Race car performance can be significantly enhanced by the addition of inverted wings to create downforce, improving traction and cornering ability. For open-wheel race series such as Formula One and Indy Racing, inverted wings and diffusers operate in ground effect, that is, in close proximity to the road, and their aerodynamic characteristics are affected [1,2]. In order to ascertain the underlying performance characteristics of race car front wings, a number of experimental investigations have been performed for an isolated wing in ground effect; a single-element [3–5], a double-element wing [6–8], a gurney flap fitted wing [9,10], a wing in a wake flow [11,12], interactions between a wing and wheel [13], and a dynamically motioned wing [14].

The experiments of Zerihan and Zhang [4,5] revealed important flow characteristics of a single-element wing in ground effect using a number of experimental methodologies, including force measurement, surface flow visualization, surface pressure measurement, laser Doppler anemometry (LDA), and particle image velocimetry (PIV). A moving ground was used to properly simulate the conditions on a race track, where a moving belt rig in the wind tunnel runs at the same speed as the freestream in order to control the boundary layer on the ground. Zerihan and Zhang [4] examined the ride height sensitivity of the downforce characteristics; the downforce behavior with respect to the ride height shows a downforce enhancement as a wing is moved closer to the ground, and then a downforce reduction is shown by further reduction in the ride height. Surface flow visualization revealed that the downforce reduction phenomenon is induced by a breakdown of edge vortices at the end plates and flow separation on the suction surface of the wing, which is induced by the large adverse pressure gradient.

If a flow is in a large adverse pressure gradient region, the streamwise momentum of the flow is reduced, and the flow may separate from the wall [15,16]. A number of separation control methods exist and have been successfully implemented in a number of different fields, such as vortex generators (VGs), VG jets, spanwise cylinder, and wall heat transfer techniques [15–18].

Lin [19,20] suggested that effective devices for separation control are those that generate streamwise vortices, such as those produced by VGs. Large-scale vortex generators (LVGs), whose device height is of the same order as the boundary layer thickness, have been used to control flow separation by transferring the momentum from the outer flow to boundary layer flow. Sub-boundary layer vortex generators (SVGs), however, appear to be more advantageous in terms of their effectiveness with a lower device height, which is just fraction of the boundary layer thickness [19–21]. Lin [19] exhibited that optimally placed vane type SVGs with a device height of 20% of the boundary layer thickness performs as well as vane type LVGs with device height of 80% of the boundary layer, but with less device drag.

Pauley and Eaton [22] studied the mean streamwise development of pairs of longitudinal vortices, generated by delta vane type VGs with a device height of 150% of the boundary layer thickness, in a turbulent boundary layer. Several vortex configurations were investigated, i.e., corotating vortices and counter-rotating vortices, inducing common-downwash and common-upwash. The streamwise decay of the peak vorticity showed that the corotating vortices decay quicker than the common-downwash vortices. The arrayed counter-rotating vortices show a slightly slower decay rate in the vortex circulation than the other configurations. Godard and Stanislas [23] attempted an optimization for delta vane type SVGs. The optimized counter-rotating sub-boundary layer vortex generators (CtSVGs) shows higher effectiveness than the corotating sub-boundary layer vortex generators (CoSVGs).

[1]Present address: Williams F1.
[2]Present address: TotalSim LLC.

Contributed by the Fluids Engineering Division of ASME for publication in the JOURNAL OF FLUIDS ENGINEERING. Manuscript received March 20, 2009; final manuscript received October 1, 2009; published online November 19, 2009. Editor: Joseph Katz.

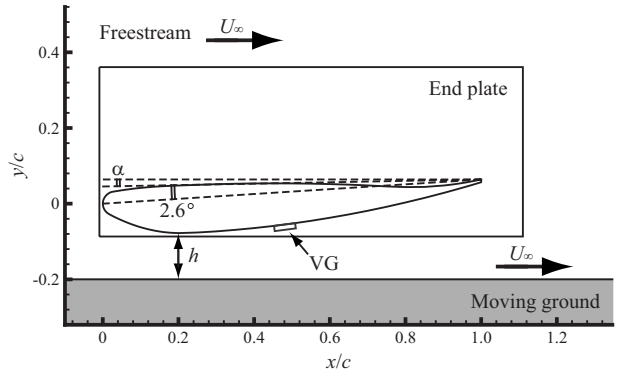

Fig. 1 Schematic of single-element wing, end plate, and VG

As described in Ref. [24], the use of VGs for an inverted wing in ground effect for separation control can be effective in terms of both downforce and efficiency. This paper investigates the flow physics that induce such force improvements, examining time-averaged and unsteady on- and off-surface flow features. Section 2 describes the experimental testing procedure in a wind tunnel, where a moving ground condition is properly simulated. The results of surface flow visualization and PIV measurement of the wake are described in Sec. 3, followed by discussion in Sec. 4. Rectangular vane type of SVGs and LVGs are tested on the suction surface of the wing, comprising counter-rotating and co-rotating configurations. Different device spacings are also studied to see how this affects the flow characteristics. Concluding remarks are included in Sec. 5.

2 Experimental Setup

2.1 Test Facility. The experiments described here are performed in the 2.1m×1.5m closed section wind tunnel at the University of Southampton. This wind tunnel has been used for a number of ground effect aerodynamics studies by different researchers, including Zerihan and Zhang [4,5,7,8,10] and Zhang and coworkers [25–27]. The tunnel is of conventional return circuit design, and is equipped with a moving belt rig and a three-component overhead balance system. The 3.2m×1.5m moving belt is controlled by slots and suction system for boundary layer removal, which gives 99.8% of the freestream velocity at 2 mm above the belt. The turbulence intensity of the freestream is about 0.3%. Further descriptions of the wind tunnel are given by Burgin et al. [28]. For the experiments presented here, the freestream velocity U_∞ and moving belt speed are set at 30 m/s, corresponding to the Reynolds number Re of 450,000 based on the wing chord c.

2.2 Experimental Models. Figure 1 shows a schematic of the single-element wing geometry and installation used. The model used is an 80% scale model of the main element of the 1998 Tyrrell 026 F1 car front wing, which is based on a NASA GA(W) profile, type LS(1)-0413, and is manufactured by carbon fiber composite. The model has a span of 1100 mm, constant chord c of 223.4 mm, and finite trailing edge of 1.65 mm, and is the same model used by Zerihan and Zhang [4,5,10]. The origin of the coordinate system is set at the leading edge of the wing. For the surface flow visualization, generic end plates of 250mm ×100mm×4mm are attached on both ends of the wing, meanwhile a size of 400mm×170mm×4mm glass end plates are used for the PIV measurement. The span of the wing is long enough such that edge vortices induced around the end plates do not affect a flow around the center portion of the wing span where the PIV measurement is performed. Therefore, the size difference of the end plates between the PIV measurement and flow visualization is deemed negligible for wake flow characteristics at the center portion. The incidence α is measured relative to a line from the trailing edge to the most swelled point on the pressure surface which corresponds to 2.6 deg relative to the chord line. The true incidence is therefore equal to the measured incidence plus 2.6 deg. When the incidence is 1 deg, corresponding to the true incidence of 3.6 deg, the upper and lower edges of the end plates are parallel to the ground. The incidence is varied by rotating about the quarter chord position. The ride height h is defined by the distance from the lowest point on the suction surface of the wing to the moving ground as the incidence is fixed at 1 deg. The ride height and incidence are fixed at $h/c=0.090$ and 1 deg in all the measurements conducted here, respectively.

Rectangular vane type VGs are employed here, comprising three configurations, which are the CtSVGs, counter-rotating large-scale vortex generators (CtLVGs), and CoSVGs. The SVG and LVG have a device height of 2 mm ($(h_{VG}/c)=0.009$) and 6 mm ($(h_{VG}/c)=0.027$), respectively. The VGs are made of aluminum plate with 0.6 mm thickness and built in pairs separated by $4h_{VG}$ at the trailing edge of the VGs. The vanes are oriented at ±15 deg relative to the streamwise direction, comprising the counter-rotating or co-rotating VG configuration. Pairs of VGs are put side by side along the span of the wing, as shown in Fig. 2. The VGs are attached on the suction surface of the wing such that the trailing edge of the VGs is fixed at $(x/c)=0.537$. The height to length ratio of the vanes is fixed at 1:4. For the CtLVG and CoSVG configurations, the device spacing d_{VG} between each device pair of the VGs is fixed at $4h_{VG}$, while close- and wide-spacings of $2h_{VG}$ and $8h_{VG}$ are also examined with the CtSVG configuration in addition to the reference-spacing of $4h_{VG}$. Unless there is a particular notation, CtSVG represents a CtSVG configuration with the reference-spacing of $4h_{VG}$, which is the same device spacing as the other VG configurations.

2.3 Experimental Methods. The flow visualization is undertaken using a mixture of liquid paraffin and fine powder Invisible Blue T70 painted on the suction surface of the wing.

PIV measurement is performed in the xy-plane along the center line of the wing using a Dantec Dynamics FlowMap PIV2100 Processor (Denmark) [29]. The laser is a New Wave Research Gemini dual Nd-YAG laser (Fremont, CA, USA) mounted downstream of the wing to illuminate the wake section. The laser sheet

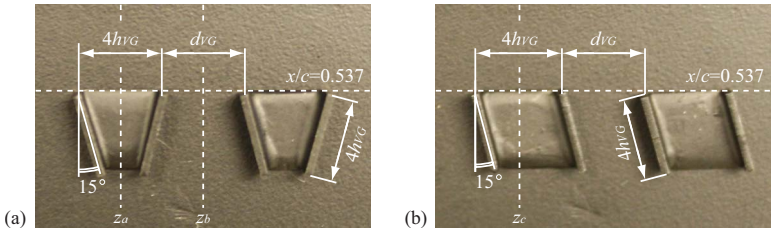

Fig. 2 Configurations of VGs on wing and laser sheet positions in PIV measurement: (*a*) counter-rotating VGs and (*b*) co-rotating VGs. Flow is from bottom to top.

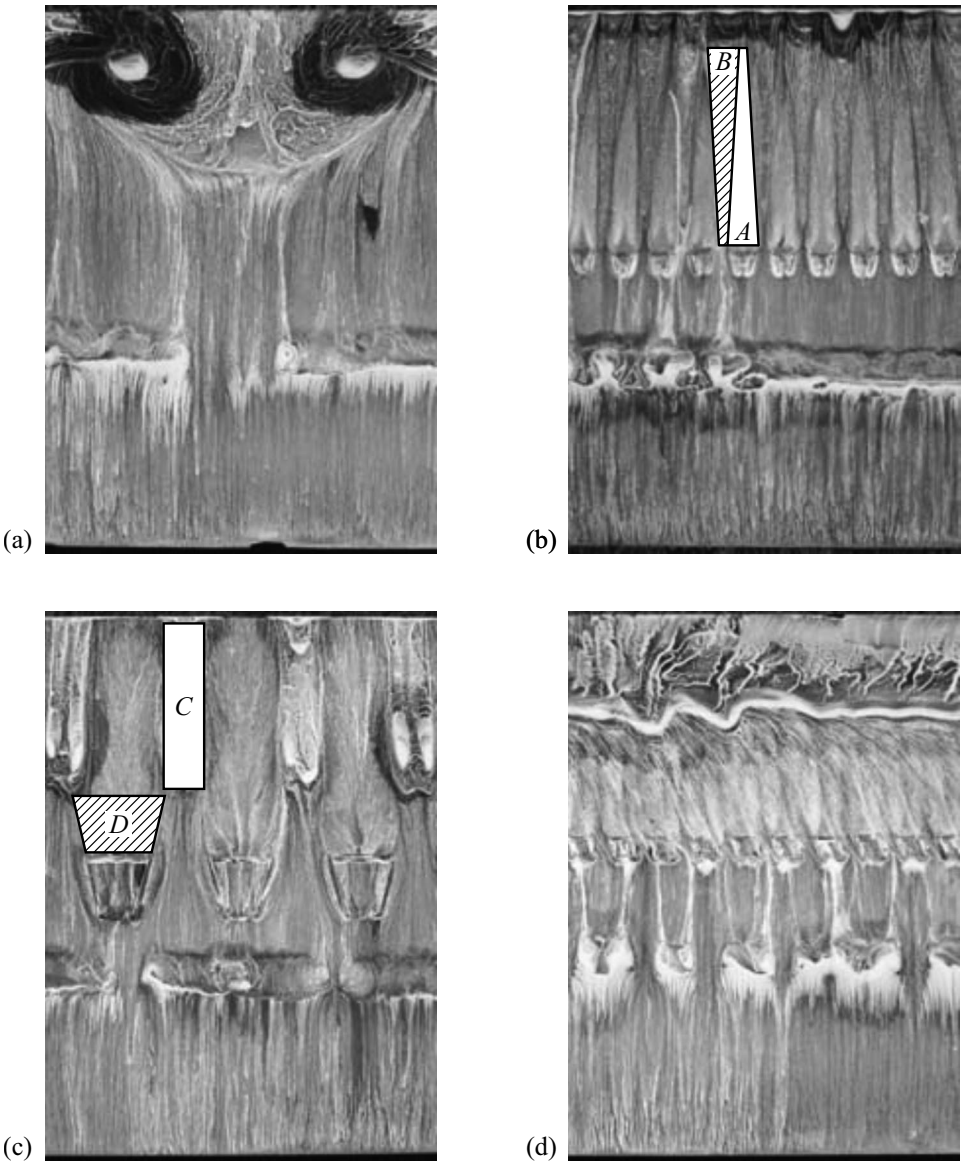

Fig. 3 Surface flow visualization on suction surface around centre portion of wing span at α=1 deg and (h/c)=0.090: (*a*) clean, (*b*) CtSVG, (*c*) CtLVG, and (*d*) CoSVG. Flow is from bottom to top.

position is altered for different VG geometries, as shown in Fig. 2, to compare the difference of the wake structure in the spanwise direction. For the counter-rotating VGs, two laser sheet positions are employed, which are at the center of the device pair z_a and at the center between the device pair z_b. A single laser sheet position is used at the center of the device pair z_c for the co-rotating VGs, since the vanes are mounted periodically. A Dantec Dynamics Hi-Sense CCD camera with a resolution of 1280×1024 pixels and a 105 mm lens is used. The time interval between the two laser pulses is 15 μs, and 500 pairs of snapshots are continuously obtained. The flow is seeded by smoke particles with a size of 1–1.5 μm. FlowManeger 4.10 software is used for postprocessing to calculate the velocity field with the adaptive cross-correlation algorithm, which uses iteration steps for offsetting the second window for cross-correlation analysis, using four refinement steps with a local median validation function to obtain a final interrogation area size of 32×32 pixels without filtering. The overlap between interrogation areas is set at 50%.

2.4 Uncertainty. The uncertainty of the PIV measurement is estimated by assessing the normalized maximum velocity deficit of the clean wing at (x/c)=1.5. The 500 PIV snapshots for each measurement are divided into five subsets containing 100 snapshots, and the uncertainty is assessed between the five subsets using procedures described in Refs. [30,31]. According to the procedures, the standard error of the measurement is given as 0.008, and hence, the uncertainty with the 95% confidence is given as 0.017, where the coverage factor of 2 is used.

3 Results

3.1 Surface Flow Visualization. Surface flow visualization results are presented here to ascertain key flow physics that drive the force and pressure characteristics presented by Kuya et al. [24]. Figure 3 illustrates results of the surface flow visualization on the suction surface around the centre portion of the wing span

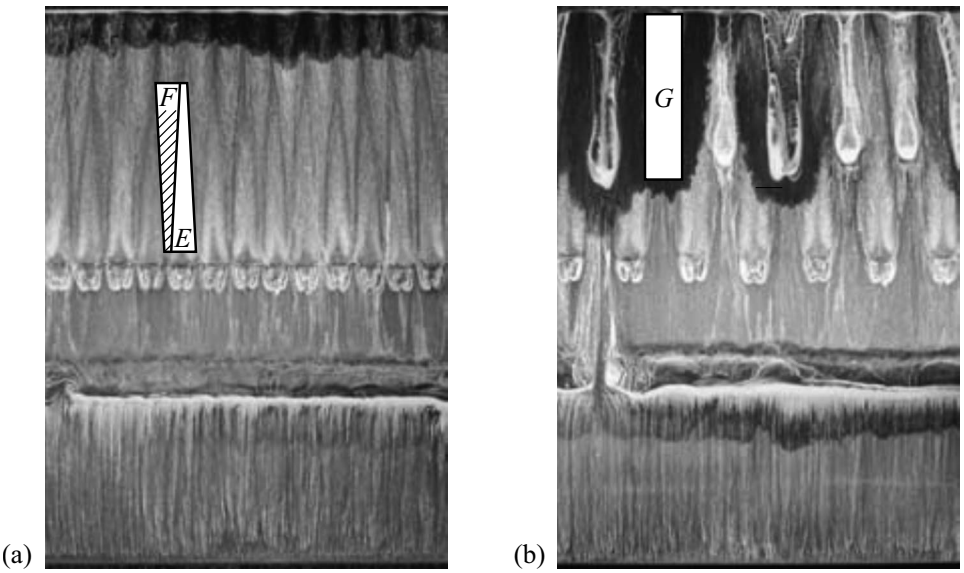

Fig. 4 Surface flow visualization on suction surface around centre portion of wing span for effect of VG device spacing at α=1 deg and (h/c)=0.090: (*a*) close-spacing and (*b*) wide-spacing. Flow is from bottom to top.

at α=1 deg and (h/c)=0.090 for the four configurations. The flow direction is from bottom to top in the figures.

All of the configurations show that the flow transitions from laminar to turbulent at about 30% chord via a short reattachment bubble in agreement with the results of Zerihan and Zhang [4]. The flow pattern near the end plates (not shown here) features the spanwise component of flow toward the wing center due to the edge vortices induced around the end plates. The edge vortices create a downwash on the suction surface, which pumps the momentum into the boundary layer flow, and thus, there is no flow separation around the spanwise end of the wing.

For the clean wing in Fig. 3(*a*), characteristic horseshoe vortices and flow separation can be seen between 65% and 80% chords. The vortices induced by the counter-rotating VGs are likely to flow straight, since the spanwise component of the secondary flow induced by the VG-generated vortices cancels each other near the surface. Meanwhile, the flow pattern of the CoSVG configuration features the spanwise component of the flow due to the lateral component of the secondary flow of the VG-generated vortices. In general, since a secondary flow induced by co-rotating vortices flows in the same direction near a surface, the spanwise component is enhanced. Downwash regions can be seen downstream of each pair of the CtSVGs as represented by the region *A* in Fig. 3(*b*). At the center of each device pair, the flow separation is suppressed by the vortices, where each vane induces a downwash on the suction surface. The vortices allow the flow to remain attached up to 95% chord, eventually breaking down at the trailing edge; the close proximity to the trailing edge inferring that the strength of the VG-generated vortices is nearly optimal. Between each device pair, an upwash region can be observed as represented by the region *B* in Fig. 3(*b*) induced by the VG-generated vortices detaching from the suction surface; the upwash enhances the flow separation. For the CtLVG configuration in Fig. 3(*c*), the flow separation is entirely suppressed at the center of each device pair to the trailing edge due to the strong downwash induced by the VG-generated vortices. In this case the horseshoe vortices are induced between each device pair at 70% chord, as denoted by the region *C*. The rotational direction of the counter-rotating vortices is likely to induce the flow outwards, deviating from the center of each device pair, as represented by the region *D*. The flow from each device pair meets at the center of the device pairs, as shown in the region *C*, where the upwash induced by the VG-generated vortices is enhanced by the two vortices, resulting in the separated flow with the horseshoe vortices. The CoSVG configuration apparently shows flow separation downstream of the VGs over the wing span at about 80% chord, as shown in Fig. 3(*d*). The separated flow pattern is more two-dimensional rather than three-dimensional as featured by the horseshoe vortices on the clean wing. As will be discussed later, the reduced effectiveness of the CoSVGs regarding the separation control is likely to be due to quicker decay of co-rotating vortices compared with counter-rotating vortices.

The close- and wide-spacings ($d_{VG}=2h_{VG}$ and $8h_{VG}$) are examined in addition to the reference-spacing ($d_{VG}=4h_{VG}$) in the CtSVG configuration. Figure 4 shows results of the surface flow visualization on the suction surface of the CtSVG configurations with close- and wide-spacings at α=1 deg and (h/c)=0.090. For the close-spacing CtSVG configuration, the flow pattern is similar to that of the reference-spacing CtSVG configuration; the regions *E* and *F* in Fig. 4(*a*) correspond to the regions *A* and *B* in the reference-spacing CtSVG configuration shown in Fig. 3(*b*). For the wide-spacing CtSVG configuration, the horseshoe vortices can be observed between each device pair, as represented by the region *G* in Fig. 4(*b*), resulting in a flow pattern similar to that of the CtLVG configuration. When the VGs are spaced closer together relative to the vortex size, the interaction with neighboring vortex pairs is significantly enhanced. On the contrary, the vortices generated by the wide-spacing CtSVG configuration appear to move apart, inducing separated flow comprising horseshoe vortices between each device pair.

3.2 Wake Characteristics. Results of the PIV measurement of the wake are presented here. Figure 5 shows mean streamwise velocity contours of the four configurations at α=1 deg and (h/c)=0.090, time-averaged over 500 PIV snapshots. The velocity is normalized by the freestream velocity. The results in the vicinity of the trailing edge of the wing and moving ground are excluded due to reflections from the solid surfaces. The figures for the counter-rotating VG configurations (Figs. 5(*b*) and 5(*c*)) show profiles at two spanwise positions ($z=z_a$ and z_b). At $z=z_a$, the vortices from the counter-rotating VGs induce downwash on the suction surface, while the upwash, which detaches from the suction surface, is induced at $z=z_b$.

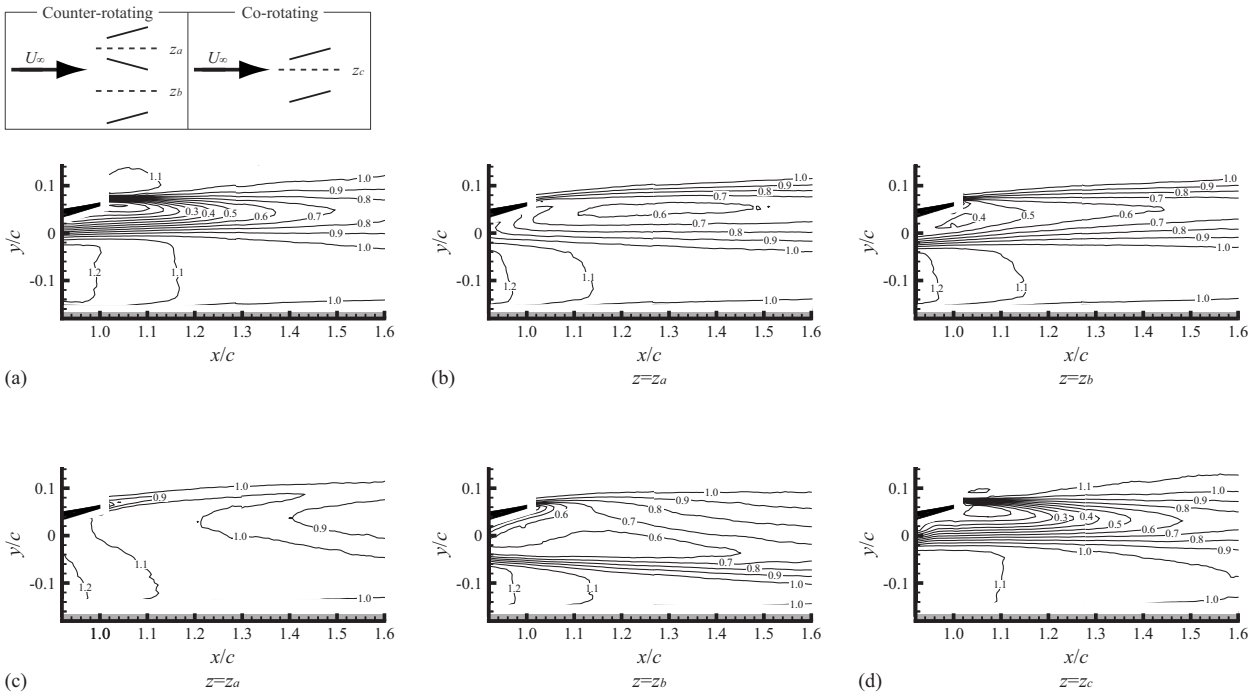

Fig. 5 Mean streamwise velocity contours at $\alpha=1$ deg and $(h/c)=0.090$: (*a*) clean, (*b*) CtSVG at $z=z_a$ and z_b, (*c*) CtLVG at $z=z_a$ and z_b, and (*d*) CoSVG at $z=z_c$

For the baseline clean wing case in Fig. 5(*a*), the wake becomes thicker as it flows downstream, reducing the velocity deficit. The flow between the wake and the moving ground is accelerated as a result of ground effect, inducing boundary layer growth on the ground (see Fig. 6). For the counter-rotating VG configurations in Fig. 5(*b*), the wake profiles at $z=z_a$ and z_b show different features, with the CtLVG configuration exhibiting more variance in the spanwise direction compared with the CtSVG configuration. Both the profiles of the CtSVG configuration at $z=z_a$ and z_b show similar wake thicknesses to the clean wing. The velocity deficit of the CtSVG configuration tends to persist farther downstream, while the wake of the clean wing shows relatively faster decay of the deficit. For the wake profile at $z=z_a$, the downwash near the suction surface induced by the VG-generated vortices appears to suppresses the flow separation accelerating the flow near the trailing edge, compared with the clean wing. For the accelerated flow between the wing and the ground, both profiles of the CtSVG configuration show similar distributions to the clean wing. The CtLVG configuration exhibits a significant effect of the VGs on the wake structure, the wake profiles at $z=z_a$ and z_b being very different, as shown in Fig. 5(*c*). The profile at $z=z_a$ shows a narrow wake distribution downstream of the trailing edge as the result of the suppression of the flow separation. Meanwhile, a significantly thicker wake is shown at $z=z_b$. For the CoSVG configuration in Fig. 5(*d*), the wake profile shows a similar distribution to that of the clean wing, while the CoSVG configuration generates a slightly thicker wake than the clean wing.

Figure 6 shows the mean streamwise velocity profiles at $(x/c)=1.5$ of the four configurations at $\alpha=1$ deg and $(h/c)=0.090$. For the counter-rotating VG configurations, profiles at the two spanwise positions ($z=z_a$ and z_b) are given. Characteristics of the velocity profiles are summarized in Table 1. The thickness of the wake is defined as the distance between the upper and lower points of the wake where the velocity is 99% of the freestream. Adding the CtSVGs to the wing reduces the thickness and increases the maximum velocity deficit of the wake compared with the clean wing. The maximum velocity deficit increases from $u_{\min}/U_\infty=0.70$ $((y/c)=0.048)$ for the clean wing to $u_{\min}/U_\infty=0.60$ $((y/c)=0.055)$ at $z=z_a$ and $u_{\min}/U_\infty=0.61$ $((y/c)=0.053)$ at

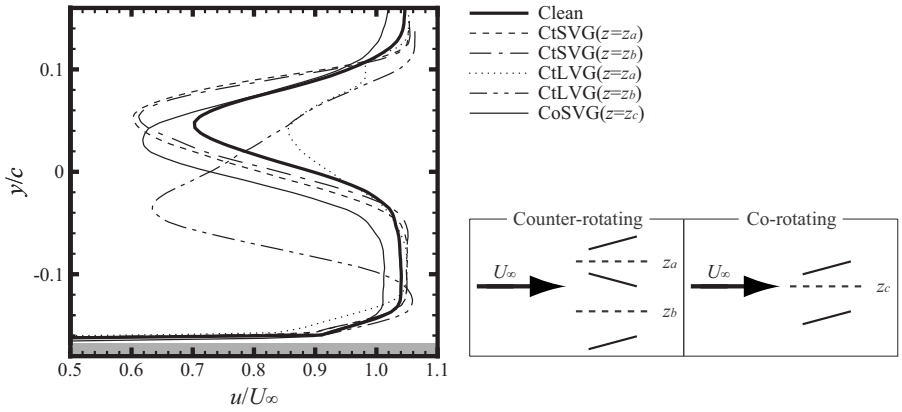

Fig. 6 Mean streamwise velocity profiles at $(x/c)=1.5$ at $\alpha=1$ deg and $(h/c)=0.090$

Table 1 Wake characteristics at $(x/c)=1.5$ at $\alpha=1$ deg and $(h/c)=0.090$

	Clean	CtSVG		CtLVG		CoSVG
		$(z=z_a)$	$(z=z_b)$	$(z=z_a)$	$(z=z_b)$	
δ_{wake}/c	0.19	0.17	0.17	0.19	0.22	0.20
u_{min}/U_∞	0.70	0.60	0.61	0.86	0.63	0.62
y/c at u_{min}	0.048	0.055	0.053	0.043	−0.037	0.032

$z=z_b$ for the CtSVG configuration. The wake thickness is reduced from $\delta_{wake}/c=0.19$ for the clean wing to $\delta_{wake}/c=0.17$ for the CtSVG configuration. Of great interest here is that both wake profiles of the CtSVG configuration show a remarkably similar distribution, thus, less variance in the spanwise direction. For the CtLVG configuration, the profiles obviously show different features from each other. The variance of the wake structure indicates that the wake flows are highly affected by the vortices generated by the CtLVGs. The velocity deficit of the CtLVG at $z=z_a$ is smaller than the others, and another small velocity deficit can be detected around $(y/c)=0.10$. The wake thickness of the CtLVG at $z=z_a$ including the small deficit is similar to that of the clean wing. Meanwhile, a significantly thicker wake is observed at $z=z_b$. The maximum velocity deficit changes from $u_{min}/U_\infty=0.70$ $((y/c)=0.048)$ for the clean wing to $u_{min}/U_\infty=0.86$ $((y/c)=0.043)$ at $z=z_a$, and $u_{min}/U_\infty=0.63$ $((y/c)=-0.037)$ at $z=z_b$ for the CtLVG configuration. The CoSVG configuration shows a larger wake compared with the clean wing. The maximum velocity deficit increases from $u_{min}/U_\infty=0.70$ $((y/c)=0.048)$ for the clean wing to $u_{min}/U_\infty=0.62$ $((y/c)=0.032)$ for the CoSVG configuration. For the accelerated flow between the wake and ground, the counter-rotating configurations show slightly higher velocity, whereas the CoSVG configuration presents lower velocity, compared with the clean wing. The boundary layer growth detected on the moving ground shows a similar rate in all four profiles.

Figure 7 shows instantaneous spanwise vorticity contours of the four configurations at $\alpha=1$ deg and $(h/c)=0.090$ to illustrate some unsteady flow features behind the wing. While only one snapshot is shown, the characteristics described here are evident in the whole set of captured PIV data. The vorticity is normalized by the freestream velocity and wing chord. The figures for the counter-rotating VG configurations (Figs. 7(*b*) and 7(*c*)) show distributions at two spanwise positions ($z=z_a$ and z_b). The vortex structure behind the clean wing is characterized by the presence of vortex shedding and a shear layer between regions of positive and negative vorticity, as shown in Fig. 7(*a*). For both distributions of the CtSVG configuration in Fig. 7(*b*), the vortices appear to spread relatively wider and the size of each shed vortex is typically smaller compared with the clean wing case. The difference between the profiles at $z=z_a$ and z_b is not obvious. The CtLVG configuration shows a significant impact of the CtLVGs on the vorticity structure in Fig. 7(*c*). At $z=z_a$, the vortices distribute only downstream of the trailing edge, and the shear layer is observed clearly. The size of each vortex is relatively small. Meanwhile, a wide range of the vortex shedding is observed at $z=z_b$. The structure of shed vortices is much more irregular compared

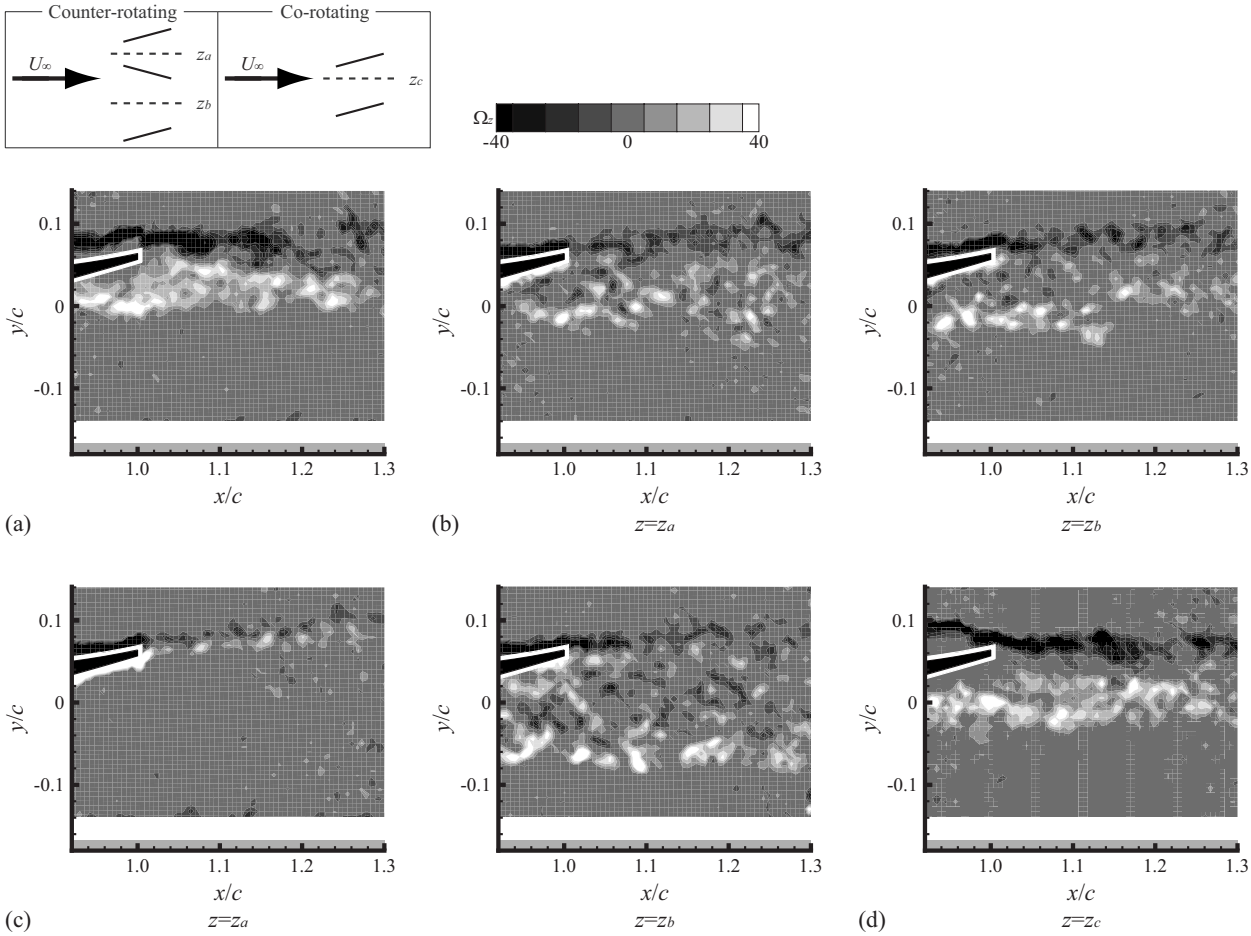

Fig. 7 Instantaneous spanwise vorticity distributions at $\alpha=1$ deg and $(h/c)=0.090$: (*a*) clean, (*b*) CtSVG at $z=z_a$ and z_b, (*c*) CtLVG at $z=z_a$ and z_b, and (*d*) CoSVG at $z=z_c$

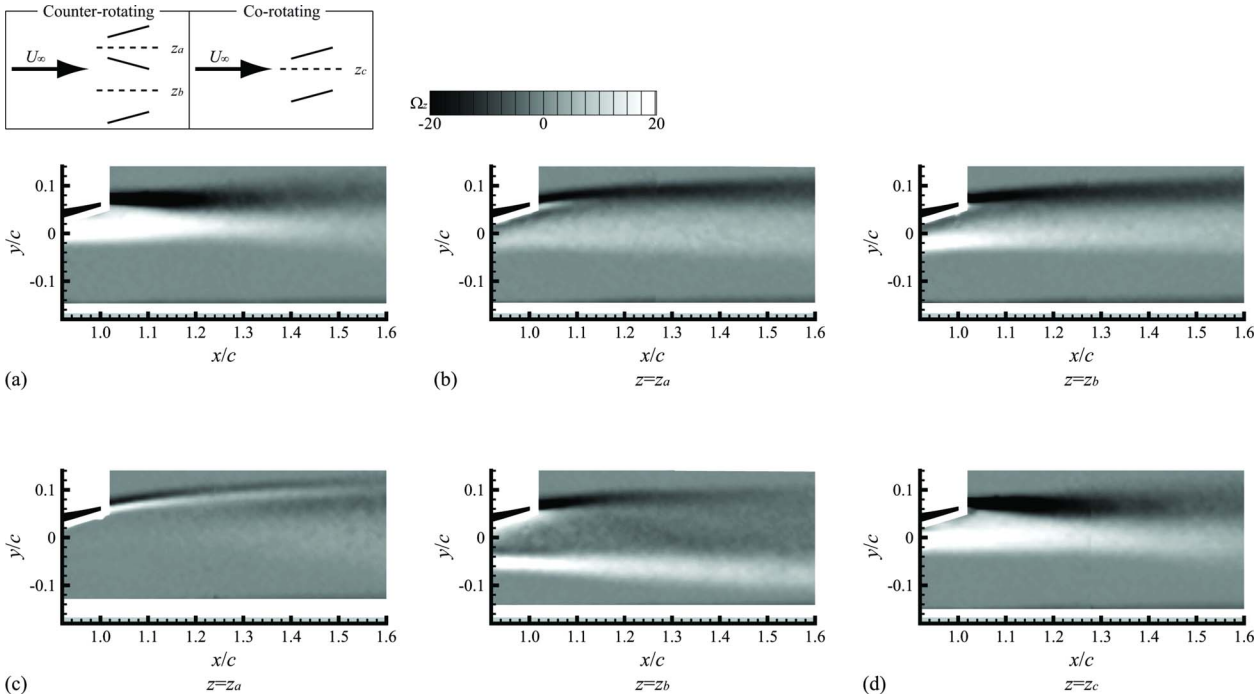

Fig. 8 Mean spanwise vorticity distributions at $\alpha=1$ deg and $(h/c)=0.090$: (*a*) clean, (*b*) CtSVG at $z=z_a$ and z_b, (*c*) CtLVG at $z=z_a$ and z_b, and (*d*) CoSVG at $z=z_c$

with the others, and the shear layer cannot be observed clearly. For the co-rotating VG configurations in Fig. 7(*d*), the structure of discrete vortices of the CoSVG configuration is similar to the clean wing.

In addition to the instantaneous unsteady features of the vorticity, the mean spanwise vorticity contours of the four configurations, time-averaged over 500 PIV snapshots, at $\alpha=1$ deg and $(h/c)=0.090$, are shown in Fig. 8. The figures for the counter-rotating VG configurations (Figs. 8(*b*) and 8(*c*)) show distributions at two spanwise positions ($z=z_a$ and z_b). The mean vorticity contours clearly explain where the positive and negative vortices and the shear layers are generated, and how they diffuse as they develop downstream. For the clean wing in Fig. 8(*a*), the positive vorticity is thicker than the negative vorticity at a region of $(x/c)\leq 1.3$ due to the flow separation on the suction surface. Both contours for the CtSVG configuration show a characteristic vorticity distribution in Fig. 8(*b*). Two positive vorticity regions are observed: one is along the suction surface of the wing, and the other is detected underneath the suction surface at $(y/c)\simeq -0.02$. Between these positive vorticity regions, the negative vorticity is observed underneath the suction surface in addition to the one generated around the pressure surface. The difference between the distributions at $z=z_a$ and z_b is not obvious; however, at $z=z_a$, the positive vorticity region near the trailing edge flows slightly further downstream than that at $z=z_b$. Additionally, the positive vorticity underneath the suction surface at $z=z_a$ shows lower degree than the value of the clean wing and the CtSVG configuration at $z=z_b$. These discrepancies of the distributions between $z=z_a$ and z_b are due to the suppression of flow separation at $z=z_a$ as revealed by the surface flow visualization. The effect of the VGs is more obvious in the CtLVG configuration in Fig. 8(*c*), as can be seen in other wake surveys. At $z=z_a$, thin distributions of the vorticity are observed downstream of the trailing edge due to the suppression of the separation. Meanwhile at $z=z_b$, the negative vorticity generated from the pressure surface and underneath the suction surface results in a thicker distribution downstream. Both distributions of the CtLVG configuration show two positive vorticity regions, as observed in the CtSVG configurations. One is shown on the suction surface of the wing, and the other underneath the suction surface at $(y/c)\simeq 0$ $(z=z_a)$ and at $(y/c)\simeq -0.05$ $(z=z_b)$. The value of the positive vorticity at $(y/c)\simeq -0.05$ $(z=z_b)$ is obviously higher than that at $(y/c)\simeq 0$ $(z=z_a)$ due to the flow separation at $z=z_b$. The vorticity distribution of the CoSVG configuration in Fig. 8(*d*) is remarkably similar to that of the clean wing. The similarity between the clean wing and CoSVG configuration can also be seen in the mean velocity distributions.

4 Discussion

Kuya et al. [24] showed that both the counter-rotating configurations can increase downforce compared with the clean wing when the wing is operated in the ground effect regime, and in particular, the use of the CtSVGs has advantages both in the downforce and efficiency under some conditions, while the CtLVG configuration indicates less efficiency. The CoSVG configuration deteriorates the wing performance in all cases. The experimentally investigated characteristics, including surface flow visualization and wake surveys, explain the physical mechanism of the separation control and the advantage of the CtSVGs compared with the others.

The vortices generated by the VGs induce downwash and upwash to the suction surface, which mixes the outer flow and the flow in the boundary layer. The downwash generated at the center of each device pair transfers the high momentum of the outer flow into the boundary layer flow, leading to the suppression of flow separation, as can be seen in the results of the surface flow visualization of the counter-rotating VG configurations. However, the interaction between the neighboring co-rotating vortices tend to cancel each other's downwash and upwash effects, resulting in a more rapid decay of the vortex, and enhances the lateral component of the flow. Therefore, the co-rotating vortices do not persist further downstream, resulting in little effect of separation control. The more rapid decay of the co-rotating vortices compared with the counter-rotating vortices captured here is in good agreement with the investigation of Pauley and Eaton [22]. Thus, it is con-

ceivable that co-rotating VGs with wider device spacings, which have less interaction between each vortex, could have a more favorable effect for separation control.

For separation control, important factors regarding the VG-generated vortices are their strength and size. The surface flow visualization reveals that the vortices induced by the CtSVGs break down at 95% chord, indicating that the vortices are sufficiently strong, but not excessively so, to make the flow overcome the adverse pressure gradient region, leading to efficient separation control at the condition tested. Meanwhile, the CtLVG configuration not only suppresses the flow separation due to the downwash on the suction surface, but also induces horseshoe vortices where the flow is separated by the upwash. The wake surveys performed by the PIV measurement show that the CtSVG configuration possesses a small spanwise variance, while the CtLVG configuration exhibits significant spanwise variances. The large variance of the CtLVG configuration indicates that vortices with excessive strength and size have not only favorable effects regarding separation control but also significant penalties. Accordingly, the device height of the VGs is important not only for the device drag but also for the strength and size of the vortices, which the VGs produce.

Regarding the effect of the device spacing, Kuya et al. [24] showed that the close-spacing CtSVG configuration exhibits a similar effect on the downforce and efficiency with respect to the reference-spacing CtSVG configuration, while the wide-spacing CtSVG configuration shows less downforce and efficiency, compared with the other spacing CtSVG configurations. Those characteristics are consistent with the results of the surface flow visualization investigated here; the close-spacing CtSVG configuration shows a similar flow pattern to that of the reference-spacing CtSVG configuration, while the wide-spacing CtSVG configuration leads to the horseshoe vortices, as shown in the CtLVG configuration.

Accordingly, as shown in the investigation of Kuya et al. [24], the CtSVG configuration exhibits the best performance thanks to the nearly optimal strength and size of the counter-rotating vortices to overcome the adverse pressure gradient region induced here with a small drag penalty. The CoSVG configuration, however, exhibits a negligible separation control capability due to the rapid decay of the co-rotating vortices.

Although the device height and spacing of the VGs are changed, the orientation angle is fixed at ± 15 deg in the current investigation. The strength of the VG-generated vortices may be altered by adjusting the orientation angle of the vane; optimized VG parameters for the rectangular vane type could be found via changing the device height, spacing, and orientation angle.

5 Concluding Remarks

An experimental investigation of the flow characteristics of an inverted wing with VGs in ground effect is performed, using surface flow visualization and wake surveys, and the following conclusions are drawn:

- Surface flow visualization of the clean wing captures the characteristic horseshoe vortices and flow separation downstream of 65–80% chord. Both the counter-rotating configurations suppress the flow separation at the center of each device pair, while the CtLVGs induce the horseshoe vortices between each device where the flow is separated. The CoSVG configuration shows the flow separation downstream of the VGs over the wing span at 80% chord.
- The close- and wide-spacings ($d_{VG}=2h_{VG}$ and $8h_{VG}$) are examined in addition to the reference-spacing ($d_{VG}=4h_{VG}$) in the CtSVG configuration. The counter-rotating vortices induced by the wide-spacing CtSVGs are likely to spread outward and induce the horseshoe vortices as the CtLVG configuration features; meanwhile, the spreading of the vortices induced by the close- or reference-spacing CtSVGs is restricted by the interaction of the vortices existing in their neighbors.
- Wake flow surveys obtained by the PIV measurement reveal significant spanwise variances in the wake behind the wing equipped with the CtLVGs, while the CtSVG configuration shows a relatively small variance in the spanwise direction. The CoSVG configuration shows very similar distributions to those of the clean wing.
- The flow physics investigated here suggests advantages of a use of the CtSVG configuration for the separation control.

Acknowledgment

Y. Kuya gratefully acknowledges the financial support of the Ministry of Education, Culture, Sports, Science, and Technology of Japan and the School of Engineering Sciences, University of Southampton. The authors would like to thank Mr. Mike Tudor-Pole for his assistance with the experiments.

Nomenclature

Roman Symbols

- c = wing chord
- d_{VG} = device spacing of the vortex generator
- h_{VG} = device height of the vortex generator
- h = wing ride height
- Re = Reynolds number ($=\rho U_\infty c/\mu$)
- U_∞ = freestream velocity
- u, v = Cartesian components of velocity (streamwise and lateral directions)
- u_{min} = maximum velocity deficit
- x,y,z = Cartesian tensor system (streamwise, lateral, and spanwise directions)
- z_a,z_b,z_c = PIV laser sheet positions

Greek Symbols

- α = wing incidence
- δ_{wake} = wake thickness
- μ = dynamic viscosity
- ρ = density
- Ω_z = nondimensional spanwise vorticity ($=(\partial v/\partial x - \partial u/\partial y)c/U_\infty$)

References

[1] Zhang, X., Toet, W., and Zerihan, J., 2006, "Ground Effect Aerodynamics of Race Cars," Appl. Mech. Rev., **59**, pp. 33–49.
[2] Katz, J., 2006, "Aerodynamics of Race Cars," Annu. Rev. Fluid Mech., **38**, pp. 27–63.
[3] Knowles, K., Donoghue, D. T., and Finnis, M. V., 1994, "A Study of Wings in Ground Effect," Loughborough University Conference on Vehicle Aerodynamics, Vol. 22, pp. 1–13.
[4] Zerihan, J., and Zhang, X., 2000, "Aerodynamics of a Single Element Wing in Ground Effect," J. Aircr., **37**(6), pp. 1058–1064.
[5] Zhang, X., and Zerihan, J., 2003, "Off-Surface Aerodynamic Measurements of a Wing in Ground Effect," J. Aircr., **40**(4), pp. 716–725.
[6] Ranzenbach, R., Barlow, J. B., and Diaz, R. H., 1997, "Multi-Element Airfoil in Ground Effect—An Experimental and Computational Study," AIAA Paper No. 1997-2238.
[7] Zhang, X., and Zerihan, J., 2003, "Aerodynamics of a Double-Element Wing in Ground Effect," AIAA J., **41**(6), pp. 1007–1016.
[8] Zhang, X., and Zerihan, J., 2004, "Edge Vortices of a Double-Element Wing in Ground Effect," J. Aircr., **41**(5), pp. 1127–1137.
[9] Katz, J., and Largman, R., 1989, "Effect of 90 Degree Flap on the Aerodynamics of a Two-Element Airfoil," ASME J. Fluids Eng., **111**, pp. 93–94.
[10] Zerihan, J., and Zhang, X., 2001, "Aerodynamics of Gurney Flaps on a Wing in Ground Effect," AIAA J., **39**(5), pp. 772–780.
[11] Soso, M. D., and Wilson, P. A., 2006, "Aerodynamics of a Wing in Ground Effect in Generic Racing Car Wake Flows," Proc. Inst. Mech. Eng., D J. Automob. Eng., **220**(1), pp. 1–13.
[12] Soso, M. D., and Wilson, P. A., 2008, "The Influence of an Upstream Diffuser on a Downstream Wing in Ground Effect," Proc. Inst. Mech. Eng., Part D (J. Automob. Eng.), **222**(4), pp. 551–563.
[13] Diasinos, S., and Gatto, A., 2008, "Experimental Investigation Into Wing Span and Angle-of-Attack Effects on Sub-Scale Race Car Wing/Wheel Interaction

Aerodynamics," Exp. Fluids, **45**(3), pp. 537–546.
[14] Coe, D., Chipperfield, A., and Williams, C., 2006, "Transient Wing in Ground Effect Aerodynamics: Comparisons of Static and Dynamic Testing," Sixth MIRA International Vehicle Aerodynamics Conference, pp. 404–410.
[15] Gad-el-Hak, M., 1990, "Control of Low-Speed Airfoil Aerodynamics," AIAA J., **28**(9), pp. 1537–1552.
[16] Gad-el-Hak, M., and Bushnell, D. M., 1991, "Separation Control: Review," ASME J. Fluids Eng., **113**, pp. 5–30.
[17] Lin, J. C., Howard, F. G., and Bushnell, D. M., 1990, "Investigation of Several Passive and Active Methods for Turbulent Flow Separation Control," AIAA Paper No. 1990-1598.
[18] Lin, J. C., Selby, G. V., and Howard, F. G., 1991, "Exploratory Study of Vortex-Generating Devices for Turbulent Flow Separation Control," AIAA Paper No. 1991-0042.
[19] Lin, J. C., 1999, "Control of Turbulent Boundary-Layer Separation Using Micro-Vortex Generators," AIAA Paper No. 1999-3404.
[20] Lin, J. C., 2002, "Review of Research on Low-Profile Vortex Generators to Control Boundary-Layer Separation," Prog. Aerosp. Sci., **38**(4–5), pp. 389–420.
[21] Lin, J. C., Howard, F. G., and Selby, G. V., 1990, "Small Submerged Vortex Generators for Turbulent Flow Separation Control," J. Spacecr. Rockets, **27**(5), pp. 503–507.
[22] Pauley, W. R., and Eaton, J. K., 1988, "Experimental Study of the Development of Longitudinal Vortex Pairs Embedded in a Turbulent Boundary Layer," AIAA J., **26**(7), pp. 816–823.
[23] Godard, G., and Stanislas, M., 2006, "Control of a Decelerating Boundary Layer. Part 1: Optimization of Passive Vortex Generators," Aerosp. Sci. Technol., **10**(3), pp. 181–191.
[24] Kuya, Y., Takeda, K., Zhang, X., Beeton S., and Pandaleon, T., 2009, "Flow Separation Control on a Race Car Wing With Vortex Generators in Ground Effect," ASME J. Fluids Eng., **131**, p. 121102.
[25] Senior, A. E., and Zhang, X., 2001, "The Force and Pressure of a Diffuser-Equipped Bluff Body in Ground Effect," ASME J. Fluids Eng., **123**, pp. 105–111.
[26] Ruhrmann, A., and Zhang, X., 2003, "Influence of Diffuser Angle on a Bluff Body in Ground Effect," ASME J. Fluids Eng., **125**, pp. 332–338.
[27] Zhang, X., Senior, A., and Ruhrmann, A., 2004, "Vortices Behind a Bluff Body With an Upswept Aft Section in Ground Effect," Int. J. Heat Fluid Flow, **25**, pp. 1–9.
[28] Burgin, K., Adey, P. C., and Beatham, J. P., 1986, "Wind Tunnel Tests on Road Vehicle Models Using a Moving Belt Simulation of Ground Effect," J. Wind Eng. Ind. Aerodyn., **22**, pp. 227–236.
[29] 2000, *FlowMap Particle Image Velocimetry Instrumentation*, 5th ed., Dantec Dynamics, Skovlunde, Denmark.
[30] Abernethy, R. B., Benedict, R. P., and Dowdell, R. B., 1985, "ASME Measurement Uncertainty," ASME J. Fluids Eng., **107**, pp. 161–164.
[31] Bell, S., 1999, "A Beginner's Guide to Uncertainty of Measurment," Measurement Good Practice Guide, **11**(2), pp. 1–33.

Pulsating Flow for Mixing Intensification in a Twisted Curved Pipe

B. Timité

M. Jarrahi

C. Castelain

H. Peerhossaini
e-mail: hassan.peerhossaini@univ-nantes.fr

Thermofluids,
Complex Flows and Energy Group,
Laboratoire de Thermocinétique,
UMR CNRS 6607,
Ecole Polytechnique-Université de Nantes,
La Chantrerie,
BP 50609,
F-44306 Nantes, France

This work concerns the manipulation of a twisted curved-pipe flow for mixing enhancement. Previous works have shown that geometrical perturbations to a curved-pipe flow can increase mixing and heat transfer by chaotic advection. In this work the flow entering the twisted pipe undergoes a pulsatile motion. The flow is studied experimentally and numerically. The numerical study is carried out by a computational fluid dynamics (CFD) code (FLUENT 6) in which a pulsatile velocity field is imposed as an inlet condition. The experimental setup involves principally a "Scotch-yoke" pulsatile generator and a twisted curved pipe. Laser Doppler velocimetry measurements have shown that the Scotch-yoke generator produces pure sinusoidal instantaneous mean velocities with a mean deviation of 3%. Visualizations by laser-induced fluorescence and velocity measurements, coupled with the numerical results, have permitted analysis of the evolution of the swirling secondary flow structures that develop along the bends during the pulsation phase. These measurements were made for a range of steady Reynolds number ($300 \leq Re_{st} \leq 1200$), frequency parameter ($1 \leq \alpha = r_0 \cdot (\omega/\nu)^{1/2} < 20$), and two velocity component ratios ($\beta = U_{max,osc}/U_{st}$). We observe satisfactory agreement between the numerical and experimental results. For high β, the secondary flow structure is modified by a Lyne instability and a siphon effect during the deceleration phase. The intensity of the secondary flow decreases as the parameter α increases during the acceleration phase. During the deceleration phase, under the effect of reverse flow, the secondary flow intensity increases with the appearance of Lyne flow. Experimental results also show that pulsating flow through a twisted curved pipe increases mixing over the steady twisted curved pipe. This mixing enhancement increases with β. [DOI: 10.1115/1.4000556]

Keywords: twisted-pipe flow, Dean cells, Lyne instability, pulsating flow, mixing, curved pipe, LDV, LIF

1 Introduction

Mixing of viscous, miscible, or immiscible fluids occurs in many industrial applications. This process is characterized by a slow mixing or a transport mechanism due to its laminar nature. In order to improve mixing in the laminar regime, various more or less complex geometrical configurations have been studied: closed configurations, in which the fluid flow is confined in a volume [1], and open configurations [2–4]. These particular geometries generate spatially chaotic trajectories even in a laminar regime and for very low Reynolds numbers. The chaotic nature of the trajectories is due not to the flow dynamics but to strictly kinematic parameters. Fluid particles, initially close together, separate exponentially in space and follow different and complex trajectories. Several studies have contributed to the understanding of mixing or dispersion phenomena in open steady spatially chaotic flows, in particular, in alternated Dean flow. To generate chaotic trajectories in a curved channel flow (Dean flow), it is necessary to introduce a "geometrical perturbation" making it possible to destroy and reconstruct the secondary flow cells generated due to the centrifugal force. This perturbation can be obtained simply by turning the curvature plane of each bend with respect to the curvature plane of the neighboring bends.

At each change in curvature plane, due to the reorientation of the centrifugal force, Dean cells will be destroyed and reconstructed in a perpendicular plane, and their position will be modified periodically. As distinct from the two-dimensional time-dependent blinking vortex system studied by Aref [1], the idea here consists in replacing the material agitators with inherent "fluid" agitators in the flow and thus in changing the temporal period by a spatial period. The particle trajectories are chaotic in an open steady laminar flow. Several studies have been carried out on this flow highlighting mixing improvement [3,5] and heat-transfer enhancement [6–8].

The aim of this work is to study a spatially chaotic flow in which a temporal dependence is imposed in order to control the flow and its properties. The basic flow oscillates around a nonzero average value. Very few studies have been done on pulsatile flows in straight tubes and even fewer on curved tubes. Analytical studies of Womersley [9] and Atabek and Chang [10] have allowed linearization of the equations controlling the pulsatile flow in a straight tube. The frequency parameter $\alpha = r \cdot (\omega/\nu)^{1/2}$ and the ratio β of oscillation amplitude influence the flow with the appearance of reverse flow in the zones in the wall vicinity.

In contrast to the main interest of most previous work, which is largely physiological applications [11–13], here we are concerned with the effect of pulsating flow on mixing enhancement in some technological applications. Our results remain applicable, however, to the human circulatory system because the parameter ranges remain very close to those of that system [14].

For pulsating flow in the curved pipes, Lyne [15] was the first to highlight a secondary flow instability called Lyne instability that involves the generation of an additional pair of counter-rotating vortices that coexist with the Dean cells [16]. The interaction among centrifugal forces, inertial effects, and viscous forces in a steady flow creates the Dean cells, and the addition of

Contributed by the Fluids Engineering Division of ASME for publication in the JOURNAL OF FLUIDS ENGINEERING. Manuscript received October 14, 2008; final manuscript received August 28, 2009; published online November 24, 2009. Editor: Joseph Katz.

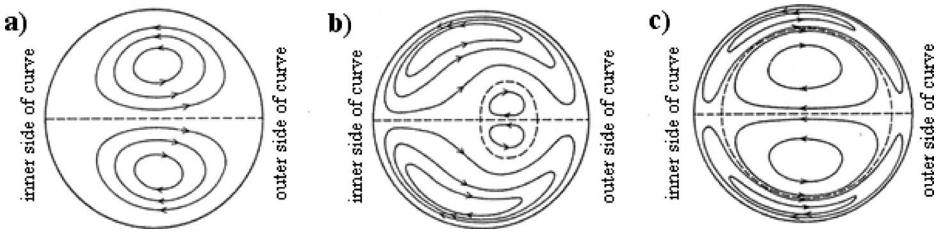

Fig. 1 (*a*) Dean cells (steady flow), (*b*) deformed Lyne instability (pulsatile flow), and (*c*) Lyne instability (pulsatile flow)

a pulsation to the flow can generate the additional Lyne vortices in some phases of oscillation. Lyne considered a pure sinusoidal flow and constructed an asymptotic expansion solution of the Navier–Stokes equation. According to this solution, when the frequency parameter α is greater than 12.9, the twin (Dean) vortex motion that characterizes steady flow transforms to a new four-vortex motion. This result was also found theoretically by Zalosh and Nelson [17], who studied pulsating flow under the influence of a pressure gradient oscillating at frequency ω. Since Ref. [17] was completed, a parallel study by Lyne [15] has appeared treating the case in which the frequency parameter is large and the pressure gradient amplitude is small. The analysis of Zalosh and Nelson [17], which follows the lines of Dean's [16] perturbation solution for steady flow, deals with small, moderate, and large values of the frequency parameter, but is also restricted to small values of the amplitude parameter. The secondary flow patterns obtained in this theoretical work were then confirmed experimentally by Bertelsen [18], who rendered the fluid motion visible by tracer particles of aluminum powder and photographed the particles using stroboscopic illumination synchronized to the frequency of oscillation. Timité et al. [19] showed that in an oscillatory flow, the secondary flow depends on the unsteady Reynolds number; for a Womersley number between 13 and 15, they observed the Lyne instability at a 360 deg curvature angle. In an analytical study, Rabadi et al. [20] observed in the case of a pulsatile flow a considerable variation of the secondary flow intensity at weak oscillation frequencies. In an experimental study in a 180 deg curved tube, Talbot and Gong [21] showed the presence of a return movement near the internal wall during the deceleration phase, and suggested the existence of an additional vortex close to the center of the duct section.

Figure 1 shows the secondary flow structures in a curved pipe in steady state (Dean cells) and in pulsating state (Lyne instability). The more complex structure obtained in pulsating flow can contribute to better mixing, and this is the principal interest of time-dependent flow in the present study. The combination of a series of alternating curved ducts and a pulsatile flow can lead to the generation of a "more chaotic" flow that can be controlled by oscillation of the mean flow. The secondary flow will be much more complex, with the possible emergence of Lyne vortices, which increase the capacity of the fluid blobs to stretch and fold and also induce reverse flows. This flow complexity is strengthened by the changes in orientation of the centrifugal force.

In this study, we characterize the flow in this geometry for various Reynolds numbers, frequency parameters, and velocity amplitude ratios. We then examine the influence of the pulsatile flow on the appearance of chaos in the alternated Dean (twisted-pipe) flow and eventual possibilities for control of the system.

2 Experimental Facilities and Procedures

2.1 Water-Tunnel Facility. A water-tunnel facility was specifically designed and constructed to provide controlled flow through the test section. Steady flow is generated in the test section by a volumetric pump from a reservoir of 300 liter capacity. The steady flow rate is measured by three calibrated flow meters with overlapping ranges, arranged in parallel. The oscillatory flow is obtained by a pulsation generator. The two flow streams join and pass through a 2.5 m straight Plexiglas tube provided to relax the flow streamlines and fully develop the flow, and also to assure stable and clean inlet conditions. From previous studies of Florio and Mueller [22], Fargie and Martin [23], and Ohmi et al. [24], correlation (1) for entrance development length in a pulsating flow is used to determine the length of this straight tube

$$L_E = 0.049 D_h \ \mathrm{Re}_{\mathrm{ta}} \tag{1}$$

2.2 Pulsation Generator. The aim here is to provide a pulsation generator in which the nondimensional frequency α and amplitude ratio β can vary independently. The pulsation generator (see Fig. 2) is composed of a Scotch-yoke mechanism to cover the large range of nondimensional laminar oscillatory flow parameters. It consists of a piston linked to an inertia wheel, two pulleys, and an asynchronous electric motor (Leroy Sommer, 1500 rpm). The pulsation generator has a crank to which a piston of $d_p = 0.04$ m diameter is connected by a metal stem; the piston stroke is controlled by the crank in steps of 20 mm up to a maximum of 200 mm. The pulsation ω is controlled by a motor reducer.

Since the flow is laminar, the motor shaft power is geared down using an epicycloidal reducer of ratio 35.5 and a belt-pulley system of ratio 2.8. A small pulley of diameter $D_1 = 100$ mm is fixed on the motor-reducer shaft, and a second pulley ($D_2 = 280$ mm) is fixed on the inertia wheel shaft. In this configuration, the wheel rotation velocity varies from 0 rpm to 15 rpm. The stainless plenum junction between the steady and oscillatory flows is situated

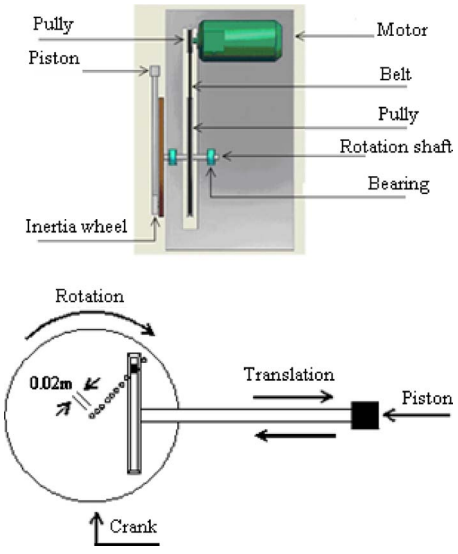

Fig. 2 Scotch-yoke mechanism

Fig. 3 Photograph of the test section

downstream of the stainless piston-cylinder. This pulsation generator lets us carry out experiments in the same range of parameters as in the numerical study.

2.3 Test Section. After the straight channel, the flow enters the test section, made of plexiglas to facilitate flow visualization and laser Doppler velocimetry (LDV). The test section is constituted of a sequence of six bends in which the curvature plane of each bend makes a 90 deg angle with that of its neighbor (see Fig. 3). This kind of geometrical arrangement was used by Jones et al. [2] to generate chaotic advection in a twisted-pipe flow. Their numerical work shows that a 90 deg angle is, in fact, optimal for efficient stirring in twisted pipes of circular cross section because the chaotic region dominates the regular region. In the present work, each bend is a 90 deg curved pipe of circular cross section ($D_0=2r_0=40$ mm) and the curvature radius is $r_c=220$ mm (curvature ratio$=\eta=r_0/r_c=0.091$). The many application domains of curved pipes in heat and mass transfer systems, industrial mixers, and reactors and also in bioengineering are a motivation for choosing this geometry as the basic element of the mixer here. The small curvature ratio was chosen to provide a strong radial pressure gradient across the bend and thus promote the rapid development of Dean roll-cells. Each of the two successive bends is separated by a 40 mm straight tube section. These elements are machined of plexiglas from the same batch so as to guarantee uniform surface quality (transparency and uniformity). The tube thickness is 5 mm for suitable mechanical resistance.

2.4 Flow Visualization and Laser Doppler Velocimetry. Axial velocity is measured by a LDV operating in backscattering mode. The measurement volume translation, data acquisition, and data analysis are controlled by an autonomous computer. To avoid optical distortion in velocity measurements, a small water box is fixed on the curved bend at $\phi=90$ deg angular position (see Fig. 4(*a*)). This box is filled with water since the refractive index of water ($n_{\text{water}}=1.33$) is close to that of plexiglas ($n_{\text{plexiglas}}=1.44$).

In order to carry out velocity measurements in the time-dependent flow, the acquisition system is synchronized with the piston motion. The acquisition system is connected to an electric power source controlled by a switching device. The acquisition system intermittently receives a voltage of 5 V from the power source at each contact between the switch and the signal emitter fixed on the Scotch yoke that moves the piston. A filter is placed between the power source and the acquisition system to improve signal quality. The velocity measurement is initialized at 5 V. Measurements by the LDV in the zone covered by the water box are carried out discontinuously in n periods. Thus, the velocity measurements are visualized on the monitor and recorded in a computer for later processing. From measurements of the instantaneous velocity, the mean velocities are reconstituted at each measurement point and for each piston position. The details of LDV system are shown in Fig. 4(*a*).

The first measurements are taken in the straight tube of hydrodynamic development length located upstream of the curved bend in order to check the sinusoidal motion generated by the Scotch-yoke system. Velocity is measured for three radial positions $r/r_0=0$, 2/5, and 4/5 in the flow cross section located 0.25 m upstream of the bend. Figure 5(*a*) shows instantaneous velocity measurements at radial position $r/r_0=2/5$ and Fig. 5(*b*) shows averaged velocities for the flow parameters $\alpha=11.24$, $\beta=1$, and $\text{Re}_{\text{st}}=280$ at three radial positions. The average velocity obtained experimentally, when compared with the analytical predictions, reveals that the Scotch-yoke system produces a sinusoidal motion. Experimental instantaneous velocities are in agreement with analytical predictions within an average deviation of 3%.

The secondary flow was visualized by the laser-induced fluorescence (LIF) technique [25]. The flow is illuminated by blue laser light (a 5 W argon ion laser source) at a wavelength of 488 nm; the reemitted light is green, of about 514 nm wavelength. An aqueous solution of fluorescein is introduced to the flow from an elevated reservoir through a special dye circuit. A cooling-heat exchanger setup, whose temperature is controlled by the signal from the working fluid temperature, is used to bring the tracer temperature close to that of the working fluid. Fluorescein solutions of mass concentration 1 mg/l were used, so that the density variation in the working fluid due to tracer addition is negligible. The tracer flow rate is adjusted by means of small high-precision valves that control dye delivery to each injection point so that it does not perturb the flow.

In this experiment, dye can be injected by two methods.

(1) In the first method, the tracer is injected with a syringe upstream of the settling chamber; the tracer is distributed over the whole section so as to allow overall visualization [3]. The secondary flow is then visualized by illuminating the cross section by a laser sheet.
(2) In the second method, called "point injection," the injector device is a hypodermic needle of 0.25 mm outer diameter, fixed at the tip of a bent tube. The injector assembly can move by micrometric displacement mechanisms in one transverse direction in the tunnel cross section. The injector set is fixed at 500 mm from the entrance of the first bend. In point injection, each injector marks the streaklines in the flow. Each dye streak marks a trajectory and one can follow the transverse stretching and deformation of the cross section of each trajectory as it passes through different bends. To do this, a traversing mechanism was constructed in which the relative position of the camera and the laser light sheet is fixed. The traversing mechanism rotates around the curvature center of the bend and allows visualization of the transverse flow at different angular positions. To avoid optical distortion in the photographs, a Plexiglas prism is used, as shown in Fig. 4(*b*). A glycerin-water mixture of refraction index close to that of plexiglas is deposited between the prism concave surface and the bend convex wall to compensate for the material changes in the optical path. The flow cross sections are viewed by a charge-coupled device (CCD) camera equipped with Schneider optics. It is crucial that images taken at different streamwise positions of the flow sections be completely comparable from the optical point of view. Images viewed by the camera are transferred directly to a digital image-processing system where they are recorded and analyzed with the aid of a small computer. The photographic recording is synchro-

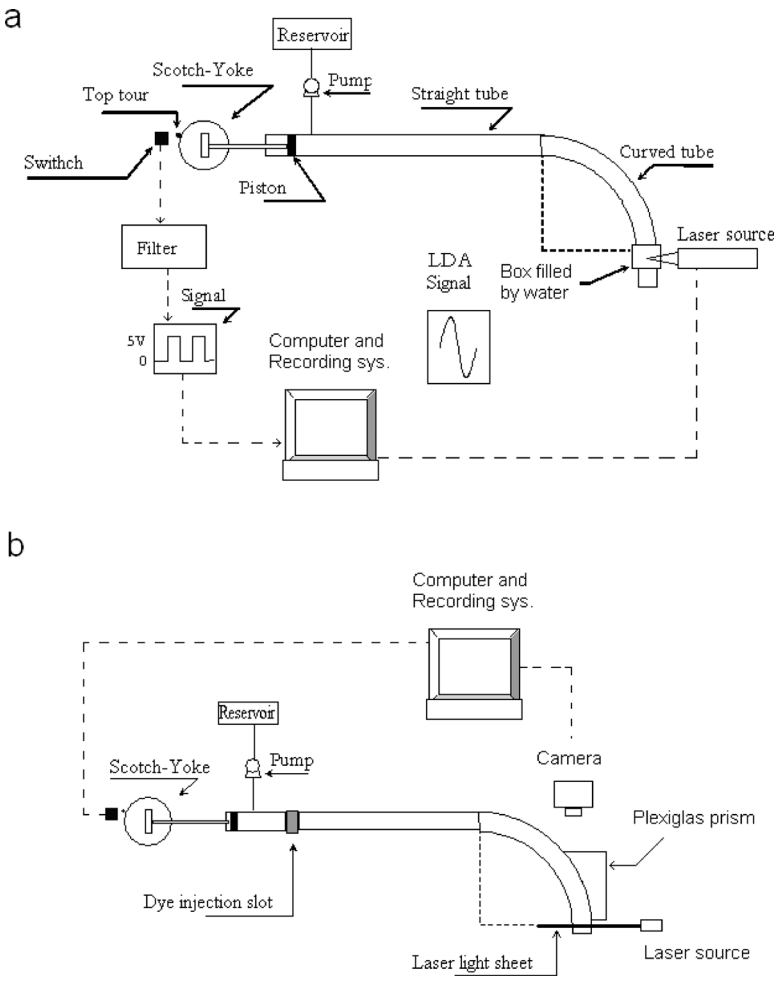

Fig. 4 Visualization setups: (*a*) LDV system and (*b*) LIF system

nized in the same way as the LDV measurements, and the camera parameters are regulated so that images are taken continuously and/or sequentially.

3 Numerical Simulations

3.1 Numerical Method and Flow Geometry. The FLUENT CFD solver was used to solve three-dimensional time-dependent Navier–Stokes equations for an incompressible flow in a curved channel of circular cross section. The CFD code lets us use a user-defined function (UDF) in the problem resolution. In the present case, the fluid is Newtonian (the fluid properties correspond to water at 300 K) and the flow is unsteady, laminar, incompressible, and isothermal. The governing equations are nonlinear and time dependent. An algorithm segregated solver algorithm used to solve the governing equations sequentially and the implicit scheme is used to linearize the equations. The segregated algorithm associated with the implicit linearization diagram offers a considerable advantage in computing time and requires less memory. All simulations were conducted by a segregated method using the SIMPLE scheme for pressure-velocity decoupling. The second-order-accurate schemes were selected to discretize the governing equations.

The geometry modeled in the numerical simulation is the same as the experimental structure of six bends described in Sec. 2.3, including the 2.5 m straight tube connected to the first bend as mentioned in Sec. 2.1. The cross section of the computational domain is discretized with quadrilateral element meshes, as shown in Fig. 6. Structured meshing was introduced in the wall vicinity to refine the calculations in this zone. The thickness of the elements in this zone is determined using the results of Takayoshi and Katsumi [26]. In order to choose the optimum number of elements for meshing the geometry, several numbers of nodes (from 40 to 60 nodes) on the perimeter of the entry section were examined. The longitudinal distance between two nodes is fixed at 0.012 m for the straight tube and at 0.002 m for the curved bends. This mesh optimization was carried out for a steady flow with a constant-velocity inlet, and ultimately it appeared reasonable to use 50 nodal points on the perimeter of the entry section to generate an optimum meshing. The result of this meshing is a cross section composed of 571 elements and globally yields a meshed geometry consisting of 835,944 elements and 3,343,776 nodes.

3.2 Boundary Conditions. Since the pulsatile flow is a superposition of a steady flow and an oscillatory flow, only the oscillatory flow needs to be modeled. In the present calculations, the velocity inlet condition is given by an analytical function UDF. The expression to characterize the pulsatile flow used in the calculations was chosen by analyzing various investigations in literature, especially experimental work. Many authors (Takayoshi and Katsumi [26], and Atabek and Chang [10]) described the pulsation by a piston system with a sinusoidal movement characterized by

$$\text{displacement: } X(t) = X_o \cos(\omega \cdot t) \tag{2}$$

$$\text{velocity: } U_{\text{osc}} = U_{\text{max,osc}} \sin(\omega \cdot t) \tag{3}$$

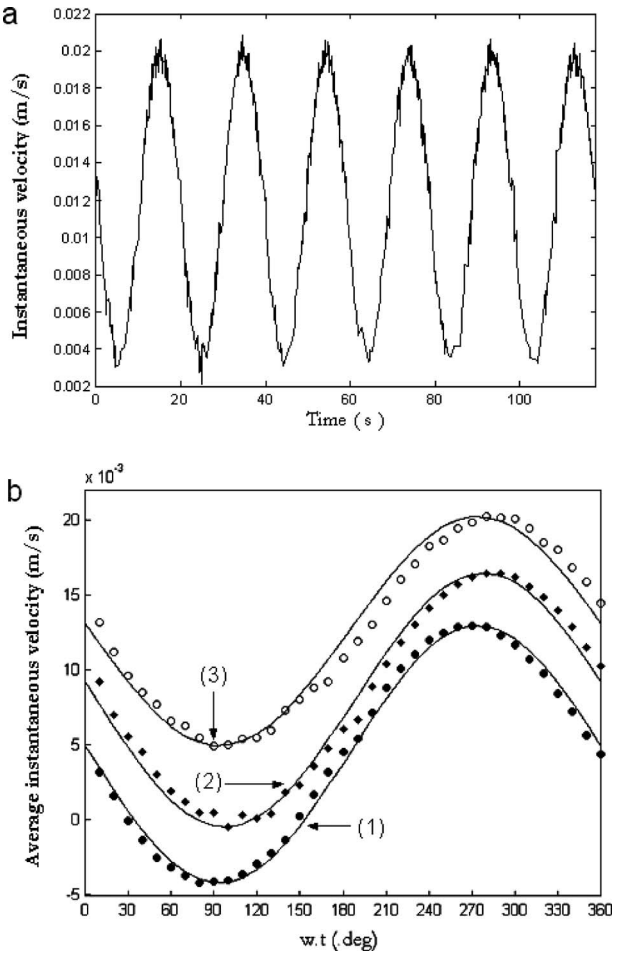

Fig. 5 (*a*) Instantaneous velocity at $r/r_0=2/5$, and (*b*) average velocity, experimental (●, ♦, and ○) and analytical (—) for $Re_{st}=280$, $\alpha=11.24$, and $\beta=1$ at (1) $r/r_0=4/5$, (2) $r/r_0=2/5$, and (3) $r/r_0=0$

The velocity amplitude $U_{max,osc}$ is the product of the piston displacement amplitude X_o and the pulsation ω. By analogy with expression (3), we establish the following UDF characterizing the oscillatory flow:

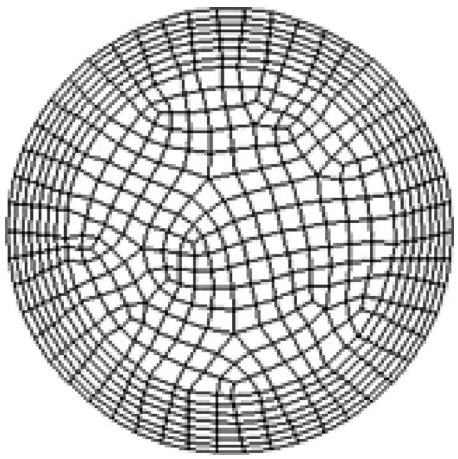

Fig. 6 Cross section meshing

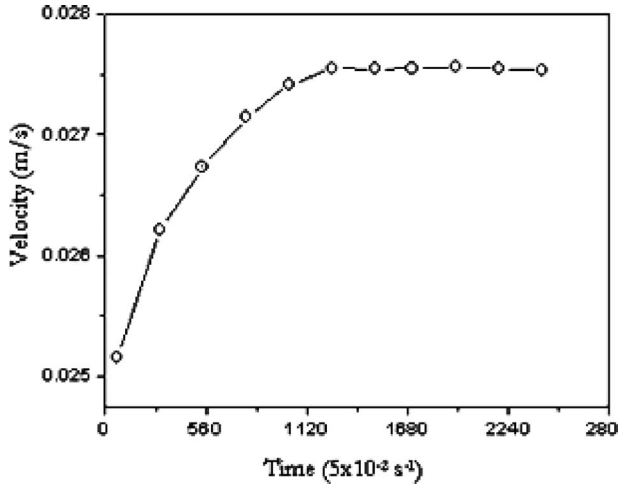

Fig. 7 Second convergence criterion: evolution of the instantaneous velocity amplitude for the same moment of $\omega \cdot t = 90$ deg versus time

$$U_{osc}(t) = |U_{max,osc}|\sin(\omega \cdot t) \tag{4}$$

Thus, by taking into account the steady component, the UDF of the pulsatile velocity inlet can be characterized by

$$U_{inst}(t) = U_{m,st}(1 + \beta \sin(\omega \cdot t)) \tag{5}$$

where ω is the frequency, t is the time, $U_{m,st}$ is the mean steady velocity flow, $U_{max,osc}$ is the peak oscillatory velocity, and $\beta = U_{max,osc}/U_{m,st}$ is the ratio of the peak oscillatory velocity component and the mean flow velocity (steady velocity component), called the velocity component ratio in the following. The velocity field is characterized by the nondimensional frequency parameter $\alpha = r_0(\omega/\nu)^{1/2}$ (ν is the kinematic viscosity), and the mean Reynolds number is defined as $Re_{st} = (U_m \cdot D_h/\nu)$.

3.3 Time Step, Convergence Criterion, and Validation. The time scales are important in resolving the governing equations for the time-dependent flows. The temporal integration method must support time steps fixed according to the slowest phenomenon while preserving solution stability. The implicit integration techniques are adequate. In grids in which different element sizes are present, the time step must be an order of magnitude smaller than or equal to the smallest element size. Thus the largest element can be integrated with a time step much below the acceptable one for these elements. The implicit algorithm choice, in general, allows convergence toward the solution. However, even for implicit methods, choosing the time step remains a delicate issue, since calculation stability is conditioned by this choice. In all our calculations, the time step is obtained by using the Courant number N_c as follows:

$$N_c = U_{m,st}dt/dx \tag{6}$$

where dt is the time step, dx is the minimal element size in the grid, and $U_{m,st}$ is the mean steady flow velocity.

In the numerical simulations, the time step is set to 12 steps/cycle or more (double). A convergence criterion for each time step is governed by a residues criterion: A residual factor equal to 10^{-4} for the mass conservation equation and a residual factor of 10^{-5} for momentum equations were used for the convergence of each time step. However, for convergence of the final calculation, a second criterion was introduced that involved following the velocity evolution at the exit of the geometry under study at the same moment as the period during the computation time. The computations are considered entirely converged when the velocity amplitude becomes invariant. Data are collected during the 3 cycles after the second validation criterion. Figure 7 shows a sample

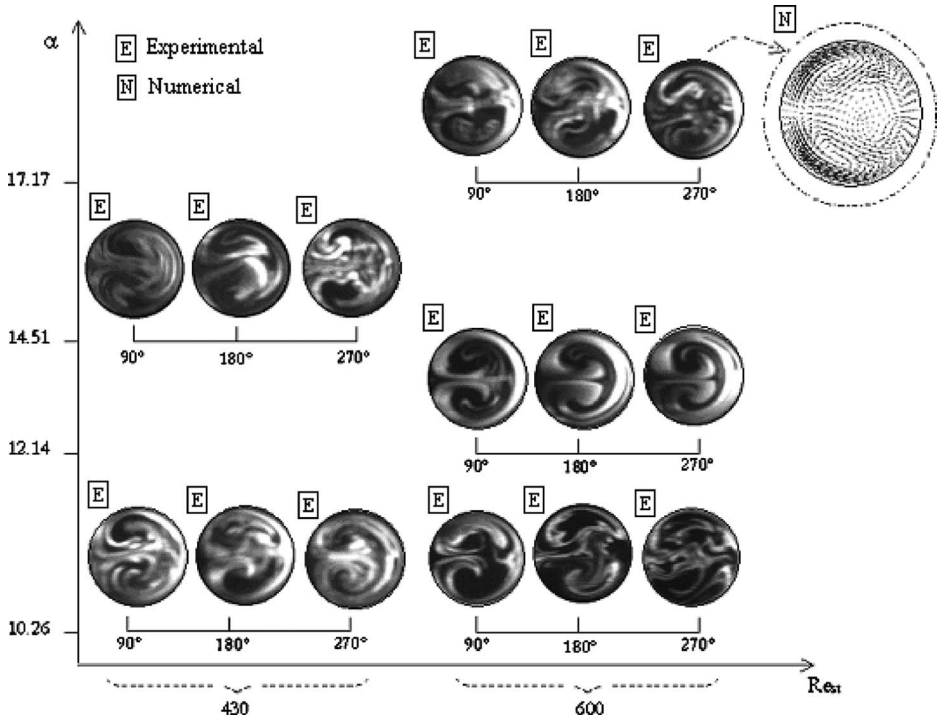

Fig. 8 Experimental and numerical results for secondary flow in the first bend versus the parameter (α) and the steady Reynolds number when $\beta=1$

instantaneous velocity amplitude evolution for different moments of $\omega \cdot t=90$ deg versus time.

For laminar steady flow in a curved pipe, accurate results can be obtained if the solution method is sufficiently accurate. The principal source of error arises in discretization and convergence of the iterative scheme. The resolution procedure for the CFD code has been validated by Fellouah et al. [27] for laminar steady flow in a curved pipe and by Timité et al. [19] for pulsatile and oscillatory straight circular tube flows.

4 Results and Discussion

4.1 Flow Characterization. After the flow characterization in the steady regime, results were obtained for a nondimensional frequency $1 \leq \alpha \leq 20$, a Reynolds number $300 \leq \mathrm{Re}_{st} < 1200$, and a velocity amplitude parameter $1 \leq \beta \leq 2$. The results of numerical calculations and experimental measurements of axial velocity are in agreement with an average deviation of 6%. From these first results a number of interesting phenomena concerning the secondary and axial flow structure can be observed.

The principal flow visualization results for the secondary flow through the first bend are shown in Fig. 8 for $\beta=1$ and 9 for $\beta=2$. For certain values of the control parameters, the secondary flow becomes more complex, in some cases with the appearance of Lyne instability and a siphon phenomenon.

For the different combinations of the flow parameters Re, α, and β three different global secondary flow structures are observed: pure Dean flow, Dean and Lyne flows, and swirl. Transitional structures between the three flow structures are also observed. In Fig. 8 for $\beta=1$ it seems that the amplitude of the oscillating velocity component is not strong enough to make the Lyne vortices appear at low α values. One must push the Reynolds number to 600 and the α value to 17.17 in order to obtain a secondary flow structure close to the combination of the Dean and Lyne vortices, as shown in the image for Re=600, $\alpha=17.17$, and $\omega \cdot t=270$ deg in Fig. 8. In the same figure it can clearly be observed that for Re=600 and $\alpha=12.14$ the Dean vortices are gradually pushed away from the concave wall as $\omega \cdot t$ increases, leaving room for the growth of the Lyne vortices. Comparison of the images for this α value ($\alpha=12.14$) and those for $\alpha=17.17$ suggests that all else equal α is the parameter that contributes to the growth of the Lyne vortices. When β is increased the Lyne instability can appear at lower values of α; for instance, in Fig. 9, for Re=600, the Lyne vortices appear at $\alpha=10.26$, much lower than $\alpha=17.17$ for $\beta=1$. This instability that appears at $\omega \cdot t=180$ deg actually starts at $\omega \cdot t=150$ deg (not shown here) with a small pair of vortices near the concave wall that persists until $\omega \cdot t=180$ deg. At this phase ($\omega \cdot t=180$ deg), the secondary flow is composed of two vortex pairs; the small developing vortex pair pushes the Dean vortex pair toward the inner wall. However, at the end of the deceleration phase ($\omega \cdot t=270$ deg), the Lyne flow yields to an asymmetrical secondary flow.

In addition, the distribution of axial velocity along the plane perpendicular to the curvature plane shows the effect of Lyne vortices on the secondary flow. Figure 10 shows the evolution of the axial velocity profiles at various phases in a period. The velocity profile, which initially has a flat parabolic form with two maxima close to the walls at $\omega \cdot t=90$ deg (sign of Dean vortices), presents three maxima at $\omega \cdot t=180$ deg: two maxima near the side walls and one at the section center corresponding to Lyne vortices. However, at the end of deceleration phase ($\omega \cdot t=270$ deg), the velocity profile shows two strong reverse-flow zones near the side walls and a deceleration at the center.

Figures 8 and 9 suggest also that higher Reynolds numbers contribute to structuring the secondary flow (though the centrifugal force), so that α and β make the Lyne vortices appear. However, at low Reynolds numbers, the effects of α and β appear through the generation of a swirl flow, as in Fig. 9 for $\beta=2$, $\alpha=10.26$, Re=430, and $\omega \cdot t=270$ deg. This phenomenological reasoning through flow visualization provides a qualitative guide for generating different secondary flows by controlling the three flow parameters; a more systematic parametric study is needed to construct a complete topological diagram of different flow regimes.

The secondary flow patterns observed in the subsequent (second, third, etc.) bends differ from those of the first bend for large-

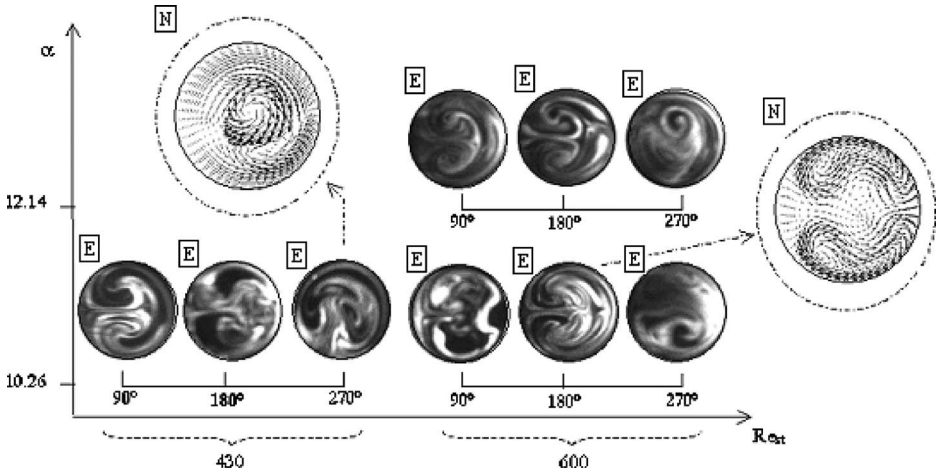

Fig. 9 Experimental and numerical results for secondary flow in the first bend versus the parameter (α) and the steady Reynolds number when β=2

amplitude velocity ratios (β). Thus, one passes from four cells (Lyne instability) in the first bend to two cells in the other bends. In addition, the siphon phenomenon observed persists in all the structures studied. Due to the variation in the centrifugal force orientation in each bend, the secondary flow cells formed in one bend are destroyed and are reconstructed in the following bend. The secondary flow after the first bend has a two-cell structure but in different directions according to the orientation of the bend curvature plane. The differences in the cell volumes are due to the change in orientation of the bends (Fig. 11), a phenomenon reported by Le Guer and Peerhossaini [28] and Duchêne et al. [29]. Disappearance in the rest of the geometry of the Lyne instability observed in the first bend may be due to the lack of sufficient curvilinear length for flow development in the following bends.

4.2 Chaotic Behavior. Mixing is mainly due to two different mechanisms: particle advection along streamlines and particle diffusion between streamlines. In alternated Dean flow, chaotic advection can be achieved by modifying the topography of the streamlines resulting from successive destruction and reproduction of the Dean cells. Nevertheless, the regular islands—where particles can be trapped—still exist; however, they are not favorable for mixing because the only mechanism of mixing for the fluid particles trapped in these islands is diffusion. The motivation

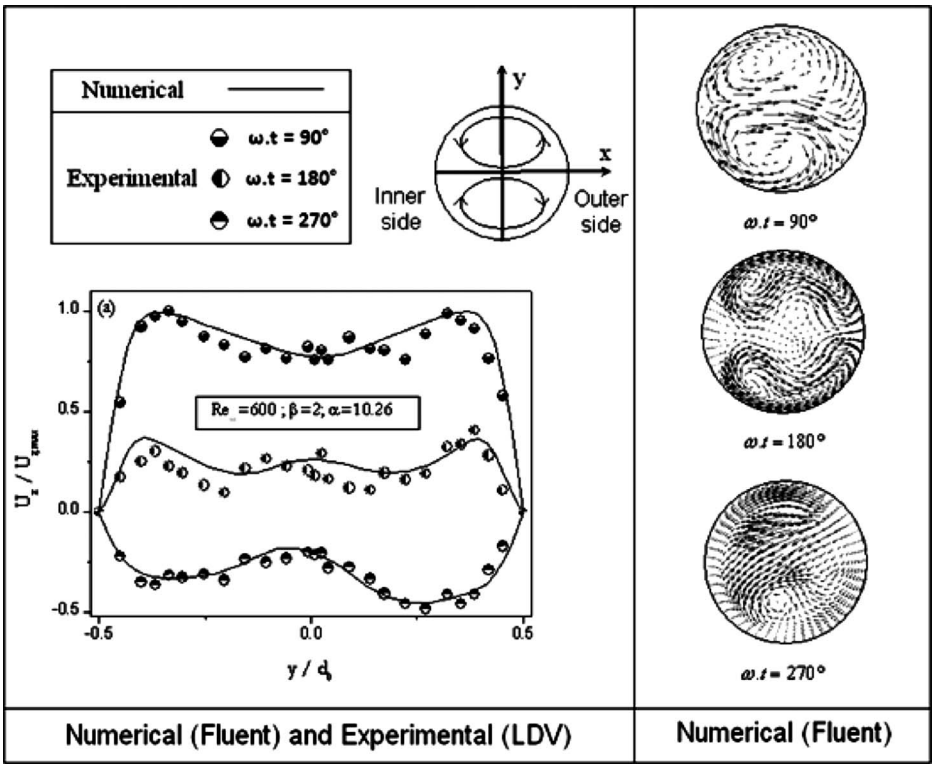

Fig. 10 (*a*) Numerical simulations (—) compared with experimental axial velocity profiles (●) in the first bend for various moments ($\omega \cdot t$) at Re_{st}=600, β=2, and α=10.26. (*b*) Numerical secondary velocity vectors in the first bend for various moments ($\omega \cdot t$).

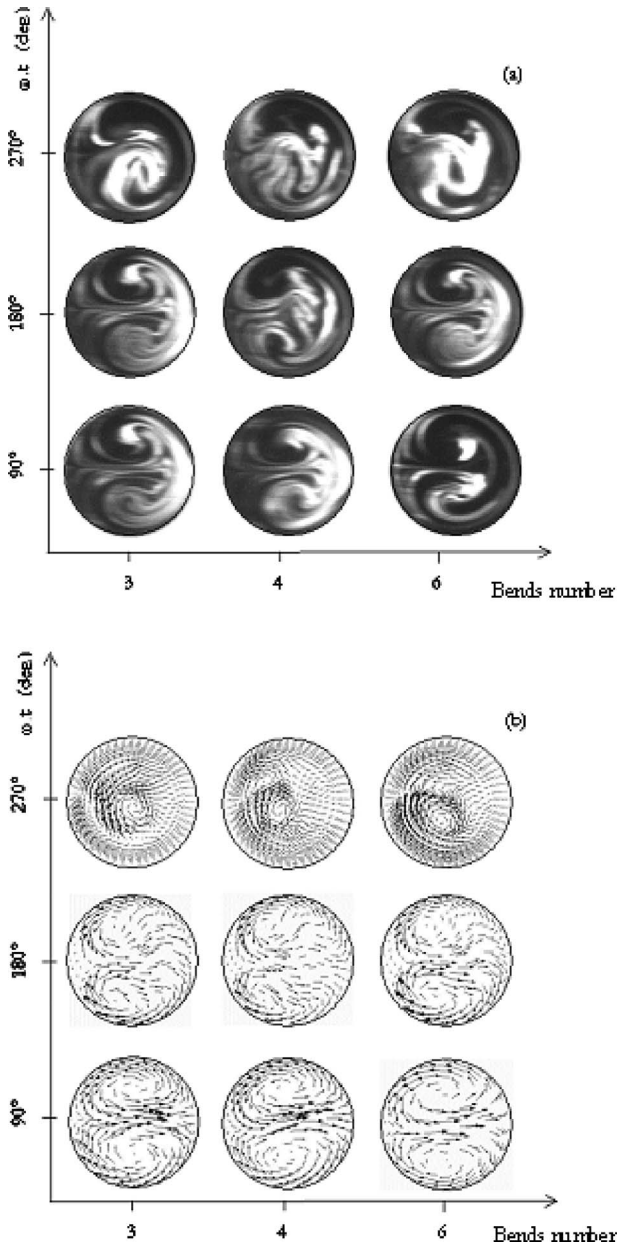

Fig. 11 Secondary flow at the exit of the bends at various moments ($\omega \cdot t$) for $Re_{st}=600$, $\beta=2$, and $\alpha=10.26$: (*a*) experimental visualization and (*b*) numerical velocity vectors

in this work is to examine whether superposition of a time-dependent flow on the steady chaotic flow can lead to a still more chaotic flow by breaking down the boundaries and decreasing the surface of these islands.

The chaotic nature of the trajectories is due not to the flow dynamics but to strictly kinematic parameters. The fluid particles initially close together (especially in a chaotic zone) separate exponentially in space and follow different and complex trajectories. The observation of particles trajectories in a time-periodic open three-dimensional flow becomes more complex than in the periodic two-dimensional and steady three-dimensional cases. In this work we follow (numerically), along the flow and at different periods, the trajectories of two fluid particles injected into the entry section at initially very close positions.

The first tracer injection was carried out in the center of the entry cross section, whereas the second injection is made near the pipe wall. For a given time, the injection is thus characterized by

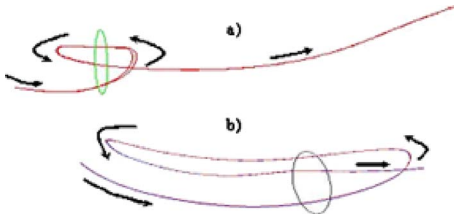

Fig. 12 Particle trajectories at the exit of the first bend for a period: (*a*) injection at the center of the inlet section and (*b*) injection near the wall

a point in space; at the next time it is characterized by another point, and so on, so that these successive points show the evolution of the particle positions over time. Figure 12 shows the periodic trajectory of the particles in the first bend during a complete pulsation cycle for the above two injection positions. If we consider a cross section perpendicular to the curvature plane, for example, the outlet of the first bend in Fig. 12, the particle crosses this section for the first time during the first part of acceleration phase ($0 \text{ deg} < \omega \cdot t < 90 \text{ deg}$). Because of the reverse flow in the deceleration phase ($90 \text{ deg} < \omega \cdot t < 270 \text{ deg}$), the particle passes through the section for a second time, and finally a third passage occurs during the second part of the acceleration phase ($270 \text{ deg} < \omega \cdot t < 360 \text{ deg}$).

It is observed that the fluid particles injected at the cross-section center have residence time much shorter than those injected near the wall. Indeed, the trajectories of the two sets of particles are completely different: particles initially trapped in the wall boundary layer have a longer reverse movement than those initially located at the flow center.

The chaotic flow behavior in Fig. 13 represents a portion of the trajectories at the exit of the second and sixth bends for a steady flow ($Re_{st}=620$) and a pulsatile flow ($Re_{st}=620$, $\beta=2$, and $\alpha=10.26$ at $\omega \cdot t=90$ deg) of two fluid particles injected at the flow center. In the pulsatile flow, the particle trajectories diverge at the exit of the second bend and are very complex, which is not the case for the steady flow. At the exit of the sixth bend, the trajectories in the pulsatile case are more diverged, whereas in the steady case the divergence is small. These observations suggest that fluid particles can follow spatially chaotic trajectories in an alternated Dean pulsatile flow. In addition, it is observed that some zones that are regular in the *steady* alternated Dean flow show a chaotic behavior in the pulsating regime.

Experimentally, for the steady regime ($Re_{st}=430$), we chose two positions that gave extreme situations for transverse spreading of the tracer: The point ($x/r_0=0$; $y/r_0=0$) shows more transverse

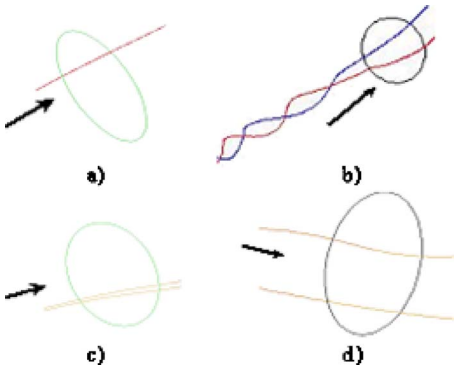

Fig. 13 Divergence of trajectories: (*a*) second bend in steady flow, (*b*) second bend in pulsatile flow ($Re_{st}=620$, $\beta=2$, and $\alpha=10.26$), (*c*) sixth bend in steady flow, and (*d*) sixth bend in pulsatile flow ($Re_{st}=620$, $\beta=2$, and $\alpha=10.26$)

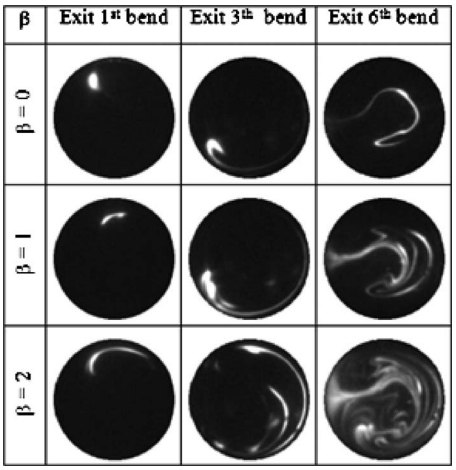

Fig. 14 Evolution of the deformation of a dye injection at the exit bend versus the amplitude velocity ratio β (Re_{st}=430 and α=10.26; injection: $x/r_0=0$; $y/r_0=0.7$)

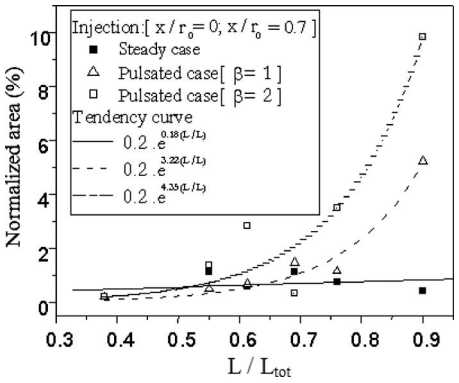

Fig. 15 Streamwise evolution of the cross-sectional area of tracer filament injected at the entrance to the first bend

spread of dye, whereas the dye injected at the point ($x/r_0=0$; $y/r_0=0.7$) spreads out less. These injection positions correspond, respectively, to the center of the pipe cross section and to a zone located near the eye of the upper Dean cell of the first bend.

Figure 14 shows the influence of the superposition of an oscillating flow on a steady flow: Fluid is trapped in "no-mixing" zones (islands) at the end of the oscillation period when the injection position is at the point ($x/r_0=0$; $y/r_0=0.7$). For $\alpha=10.26$, the influence of the variation in β can be explained as follows: at the exit of the first bend for the steady flow ($\beta=0$) the dye spot stays close to the injection position with no appreciable stretching, but after an oscillation is added to the steady flow, this stretching becomes stronger and stronger. The same tendency can be seen at the exit of the other bends in which the dye covers almost two-thirds of the cross-section surface at the exit of the third bend when $\beta=2$. Finally, at the exit of the sixth bend, the dye is spread all over the section for $\beta=2$.

The experimental study of the process of tracer stretching and folding made it possible to observe the structure evolution due to the pulsation. The main result is that the superposition of an oscillating flow on a steady flow induces far more complex particle trajectories, within some cases, the destruction of the trapped fluid zones.

4.3 Measurement of Stretching. Stretching is an important phenomenon in applications because it improves mixing. We have followed experimentally the stretching of a tracer blob along the flow in the successive bends. The curve in Fig. 15 shows the evolution of the tracer cross-sectional area with streamwise distance for injection point ($x/r_0=0$; $y/r_0=0.7$) (the cross-sectional area of the tracer blobs is normalized by the total image area). All the curves show exponential area spreading of the form A_0e^{aL/L_t}, where a and A_0 are constants. By examining the evolution of area versus the normalized longitudinal coordinate L, we notice that the stretching increases with the velocity amplitude ratio. We observe, for this injection position, no significant spreading in the steady case since the injection point is situated in the center of a Dean vortex, which is an elliptic point of the flow. In steady twisted-pipe chaotic flow (the case of the present work without pulsation), fluid particles situated in the elliptic regions end up being trapped in the Kolmogorov–Arnold–Moser (KAM) regular zones, which they cannot leave to mix with the rest of the flow. The horizontal line in Fig. 15 represents the mixing evolution of these points in a steady chaotic flow. However, in the pulsatile cases, the dye blob originally injected in an elliptic point in the first bend spreads exponentially and reaches values at the exit of the sixth bend that are of the order of five to ten times its initial cross-sectional area at the injection point. Therefore it can be concluded that flow pulsation can break up the KAM zones and liberate the trapped fluid particles. The undispersed zones are transformed into zones of strong dispersion by the periodic flow pulsation.

To illustrate this observation, we compare the values of the exponents obtained for the two pulsatile cases. The exponent $a>0$ can be considered here the equivalent of a Lyapunov exponent. In the steady regime of the same flow, areas exist that are able to stretch the dye strongly, whereas in others, the dye is stretched very little. However, the superposition of an oscillating flow on this steady flow reduced the likelihood of the nonstretching zones and allowed control and reduction in the regular zones by choice of an appropriate velocity amplitude ratio. For steady chaotic flow in a twisted pipe, Castelain et al. [3] showed experimentally that tracer blob cross-sectional area increases exponentially as a function of distance along the flow. Our experimental results here show that, all else equal, the exponent a in a pulsatile chaotic flow is larger in pulsatile chaotic flow than in steady chaotic flow. In addition, Fig. 15 shows that in a pulsatile chaotic flow the exponent a is an increasing function of β: for $\beta=1$, $a=3.22$ and for $\beta=2$, $a=4.35$. Further investigation is needed to correlate a with β and also with α.

4.4 Conclusions. Experimental and numerical studies of alternated Dean pulsatile flow showed an important modification of the secondary flow structure due to the pulsation. For certain control parameters, the secondary flow becomes more complex, in some cases with the appearance of Lyne instability or swirling structures due to the periodic movement. The modification of the secondary flow cells due to the temporal dependence of the flow, coupled with the destruction and reconstruction of the cells at each bend, generates a more chaotic flow and hence better fluid mixing. It is believed that the more chaotic nature of pulsatile chaotic flow (compared with the steady chaotic flow) is mainly due to the breakdown of KAM zones and reduction in the likelihood of generation of regular islands in the flow.

This work shows that tracer dispersion increases exponentially with distance along the pulsating twisted pipe in the same manner as in a steady chaotic (twisted-pipe) flow. However, all else equal, the exponent in the pulsating flow is larger than in the steady flow and is an increasing function of β the velocity amplitude ratio.

Nomenclature

d_o = tube diameter, $d_o=D_h$
d_p = piston diameter
dt = time step
dx = minimal element size
D_1, D_2 = pulley diameters

D_h = hydraulic diameter
Dn = Dean number, $\mathrm{Dn} = U_m D_h / \nu \sqrt{D_h / Rc}$
L = longitudinal coordinate
L_E = entrance length
n = refractive index
N_c = Courant number
r = radial coordinate
r_0 = tube radius
r_c = curvature radius
Re = Reynolds number, $U_m D_h / \nu$
t = time
U = axial velocity
x, y = space coordinates
X_0 = amplitude of piston displacement
$X(t)$ = piston position

Greek Symbols

α = Womersley number, $r_0(\omega/\nu)^{1/2}$
β = velocity components ratio=$(U_{\max,\mathrm{osc}}/U_{\mathrm{st}})$
Φ = angular position
η = curvature ratio of the curved pipe, r_0/r_c
ν = kinematic viscosity
ω = angular frequency

Subscripts

m = mean
max = maximum
osc = oscillating component
st = steady component
z = axial component
ta = time-averaged value
tot = total

References

[1] Aref, H., 1984, "Stirring by Chaotic Advection," J. Fluid Mech., **143**, pp. 1–21.
[2] Jones, S. W., Thomas, O. M., and Aref, H., 1989, "Chaotic Advection by Laminar Flow in Twisted Pipe," J. Fluid Mech., **209**, pp. 335–357.
[3] Castelain, C., Mokrani, A., Le Guer, Y., and Peerhossaini, H., 2001, "Experimental Study of Chaotic Advection Regime in a Twisted Duct Flow," Eur. J. Mech. B/Fluids, **20**, pp. 205–232.
[4] Khakhar, D. V., Franjione, J. G., and Ottino, J. M., 1987, "A Case Study of Chaotic Mixing in Deterministic Flows: The Partitioned Pipe Mixer," Chem. Eng. Sci., **42**(12), pp. 2909–2926.
[5] Castelain, C., Mokrani, A., Legentilhomme, P., and Peerhossaini, H., 1997, "Residence Time Distribution in Twisted Pipe Flows: Helically Coiled System and Chaotic System," Exp. Fluids, **22**, pp. 359–368.
[6] Acharya, N., Sen, M., and Chang, H. C., 1992, "Heat Transfer Enhancement in Coiled Tubes by Chaotic Mixing," Int. J. Heat Mass Transfer, **35**, pp. 2475–2489.
[7] Acharya, N., Sen, M., and Chang, H. C., 1994, "Thermal Entrance Length and Nusselt Numbers in Coiled Tubes," Int. J. Heat Mass Transfer, **37**, pp. 336–340.
[8] Chagny, C., Castelain, C., and Peerhossaini, H., 2000, "Chaotic Heat Transfer for Heat Exchanger Design and Comparison With a Regular Regime for a Large Range of Reynolds Numbers," Appl. Therm. Eng., **20**(17), pp. 1615–1648.
[9] Womersley, R., 1955, "Method for the Calculation of Velocity, Rate of Flow and Viscous Drag in Arteries When Pressure Gradient Is Known," J. Physiol., **127**, pp. 553–563.
[10] Atabek, H. B., and Chang, C. C., 1961, "Oscillatory Flow Near the Entry of a Circular Tube," Z. Angew. Math. Phys., **12**, pp. 185–201.
[11] Pedley, T. J., 1980, *The Fluid Mechanics of Large Blood Vessels* (Cambridge Monographs on Mechanics and Applied Mathematics), Cambridge University Press, Cambridge, pp. 160–224.
[12] Zabielski, L., and Mestel, A. J., 1998, "Unsteady Blood Flow in a Helically Symmetric Pipe," J. Fluid Mech., **370**, pp. 321–345.
[13] Deplano, V., and Siouffi, M., 1999, "Experimental and Numerical Study of Pulsatile Flows Through Stenosis: Wall Shear Stress Analysis," J. Biomech., **32**, pp. 1081–1090.
[14] Hamakiotes, C. C., and Berger, S. A., 1990, "Periodic Flows Through Curved Tubes: The Effect of the Frequency Parameter," J. Fluid Mech., **210**, pp. 353–370.
[15] Lyne, W. H., 1971, "Unsteady Viscous Flow in a Curved Pipe," J. Fluid Mech., **45**(1), pp. 13–31.
[16] Dean, W. R., 1927, "Note on the Motion of Fluid in a Curved Pipe," Philosophical Magazine, **20**, pp. 208–223.
[17] Zalosh, R. G., and Nelson, W. G., 1973, "Pulsating Flow in a Curved Tube," J. Fluid Mech., **59**(4), pp. 693–705.
[18] Bertelsen, A. F., 1975, "An Experimental Investigation of Low Reynolds Number Secondary Streaming Effects Associated With an Oscillating Viscous Flow in a Curved Pipe," J. Fluid Mech., **70**, pp. 519–527.
[19] Timité, B., Castelain, C., and Peerhossaini, H., 2009, "Pulsatile Viscous Flow in a Curved Pipe: Effects of Pulsation on the Development of the Secondary Flow," Int. J. Heat Fluid Flow, submitted.
[20] Rabadi, N. J., Simon, M. A., and Chow, J. C. F., 1980, "Numerical Solution for Fully Developed, Laminar Pulsating Flow in Curved Tubes," Numer. Heat Transfer, **3**, pp. 225–239.
[21] Talbot, L., and Gong, K. O., 1983, "Pulsatile Entrance Flow in a Curved Pipe," J. Fluid Mech., **127**, pp. 1–25.
[22] Florio, J. P., and Mueller, W. K., 1968, "Development of a Periodic Flow in a Rigid Tube," ASME J. Basic Eng., **90**, pp. 395–399.
[23] Fargie, D., and Martin, B. W., 1971, "Developing Laminar Flow in a Pipe of Circular Cross-Section," Proc. R. Soc. London, **321**, pp. 461–476.
[24] Ohmi, M., Usui, T., Fukawa, M., and Hirasaki, S., 1976, "Pressure and Velocity Distributions in Pulsating Laminar Pipe Flow," Bull. JSME, **19**(129), pp. 298–306.
[25] Peerhossaini, H., and Wesfreid, J. E., 1988, "On the Inner Structure of the Streamwise Görtler Rolls," Int. J. Heat Fluid Flow, **9**, pp. 12–18.
[26] Takayoshi, M., and Katsumi, N., 1980, "Unsteady Flow in Circular Tube (Velocity Distribution of Pulsating Flow)," Bull. JSME, **23**(186), pp. 1990–1996.
[27] Fellouah, H., Castelain, C., Ould El Moctar, A., and Peerhossaini, H., 2006, "A Criterion for Detection of the Onset of Dean Instability in Newtonian Fluids," Eur. J. Mech. B/Fluids, **25**, pp. 505–531.
[28] Le Guer, Y., and Peerhossaini, H., 1991, "Order Breaking in Dean Flow," Phys. Fluids A, **3**, pp. 1029–1032.
[29] Duchêne, C., Peerhossaini, H., and Michard, P. J., 1995, "On the velocity Field and Tracer Patterns in a Twisted Duct Flow," Phys. Fluids, **7**(6), pp. 1307–1317.

Direct Numerical Simulations of the Flow Past a Cylinder Moving With Sinusoidal and Nonsinusoidal Profiles

Osama A. Marzouk
Department of Engineering Science and Mechanics,
Virginia Polytechnic Institute and State University,
Blacksburg, VA 24061
e-mail: omarzouk@vt.edu

We perform direct numerical simulations of the flow past a circular cylinder undergoing a one-degree-of-freedom transverse oscillation. The displacement follows a sine function raised to an arbitrary integer power ranging from 1 to 8. When the displacement power is above 2, we have multifrequency oscillation, and the number of Fourier components in the oscillation increases with the power, but they are either odd or even multiples of the input (argument) frequency of the displacement function. We study the responses of the nondimensional lift and drag under these different oscillation profiles and the transfer of nondimensional mechanical energy due to the oscillation, and their trends as the power (hence the number of Fourier components in the oscillation) increases. For odd powers, the energy is transferred to the cylinder; whereas for even powers, it is transferred to the flow. A unity power (harmonic oscillation) corresponds to the maximum energy transfer to the cylinder, which can explain the occurrence of this profile in the case when the cylinder is free to oscillate due to the vortex-induced vibration (VIV) phenomenon. The lift exhibits a mean value only with even powers above 2. The results show that the lift is driven to a large extent by the acceleration of the oscillation rather than its velocity. This should be considered when modeling the fluid-structure coupling in reduced-order VIV models. [DOI: 10.1115/1.4000406]

1 Introduction

Experimental and numerical studies of an elastically-mounted circular cylinder that is freely vibrating in a uniform-stream at low Reynolds numbers [1–7] have shown that shedding is synchronized at or close to the oscillation frequency; thus, the vibration organizes the shedding into distinct cells, the longest of which is synchronized with the vibration [8]. There are experimental studies conducted at higher Reynolds numbers (e.g., 3500–10,000 [9] and 10,000–60,000 [10]), which report this synchronization (also known as "lock-in"). This tendency of the free vibration to follow a simple harmonic motion (at medium and high Reynolds numbers, the vibration is not as simple as in the case of low Reynolds numbers) increases as the displacement amplitude increases in the upper branch of the cylinder response, when its natural frequency is close to the shedding frequency in the wake when the motion is restrained.

Based on this observation, theoretical analysis and reduced-order models for the coupling between the nondimensional lift and the induced vibration of a cylinder have assumed a sinusoidal profile for the oscillation [11–16]. These studies, and most of the work done on forced oscillation of a cylinder, consider a transverse-displacement profile described as a simple sine function, thereby containing a single Fourier component at the oscillation frequency. In order to explain why the nature favors the nearly-sinusoidal profile for the VIV, we should consider nonsinusoidal oscillations and examine the difference in the flow features from the sinusoidal one. When the oscillation is forced, we can apply a wide range of oscillation profiles. Meneghini and Bearman [17] applied a square-wave, saw-tooth, and parabolic-type profiles at $\mathrm{Re}=200$ using two-dimensional (2D) simulations based on vortex-in-cell formulation incorporating diffusion. It should be mentioned that for parabolic-type displacement, the velocity has a saw-tooth profile and the acceleration has a square-wave profile. Consequently, all these three nonsinusoidal profiles of oscillation exhibit repeated discontinuities in the displacement, velocity, acceleration, or a combination of them, which is not acceptable physically. Such discontinuous oscillations resulted in glitches in the obtained lift and drag corresponding to these oscillations.

In this study, we consider sinusoidal (harmonic) and nonsinusoidal oscillation, whose displacement, velocity, and acceleration are all continuous in time, thereby avoiding unrealistic discontinuities in the obtained time-dependent lift or drag. The nonsinusoidal oscillations are based on a sine function (with an argument angular frequency Ω) for the displacement, which is raised to an integer (odd or even) power Π. When $\Pi=1$, this generalized oscillation reduces to a simple sine function with frequency Ω. When $\Pi=2$, the oscillation has a single Fourier component but at 2Ω in addition to a nonzero mean displacement. When $\Pi>2$, the oscillation exhibits more than one Fourier component, which is located at even multiples of Ω for even Π and at odd multiples of Ω for odd Π. When Π is even, the displacement has a mean value, but the velocity and acceleration always have a zero mean. We consider values of Π up to 8, which is high enough to infer the trend of the lift and drag in response to increasing Π (thus increasing the number of Fourier components in the oscillation). We compare the responses of the lift and drag, as well as the energy transfer, due to the oscillation in the case of nonsinusoidal oscillation to those in the case of sinusoidal one. Because the ratio of the amplitudes of the Fourier components, when $\Pi>2$, in the velocity and acceleration of the oscillation are different, the current oscillation configuration enables us to examine, which one has a dominant effect on the lift by examining the amplitudes of its corresponding Fourier components. This is important when establishing a reduced-order model with two coupled ordinary differential equations (ODEs) governing the displacement of the induced vibration and the lift because a coupling term representing

Contributed by the Fluids Engineering Division of ASME for publication in the JOURNAL OF FLUIDS ENGINEERING. Manuscript received April 23, 2009; final manuscript received September 25, 2009; published online November 12, 2009. Editor: Joseph Katz.

the influence of the vibration on the lift is needed in the ODE of the lift (also known as "wake oscillator"). This term is typically assumed to be proportional to the cylinder velocity [15,18,19]. We show that the cylinder acceleration is a more appropriate choice because it influences the lift more than the velocity.

2 Flow Model

The nondimensional continuity and vector momentum equation governing flow field, in an arbitrary Lagrangian–Eulerian (ALE) formulation, are

$$\nabla \cdot \boldsymbol{u} = 0 \tag{1}$$

$$\frac{\partial \boldsymbol{u}}{\partial t} + (\boldsymbol{u} - \hat{\boldsymbol{u}}) \cdot \nabla \boldsymbol{u} = -\nabla p + \frac{1}{\mathrm{Re}} \nabla^2 \boldsymbol{u} \tag{2}$$

where $\boldsymbol{u}$ and $\hat{\boldsymbol{u}}$ are the nondimensional velocity vectors of the flow particles and grid nodes, respectively; p is the nondimensional pressure; and Re is the Reynolds number. The nondimensionalization scales for the length, velocity, and pressure are the cylinder diameter, uniform-stream velocity, and twice the uniform-stream dynamic pressure; respectively. Only the second element of $\hat{\boldsymbol{u}}$ is nonzero, and it is a function of time for a particular grid node. We use the artificial-compressibility method to establish appropriate coupling between the velocity and pressure fields of the flow [20]. Whereas this method was initially [20] introduced to solve steady problems, the concept was extended and used successfully [21–23] for unsteady ones.

The governing equations are discretized using a third-order upwind scheme for the convective terms and central second-order difference for the diffusion terms. We discuss here the differencing for the convection terms (the differencing for the diffusion terms is straightforward), which need special care in their treatment to avoid introducing spurious higher-order derivatives. Two-point (first-order) upwind schemes are known to produce numerical dissipation, which automatically suppresses any oscillations caused by the nonlinear convective fluxes, but can adversely affect the accuracy of the solution in the regions of large velocity gradients. Whereas small dissipation is a favorable property of a numerical scheme because it enhances its stability, excessive dissipation is very undesirable and it means that the numerically-calculated derivatives are smaller than the true ones [24]. On the other hand, applying the central differencing to the convective terms leads to strong nonphysical oscillations for convection-dominated flows [25]. Higher-order upwinding differencing (three or more points) has the advantage of stabilizing the scheme while introducing minimal dissipation. The third-order upwind differencing is applied here with flux-splitting treatment. Besides the favorable stabilizing effect without excessive dissipation, it takes into account the propagation direction of the artificial waves introduced by the artificial-compressibility method. We should add that central differencing for the convective terms does not contribute to the diagonal of the coefficient matrix, whereas upwind differencing does and consequently enhances the convergence.

The differencing scheme for the convective flux is illustrated for a single coordinate x. In the current problem with body-fitted grid, the procedure is applied separately for each generalized curvilinear coordinate. The model conservative hyperbolic system is

$$\frac{\partial \boldsymbol{q}}{\partial t} + \frac{\partial \boldsymbol{f}}{\partial x} = 0 \tag{3}$$

where $\boldsymbol{q}$ is the vector of nondimensional dependent variables ($[p,u,v]^T$ here) and $\boldsymbol{f}$ is the inviscid flux vector. The semidiscrete form of Eq. (3) is

$$\left(\frac{\partial \boldsymbol{q}}{\partial t}\right)_i + \frac{\boldsymbol{f}^*_{i+1/2} - \boldsymbol{f}^*_{i-1/2}}{\Delta x} = 0 \tag{4}$$

where $\boldsymbol{f}^*$ is the numerical inviscid flux vector and i is the grid-point index. The way $\boldsymbol{f}^*$ is calculated determines the order of the scheme. We use third-order $\boldsymbol{f}^*$ as follows:

$$\boldsymbol{f}^*_{i+1/2} = \tfrac{1}{2}(\boldsymbol{f}(\boldsymbol{q}_{i+1}) + \boldsymbol{f}(\boldsymbol{q}_i)) + \tfrac{1}{6}(\Delta \boldsymbol{f}^+_{i-1/2} - \Delta \boldsymbol{f}^+_{i+1/2} + \Delta \boldsymbol{f}^-_{i+1/2} - \Delta \boldsymbol{f}^-_{i+3/2}) \tag{5}$$

where

$$\Delta \boldsymbol{f}^{\pm}_{i+1/2} = A^{\pm}(\bar{\boldsymbol{q}}) \Delta \boldsymbol{q}_{i+1/2} \tag{6}$$

are the fluxes across positive or negative traveling waves. A is the Jacobian matrix $\partial \boldsymbol{f} / \partial \boldsymbol{q}$, and

$$\bar{\boldsymbol{q}} = \tfrac{1}{2}(\boldsymbol{q}_{i+1} + \boldsymbol{q}_i)$$

$$\Delta \boldsymbol{q}_{i+1/2} = \boldsymbol{q}_{i+1} - \boldsymbol{q}_i$$

$$A^+ = X \Lambda^+ X^{-1}$$

$$A^- = A - A^+$$

The columns of the matrix X are the right eigenvectors of A, and the diagonal matrix Λ^+ contains the positive eigenvalues of A.

We use the implicit three-level second-order time integration scheme, with a nondimensional time step equal to 0.02. We use an O-grid with 180×240 nodes in the radial and circumferential directions, respectively, which extends to 48 cylinder diameters to minimize blockage effects [26]. The grid is clustered in the radial direction with exponential profile to resolve properly the shear layers around the cylinder (or vortex structures in separated regions). The grid step in the radial direction increases from $(\Delta r)_1 = 0.00742$ cylinder diameter at the cylinder surface to $(\Delta r)_{179} = 0.57449$ cylinder diameter at the outer boundary. In the circumferential direction, the grid is uniform with a step size corresponding to 1.5 deg. Therefore, the smallest arc length between two grid nodes at the cylinder surface is 0.01310 cylinder diameter. The largest arc length between two grid nodes is at the outer boundary and is equal to 0.62832 cylinder diameter. The grid is deformed in the course of the simulation due to the cylinder oscillation such that the mentioned lower and upper limits of the arc length are preserved. On the other hand, the motioned limits of the grid step in the radial direction change slightly depending on the actual distance between a grid node on the cylinder surface and the corresponding grid node on the outer boundary. This distance is uniform and equal to 23.5 cylinder diameters in the case of static grid, which is used at the begging of the simulation. As will be mentioned later, the maximum cylinder displacement is 0.15 cyl-

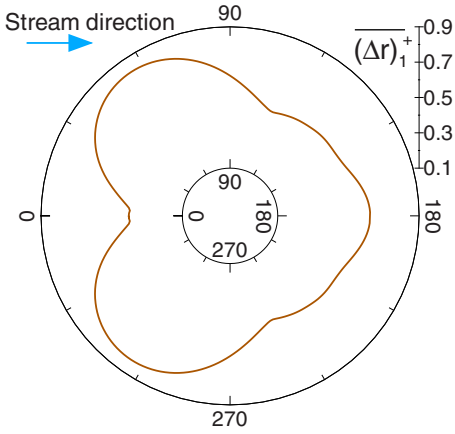

Fig. 1 The mean of friction-nondimensionalized smallest grid step in the radial direction at Re=300 for Π=5 and Ψ=0.15

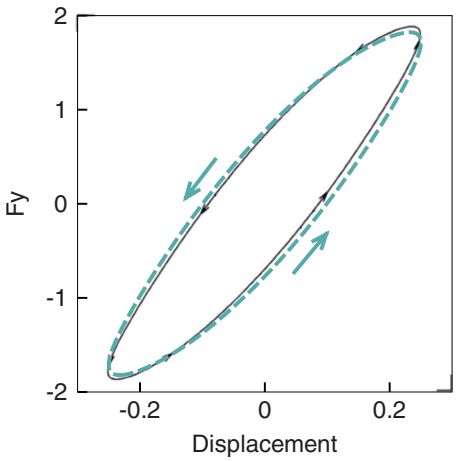

Fig. 2 The F_y displacement trajectory at Re=500 for $\Pi=1$ and $\Psi=0.25$; from our flow model (dashed line) compared with the one in Ref. [27] (solid line) for validation

inder diameter, which is very small compared with 23.5; and consequently the variations in the mentioned limits of the grid step in the radial direction are insignificant. To examine the suitability of the radial resolution near the surface, we calculate the friction-nondimensionalized $(\Delta r)_1$ according to the following nondimensional expression

$$(\Delta r)_1^+ = (\Delta r)_1 u_* \ \mathrm{Re} \tag{7}$$

$$u_* = \sqrt{\frac{1}{\mathrm{Re}} \frac{\partial\ \mathrm{mag}(\vec{u})}{\partial r}} \tag{8}$$

where u_* is the nondimensional friction velocity (modified to accommodate separated-flow regions), and mag() represents a vector magnitude. The derivative in Eq. (8) is calculated numerically using forward difference. In Fig. 1, the mean values of $(\Delta r)_1^+$ (designated by $\overline{(\Delta r)_1^+}$) are shown for a representative deformed-grid case with $\Pi=5$. The maximum value of $\overline{(\Delta r)_1^+}$ in this figure is 0.8505, and its average value is 0.5013. Therefore, $\max(\overline{(\Delta r)_1^+}) < 1$, which provides good resolution.

As a validation test, we consider the sinusoidal oscillation of a cylinder with amplitude 0.25 cylinder diameter at Re=500 and compare the trajectory made by the nondimensional lift F_y and cylinder displacement in Fig. 2, with the direct numerical simulation in Ref. [27] (using spectral element method). The two trajectories are close to each other. For the rest of results, we set Re =300.

To check the sensitivity of the results to changes in the adopted "reference" grid size (its diameter is 48 cylinder diameters), number of grid points (180×240), and nondimensional time step ($\Delta t=0.02$), we consider the case of restrained cylinder and perform two test simulations with the same reference grid but with smaller nondimensional time steps (0.01 and 0.005). We perform a third test simulation with the same reference nondimensional time step but with a larger grid size (68 cylinder diameters), and the grid points are increased to 255×340. These grid parameters were chosen such that the total grid area and number of points are twice those for the reference grid. In the fourth test simulation, the nondimensional time step and the grid size are the same as the reference ones, but the number of grid points is doubled in each direction (360×480). For each test simulation, we find the mean of the nondimensional drag $\bar{F}_x$, its standard deviation $[F_x]$, and the standard deviation of the nondimensional lift $[F_y]$. We compare in Table 1 the relative absolute difference of these values with respect to those obtained with the reference grid and nondimensional time step. For example,

$$|\Delta[F_x]| = \frac{\mathrm{abs}([F_x]-[F_x]_{\mathrm{ref}})}{[F_x]_{\mathrm{ref}}}$$

The reference values are $\bar{F}_x=1.376$, $[F_x]=0.0567$, and $[F_y]=0.649$. As shown in Table 1, all differences are less than 1%, thereby indicating the suitability of the adopted grid and time step in this study.

Table 1 Sensitivity to grid and time step

Grid points, size, Δt	$\lvert\Delta\bar{F}_x\rvert$ (%)	$\lvert\Delta[F_x]\rvert$ (%)	$\lvert\Delta[F_y]\rvert$ (%)
180×240, 48, 0.02	0	0	0
180×240, 48, 0.01	−0.05	0.54	−0.59
180×240, 48, 0.005	−0.04	0.18	−0.62
255×340, 68, 0.02	−0.47	0.15	−0.03
360×480, 48, 0.02	−0.22	0.93	0.34

3 Motion Configuration

The displacement follows a sine function raised to an integer power. The nondimensional displacement, velocity, and acceleration of the cylinder are described as

$$\text{displacement} = \Psi\ \sin(\Omega t)^{\Pi} \tag{9}$$

$$\text{velocity} = \Omega\Psi\Pi\ \sin(\Omega t)^{\Pi-1}\cos(\Omega t) \tag{10}$$

$$\text{acceleration} = \Omega^2\Psi\Pi\ [(\Pi-1)\cos(\Omega t)^2\ \sin(\Omega t)^{\Pi-2} - \sin(\Omega t)^{\Pi}] \tag{11}$$

Equations (10) and (11) indicate that integer values of Π do not lead to any singularities in the velocity or acceleration when

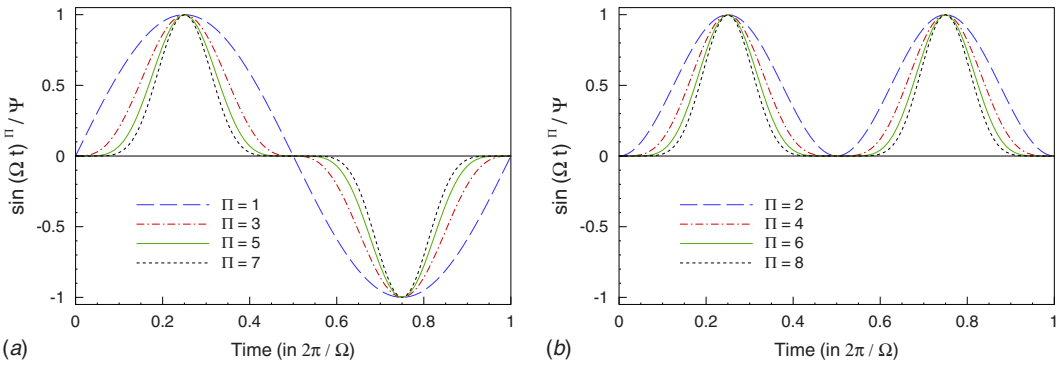

Fig. 3 Illustration of the effect of Π on the normalized displacement over one Ω period

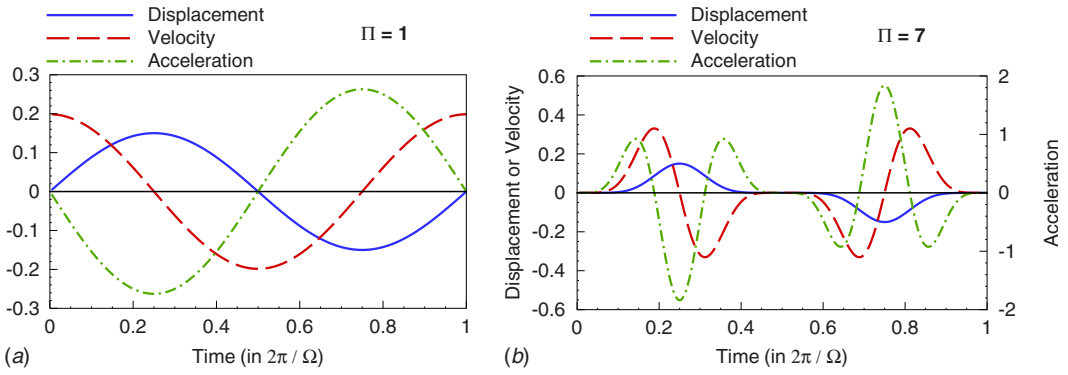

Fig. 4 The nondimensional displacement, velocity, and acceleration of the oscillation for odd values of Π=1 and 7 over one Ω period

$\sin(\Omega t)=0$. Such singularities, however, take place if noninteger values of $\Pi<2$ are used, which is not the case here.

Using trigonometric identities, the above equations for the nondimensional displacement, velocity, and acceleration of the cylinder can be expressed as a finite series as follows:

$$\text{displacement} = \sum_k D_k \cos(k\Omega t), \quad k = 0,2, \ldots, \Pi \tag{12}$$

$$\text{velocity} = \sum_k V_k \sin(k\Omega t), \quad k = 2,4, \ldots, \Pi \tag{13}$$

$$\text{acceleration} = \sum_k A_k \cos(k\Omega t), \quad k = 2,4, \ldots, \Pi \tag{14}$$

for even Π, and

$$\text{displacement} = \sum_k D_k \sin(k\Omega t), \quad k = 1,3, \ldots, \Pi \tag{15}$$

$$\text{velocity} = \sum_k V_k \cos(k\Omega t), \quad k = 1,3, \ldots, \Pi \tag{16}$$

$$\text{acceleration} = \sum_k A_k \sin(k\Omega t), \quad k = 1,3, \ldots, \Pi \tag{17}$$

for odd Π.

We will set Ω to be equal to the nondimensional angular shedding frequency in the wake of the restrained cylinder. We found that the nondimensional lift F_y has only significant Fourier components corresponding to those existing in the applied oscillation. For even Π, there is still a Fourier component at Ω although the oscillation does not have a Fourier component at that frequency. In addition, a small mean nondimensional lift $\bar{F}_y$ exists in the case of even $\Pi>2$. Therefore, we can express F_y as a finite series as follows:

$$F_y = \bar{F}_y + F_1 \cos(k\Omega t + \psi_1) + \sum_k F_k \cos(k\Omega t + \psi_k), \quad k = 2,4, \ldots, \Pi \tag{18}$$

for even Π, and

$$F_y = \sum_k F_k \cos(k\Omega t + \psi_k), \quad k = 1,3, \ldots, \Pi \tag{19}$$

for odd Π. Although we found that the nondimensional drag F_x can be approximated as well by a finite series, with Fourier components at integer multiples of Ω (in addition to a mean value $\bar{F}_x$), it has more components than F_y, which are not as directly related to the components in the oscillation as F_y. This can be explained by the fact that F_y is aligned with the oscillation and by the shedding mechanism through which vortices contribute unequally to F_y and F_y [28]. Therefore, we will limit our analysis for F_x to its mean and standard deviation and will not present the results of its spectral analysis.

Because F_y is colinear with the oscillation velocity, mechanical energy is transferred either to or from the cylinder. Over one Ω period (or $2\pi/\Omega$), the nondimensional amount of transferred energy (being positive if transferred to the cylinder) is expressed as follows:

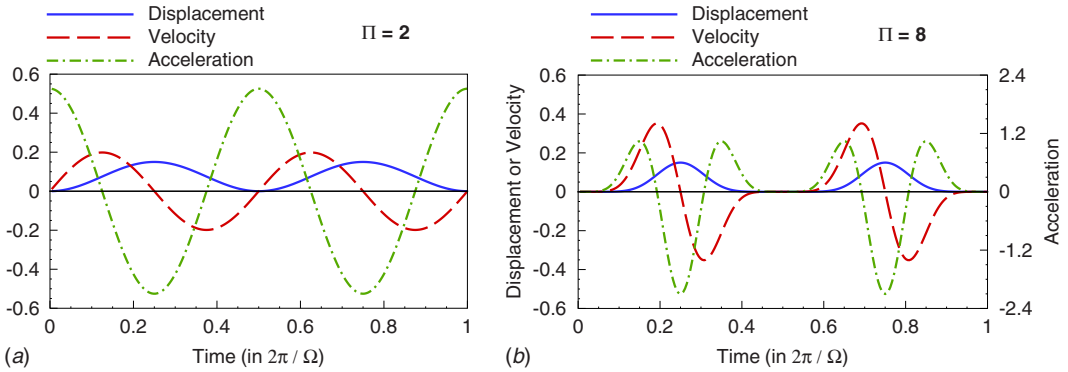

Fig. 5 The nondimensional displacement, velocity, and acceleration of the oscillation for even values of Π=2 and 8 over one Ω period

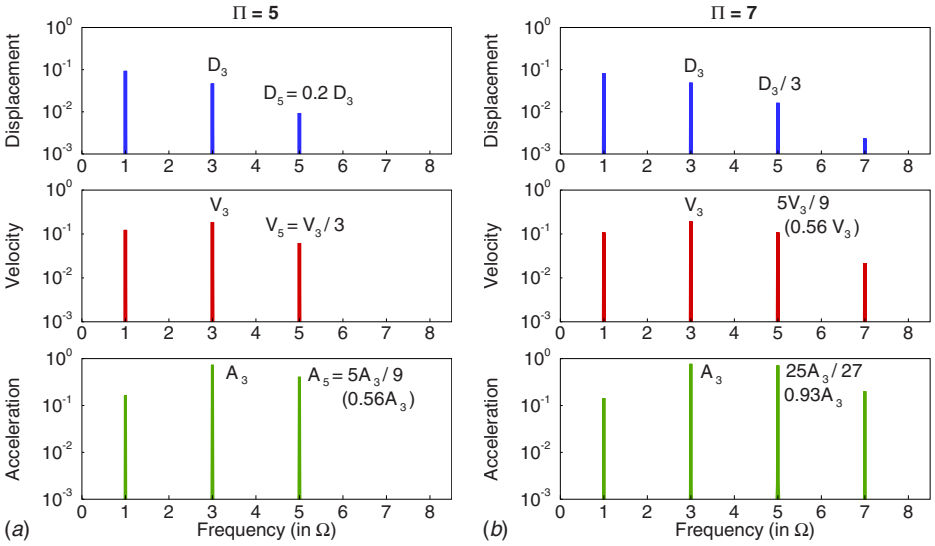

Fig. 6 Amplitudes of the Fourier components in the displacement, velocity, and acceleration of the oscillation for Π=5 and 7

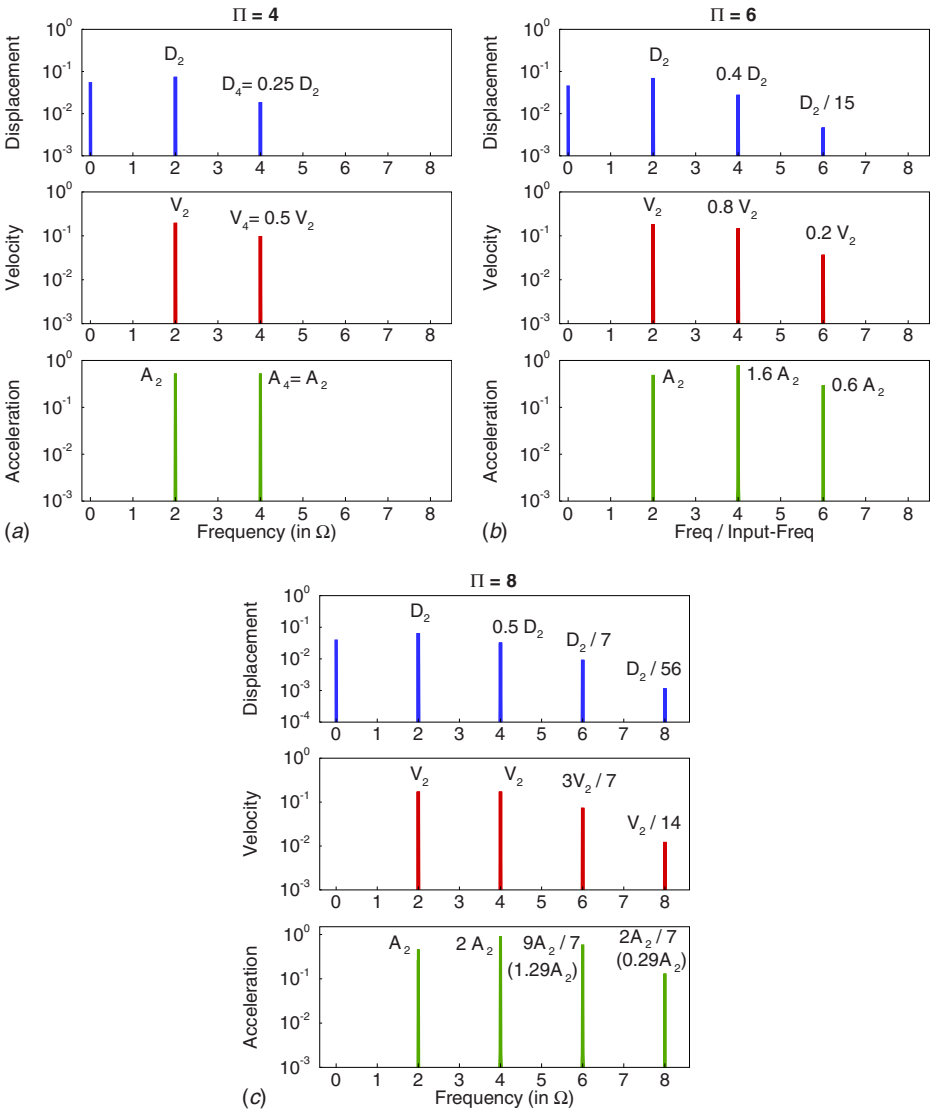

Fig. 7 Amplitudes of the Fourier components in the displacement, velocity, and acceleration of the oscillation for Π=4, 6, and 8

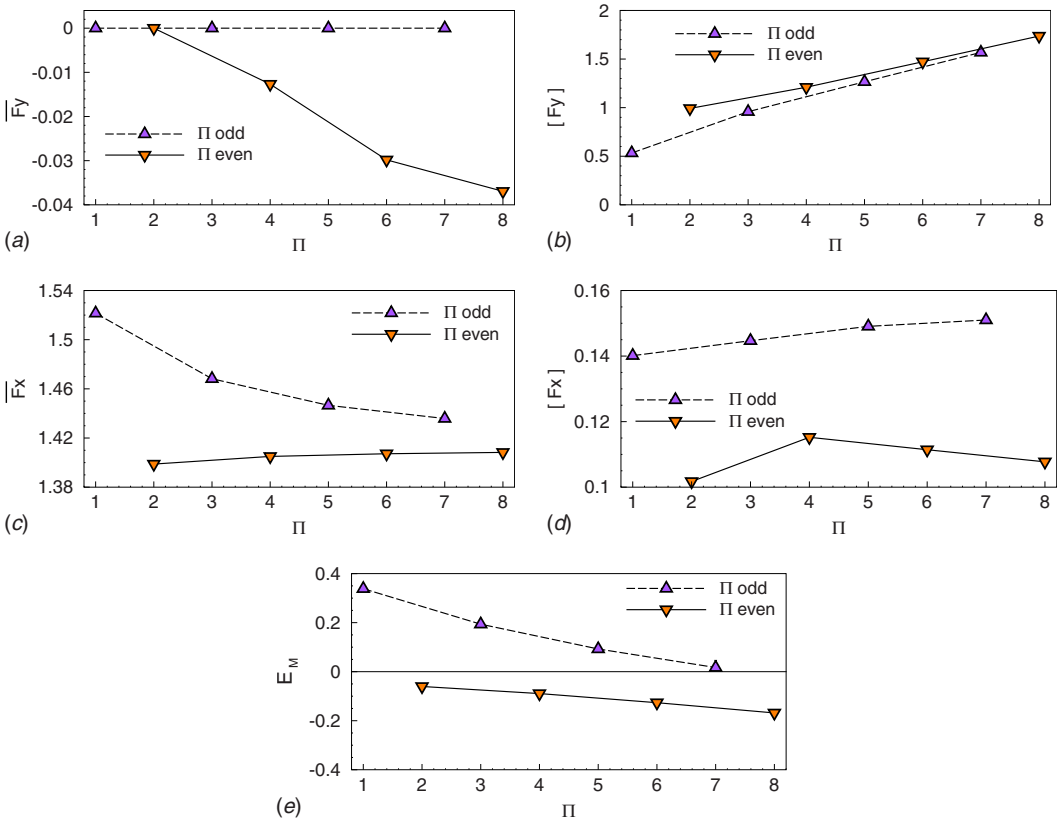

Fig. 8 Results of analyzed lift and drag, and the energy transfer for odd and even values of Π

$$E_M = \frac{2\pi}{\Omega}\left[\frac{\Omega V_1 F_1}{2}\sin(\psi_1) + \sum_k \frac{k\Omega V_k F_k}{2}\sin(\psi_k)\right], \quad k = 0,2,\ldots,\Pi \tag{20}$$

for even Π, and

$$E_M = \frac{2\pi}{\Omega}\sum_k \frac{k\Omega V_k F_k}{2}\sin(\psi_k), \quad k = 1,3,\ldots,\Pi \tag{21}$$

for odd Π. In Eq. (20) for the case of even Π, although a small nonzero $\bar{F}_y$ exists, the mean velocity of the cylinder is zero; thus, $\bar{F}_y$ does not contribute to E_M.

4 Results

We first demonstrate the difference between the standard sinusoidal (Π=1) and other displacement profiles Π>1. We group the odd-Π cases together and the even-Π ones together because each group has some common features that do not exist in the other group, as discussed earlier and will be shown here. The normalized displacement (having a unity amplitude) for all profiles that we apply in this study are compared in Fig. 3 over a single period of Ω (i.e., $2\pi/\Omega$). As Π increases, the displacement exhibits steeper peaks (or valleys), which are separated by regions of nearly-zero slowly-varying displacement. These changes in the displacement profile attenuate as Π increases. Therefore, we expect to find an asymptotic behavior for F_y, F_x, and E_M at high values of Π.

We then provide more details about the oscillation profiles with the specific value of Ψ we use here, which is 0.15. To generalize the results, we will use the period $2\pi/\Omega$ as a time unit. In Fig. 4, the nondimensional displacement, velocity, and acceleration of the oscillation for the largest and smallest values of odd Π we consider (Π=1 and 7) are compared over a single period of Ω. The corresponding oscillation profiles for the largest and smallest even values of applied Π (Π=2 and 8) are shown in Fig. 5.

The amplitudes of the Fourier components in the displacement, velocity, and acceleration (D_k, V_k, and A_k, respectively) are shown in Fig. 6 for odd Π=5 and 7, and in Fig. 7 for even Π=4, 6, and 8. We only show in these figures the cases where more than one Fourier component exist other than the one at Ω (thus Π>3). These figures will be compared with their counterparts for F_y, in which we focus on the Fourier components other than the one at Ω, as we will explain later. For odd Π, we use the amplitude at 3Ω as a scale for other amplitudes; and for even Π, we use the amplitude at 2Ω as a scale for the rest of amplitudes.

For each value of Π, we calculated the mean and standard deviation of F_x and F_y, and calculated E_M. The results of these quantities are shown in Fig. 8. Responses to odd and even values of Π follow two different trends, which asymptotically merge only for the standard deviation $[F_y]$, increasing linearly with Π. The mean $\bar{F}_y$ is nonzero and always negative for even Π>2; it decreases continuously with Π. The mean $\bar{F}_x$ seems to converge to a constant value near 1.42, which is slightly above (103%) the value corresponding to a restrained cylinder at this Re as we obtained in our simulations. On the other hand, $[F_x]$ and E_M continue to follow different curves for odd and even Π. Both curves for $[F_x]$ are remarkably above the obtained value corresponding to a restrained cylinder, which is 0.0567. Thus any oscillation, regardless of its profile, strongly amplifies $[F_x]$, but the amplification is larger for odd Π. For odd Π, E_M is always positive (energy is transferred to the cylinder), and its largest value (and the smallest $[F_y]$) is at Π=1 (the case of standard sinusoidal oscillation). This value decreases and asymptotically approaches zero as Π increases. In contrast, E_M is always negative for even Π, and it continues to decrease as Π increases. Therefore, the sinusoidal profile of the free vibration is the most effective one in sustaining

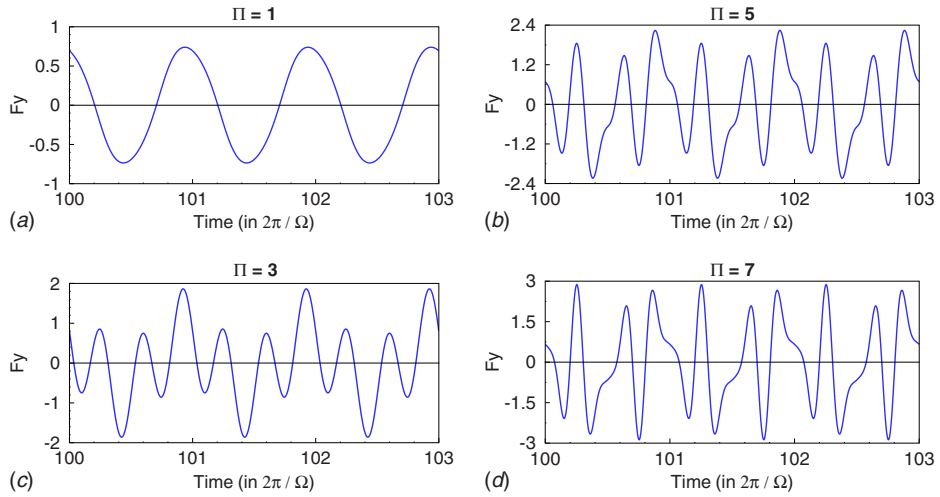

Fig. 9 Nondimensional lift for odd values of Π over three Ω periods

the VIV. Moreover, no VIV can exist with even Fourier components of Ω (with Ω being the frequency of synchronization with a dominant component of the induced displacement) because negative E_M is not realistic in that case.

In Fig. 9, we compare F_y over three periods of Ω for odd values of Π. The nearly-sinusoidal profile for Π=1 is clearly altered due to existence of other odd Fourier components in F_y as Π increases. However, F_y for Π=5 and 7 are qualitatively similar. We note a similar feature for even values of Π in Fig. 10, where increasing Π above 6 mainly intensifies F_y (as also indicated by the trends of $[F_y]$ in Fig. 8) but does not significantly alter its pattern. The qualitative pattern of F_x also converges at high Π. The results of F_x over three periods of Ω for the largest and smallest odd and even values of Π are shown in Figs. 11 and 12, respectively. Comparing Fig. 11 to Fig. 9 and Fig. 12 to Fig. 10 (one should notice that the vertical axes of the plots in Figs. 9 and 10 have increasing ranges with Π, which was not necessary in Figs. 11 and 12) demonstrates that the intensity of F_x is much less responsive to Π than the intensity of F_y.

We show in Fig. 13 the amplitudes of the Fourier components in F_y for Π>3. In these cases, there are at least two Fourier components in the oscillations (excluding the mean value and the component at Ω). We do not consider the value of F_1 in the following analysis because when the cylinder is restrained, there will be a dominant F_1 although no oscillation components exists at this frequency. Therefore, F_1 is not mainly driven by the oscil-

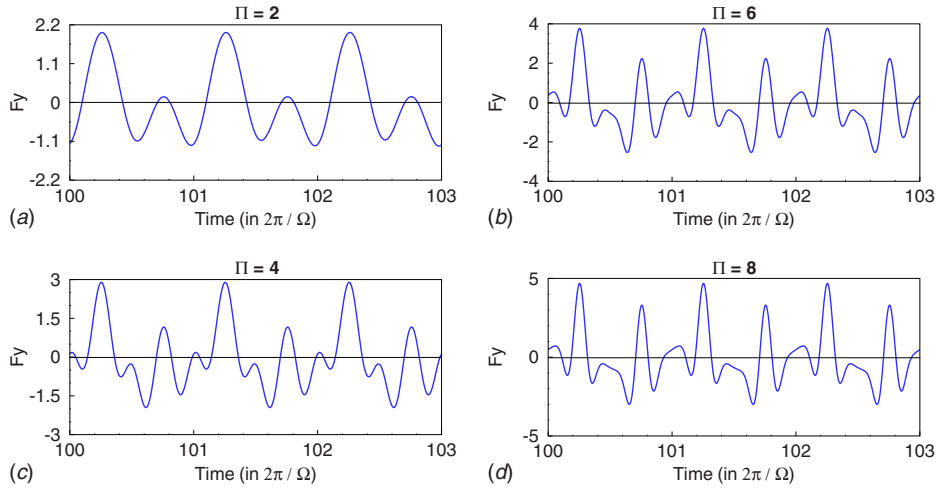

Fig. 10 Nondimensional lift for even values of Π over three Ω periods

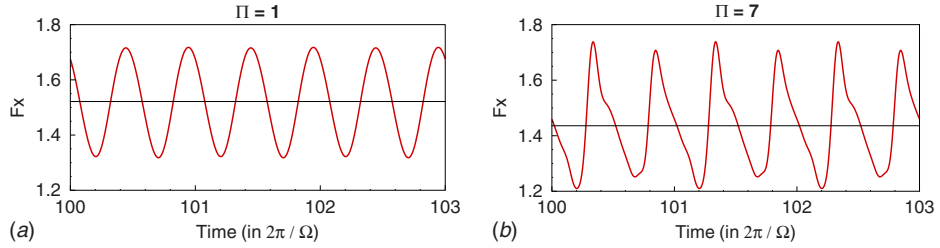

Fig. 11 Nondimensional drag for odd values of Π=1 and 7 over three Ω periods

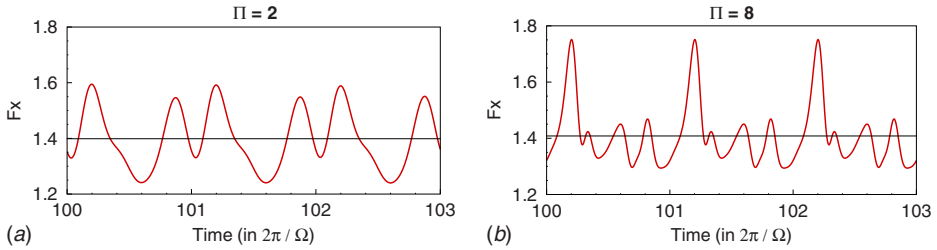

Fig. 12 Nondimensional drag for even values of $\Pi=2$ and 8 over three Ω periods

lation as the other Fourier components in F_y, but it includes the effect of a self-excited shedding in the wake at Ω. The values of F_1 at different Π are shown in Fig. 14. We go back to Fig. 13, which has ratios of amplitudes of F_y (again, not considering the mean value and F_1). For $\Pi=5$, $F_5/F_3=0.57$; and we recall that Fig. 6 showed that $A_5/A_3=0.56$, whereas $V_5/V_3=0.333$. For $\Pi=7$, $F_5/F_3=0.94$, which is close to $A_5/A_3=0.93$, whereas $V_5/V_3=0.56$. For $\Pi=4$, $F_4/F_2=0.93$; and we recall that Fig. 7 showed that $A_4/A_2=1$, whereas $V_4/V_2=0.5$. For $\Pi=6$, $F_4/F_2=1.51$ and $F_6/F_2=0.57$, which are close to $A_4/A_2=1.6$ and $A_6/A_2=0.6$, whereas $V_4/V_2=0.8$ and $V_6/V_2=0.2$. For $\Pi=8$, $F_4/F_2=1.89$, $F_6/F_2=1.22$, and $F_8/F_2=0.28$, which are close to $A_4/A_2=2$, $A_6/A_2=1.29$, and $A_8/A_2=0.29$, whereas $V_4/V_2=1$, $V_6/A_2=0.43$, and $V_8/A_2=0.071$. These similarities in the amplitudes ratios in F_y with their counterparts in the acceleration of the oscillation (as compared with the velocity of the oscillation) indicates that F_y is mainly influenced by the motion acceleration, which should act as the coupling term in a wake oscillator, coupling a nonlinear (self-excited) ODE for F_y with a forced (with the forcing being proportional to F_y) linear ODE for the induced vibration, as a reduced-order model for VIV problem. Therefore, the common choice of the velocity as a form of coupling does not reflect the physics of the problem. It should be mentioned here that when Hartlen and Currie [18] first proposed this velocity-based coupling, they stated that it was an "arbitrary" choice, and there was no physical justification or simplified analysis behind it. Based on our findings, we expect acceleration-based coupling to achieve better matching with existing VIV results. This finding can be supported by noticing that the asymmetry in F_y that occurs only for even $\Pi>2$ coincides with the fact that in these cases, there is imbalance in the acceleration of oscillation in terms of uneven peaks and valleys (see Fig. 5). The velocity of the oscillation does not exhibit this feature, and if it was the driving force for F_y, then we would expect $\bar{F}_y$ to be zero for these cases. The deviation between the ratios of F_k and ratios of D_k is even larger than the one we showed for V_k. We comment here that the above procedure of comparing the amplitudes ratios in F_y and other variables of the oscillation implicitly assumes linearity in F_y. Nevertheless, we do not intend to neglect nonlinear effects in F_y (such as the interaction of F_k), which is in fact demonstrated in the imperfect similarity between the spectra of F_y and oscillation (e.g., the additional number of Fourier components in F_y and the mismatched amplitude ratio of F_1).

5 Conclusions

We compared the effects of applying sinusoidal and nonsinusoidal (but continuous) transverse oscillation profiles to a circular

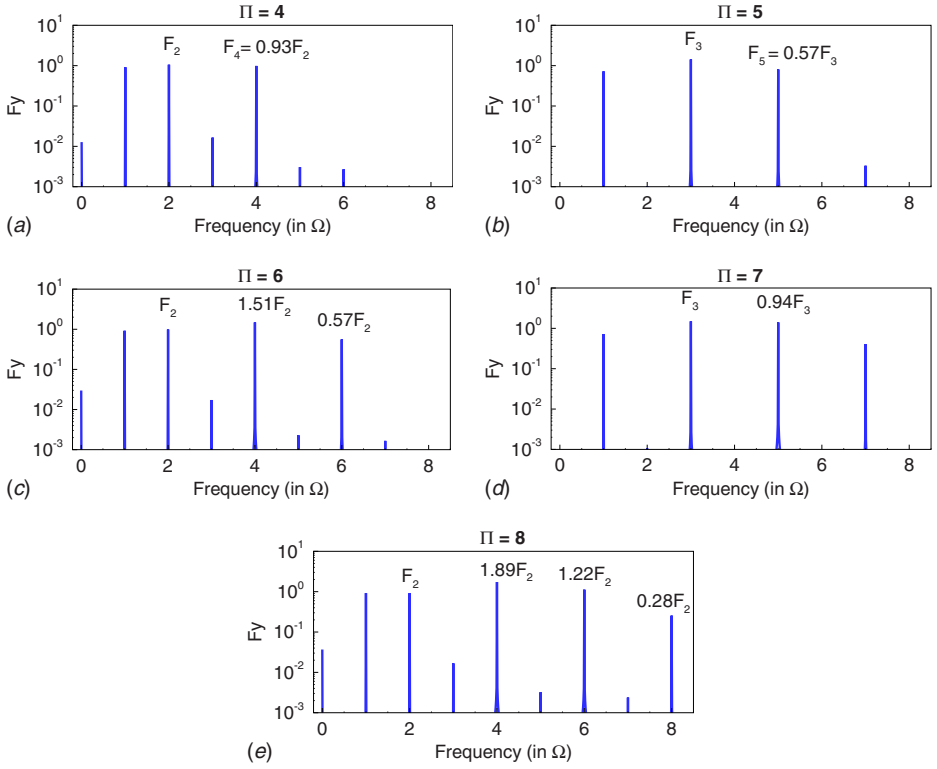

Fig. 13 Amplitudes of the Fourier components in the nondimensional lift for $\Pi=4-8$

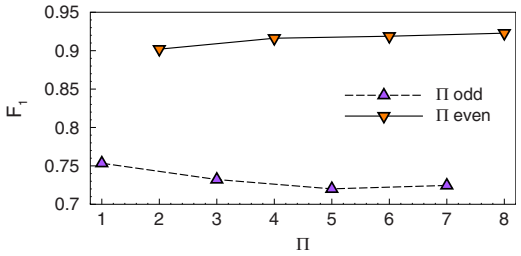

Fig. 14 Amplitude of the Fourier component in the nondimensional lift at Ω for odd and even Π

cylinder placed in a uniform-stream. The standard sinusoidal-oscillation case has received a lot of attention in other works, but it is not known how the response of the lift, drag, and mechanical energy transfer will be different when other oscillations are applied. Comparing the results from the standard sinusoidal oscillation to other (seven) ones showed that maximum energy transfer to the cylinder (thus enhancing the VIV in case of free vibration) corresponds to the standard sinusoidal oscillation, which was reported in previous experiments and simulations for the VIV problem at comparable Reynolds numbers. The responses of the lift, drag, and energy transfer are very different depending on whether the oscillation consists of even or odd harmonics. Spectral analysis of the lift and oscillation showed that the lift is mainly driven by the acceleration. This finding is supported by the conditional asymmetry in the lift that occurs only for certain profiles of non-sinusoidal oscillations.

Acknowledgment

The author would like to thank the Advanced Supercomputing (NAS) Division at NASA Ames Research Center, and also Professor Ali H. Nayfeh in the Department of Engineering Science and Mechanics at Virginia Polytechnic Institute and State University.

Nomenclature

A_k = kth Fourier-component amplitude of acceleration
D_k = kth Fourier-component amplitude of displacement
E_M = nondimensional mechanical energy over $2\pi/\Omega$
F_k = kth Fourier-component amplitude of F_y
F_x = nondimensional drag on the cylinder
F_y = nondimensional lift on the cylinder
V_k = kth Fourier component of velocity
$[..]$ = standard deviation
$\overline{..}$ = mean value
Π = power in the displacement function
Ω = input frequency to the displacement function
Ψ = amplitude of the displacement function

Subscripts

k = index of Fourier components (frequency=$k\Omega$)

References

[1] Anagnostopoulos, P., and Bearman, P. W., 1992, "Response Characteristics of a Vortex-Excited Cylinder at Low Reynolds Numbers," J. Fluids Struct., **6**, pp. 39–50.
[2] Gharib, M. R., Shiels, D., Gharib, G., Leonard, A., and Roshko, A., 1997, "Exploration of Flow-Induced Vibration at Low Mass and Damping," Proceedings of the Fourth International Symposium on Fluid-Structure Interactions, Aeroelasticity, Flow-Induced Vibration & Noise, Dallas, TX, Vol. 1, pp. 75–81.
[3] Fujarra, A. L. C., Meneghini, J. R., Pesce, C. P., and Parra, P. H. C. C., 1998, "An Investigation of Vortex-Induced Vibration of a Circular Cylinder in Water," Proceedings of the First Bluff Body Wakes and Vortex-Induced Vibrations Conference and ASME FEDSM, Washington, DC.
[4] Zhou, C. Y., So, R. M. C., and Lam, K., 1999, "Vortex-Induced Vibrations of an Elastic Circular Cylinder," J. Fluids Struct., **13**, pp. 165–189.
[5] Blackburn, H. M., Govardhan, R. N., and Williamson, C. H. K., 2001, "A Complementary Numerical and Physical Investigation of Vortex-Induced Vibration," J. Fluids Struct., **15**, pp. 481–488.
[6] Shiels, D., Leonard, A., and Roshko, A., 2001, "Flow-Induced Vibration of a Circular Cylinder at Limiting Structural Parameters," J. Fluids Struct., **15**, pp. 3–21.
[7] Prasanth, T. K., and Mittal, S., 2008, "Vortex-Induced Vibrations of a Circular Cylinder at Low Reynolds Numbers," J. Fluid Mech., **594**, pp. 463–491.
[8] Pantazopoulos, M. S., 1994, "Vortex-Induced Vibration Parameters: Critical Review," Proc. 13th Int. Conf. on Offshore Mech. & Arctic Eng., Houston, TX, 1, pp. 199–255.
[9] Khalak, A., and Williamson, C. H. K., 1999, "Motions, Forces, and Mode Transitions in Vortex-Induced Vibrations at Low Mass-Damping," J. Fluids Struct., **13**(7–8), pp. 813–851.
[10] Vikestad, K., Vandiver, J. K., and Larsen, C. M., 2000, "Added Mass and Oscillation Frequency for a Circular Cylinder Subjected to Vortex-Induced Vibrations and External Disturbance," J. Fluids Struct., **14**, pp. 1071–1088.
[11] Griffin, O. M., Skop, R. A., and Koopmann, G. H., 1973, "The Vortex-Excited Resonant Vibrations of Circular Cylinders," J. Sound Vib., **31**(2), pp. 235–249.
[12] Iwan, W. D., and Blevins, R. D., 1974, "A Model for Vortex Induced Oscillation of Structures," ASME J. Appl. Mech., **41**(3), pp. 581–586.
[13] Di Silvio, G., Angrilli, F., and Zanardo, A., 1975, "Fluidelastic Vibrations: Mathematical Model and Experimental Result," Meccanica, **10**(4), pp. 269–279.
[14] Staubli, T., 1983, "Calculation of the Vibration of an Elastically Mounted Cylinder Using Experimental Data From Forced Vibration," ASME J. Fluids Eng., **105**(2), pp. 225–229.
[15] Mureithi, N. W., Goda, S., and Kanki, H., 2001, "A Nonlinear Dynamics Analysis of Vortex-Structure Interaction Models," ASME J. Pressure Vessel Technol., **123**(4), pp. 475–479.
[16] Leontini, J. S., Stewart, B. E., Thompson, M. C., and Hourigan, K., 2006, "Predicting Vortex-Induced Vibration From Driven Oscillation Results," Appl. Math. Model., **30**, pp. 1096–1102.
[17] Meneghini, J. R., and Bearman, P. W., 1996, "Numerical Simulation of the Interaction Between the Shedding of Vortices and Square-Wave Oscillations Applied to a Circular Cylinder," Second International Conference on Hydrodynamics, Hong Kong, Vol. 2, pp. 785–790.
[18] Hartlen, R. T., and Currie, I. G., 1970, "Lift-Oscillator Model of Vortex Vibration," J. Eng. Mech., **96**, pp. 577–591.
[19] Krenk, S., and Nielsen, S. R. K., 1999, "Energy Balanced Double Oscillator Model for Vortex-Induced Vibrations," J. Eng. Mech., **125**(3), pp. 263–271.
[20] Chorin, A. J., 1967, "A Numerical Method for Solving Incompressible Viscous Flow Problems," J. Comput. Phys., **2**, pp. 12–26.
[21] Rogers, S. E., and Kwak, D., 1990, "Upwind Differencing Scheme for the Time-Accurate Incompressible Navier-Stokes Equations," AIAA J., **28**(2), pp. 253–262.
[22] Ahn, H. T., and Kallinderis, Y., 2006, "Strongly Coupled Flow/Structure Interactions With a Geometrically Conservative ALE Scheme on General Hybrid Meshes," J. Comput. Phys., **219**, pp. 671–696.
[23] Marzouk, O. A., and Nayfeh, A. H., 2008, "Fluid Forces and Structure-Induced Damping of Obliquely-Oscillating Offshore Structures," Proc. 18th Int. Offshore (Ocean) & Polar Eng. Conf. and Exhibition, Vancouver, Canada, 3, pp. 460–468.
[24] Marzouk, O. A., 2008, "A Two-Step Computational Aeroacoustics Method Applied to High-Speed Flows," Noise Control Eng. J., **56**(5), pp. 396–410.
[25] Fletcher, C. A. J., 1991, *Computational Techniques for Fluid Dynamics*, Vol. II, 2nd ed., Springer-Verlag, Germany.
[26] Ravoux, J. F., Nadim, A., and Haj-Hariri, H., 2003, "An Embedding Method for Bluff Body Flows: Interactions of Two Side-by-Side Cylinder Wakes," Theor. Comput. Fluid Dyn., **16**, pp. 433–466.
[27] Blackburn, H. M., and Henderson, R. D., 1999, "A Study of Two-Dimensional Flow Past an Oscillating Cylinder," J. Fluid Mech., **385**, pp. 255–286.
[28] Ericsson, L. E., 1980, "Karman Vortex Shedding and the Effect of Body Motion," AIAA J., **18**(8), pp. 935–944.

Unsteady Velocity Profiles in Laminar and Turbulent Water Hammer Flows

Alireza Riasi[1]
e-mail: ariasi@ut.ac.ir

Ahmad Nourbakhsh
Professor

Mehrdad Raisee
Associate Professor

Department of Mechanical Engineering,
University of Tehran,
P.O. Box 11155-4563,
Tehran, Iran

The behavior of unsteady velocity profiles in laminar and turbulent water hammer flows is numerically investigated. In this way, the governing equations for the quasitwo-dimensional equations of transient flow in pipe are solved by using the modified implicit characteristics method. A k-ω turbulence model which is accurate for two-dimensional boundary layers under adverse and favorable pressure gradients is applied. The numerical results for both steady and unsteady turbulent pipe flows are in good agreement with the experimental data. The results indicate that both decelerating and accelerating flows are produced in a wave cycle of water hammer. During deceleration of the flow, a region of reverse flows and also strong gradients is formed near to the pipe wall. In case of the turbulent water hammer, this region is very close to the pipe wall compared with the laminar water hammer. Moreover, point of inflection and also point of zero velocity are formed in the unsteady velocity profile due to the water hammer problem. The results show that the point of zero velocity does not move very far from its initial location, while the point of inflection moves rapidly from the wall. [DOI: 10.1115/1.4000557]

Keywords: water hammer, unsteady velocity profile, k-ω turbulence model, inflection point

1 Introduction

In pressurized pipes and channels, the perturbation in the fluid is produced as the result of several problems including starting or failure in pump and turbine and also fast opening or closing of the valve in order to regulate the flow rate. These actions result in a series of positive and negative pressure waves, which move along the pipe and channel with wave speed. Regarding these positive and negative pressure waves, several problems, such as pipe failure, hydraulic equipment damage, cavitations, and corrosion, might be expected. An accurate simulation of transient flows is currently required, especially if the transient simulation is necessary beyond the first wave cycle, including in (i) complex piping systems, if the fluid behavior depends on the pressure damping rate of sequential wave cycles and (ii) accurate water quality modeling in pipe networks for predicting the velocity profile, wall shear stress, and turbulence structure.

For this purpose, the two-dimensional (2D) equations of water hammer should be solved using appropriate turbulence models.

The behavior of unsteady velocity profiles in water hammer problems has been studied by several researchers such as Silva-Araya and Chaudhry [1], Ghidaoui and Kolyshkin [2], and Wahba [3]. In spite of these studies, a comprehensive study for the behavior of unsteady velocity profiles due to water hammer problems has not been presented in the literature considering the effects of shear stress profiles, wall shear stress variations, pressure gradient variations, reverse flows, points of zero velocity, and inflection points.

A desirable method to solve the 2D equations of water hammer is the implicit characteristics method. This method was first introduced by Vardy and Hwang [4] and subsequently modified by Zhao and Ghidaoui [5]. The characteristic-based method is a powerful method to solve the hyperbolic equations. For example, a characteristic-based method was used by Drikakis et al. [6] to solve the 2D laminar incompressible Navier–Stokes equations. In this method, the partial differential equations are converted into ordinary differential equations along the characteristic lines.

To model the turbulence structure of water hammer problems, several algebraic turbulence models were used by Vardy and Hwang [4], Silva-Araya and Chaudhry [1,7], Pezzinga [8], Zhao and Ghidaoui [5], and Wahba [9]. Because of some shortcomings in algebraic turbulence models, Zhao and Ghidaoui [10] used the low-Re number k-ε model of Fan et al. [11] to simulate turbulent water hammer flows. Drikakis and Goldberg [12] showed that the low-Re wall-distance-free (WDF) turbulence models (e.g., WDF k-ε model) predicts more accurate results for the dissipation rate than the models, which explicitly involve the distance from the wall (e.g., the k-ε model of Fan et al.). They implemented these turbulence models in conjunction with a characteristic-based method to solve the two-dimensional incompressible Navier–Stokes equations. One shortcoming of the k-ε model is that it requires several modifications to be suitable for unsteady turbulent flows with adverse and favorable pressure gradients.

The main objectives of the present work are (i) to solve two-dimensional water hammer equations using modified implicit characteristics method in conjunction with a k-ω turbulence model and (ii) to investigate the behavior of unsteady velocity profiles considering the effects of shear stress profiles, wall shear stress variations, pressure gradient variations, reverse flows, points of zero velocity, and inflection points.

2 Mathematical Modeling and Numerical Procedure

As shown by Vardy and Hwang [4], the continuity and momentum equations for transient flow in pipes can be written as

$$\frac{\partial H}{\partial t} + \frac{a^2}{g}\frac{\partial u}{\partial x} + \frac{a^2}{g}\frac{1}{r}\frac{\partial rv}{\partial r} = 0 \tag{1}$$

$$\frac{\partial u}{\partial t} + g\frac{\partial H}{\partial x} = \frac{1}{r\rho}\frac{\partial}{\partial r}\left(r\left(\rho\nu\frac{\partial u}{\partial r} - \rho\overline{u'v'}\right)\right) \tag{2}$$

where t is the time, x *is* the distance along the pipe, $H(x,t)$ is the

[1]Corresponding author.

Contributed by the Fluids Engineering Division of ASME for publication in the JOURNAL OF FLUIDS ENGINEERING. Manuscript received January 12, 2009; final manuscript received October 7, 2009; published online November 19, 2009. Editor: Joseph Katz.

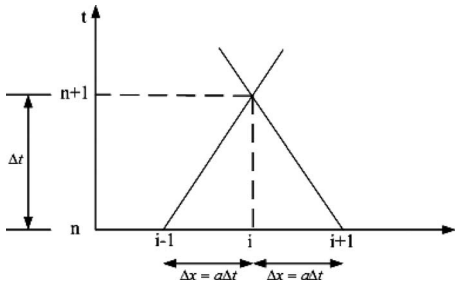

Fig. 1 Positive and negative characteristics for water hammer problem

piezometric head, $u(x,r,t)$ is the axial velocity, $v(x,r,t)$ is the radial velocity, u' is the fluctuation velocity in longitudinal direction, v' is the fluctuation velocity in radial direction, a is the acoustic wave velocity, g is the gravitational acceleration, ρ is the density, and v is the kinematic viscosity of the fluid.

According to the Boussinesq approximation, the turbulent shear stress is given by

$$-\rho\overline{u'v'} = \rho\nu_t\frac{\partial u}{\partial r} \tag{3}$$

where ν_t is the eddy-viscosity, as defined below. Equations (1) and (2) form a system of hyperbolic-parabolic partial differential equations. Vardy and Hwang [4] used a hybrid solution approach in which the hyperbolic part and the parabolic part of the governing equations are solved using the method of characteristics and finite difference, respectively. With linear combination of Eqs. (1) and (2), the following characteristic equations, describing perturbations movement at speeds $+a$ and $-a$ relative to the fluid and along the positive and negative characteristics (Fig. 1), are formed

$$C^+: \quad \frac{dH}{dt} + \frac{a}{g}\frac{du}{dt} = -\frac{a^2}{g}\frac{1}{r}\frac{\partial(rv)}{\partial r} + \frac{a}{g}\frac{1}{r\rho}\frac{\partial(r\tau)}{\partial r} \quad \text{along} \quad \frac{dx}{dt} = +a \tag{4a}$$

$$C^-: \quad \frac{dH}{dt} - \frac{a}{g}\frac{du}{dt} = -\frac{a^2}{g}\frac{1}{r}\frac{\partial(rv)}{\partial r} - \frac{a}{g}\frac{1}{r\rho}\frac{\partial(r\tau)}{\partial r} \quad \text{along} \quad \frac{dx}{dt} = -a \tag{4b}$$

where $\tau = \rho\nu(\partial u/\partial r) - \rho\overline{u'v'}$.

In unsteady turbulent pipe flows, the use of a high resolution grid is essential to calculate accurately the important variables such as velocity, turbulent kinetic energy, and specific dissipation rate. For this purpose a nonuniform mesh consisting fine enough in the near-wall region is used. In this way, the number of meshes in the radial and the longitudinal directions is N_r and N_x, respectively (Fig. 2).

According to Fig. 1, the characteristic equations are integrated along the positive and the negative characteristics. The terms in the right hand side of Eq. (4) are approximated as weighted average of the relevant values at successive times n and $n+1$ along the characteristic lines. Thus, the following equation is obtained [5]:

$$\begin{aligned} C^+: \quad & H_i^{n+1} - \omega_1 C_{v1}(j)(rv)_{i,j-1}^{n+1} + \omega_1 C_{v2}(j)(rv)_{i,j}^{n+1} - \omega_2 C_{u1}(j)u_{i,j-1}^{n+1} \\ & + \left[\frac{a}{g} + \omega_2 C_{u2}(j)\right]u_{i,j}^{n+1} - \omega_2 C_{u3}(j)u_{i,j+1}^{n+1} = H_{i-1}^n + (1 \\ & - \omega_1)C_{v1}(j)(rv)_{i-1,j-1}^n - (1-\omega_1)C_{v2}(j)(rv)_{i-1,j}^n + (1 \\ & - \omega_2)C_{u1}(j)u_{i-1,j-1}^n + \left[\frac{a}{g} - (1-\omega_2)C_{u2}(j)\right]u_{i-1,j}^n + (1 \\ & - \omega_2)C_{u3}(j)u_{i-1,j+1}^n \end{aligned} \tag{5a}$$

$$\begin{aligned} C^-: \quad & H_i^{n+1} - \omega_1 C_{v1}(j)(rv)_{i,j-1}^{n+1} + \omega_1 C_{v2}(j)(rv)_{i,j}^{n+1} + \omega_2 C_{u1}(j)u_{i,j-1}^{n+1} \\ & - \left[\frac{a}{g} + \omega_2 C_{u2}(j)\right]u_{i,j}^{n+1} + \omega_2 C_{u3}(j)u_{i,j+1}^{n+1} = H_{i+1}^n + (1 \\ & - \omega_1)C_{v1}(j)(rv)_{i+1,j-1}^n - (1-\omega_1)C_{v2}(j)(rv)_{i+1,j}^n - (1 \\ & - \omega_2)C_{u1}(j)u_{i+1,j-1}^n - \left[\frac{a}{g} - (1-\omega_2)C_{u2}(j)\right]u_{i+1,j}^n - (1 \\ & - \omega_2)C_{u3}(j)u_{i+1,j+1}^n \end{aligned} \tag{5b}$$

where ω_1 and ω_2 are the weighting coefficients, superscript n is the temporal location, and subscripts i and j are the spatial location.

The coefficients C_{v1}, C_{v2}, C_{u1}, C_{u2}, and C_{u3} are defined as follows:

$$\begin{aligned} C_{v1}(j) &= C_{v2}(j) = \frac{a^2\Delta t}{g}\frac{1}{\bar{r}_j\Delta r_j} \\ C_{u1}(j) &= \frac{a\Delta t(\nu+\nu_{t_{j-1}})}{g}\frac{1}{\bar{r}_j\Delta r_j}\frac{r_{j-1}}{(\bar{r}_j-\bar{r}_{j-1})} \\ C_{u3}(j) &= \frac{a\Delta t(\nu+\nu_{t_j})}{g}\frac{1}{\bar{r}_j\Delta r_j}\frac{r_j}{(\bar{r}_{j+1}-\bar{r}_j)} \\ C_{u2}(j) &= C_{u1}(j) + C_{u3}(j) \\ r_j &= \sum_{m=1}^{j}\Delta r_m \\ \bar{r}_j &= (r_{j-1}+r_j)/2 \end{aligned} \tag{6}$$

where $\Delta r_m = r_m - r_{m-1}$.

At a given time t and a location x along the pipe, Eqs. (5*a*) and (5*b*) are valid for each r_j and, consequently, $2N_r$ linear simultaneous characteristics provided for $2N_r$ unknowns $H_i^{n+1}, u_{i,1}^{n+1}, u_{i,2}^{n+1}, \ldots, u_{i,N_r}^{n+1}, v_{i,1}^{n+1}, v_{i,2}^{n+1}, \ldots, v_{i,N_r-1}^{n+1}$. On the other hand, a linear system of equations $AX=B$ is produced, where $A_{2Nr\times 2Nr}$=coefficient matrix, $X_{2Nr\times 1}$=unknowns matrix, and $B_{2Nr\times 1}$=right hand side matrix. Since the method of Vardy and Hwang [4] is very time consuming, Zhao and Ghidaoui [5] converted the linear system of equations $AX=B$ into the two sublinear systems of equations with a tridiagonal coefficient matrix.

2.1 Boundary Condition. At the inlet, the head is predetermined and the radial velocity components assumed to be zero. For axial velocity components, N_r negative characteristics (Eq. (5*b*)) are valid and should be simultaneously solved.

At the closed valve, all axial velocity components are zero and N_r positive characteristics (Eq. (5*a*)) are solved simultaneously to yield $H_N^{n+1}, v_{N,1}^{n+1}, v_{N,2}^{n+1}, \ldots, v_{N,N_r-1}^{n+1}$.

To illustrate the implementation of the wall boundary condition, the no slip condition is imposed at the solid surface aligned along $r_{Nr}=R$. Thus,

$$\begin{aligned} v_{i,N_r} &= 0.0 \\ u_{i,N_r+1} &= -u_{i,N_r} \end{aligned} \tag{7}$$

For the axial boundary condition, the symmetric condition for axial velocity components is assumed and the radial velocity components set to be zero.

3 Turbulence Modeling

Wilcox's k-ω model [13] is a two equation turbulence model, which allows accounting for history effects such as convection and diffusion of turbulence energy. According to Wilcox [13], this

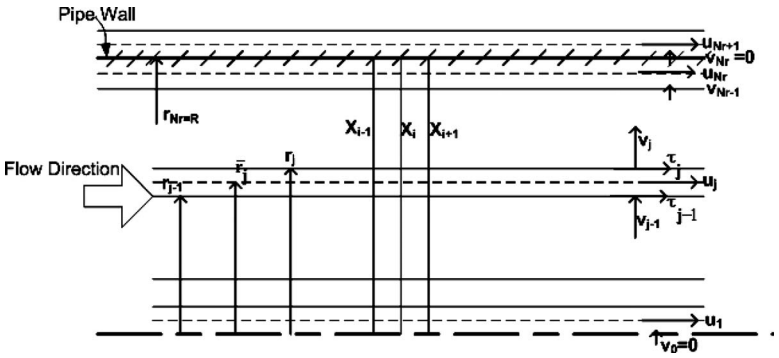

Fig. 2 Introduction of variables in a part of pipe for implicit characteristics method

turbulence model is very accurate in prediction of 2D boundary layer under adverse and favorable pressure gradients. Moreover, the k-ω model can be integrated through the viscous sublayer without using any viscous damping. The k and ω equations and eddy-viscosity formulation in Wilcox's k-ω model are written as

$$\frac{\partial k}{\partial t} = \frac{1}{r}\frac{\partial}{\partial r}\left[r(\nu + \sigma^* \nu_t)\frac{\partial k}{\partial r}\right] + \nu_t\left(\frac{\partial u}{\partial r}\right)^2 - \beta^* k\omega$$

$$\frac{\partial \omega}{\partial t} = \frac{1}{r}\frac{\partial}{\partial r}\left[r(\nu + \sigma \nu_t)\frac{\partial \omega}{\partial r}\right] + \alpha \nu_t \frac{\omega}{k}\left(\frac{\partial u}{\partial r}\right)^2 - \beta\omega^2 \tag{8}$$

$$\nu_t = \frac{k}{\omega}$$

here k is kinetic energy of turbulence fluctuation per unit mass, and ω is specific dissipation rate.

Following Wilcox [13], the closure coefficients are

$$\alpha = \tfrac{5}{9}, \quad \beta = \tfrac{3}{40}, \quad \beta^* = \tfrac{9}{100}, \quad \sigma = \tfrac{1}{2}, \quad \sigma^* = \tfrac{1}{2} \tag{9}$$

Since in usual water hammer problems the Mach number is very small, the convective terms can be neglected in the k and ω equations. In the present study, the diffusion terms are discretized using the implicit central difference expression, and the remaining terms are discretized with an explicit finite difference scheme. Finally, two tridiagonal matrix systems are solved for k and ω in each time step.

At the pipe axis, symmetric boundary conditions for k and ω are assumed

$$\frac{\partial k}{\partial r} = 0, \quad \frac{\partial \omega}{\partial r} = 0 \tag{10}$$

For wall boundary condition, the kinetic energy of turbulence, k, is set to zero. In order to facilitate integration of the k-ω turbulence model through the viscous sublayer, Wilcox [13] showed that the specific dissipation rate, ω, must satisfy the following asymptotic solution as the wall approached:

$$\omega \to \frac{6\nu}{\beta y^2} \quad y \to 0 \tag{11}$$

4 Steady State Turbulent Pipe Flow

The steady state turbulent velocity profile is required as the initial condition for water hammer problem. For fully-developed pipe flows, the momentum equation for pipe flow is simplified to the following first order ordinary differential equation [13]:

$$(\nu + \nu_t)\frac{du}{dr} = -u_\tau^2 \frac{r}{R} \tag{12}$$

in which u_τ=friction velocity, which is obtained for fully-developed pipe flows as

$$u_\tau = \sqrt{\frac{\tau_w}{\rho}} = \sqrt{\frac{fV_0^2}{8}} \tag{13}$$

where τ_w is the wall shear stress, f is the Darcy–Weisbach factor, and V_0 is the initial bulk velocity in the pipe. An iteration routine is applied for steady state turbulent velocity calculation. For this purpose, an arbitrary steady state velocity is assumed. Then the k and ω equations are solved for evaluation of the eddy-viscosity (v_t), and finally Eq. (12) is integrated for velocity profile computation. This procedure is repeated until the steady sate turbulent velocity profile is obtained. In order to achieve the desirable flow rate, a shooting procedure for the friction coefficient is adopted. The initial values for k and ω should be assumed before the steady state computation is performed. According to Martinuzzi and Pollard's [14] suggestion and knowing the fact that $\omega = \varepsilon/(\beta^* k)$ [13], we have

$$k = 0.005V_0^2$$
$$\omega = C_\mu k^{1/2}/(0.015\beta^* D) \tag{14}$$

where the value of constant C_μ is 0.09.

In order to resolve the variation in important variables, such as velocity, turbulent kinetic energy, and specific dissipation rate within the viscose sublayer, in all computations the first grid node adjacent to the wall should satisfy the following criteria:

$$y^+ = \frac{u_\tau y}{\nu} < 1 \tag{15}$$

where y^+ is the dimensionless sublayer scaled distance.

It is worth mentioning that the results presented in this paper have been obtained using a fine mesh with 200×83 grid nodes in the axial and radial directions, respectively. A grid dependency study, using a finer mesh with 200×114 grid nodes, has been performed, which shows no major changes on the results. Therefore, the results presented here can be considered as grid-independent.

5 Model Verification

To validate the presented method, which must work well for both steady and unsteady turbulence pipe flows, the computed velocity profile in the steady state turbulent pipe flow are compared with the experimental data of Laufer [15] and Brunone et al. [16] in Fig. 3. As can be noted, agreement between the computed and measured data is satisfactory in both cases.

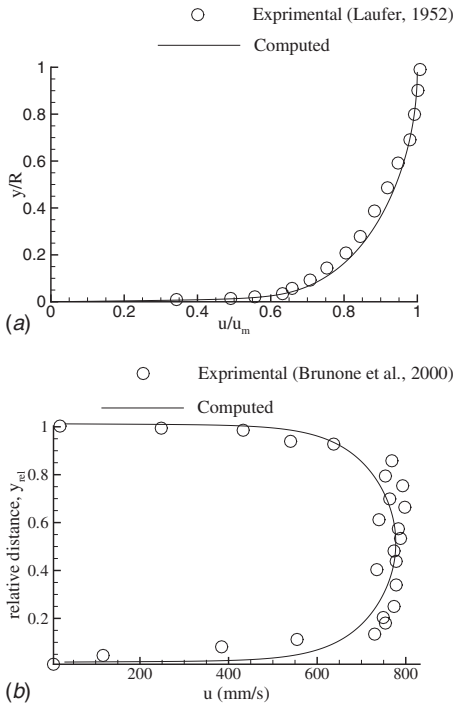

Fig. 3 Velocity profile in steady turbulent pipe flow: (*a*) Re =40,000 and (*b*) Re=58,650

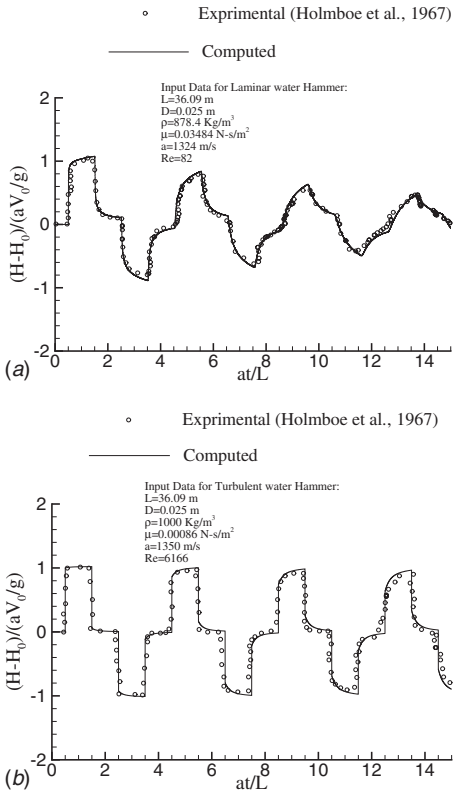

Fig. 5 Pressure-time history at the pipe-midpoint: (*a*) laminar water hammer, Re=82 and (*b*) turbulent water hammer, Re =6166

To validate the unsteady friction model developed in this paper, the computed data are compared with the measured data of Holmboe and Rouleau [17] for the laminar and the turbulent water hammer. The experimental schematic is shown in Fig. 4. When the down stream valve is suddenly closed, a strong transient flow is produced in the pipe line.

Figure 5 presents comparisons between computed and measured pressure heads at the middle of the pipe and also for the both laminar and turbulent water hammer. The input data for these cases are also shown in these figures. The time axis is normalized by the wave travel time from the reservoir to the valve (i.e., L/a). The pressure axis is also normalized by the Joukowsky head (i.e., aV_0^2/g). It is clearly observed that the agreement between computed and measured data is excellent and both the pressure amplitude, and the pressure phase are accurately resolved by the simulations.

6 Behavior of Unsteady Velocity Profiles

As the main purpose of this paper is to investigate the behavior of velocity profiles due to water hammer, three different test cases (test no. 1 from Ref. [17]; test no. 2 from Ref. [18]; and test no. 3 from Ref. [16]) are taken into consideration. The relevant parameters for these test cases are listed in Table 1. The working fluid is oil for test no. 1 and water for test nos. 2 and 3. The pipe material is copper for test nos. 1 and 2 and polyethylene for test no. 3. The flow regime is laminar for test no. 1 and turbulent for test nos. 2 and 3.

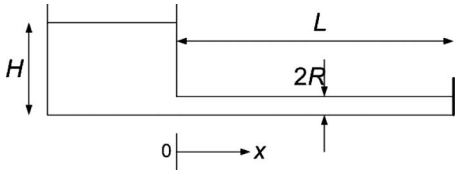

Fig. 4 Experimental apparatus with copper pipe line [17]

In the water hammer phenomenon, there are two important time scales. First is the time scale of the pressure wave, which is in order of L/a. Second is the time scale for the generated shear pulse due to passage of the pressure wave. This time scale is computed from the moment, which the shear pulse is generated, at the wall to the moment, where the turbulent structure is significantly changed throughout the pipe cross section. He and Jackson [19] found that the second time scale is in the order of $D/(2^{1/2}u_\tau)$. Ghidaoui et al. [20] introduced a useful nondimensional parameter P, which is the ratio of the two mentioned time scales and defined as

$$P = \frac{\sqrt{2}D/2u_\tau}{L/a} \tag{16}$$

By the time the valve is suddenly closed, the water hammer problem happens and the positive pressure wave travels from the valve to the reservoir. Figure 6 presents the velocity profiles for the turbulent water hammer in the two cases (a) $P \gg 1$ and (b) $P \approx 1$ and in the first wave cycle of water hammer.

Regarding Fig. 6, when the positive pressure wave passes from the pipe-midpoint ($t=0.6L/a$), a uniform shift in the velocity profile is induced in the whole of pipe cross section, and because of the no slip condition at the pipe wall, a strong gradient and a vortex ring (reverse flow) are formed around the pipe. The generated vortex ring is subsequently diffused toward the pipe center. When the reflected positive pressure wave passes from the midpoint of the pipe ($t=1.6L/a$), the direction of the flow changes behind the compression wave and is directed from the valve to the reservoir, and another vorticity pulse is generated at the pipe wall. The same condition occurs when the negative pressure wave coming from the valve ($t=2.6L/a$) and also when the reflected negative wave passes from the pipe-midpoint ($t=3.6L/a$). The process of velocity shift, vortex generation, and vortex diffusion continues

Table 1 the details for the *test* cases examined

Test No.	Pipe length (m)	Pipe diameter (m)	Density (kg/m^3)	Wave velocity (m/s)	Initial velocity (m/s)	Dynamic viscosity ($N\,s/m^2$)	Reynolds no.	P
1	26.09	0.025	878.4	1324	0.13	0.03483	82	-
2	37.2	0.022	1000	1319	0.2	0.001141	3856	40
3	352.0	0.0938	1000	340	0.71	0.001141	58,650	2

to occur as long as the water hammer wave is present in the pipe. As shown in Fig. 6, with the exception of a region near the pipe wall, the shape of the velocity profile remains unchanged. Figure 7 shows the velocity contours when the positive pressure wave arrives to the reservoir. In this figure, the velocity contours are normalized as a percentage of the initial bulk velocity (V_0). It is evident from Fig. 7 that a very thin region of the reverse flow is formed near the pipe wall.

Regarding Fig. 6 and for the case of $P \gg 1$, the fully-developed velocity profile is not achieved at $t=1.6\ L/a$ and $t=3.6\ L/a$, whereas the almost fully-developed velocity profile is formed in the case of $P \approx 1$. The main reason for this difference is that after passage of the reflected positive pressure ($t=1.6\ L/a$), the unsteady velocity profiled does not have enough time to form its fully-developed shape. Therefore, the nonequilibrium condition in case of $P \gg 1$ is much stronger than that in the case of $P \approx 1$. The same condition is hold for $t=3.6\ L/a$.

The unsteady velocity profiles for the laminar water hammer are shown in Fig. 8. The behavior of the velocity profile in the laminar water hammer is very similar to those mentioned for the turbulent water hammer. The main difference is that for the turbulent water hammer, the strong gradient, and the reverse flow region is very close to the pipe wall compared with the laminar water hammer.

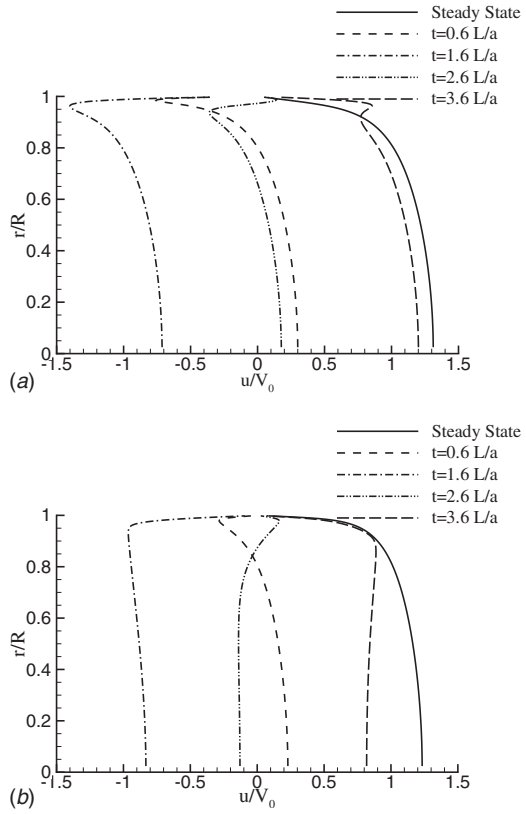

Fig. 6 Velocity profiles at the pipe-midpoint for the turbulent water hammer: (*a*) test no. 2, *P*=40 and (*b*) test no. 3, *P*=2

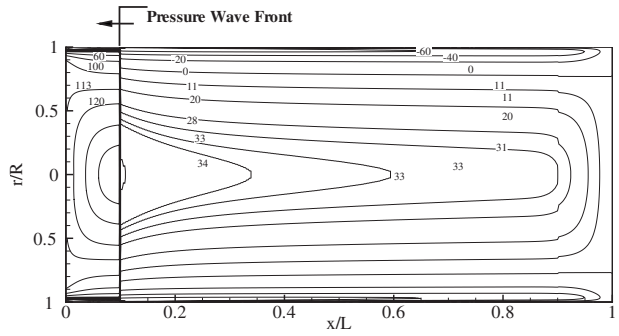

Fig. 7 Velocity contours along the pipe length for test no. 2 (the velocity values are normalized as a percentage of initial bulk velocity)

6.1 Decelerating and Accelerating Flows in Water Hammer Problem. Both decelerating and accelerating flows are produced in a wave cycle of water hammer that is fully described below.

6.1.1 Sudden deceleration. In a wave cycle of water hammer, sudden deceleration flow happens in two periods of time: (a) when the positive pressure wave travels from valve to the reservoir ($0 < t < L/a$) and (b) when the negative pressure wave travels from valve to the reservoir ($2L/a < t < 3L/a$). Figure 9 shows the shear stress profiles at the middle of pipe and in the first wave cycle of the water hammer. Immediately after the passage of the positive pressure wave from the pipe-midpoint ($t=0.6\ L/a$), the average velocity is very close to zero even though the velocity gradient and the consequent shear stress are very significant. The velocity and the shear stress at the near wall have signs opposite to the velocity in the core flow (see Figs. 6 and 9). This phenomenon is called the Richardson annular effect.

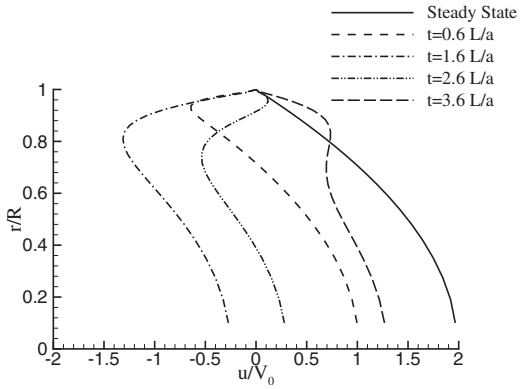

Fig. 8 Velocity profiles at the pipe-midpoint for the laminar water hammer, test no. 1

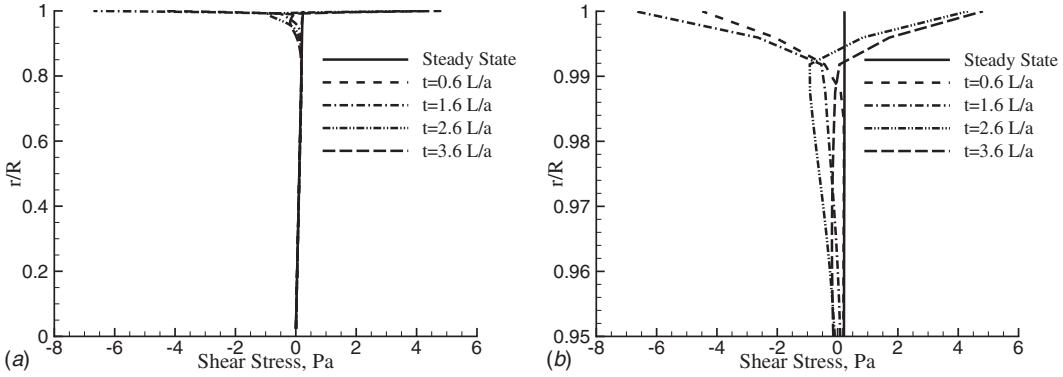

Fig. 9 Shear stress profiles at the pipe-midpoint for the turbulent water hammer, test no 2: (*a*) in the whole cross section of the pipe and (*b*) in the pipe near wall

6.1.2 Sudden acceleration. Similarly, sudden acceleration flow happens in two periods of time in a wave cycle of water hammer: (a) when the reflected positive pressure wave travels from the reservoir to the valve ($L/a<t<2L/a$) and (b) when the reflected negative pressure wave travels from the reservoir to the valve ($3L/a<t<4L/a$). When the reflected positive pressure wave passes from the pipe-midpoint ($t=1.6\ L/a$), the average velocity suddenly changes from zero (the velocity profile at the wall is still in nonequilibrium caused by the previous passage of a pressure wave, but the cross section averaged velocity is equal to zero) to some finite value. The velocity and the shear stress at the wall have the same signs as the velocity in the core flow.

6.2 Pressure Gradient and wall Shear Stress in Water Hammer Problem. The computed pressure gradient at the middle of the pipe as a function of time is shown in Fig. 10(*a*). The sharp peaks in this figure are approximations of the strong pressure gradient of the traveling wave. They appear in pairs of the same sign indicating the direction of the acceleration.

The oscillations of the wall shear stress are shown in Fig. 10(*b*). According to this figure, two different steps can be identified for the wall shear stress oscillation. The first step is a sudden rise in wall shear stress, which is caused directly by the passage of the pressure wave. Kucienska [21] showed that this shear stress peak is approximately proportional to the amplitude of the pressure wave. The second step is the relaxation of the wall shear stress. During this relaxation phase, the shear stress tends exponentially from the value caused by the pressure wave to the value corresponding to the new steady state. This situation is achieved if the flow conditions remained unchanged after the passage of the pressure wave which had caused the shear stress peak.

6.3 Points of Inflection and Zero Velocity. Velocity profiles due to water hammer problems are highly unstable due to their inflection nature. The inflection points are references of instability in steady inviscid flows, and experience has shown that they are points of particular interest in viscous stability studies as well. Weinbaum and Parker [22] suggested that the location of the point of inflection to the point of zero velocity is very important. To analyze the stability of inflectional velocity profiles with reverse flow near a wall, Das and Arakeri [23] concluded that the following variables should be taken into account.

1. The proper velocity scale is $\Delta u=u_{\max}-u_{\min}$.
2. The proper lengthy scale is the boundary layer thickness.

Therefore, the local Reynolds number is defined as $\mathrm{Re}_\delta=\Delta u\delta/v$. Figures 11 and 12 show the maximum and the minimum velocities, local Reynolds number, point of inflection, and point of zero velocity after the passage of positive pressure wave from the pipe-midpoint. These figures are plotted for the laminar water hammer (test no.1) and the turbulent water hammer (test no.3), respectively. As shown in Figs. 11(*c*) and 12(*c*), the point of zero velocity does not move very far from its initial location, while the point of inflection moves rapidly from the wall as consequent the profiles tend to become more unstable. However, the reduction in the Reynolds number with the time makes the profiles more stable (Figs. 11(*b*) and 12(*b*)). Consequently, the instability condition depends on the balance between these two competing effects.

7 Conclusions

The behavior of unsteady velocity profiles in laminar and turbulent water hammer problems has been numerically studied. To this end, the governing equations for transient flows are solved by using the modified implicit characteristics method. A k-ω turbulence model, which is accurate for two-dimensional boundary layers under adverse and favorable pressure gradients, is applied. The

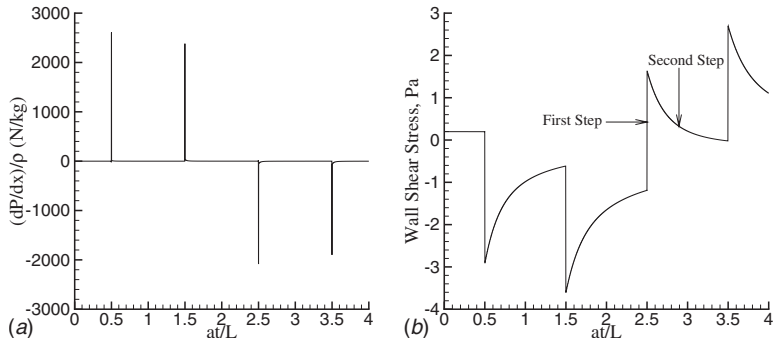

Fig. 10 (*a*) Pressure gradient and (*b*) wall shear stress at the pipe-midpoint and for the turbulent water hammer, test no. 2

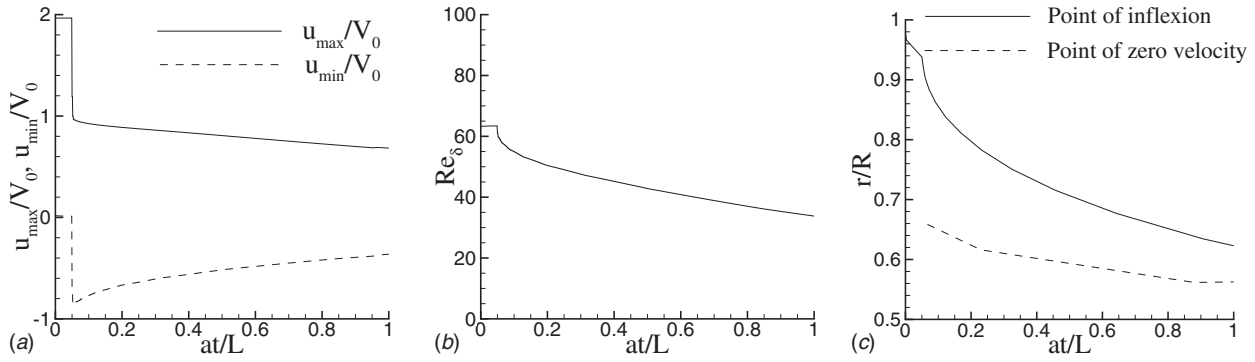

Fig. 11 (*a*) Calculated normalized maximum and minimum velocities, (*b*) local Reynolds number, and (*c*) point of zero velocity and point of inflection in the laminar water hammer, test no. 1

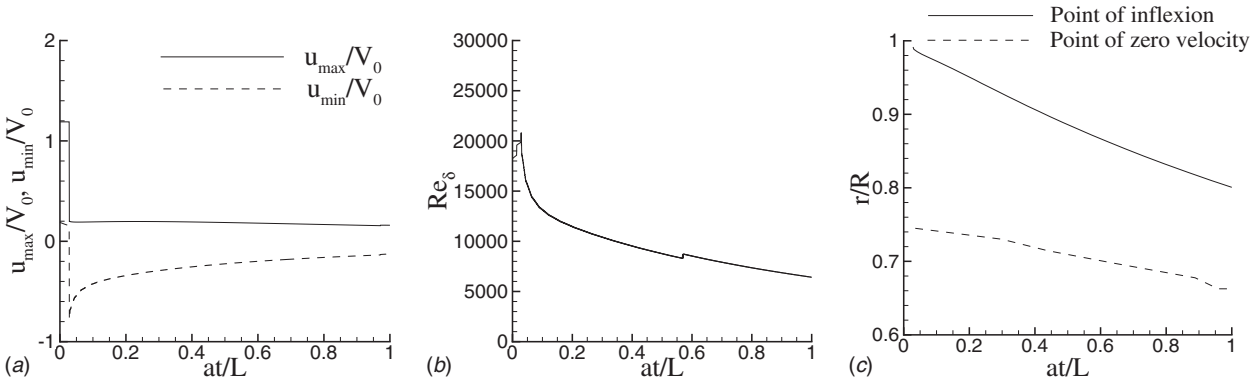

Fig. 12 (*a*) Calculated normalized maximum and minimum velocities, (*b*) local Reynolds number, and (*c*) point of zero velocity and point of inflection in the turbulent water hammer, test no. 3

results indicate that during the deceleration of the flow, a region of reverse flows and strong gradients is formed near to the pipe wall. In case of the turbulent water hammer, this region is very close to the pipe wall compared with the laminar water hammer. The velocity and the shear stress at the near wall have the signs opposite to the velocity in the core flow during deceleration of the flow. On the contrary, the velocity and the shear stress at the near wall have the same signs as the velocity in the core flow for the accelerating flow. Moreover, point of inflection and also point of zero velocity are formed in the unsteady velocity profile due to the water hammer problem. The point of zero velocity does not move very far from its initial location, while the point of inflection moves rapidly from the wall.

Acknowledgment

The authors wish to extend their utmost gratitude to Hydraulic Machinery Research Institute (HMRI) for their support and cooperation.

Nomenclature

a = acoustic wave velocity
C_μ = constant in eddy-viscosity
D = pipe diameter
f = Darcy–Weisbach friction factor
g = gravity acceleration
H = piezometric head
k = kinetic energy of turbulence fluctuation per unit mass
L = pipe length
r = radial coordinate measured from the pipe center line
R = pipe radius
P = pressure
Re = Reynolds number
Re_δ = local Reynolds number
t = time
u = longitudinal velocity
u_{max} = maximum velocity
u_{min} = minimum velocity
u_τ = friction velocity
u' = fluctuation velocity in the longitudinal direction
Δu = $u_{max}-u_{min}$
v = radial velocity
v' = fluctuation velocity in the radial direction
V_0 = initial bulk velocity
x = longitudinal coordinate
y = radial coordinate measured from the pipe wall
y_{rel} = relative distance transverse to pipe axis
y^+ = dimensionless sublayer scaled distance

Greek Symbols

α, β, β^*, σ, and σ^* = closure coefficient for the k-ω model
δ = boundary layer thickness
ε = dissipation per unit mass
υ = kinematics viscosity
υ_t = eddy-viscosity
ρ = density
τ = shear stress
ω = specific dissipation rate
ω_1 and ω_2 = implicit parameter for shear stress

Subscripts

i = mesh point location in the longitudinal direction

j = mesh point location in the radial direction
r = component in the radial direction
w = wall
x = component in the longitudinal direction
0 = steady state

Superscripts

n = time iteration
$+$ = sublayer scaled value
$*$ = dimensionless quantities

References

[1] Silva-Araya, W. F., and Chaudhry, M. H., 1997, "Computation of Energy Dissipation in Transient Flow," J. Hydraul. Eng., **123**(2), pp. 108–115.
[2] Ghidaoui, M. S., and Kolyshkin, A. A., 2001, "Stability Analysis of Velocity Profiles in Water Hammer Flows," J. Hydraul. Eng., **127**(6), pp. 499–512.
[3] Wahba, E. M., 2008, "Modelling the Attenuation of Laminar Fluid Transients in Piping systems," Appl. Math. Model., **32**, pp. 2863–2871.
[4] Vardy, A. E., and Hwang, K. L., 1991, "A Characteristic Model of Transient Friction in Pipes," J. Hydraul. Res., **29**(5), pp. 669–685.
[5] Zhao, M., and Ghidaoui, M. S., 2003, "Efficient Quasi-Two-Dimensional Model for Water Hammer Problems," J. Hydraul. Eng., **129**(12), pp. 1007–1013.
[6] Drikakis, D., Govatsos, P. A., and Papantonis, D. E., 1994, "A Characteristic Based Method for Incompressible Flows," Int. J. Numer. Methods Fluids, **19**(8), pp. 667–685.
[7] Silva-Araya, W. F., and Chaudhry, M. H., 2001, "Unsteady Friction in Rough pipes," J. Hydraul. Eng., **127**(7), pp. 607–618.
[8] Pezzinga, G., 2000, "Evaluation of Unsteady Flow Resistances by Quasi-2D or 1D Models," J. Hydraul. Eng., **126**(10), pp. 778–785.
[9] Wahba, E. M., 2006, "Runge-Kutta Time-Stepping Schemes With TVD Central Differencing for the Water Hammer Equations," Int. J. Numer. Methods Fluids, **52**(5), pp. 571–590.
[10] Zhao, M., and Ghidaoui, M. S., 2006, "Investigation of Turbulence Behavior in Pipe Transient Using a k-ε Model," J. Hydraul. Res., **44**(5), pp. 682–692.
[11] Fan, S., Lakshminarayana, B., and Barnett, M., 1993, "Low-Reynolds Number k-ε Model for Unsteady Turbulent Boundary Layer Flows," AIAA J., **31**(10), pp. 1777–1784.
[12] Drikakis, D., and Goldberg, U., 1998, "Wall-Distance-Free Turbulence models Applied to Incompressible Flows," Int. J. Comput. Fluid Dyn., **10**(3), pp. 241–253.
[13] Wilcox, D. C., 1994, *Turbulence Modelling for CFD*, DCW Industries, La Canada, CA.
[14] Martinuzzi, R., and Pollard, A., 1989, "Comparative Study of Turbulence Models in Predicting Turbulent Pipe Flow. Part I: Algebraic Stress and k-ε Models," AIAA J., **27**(1), pp. 29–36.
[15] Laufer, J., 1952, "The Structure of Turbulence in Fully Developed Pipe Flow," NACA Report No. 1174.
[16] Brunone, B., Karney, B. W., Mecarelli, M., and Ferrante, M., 2000, "Velocity Profiles and Unsteady Pipe Friction in Transient Flow," J. Water Resour. Plann. Manage., **126**(4), pp. 236–244.
[17] Holmboe, E. L., and Rouleau, W. T., 1967, "The Effect of Viscous Shear on Transients in Liquid Lines," ASME J. Basic Eng., **89**(1), pp. 174–180.
[18] Bergant, A., and Tijsseling, A., 2001, "Parameters Affecting Water Hammer Wave Attenuation, Shape and Timing," Proceedings of the Tenth International Meeting of the IAHR Work Group on the Behaviour of Hydraulic Machinery Under Steady Oscillatory Conditions, Trondheim, Norway, p. 12, Paper No. C2.
[19] He, S., and Jackson, J. D., 2000, "A Study of Turbulence under Conditions of Transient Flow in a Pipe," J. Fluid Mech., **408**, pp. 1–38.
[20] Ghidaoui, M. S., Mansour, S. G. S., and Zhao, M., 2002, "Applicability of Quasi-Steady and Axisymmetric Turbulence Models in Water Hammer," J. Hydraul. Eng., **128**(10), pp. 917–924.
[21] Kucienska, B., 2004, "Friction Relaxation Model for Fast Transient Flows," Ph.D. thesis, University of Catholique de Louvain, Belgium.
[22] Weinbaum, S., and Parker, K. H., 1975, "The Laminar Decay of Suddenly Blocked Channel and Pipe Flows," J. Fluid Mech., **69**(4), pp. 729–752.
[23] Das, D., and Arakeri, J. H., 1998, "Transition of Unsteady Velocity Profiles With Reverse Flow," J. Fluid Mech., **374**, pp. 251–283.

Application of Fractional Scaling Analysis to Loss of Coolant Accidents: Component Level Scaling for Peak Clad Temperature

Ivan Catton
UCLA–MAE,
P.O. Box 951597,
48-121 Engineering IV,
Los Angeles, CA 90195-1597
e-mail: catton@ucla.edu

Wolfgang Wulff
11 Hamilton Road,
Setauket, NY 11733
e-mail: wolfgangwulff@optonline.net

Novak Zuber
703 New Mark Esplanade,
Rockville, MD 20850
e-mail: wulff@bnl.gov

Upendra Rohatgi
Brookhaven National Laboratory,
Building 475B,
Upton, NY 11973 USA
e-mail: rohatgi@bnl.gov

*Fractional scaling analysis (FSA) is demonstrated here at the component level for depressurization of nuclear reactor primary systems undergoing a large-break loss of coolant accident. This paper is the third of a three-part sequence. The first paper by Zuber et al. (2005, "Application of Fractional Scaling Analysis (FSA) to Loss of Coolant Accidents (LOCA), Part 1. Methodology Development," Nucl. Eng. Des., **237**, pp. 1593–1607) introduces the FSA method; the second by Wulff et al. (2005, "Application of Fractional Scaling Methodology (FSM) to Loss of Coolant Accidents (LOCA), Part 2. System Level Scaling for System Depressurization," ASME J. Fluid Eng., to be published) demonstrates FSA at the system level. This paper demonstrates that a single experiment or trustworthy computer simulation, when properly scaled, suffices for large break loss of coolant accident (LBOCAs) in the primary system of a pressurized water reactor and of all related test facilities. FSA, when applied at the system, component, and process levels, serves to synthesize the world-wide wealth of results from analyses and experiments into compact form for efficient storage, transfer, and retrieval of information. This is demonstrated at the component level. It is shown that during LBOCAs, the fuel rod stored energy is the dominant agent of change and that FSA can rank processes quantitatively and thereby objectively in the order of their importance. FSA readily identifies scale distortions. FSA is shown to supercede use of the subjectively implemented phenomena identification and ranking table and to minimize the number of experiments, analyses and computational effort by reducing the evaluation of peak clad temperature (PCT) to a single parameter problem, thus, greatly simplifying uncertainty analysis.*
[DOI: 10.1115/1.4000370]

Keywords: information synthesis, fractional rate of change, fractional scaling, holistic scaling approach, hierarchy of complex system processes

1 Introduction

There are many reasons to look for better ways to compute essential elements of the thermal hydraulics of a nuclear power station. Most of the reasons have to with safety and the demonstration of how safe a particular configuration is. This means any method of reducing uncertainty is a worthwhile effort. What we hope to demonstrate is that a transparent method of utilizing experimental data to demonstrate performance with quantifiable uncertainty can be developed using fractional scaling analysis (FSA). This paper is the third of a three-part sequence. The first paper by Zuber et al. [1] introduces the FSA method; the second by Wulff et al. [2] demonstrates FSA at the system level. This paper demonstrates that a single experiment or trustworthy computer simulation, when properly scaled, suffices for LBOCAs in the primary system of a pressurized water reactor and of all related test facilities. We have chosen peak clad temperature (PCT) for this because it is the most prominent figure of merit and used heavily in the licensing process. We will show that with FSA, the entire process can be cast into a one parameter problem (the local fuel pin Biot number) making an uncertainty estimation particularly straightforward and efficient.

The present thermal hydraulic design of a nuclear power plant must meet the acceptance criteria that resulted from the 1972-73 AEC rule-making hearings on the emergency core cooling system (ECCS). Very little has changed since, in spite of the many years that have passed during which a large amount of experimental work was done and a major code development effort was undertaken.

A major effort of the designer is to demonstrate that the new plant is robust and that Title 10 CFR Part 50, Appendix K is met. Without having a plant available for experimentation, large numbers of calculations are done using tools of varying pedigrees. The argument is made that the data from experimental studies are used to qualify the computer models, and the computer models are to be used to scale-up from the model experiments to the plant.

A significant part of this effort is usually devoted to the small break loss of coolant (SBLOCA) and large-break loss of coolant accident (LBLOCA) and Chapter 15 events. Because there has been no systematic treatment of available data, the process weighs heavily on engineering judgment coupled with the experimental data and code calculation results. The finished product is most likely overly conservative because that is the only way unsubstantiated engineering judgment will be accepted. The process is both

Contributed by the Fluids Engineering Division of ASME for publication in the JOURNAL OF FLUIDS ENGINEERING. Manuscript received May 28, 2009; final manuscript received September 8, 2009; published online November 19, 2009. Editor: Joseph Katz.

time-consuming and very costly. The recent effort to certify the Westinghouse AP600 is a good example of the process.

The past 30 years have produced, at an overall cost of over $1.5 billion, a tremendous wealth of experimental results from integral-effects test facilities, and also analytical results from computer simulations. These results have been tabulated, plotted, and individually described, but never comprehensively interpreted to provide universal insight in reactor systems response, component interactions, and dominant processes during postulated accidents.

Furthermore, the T/H data obtained during the past 30 years are presented in an unimaginably large number of dimensional plots and tables in a vast number of reports, which are distributed worldwide over many libraries in industry, national laboratories, and universities. Each plot or table presents in most cases the history of a single (dimensional) state variable as a function of actual (dimensional) time, for one set of circumstances in one particular plant or test facility. Many of these data records are repeated in similar conditions (large-break loss of coolant accident) but in different plants. In fact, similar transients in all power plants and integral-effects test facilities should all be combined in the same dimensionless plots and thereby reveal common processes and component interactions in terms of dimensionless parameters.

Since the information is now only fragmentary and disconnected, it is unmanageable and cannot be readily accessed. Since the information is not interpreted, its universal features cannot be understood and applied by current and future generations of designers and safety experts. Furthermore, due to the passage of time a number of experimental data reports and tapes, as well as some computer codes, have already been lost and can no longer be retrieved.

The synthesis of fragmented and scattered data is performed at the component level by means of a scaling approach that assigns to each process (i) a dimensionless effect metric Ω_i, which quantifies the contribution of that process to the fractional change of a corresponding state variable in a given component. The effect metric Ω_i is the product of process characteristic time t_{ref} (e.g., fluid residence or replacement time, etc.) and specific time rate of fractional change ω_i, i.e., the ratio of process transport rate over component content of a given preserved quantity (mass, energy, etc.). Thus, this level generates quantitative criteria (one for each component) for evaluating component effects on a state variable.

What is presented here is only for the first part of a LBLOCA. It was chosen because we are all familiar with its role in the design of nuclear power stations and the cost of licensing and refueling calculations. With a small amount of effort the results presented herein could be put to use immediately. Further improvement will require a more thorough delineation of the hierarchy of processes involved and data synthesis and will lead to scaling criteria for design of experiments, assessing the effects of scale distortion, support of uncertainty analyses, and many other benefits including being able to optimize some of the characteristics of a plant.

2 Fractional Scaling at the Component Level

In this section, we use FSA to estimate PCT. This is based on a simple fuel thermal analysis given in Appendix A. The decay heat is then cast into an appropriate form using the effective (aggregate) thermal properties derived in Appendix B, and the pin response is determined in the form of a single parameter.

2.1 Fuel Thermal Analysis. The quantity to be changed is the *fuel and clad* energy above the energy that the fuel and clad had when at the initial clad surface temperature

$$\Delta E = \sum_{i}^{f,c} [\langle T_i \rangle - T_{w,0}](A\rho c)_i = [\langle T \rangle - T_{w,0}] \sum_{i}^{f,c} (A\rho c)_i \tag{1}$$

where the bracketed terms, $\langle - \rangle$, are aggregates of averages over the clad and the fuel, *E is the* energy per unit length of the fuel pin, A is the cross-sectional area, ρc is the volumetric heat capacity, and the subscript i denotes either clad or fuel. An expression for $\langle T \rangle - T_{w,0}$ derived in Appendix A, Eq. (A16), is

$$\langle T \rangle - T_{w,0} = \langle T \rangle_0 - T_{w,0} + \frac{\int_0^t q'(t)dt - \int_0^t h_c \xi (T_w - T_s)dt}{\sum_{i=f,c} (A\rho c)_i}$$

$$= \langle T \rangle_0 - T_{w,0} + \frac{q_0' \bar{f} t - \int_0^t h_c \xi (T_w - T_s)dt}{\sum_{i=f,c} (A\rho c)_i} \tag{2}$$

where $q'(t)$ is the decay heat at time t, $\bar{f}$ is the time-average decay heat fraction, t is the time measured from the onset of the event, h is the convective heat transfer coefficient, and ξ is the pin circumference. The subscripts c, f, s, and 0 denote, respectively, cladding, fuel pellet, coolant, and initial time.

To simplify the analysis, the decay heat fraction, $f(t)$, has been defined as

$$f(t) = \frac{q'(t)}{q_0'} = \frac{q_d'(t)}{q_0'} \tag{3}$$

where q_0' is the initial full-power before scram, and q_d' is the power after scram with

$$f(0) = 1 \tag{4}$$

and use is made of a time-average fractional decay heat level $\bar{f}$ defined as shown

$$\bar{f}(t) = \frac{1}{t} \int_0^t f(\hat{t}) d\hat{t} \tag{5}$$

An expression derived for the excess clad temperature in Appendix A, Eq. (A19), is

$$T_w - T_{w,0} = (1 - f)(\langle T \rangle_0 - T_{w,0}) + \frac{\bar{f} q_0' t - \int_0^t h_c \xi (T_w - T_s)dt}{\sum_{i=f,c} (A\rho c)_i} \tag{6}$$

where the first term is the result of thermal relaxation within the pin, the first term in the numerator of the second term is the decay heat contribution, and the second is the convective losses.

The time rate of change of the overall aggregate of the clad and fuel average pin temperatures relative to the initial clad temperature is found by differentiating Eq. (2), time rate of change of the pin energy, with respect to time

$$\frac{d(\langle T \rangle - T_{w,0})}{dt} = \frac{q_0' f(t) - h_c \xi (T_w - T_s)}{\sum_{i=f,c} (A\rho c)_i} \tag{7}$$

Equation (7) is normalized with the initial value of the temperature difference, see Eq. (A17)

$$\langle T \rangle_0 - T_{w,0} = \frac{q_0'}{8\pi k_f} \frac{\sum_{i=f,c} C_i (A\rho c)_i}{\sum_{i=f,c} (A\rho c)_i} = \frac{q_0'}{\bar{K}_{\text{pin}}} \tag{8}$$

Equation (8) shows the relationship between the initial fuel and clad temperatures and the dependence on K_{pin}, derived in Appendix B, where

$$\bar{K}_{\text{pin}} = \frac{8\pi k_f \sum_{i=f,c} (A\rho c)_i}{\sum_{i=f,c} C_i (A\rho c)_i} \tag{9}$$

clearly demonstrating the aggregate nature of the *effective* thermal conductivity of the pin. Scaling Eq. (7) yields

$$\frac{d\langle\theta\rangle}{dt} = \omega_D - \omega_c(\theta_w - \theta_s) \tag{10}$$

where ω_D is the fractional rate of change (FRC) for decay heat

$$\omega_D = \frac{\bar{f} q_0'}{(\langle T\rangle_0 - T_{w,0}) \sum_{i=f,c} (A\rho c)_i} = \omega_{D,0} \bar{f} \tag{11}$$

and ω_c is the FRC for convective cooling

$$\omega_c = \frac{h_c \xi}{\sum_{i=f,c} (A\rho c)_i} \tag{12}$$

Equation (10) is identical to Eq. (A11) in Appendix A in Ref. [1]. Time on the left hand side of Eq. (10) is dimensional, and its time constant will be different than that of the two FRCs. Note the aggregate nature of the elements of Eqs. (11) and (12). The dimensionless temperatures and FRCs all reflect the aggregate nature of the fuel pin.

Three dimensionless temperatures result from the normalization. The three dimensionless temperatures are the dimensionless excess pin average temperature

$$\langle\theta\rangle = \frac{\langle T\rangle - T_{w,0}}{\langle T\rangle_0 - T_{w,0}} \quad \text{with} \quad \langle\theta\rangle_0 = 1 \quad \text{at} \quad t = 0 \tag{13}$$

the dimensionless clad temperature

$$\theta_w = \frac{T_w - T_{w,0}}{\langle T\rangle_0 - T_{w,0}} \quad \text{with} \quad \theta_{w,0} = 0 \quad \text{at} \quad t = 0 \tag{14}$$

and the dimensionless coolant temperature

$$\theta_s = \frac{T_s - T_{w,0}}{\langle T\rangle_0 - T_{w,0}} \quad \text{with} \quad \theta_{s,0} = \frac{-q_0'}{h_{c,0}\xi(\langle T\rangle_0 - T_{w,0})} \quad \text{at} \quad t = 0 \tag{15}$$

With this scaling, Eq. (2) can be rewritten

$$\langle\theta\rangle = 1 + \omega_D t - \int_0^t \omega_c(\theta_w - \theta_s)dt \tag{16}$$

Normalizing the clad excess temperature, Eq. (6), by the initial excess temperature yields

$$\theta_w = (1 - f) + \omega_D t - \int_0^t \omega_c(\theta_w - \theta_s)dt \tag{17}$$

Equation (17) defines the *dimensionless clad temperature*, θ_w, and its relationship to the FRCs. The first term on the right-hand side of Eq. (17) is the fractional rise of clad surface temperature due to stored energy $(1-f)$. The second term, $\omega_D t$, is the decay heat contribution at time t and the third term represents heat loss due to convective cooling. Although the decay heat and convective contributions are relatively small, the peak value cannot be determined without considering both, see Sec. 2.3. Equation (17) could be used for simulation. In this case we chose not to because our focus was on PCT.

2.2 Decay Heat Fraction. The decay power curve can be approximated by $f(t) = 0.066 t^{-0.2}$. To accommodate the singularity at $t=0$, $f(t)$ is approximated by

$$f(t) = \frac{0.066}{(\varepsilon + ts^{-1})^{0.2}} \tag{18}$$

where $\varepsilon = 0.066^5 = 1.252 \times 10^{-6}$ The time-average, found from Eq. (5) using Eq. (18), is given by

$$\bar{f}(t) = \frac{0.066s}{0.8t}\left[\left(\frac{t}{1s} + \varepsilon\right)^{0.8} - \varepsilon^{0.8}\right] t > 0 \tag{19}$$

The time unit (1 s) is introduced in Eqs. (18) and (19) to indicate that the time must be entered in seconds. Pure numbers are used for fractional exponentiation.

Evaluating Eq. (17) at the time of PCT, denoted by an asterisk, leads to a particularly simple expression

$$\theta_w^* = \frac{T_w^* - T_{w,0}}{\langle T\rangle_0 - T_{w,0}} = (1 - f^*) + \omega_D t^* - \omega_c \int_0^{t^*} (\theta_w + \theta_s)dt$$
$$= (1 - f^*) + \Omega_D^* - \Omega_c^* \tag{20}$$

where the *decay heat fraction*, Eq. (18), at t^* is given by

$$f^*(t) = \frac{0.066}{(\varepsilon + t^* s^{-1})^{0.2}} \tag{21}$$

and the heat transfer coefficient in ω_c has been assumed to be a suitable average. The decay heat fractional change metric, Ω_D^* in Eq. (20) is

$$\Omega_D^* = W_D t^* = \omega_{D,0} \bar{f}^* t^* \tag{22}$$

and also depends on t^* (it is proportional to $(t^*)^{4/5}$). Note that $\omega_{D,0}$ is the value of ω_D at the initiation of the pin heat up. The convective fractional change metric, Ω_c^*, also dependent on t^*, is given by

$$\Omega_c^* = \omega_c \int_0^{t^*} (\theta_w + \theta_s)dt \tag{23}$$

2.3 Peak Clad Temperature. The peak value of θ_w, see Eq. (17), occurs at about the time convective cooling balances the decreasing decay heat power. This occurs when the time derivative of θ_w is equal to zero

$$\frac{d\theta_w}{dt} = -\frac{df}{dt} + \omega_{D,0} f - \omega_c(\theta_w - \theta_s) = 0 \tag{24}$$

The relationship between θ_w and $\langle\theta\rangle$ is needed because the peak values may not occur at the same time. This is found using Eqs. (16) and (17) to obtain

$$\theta_w = \langle\theta\rangle - f \tag{25}$$

from which it is found that

$$\frac{d\theta_w}{dt} = 0 = \frac{d\langle\theta\rangle}{dt} - \frac{df}{dt} = \omega_{D,0} f - \omega_c[\langle\theta\rangle - f + \theta_s] - \frac{df}{dt} \tag{26}$$

Since the cooler steam temperature is close to the initial clad temperature, it is assumed that

$$(i) \quad \theta_s \ll 1$$

With this assumption, and the assumption the that the decay heat at the time of the clad temperature peak is nearly constant, although the derivative could be calculated from Eq. (18)

$$(ii) \quad t = t^*: \frac{df}{dt} \approx 0$$

integration of Eq. (10) yields

$$\langle\theta\rangle = (\omega_{D,0} + \omega_c) \int_0^t f(t') e^{-\omega_c(t-t')} dt' + e^{-\omega_c t} \tag{27}$$

Catton et al. [4] pointed out that

$$(iii)\quad \omega_c \ll \omega_{D,0}$$

$$(iv)\quad \omega_c t \ll 1$$

enabling us to write

$$\langle\theta\rangle \cong 1 + (\omega_{D,0} + \omega_c)(1 - \omega_c t)\bar{f}(t)t - \omega_c \int_0^t f(t')t'dt' \tag{28}$$

which is then further reduced to

$$\langle\theta\rangle \approx 1 + (\omega_{D,0}) \int_0^t f(t')dt' = 1 + \omega_{D,0}\bar{f}t = 1 + \Omega_D \tag{29}$$

showing that the pin mean temperature rises because of decay heat. Substitution of Eq. (29) into Eq. (25) yields the scaled clad temperature, the same result obtained earlier (see Eq. (20)) but without the convective cooling

$$\theta_w = (1 - f) + \Omega_D \tag{30}$$

Equation (30) shows that the clad surface temperature rise is primarily due to the decay heat-related pin mean temperature rise and to the equalization of stored energy. The latter overpowers the former. To find the peak temperature, θ_w^*, however, the time at which Eq. (24) is true must be found. Assumption (ii) reduces Eq. (26) to a form that allows the time of the blow down peak to be determined

$$t = t^*: \quad \omega_c(\langle\theta^*\rangle + \theta_s) = f^*(\omega_c + \omega_{D,0}) \tag{31}$$

With Eq. (22) and assumptions (i) and (ii), Eq. (31) can be rewritten to yield

$$\frac{f^*}{\Omega_D^* + 1} = \frac{\omega_c}{\omega_{D,0} + \omega_c} \approx \frac{\omega_c}{\omega_{D,0}} = \frac{h_c\xi(\langle T\rangle_0 - T_{w,0})}{q_0'} = N_{\mathrm{Bi}} \tag{32}$$

where it can be shown with Eqs. (A17) and (B2) that the pin aggregate Biot number, N_{Bi}, is given by

$$N_{\mathrm{Bi}} = \frac{h_c\xi}{\bar{K}_{\mathrm{pin}}} \tag{33}$$

$\bar{K}_{\mathrm{pin}}$ is the pin effective (aggregate) thermal conductivity given by Eq. (9) (derived in Appendix B as Eq. (B3)) and $N_{\mathrm{Bi}} \ll 1$. The PCT, θ_w^*, is an implicit function of the time, t^*, that the peak occurs. The time, t^*, can be estimated from Eq. (31) when the time dependence of the decay heat and the convective heat transfer coefficient are known.

Available experimental data can be synthesized by plotting it in the form given by Eq. (20). Elimination of f^* from Eq. (20), however, provides a form that better demonstrates the effectiveness of convective cooling. This is done by substituting Eq. (32) into Eq. (20) to yield

$$\theta_w^* = (\Omega_D^* + 1)[1 - N_{\mathrm{Bi}}] \tag{34}$$

The more the $\theta_w^*(\Omega^*, N_{\mathrm{Bi}})$ data fall below the $\theta_w^* = (\Omega_D^* + 1)$ line, the more effective is the convective cooling.

The value of this simple relationship is demonstrated in Fig. 1, where one can see that an effective Biot number can be found for every value of full scale PCT data by drawing a straight line through "0" on the $1+\Omega_D^*$ axis and noting that the vertical axis intercept is just $(1-N_{\mathrm{Bi}})$. This makes data from facilities with electrical heating of much more value because the results can be directly translated to a figure like that shown in Fig. 1.

Equation (32) shows that for a given decay heat curve $f(t)$, Ω_D^* depends on the FRCs of convective cooling, the pin Biot number $N_{\mathrm{Bi}} = \omega_c / \omega_{D,0}$, and the decay heat, respectively, or on $\omega_{D,0}$, and Eq. (31) is transcendental because of the fractional exponent of time in the decay heat curve. MATHCAD was used to solve Eq. (31) for time t^* with the "Find" command using the expression for $f(t)$ given by Eq. (19). The fractional change metric Ω_D^* is then determined for $0.015 < N_{\mathrm{Bi}} < 0.030$ and $0.2 < \omega_{D,0} < 1.0$ which includes the known $\omega_{D,0} = 0.46$ for nuclear fuel with uniform heating. With appropriate thermal resistances for wire ceramic insulator geometries in Eq. (20), it should also encompass electrically heated rods in test facilities. The values of N_{Bi} were based on reasonable values of steam cooling. The result is the linear relationship between normalized peak clad temperature and the fractional change metric Ω_D^* shown in Fig. 2.

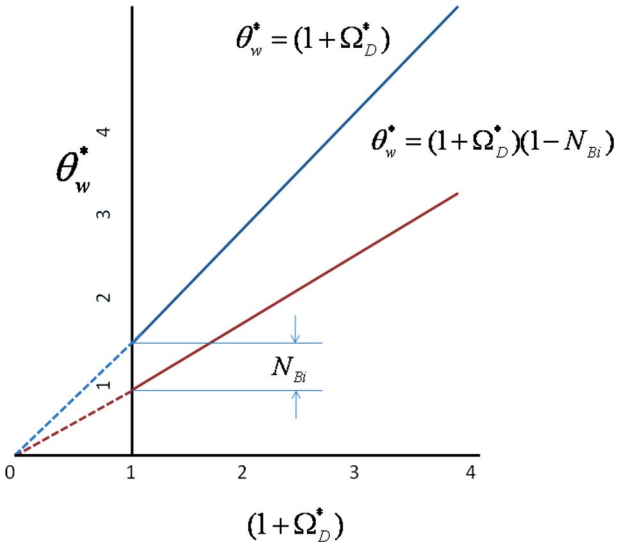

Fig. 1 Dimensionless temperature and its relationship to Biot number and the decay heat fractional change metric

When the Ω_D^* results were used to compute the normalized PCT θ_w^* in the same Biot number $\omega_{D,0}$ and ranges, it was found that the points fell almost completely on a single line. This result demonstrates the potential power of FSA and that when the convective cooling varies between 1.5% and 3.0% of full-power heating, the results can be plotted on a single line with very little scatter. Detailed test data, however, are needed to confirm this result.

The benefits of the Biot number being the only *parameter* in an evaluation of the peak clad temperature are noteworthy. First, as shown by Fig. 1, it will be easy to synthesize the data in a form that is useful. Second, a number of the parameters needed in our large codes, such as fuel thermal conductivity, gap conductance, and steam cooling heat transfer coefficient, can be lumped together and a multiparameter uncertainty analysis is reduced to a *single* parameter uncertainty analysis. This will enable one to

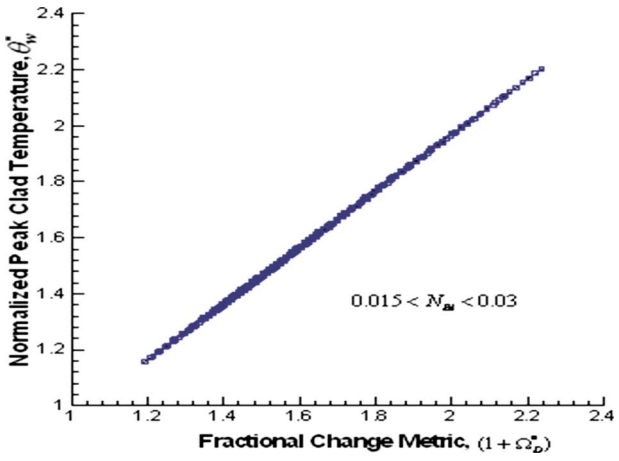

Fig. 2 Normalized PCT for $0.015 < N_{\mathrm{Bi}} < 0.03$

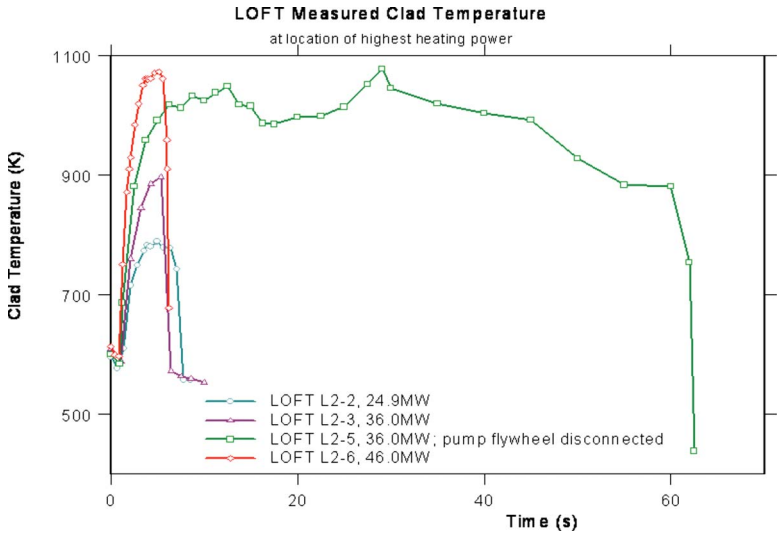

Fig. 3 LOFT measured clad temperature at the location of the peak heating rate

overcome the present lack of resources and enable one to accomplish a statistically reliable uncertainty analysis.

3 Application

Data were obtained for several loss of flow test (LOFT) experiments, see Ref. [3], and were shown in Fig. 3. The peak clad temperature is seen to show a great deal of sensitivity, as expected, to the linear heating rate. LOFT test L2-5It is with the pump flywheel disengaged, thereby allowing the pumps to coast down very fast reducing the liquid delivered to the core and delaying precursor cooling (ECC). The core remains in vapor cooling for a long time. The three other peaks are precursor cooling results. Following the scaling rules developed in this work, Fig. 4 was prepared.

The scaled data collapse the 24.9 MW and 36.0 MW cases onto essentially a single line, Fig. 4. The 46.0 MW case shows a higher peak value of the clad temperature. It should be noted, however, that we are not certain whether the recorded maximum linear heating rate and the location of the recorded maximum temperature are the same. Even so, the data collapse is significant and brings all the data quite close to each other (well within the uncertainty ascribed to predictions using large computer codes). To put this in perspective, a compilation of blowdown peak clad temperatures from Ref. [4], Fig. 5, is shown below. The linear character shown by Fig. 1 can clearly be seen with the slope of the line being reproduced by the analysis given here [4]. The slope of a straight line through the blowdown PCT data generated by Catton et al. [4] can be compared with

$$S = (1 - f^*)/\bar{K}_{\text{spin}}$$

The scaling given in Sec. 2.1 allows Fig. 4 to be prepared when the fuel pin characteristics are known. The simplicity of the results and their ease of use are obvious. Unfortunately the supporting data needed to do this and to collapse the scatter shown in the work of Catton et al. [4] were not available to the authors.

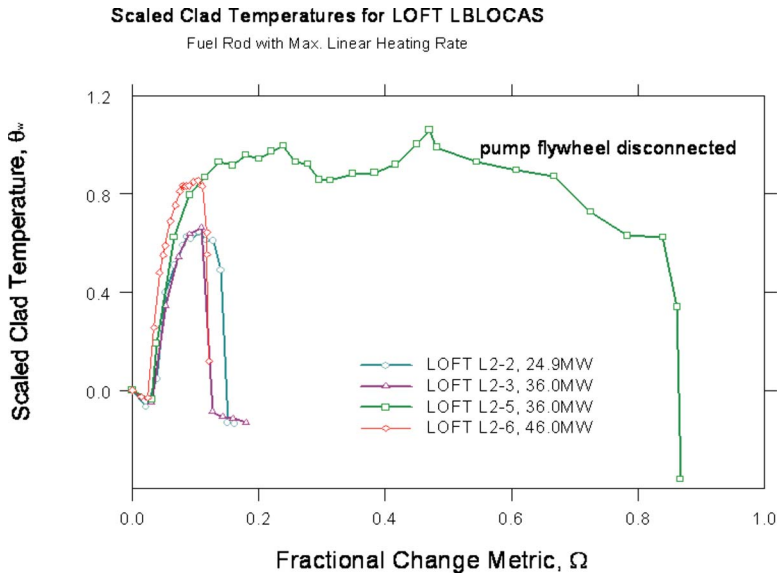

Fig. 4 Scaled LOFT clad temperatures at the location of the peak heating rate-fractional change metric

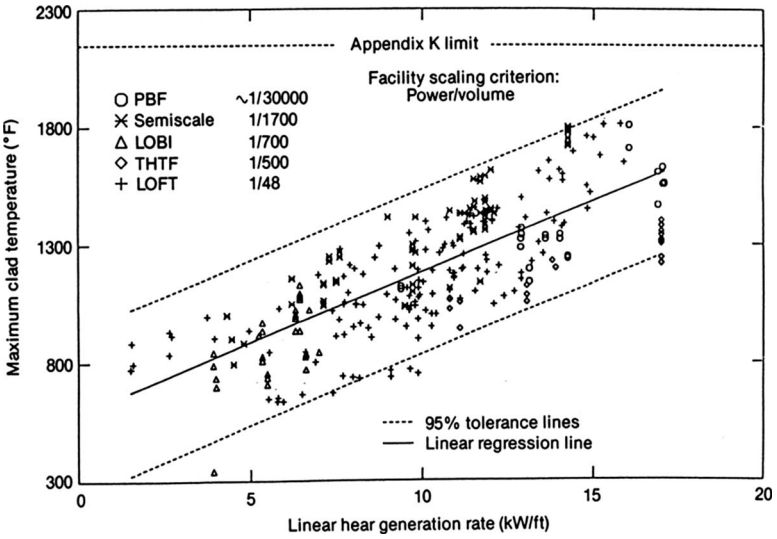

Fig. 5 A compilation of blowdown peak clad temperature measurements and their relationship to linear heat generation rate

4 Conclusions

The results of our scaling analysis based on FSA are preliminary but show a great deal of promise. The uncertainties in the results are comparable to those obtained with our best large computer codes and only require simple scaling to achieve. The comparison is not surprising because large codes, such as TRAC or RELAP5 are tuned to compare, as well as is possible to the same body of knowledge, as is shown in Fig. 5. In contrast to the earlier work by Catton et al. [4] details of the test facility fuel or simulated fuel pins can easily be incorporated into a prediction of the peak blowdown value. This would have been done here but the detailed data used to construct Fig. 5 were not available to us.

An estimate of the PCT resulting from a LBLOCA has been reduced to a single parameter problem, the local fuel pin Biot number, that will allow well substantiated uncertainty estimates to be made. More data of the type shown in Fig. 1 will need to be evaluated to ascertain the range of Biot number needed to efficiently and appropriately perform such an uncertainty analysis.

How synthesis of data, information, and knowledge about a component, the fuel pin, can be achieved has been demonstrated. The scaling synthesis identified the governing processes and generated hierarchies that rank their relevance to a T/H process in a NPP. The hierarchies could serve as a basis for developing advanced computational capabilities, as well as for performing experiments of interest to advanced NPP. Available data could be cast in a format efficient for preserving and transmitting technical information and knowledge to future generations of nuclear engineering students and practitioners. The results of such synthesis could be improved process/operating *efficiency* and the resulting *large economic savings* to the industry and to government (which can then be passed on to commerce and to taxpayers).

The large number of code computations currently performed by industry, national laboratories, and government are *not* needed. The demonstrated scaling synthesis can provide a technically sound basis for significantly reducing the number of code calculations concerned with NPP refueling, licensing, and power uprating. Such a reduction will be of great economic benefit to nuclear power technology.

We believe that application of FSA to the LBLOCA is only a beginning. A large number of other problems, such as SBLOCA, could also be addressed. Here the metric would be core level. Application to GEN IV plants could yield many benefits ranging from guidance in experimental confirmation of safety issues to sizing of the various safety components by enabling one to use the large amounts of data presently available. A major feature of FSA is its transparency.

Our goals were to demonstrate a process and FSA and to discuss its benefits. We have achieved both goals in spite of the limited data available to us. The resulting relationship shown in Fig. 2 and method for data evaluation described by Fig. 1 make the LBLOCA amenable to a true uncertainty analysis without the usual caveats needed to rationalize limited statistics.

Appendix A: Fuel Thermal Analysis

We begin fuel thermal analysis by writing an expression for the energy per unit length of the fuel pin, E

$$E = \sum_{i}^{f,c} \langle T_i \rangle (A\rho c)_i = \langle T \rangle \sum_{i}^{f,c} (A\rho c)_i \tag{A1}$$

where A is the cross-sectional area, ρc is the volumetric heat capacity, T is the temperature, and the constituent area-averaged temperatures are defined by

$$\langle T_i \rangle = \frac{2}{R_1^2} \int_0^{R_1} T(r) r dr \quad \text{for the pellet}$$

$$= \frac{2}{R_2^2 - R_1^2} \int_{R_1}^{R_2} T(r) r dr \quad \text{for the clad} \tag{A2}$$

The fuel pin heat capacity weighted average temperature $\langle T \rangle$ is defined by Eq. (A1). R_1 is the pellet radius and $R_2 = R_1 + s$ is the cladding outer radius (s is the clad thickness). The gap width δ is ignored in the first of Eqs. (A2).

Simple energy balances yield the time dependence of the overall pin energy at time t

$$E - E_0 = q_0' \bar{f} t - \int_0^t h\xi (T_w - T_s) dt \tag{A3}$$

and the clad energy at time t

$$E_c - E_{c,0} = E_{f,0} - E_f + q_0'\bar{f}t - \int_0^t h\xi(T_w - T_s)dt \tag{A4}$$

and when combined with Eqs. (A1) and (A2) yields the pin area-averaged temperature

$$(\langle T\rangle - \langle T\rangle_0)\sum_{i=f,c}(A\rho c)_i = q_0'\bar{f}t - \int h\xi(T_w - T_s)dt \tag{A5}$$

and clad temperature

$$(A\rho c)_c(\langle T_c\rangle - \langle T_c\rangle_0) = (A\rho c)_f(\langle T_f\rangle_0 - \langle T_f\rangle) + q_0'\bar{f}t - \int_0^t h\xi(T_w - T_s)dt \tag{A6}$$

at time t. Here, q_0' denotes the linear heating rate, $\bar{f}$ denotes the time-average decay heat fraction, h denotes the convective heat transfer coefficient and ξ denotes the pin circumference. The subscripts c, f, s, and 0 denote, respectively, cladding, fuel pellet, coolant, and initial time.

The uniform fission power produces the familiar parabolic temperature distribution in the pellet, with the difference between area-averaged and surface temperatures being

$$\langle T_f\rangle - T_1 = \frac{q'''R_1^2}{8k_f} = \frac{q'}{8\pi k_j} \tag{A7}$$

Because the thicknesses of gas gap and clad are small, their temperature drops can be approximated by linear temperature drops

$$T_1 - T_2 \frac{q'}{2\pi h_{\text{gp}}(R_1 + \delta/2)} = \frac{q'}{8\pi k_f}\frac{4k_f}{h_{\text{gp}}(R_1 + \delta/2)} \quad \text{gas gap}$$

$$T_2 - T_w \frac{q'}{2\pi k_c}\frac{s}{(R_1 + \delta + s/2)} = \frac{q'}{8\pi k_f}\frac{4k_f}{k_c}\frac{s}{R_1 + \delta + s/2} \quad \text{clad} \tag{A8}$$

Subscripts 1, 2, and w denote, respectively, pellet surface, inner, and outer clad surface. The addition of Eqs. (A7) and (A8) gives the pellet area-averaged temperature

$$\langle T_f\rangle = T_w + \frac{C_f}{8\pi k_f}q' \tag{A9}$$

with the normalized thermal *series resistance* from the fuel pellet to the outer clad, taken relative to the resistance of the fuel being

$$C_f = 1 + \frac{4k_f}{h_{\text{gap}}(R_1 + \delta/2)} + \frac{4k_f s}{k_c(R_1 + \delta + s/2)} \tag{A10}$$

Note that electrically heated elements are represented by simply changing the "1" to a "2" when the wire is thin relative to the thickness of the ceramic wire. Similarly, the cladding area-averaged temperature, the mean between T_2 and T_w, is

$$\langle T_c\rangle = T_w + \frac{q'}{2\pi k_c}\frac{s}{R_1 + \delta + s/2} = T_w + \frac{C_c}{8\pi k_f}q' \tag{A11}$$

with the normalized thermal resistance of the cladding being

$$C_c = \frac{2k_f}{k_c}\frac{s}{R_1 + \delta + s/2} \tag{A12}$$

Substitution of Eqs. (A9) and (A11) into Eq. (A1) for $t=0$ yields

$$E_0 = T_{w,0}\sum_{i=f,c}(A\rho c)_i + \frac{q_0'}{8\pi k_f}[C_f(A\rho c)_f + C_c(A\rho c)_c] \tag{A13}$$

and for $t>0$

$$E = T_w\sum_{i=f,c}(A\rho c)_i + \frac{q_d'}{8\pi k_f}[C_f(A\rho c)_f + C_c(A\rho c)_c] \tag{A14}$$

Substituting Eqs. (A13) and (A14) into Eq. (A5), and solving for the clad surface temperature rise yields

$$T_w - T_{w,0} = \left[\frac{\bar{f}t}{\sum_{i=f,c}(A\rho c)_i} + \frac{(1-f)}{8\pi k_f}\frac{C_f(A\rho c)_f + C_c(A\rho c)}{\sum_{i=f,c}(A\rho c)_i}\right]q_0' \tag{A15}$$

where f is the decay heat fraction defined in Eq. (A5). Equation (A15) differs from that in Ref. [4] because they ignored the clad. Notice that the excess wall temperature is, at a given time t and with a given decay heat fraction $f(t)$, a linear function of the initial linear heating rate. The first term in Eq. (A15) is the contribution from decay heat, the second is from equalization of temperature in the pellet and the clad.

The average excess fuel-plus-clad temperature found from Eqs. (A1) and (A3) is

$$\langle T\rangle - T_{w,0} = \langle T\rangle_0 - T_{w,0} + \frac{q_0'\bar{f}t - \int_0^t h\xi(T_w - T_s)dt}{\sum_{i=f,c}(A\rho c)_i} \tag{A16}$$

From Eqs. (A13) and (A14), one finds for the initial average excess fuel-plus-clad temperature

$$\langle T\rangle_0 - T_{w,0} = \frac{q_0'}{8\pi k_f}\frac{(A\rho c)_f C_f + (A\rho c)_c C_c}{\sum_{i=c,f}(A\rho c)_i} \tag{A17}$$

where the pin mean temperature $\langle T\rangle_0$ is found from Eq. (A1) when $t=0$

$$\langle T\rangle_0 = \frac{(A\rho c)_f\langle T_f\rangle_0 + (A\rho c)_c\langle T_c\rangle_0}{[(A\rho c)_f + (A\rho c)_c]} \tag{A18}$$

The only assumption in Eq. (A17) is that the fission power is initially uniform in the pellet and that the thermophysical properties are functions only of average fuel and clad temperatures. Equation (A17) reduces Eq. (A15) to

$$T_w - T_{w,0} = \frac{\bar{f}tq_0'}{\sum_{i=f,c}(A\rho c)_i} + (1-f)(\langle T\rangle_0 - T_{w,0}) - \frac{\int_0^t h\xi(T_w - T_s)dt}{\sum_{i=f,c}(A\rho c)_i} \tag{A19}$$

Appendix B: Pin Response

If one defines the total thermal resistance, each between fuel and outer clad surface and clad and the outer clad surface by their un-normalized reciprocals of conductance

$$\frac{1}{\bar{K}_f} = \frac{1}{8\pi k_f} + \frac{1}{2\pi h_{\text{gp}}(R_1 + \delta/2)} + \frac{s}{2\pi k_c(R_1 + \delta + s/2)}$$

$$\frac{1}{\bar{K}_c} = \frac{s}{4\pi k_c(R_1 + \delta + s/2)} \tag{B1}$$

It should be noted that they are neither area- nor volume-averaged impedances and that they both involve system geometry, transport properties, and process characteristics (gap). Yet, the definitions allow the similarities between the fuel pellet and the

fuel pin response to be shown. The factor multiplying q_0' in Eq. (A17) can be written in terms of the thermal resistance, with the aid of Eq. (B1), as

$$\frac{1}{8\pi k_f}\frac{\sum_{i=f,c} C_i(A\rho c)_i}{\sum_{i=f,c}(A\rho c)_i} = \frac{C_{\text{pin}}}{8\pi k_f} = \frac{\sum_{i=f,c}\left(\frac{A\rho c}{\bar{K}}\right)_i}{\sum_{i=f,c}(A\rho c)_i} \equiv \frac{1}{\bar{K}_{\text{pin}}} \tag{B2}$$

The composite of fuel pellet, gas gap and clad is called the *effective* thermal conductivity of the pin. The derivation of the effective pin conductivity was possible only after the derivations culminating in Eq. (B2).

An *effective* (aggregate) void fraction-weighted thermal diffusivity can be obtained from Eq. (B2)

$$\frac{1}{\bar{K}_{\text{pin}}} = \frac{1}{\sum_{i=f,c}(A\rho c)_i}\frac{\bar{A}_{\text{pin}}}{\bar{A}_{\text{pin}}}\sum_{i=f,c}\frac{1}{K_i}(A\rho c)_i = \frac{1}{\sum_{i=f,c}(\alpha\rho c)_i}\sum_{i=f,c}\left(\frac{\alpha\rho c}{\bar{K}}\right)_i$$

$$= \frac{1}{\langle\rho c\rangle_{\text{pin}}}\sum_{i=f,c}\left(\alpha\frac{\rho c}{\bar{K}}\right)_i \tag{B3}$$

where $\langle\rho c\rangle_{\text{pin}}$ is defined by

$$\frac{\langle\rho c\rangle_{\text{pin}}}{\bar{K}_{\text{pin}}} = \sum_{i=f,c}\left(\alpha\frac{\rho c}{\bar{K}}\right)_i \tag{B4}$$

where $\alpha = A_i/A_{\text{pin}}$ and $\bar{A}_{\text{pin}} = \pi(R_1+s)^2$ is the pin cross-sectional area.

Since $k/\rho c$ is the thermal diffusivity, let $\bar{\kappa} = \bar{K}/\rho c$ be the aggregate or *effective diffusivity*, realizing that the effective diffusivity is not a volume-averaged thermophysical property but a hybrid composite of thermophysical properties, transport properties, process parameters (gap conductance) and geometry. It depends on the mean temperatures of the pellet and of the clad. Equation (B20) gives the reciprocal of the pin effective diffusivity

$$\frac{1}{\bar{\kappa}_{\text{pin}}} = \sum_{i=f,c}\left(\frac{\alpha}{\bar{\kappa}_{\text{pin}}}\right) \tag{B5}$$

Equation (B2) reduces Eqs. (A9), (A11), and (A17) to

$$\langle T\rangle - T_w = \frac{q'}{\bar{K}_{\text{pin}}} \tag{B6}$$

$$\langle T_f\rangle - T_w = \frac{q'}{\bar{K}_f} \tag{B7}$$

$$\langle T_c\rangle - T_w = \frac{q'}{\bar{K}_c} \tag{B8}$$

References

[1] Wulff, W., Zuber, N., Rohatgi, U. S., and Catton, I., 2009, "Application of Fractional Scaling Analysis (FSA) to Loss of Coolant Accidents (LOCA): Methodology Development," Nucl. Eng. Des., **237**, pp. 1593–1607.

[2] Wulff, W., Zuber, N., Rohatgi, U. S., and Catton, I., 2009, "Application of Fractional Scaling Analysis to Loss of Coolant Accidents, System Level Scaling for System Depressurization," ASME J. Fluid Eng., **131**(8), p. 081402.

[3] Reeder, D. L., 1978, "LOFT System and Test Description (5.5-ft Nuclear Core 1 LOCES)," TREE-1208, EG&G Idaho, Inc., Jul., Report No. NUREG/CR-0247.

[4] Catton, I., Duffey, R. B., Shaw, R. A., Boyack, B. E., Griffith, P., Katsma, K. R., Lellouche, G. S., Levy, S., Rohatgi, U. S., Wilson, G. E., Wulff, W., and Zuber, N., 1990, "Quantifying Reactor Safety Margins Part 6: A Physically Based Method of Estimating PWR Large Break Loss of Coolant Accident PCT," Nucl. Eng. Des., **119**(1), pp. 109–117.

Improving the Spatial Resolution and Stability by Optimizing Compact Finite Differencing Templates

Stephen A. Jordan
Naval Undersea Warfare Center,
Newport, RI 02842
e-mail: stephen.jordan@navy.mil

Parameter optimization is an excellent path for easily raising the resolution efficiency of compact finite differencing schemes. Their low-resolution errors are attractive for resolving the fine-scale turbulent physics even in complex flow domains with difficult boundary conditions. Most schemes require optimizing closure stencils at and adjacent to the domain boundaries. But these constituents can potentially degrade the local resolution errors and destabilize the final solution scheme. Current practices optimize and analyze each participating stencil separately, which incorrectly quantifies their local resolution errors. The proposed process optimizes each participant simultaneously. The result is a composite template that owns consistent spatial resolution properties throughout the entire computational domain. Additionally, the optimization technique leads to templates that are numerically stable as understood by an eigenvalue analysis. Finally, the predictive accuracy of the optimized schemes are evaluated using four canonical test problems that involve resolving linear convection, nonlinear Burger wave, turbulence along a flat plate, and circular cylinder wall pressure. [DOI: 10.1115/1.4000576]

1 Introduction

A well-understood fact about compact finite differencing is their intrinsic ability to improve the spatial resolution of the associated fine-scale physics. Reaching extreme orders of numerical accuracy within the computational domain is essentially limitless (given enough solution points) that emerge spectral-like in view of sufficiently resolving the highest wavenumbers. Given the same number of computational points, the implicit compact stencils raise the formal accuracy by two-orders when compared to their explicit counterpart. Concurrently, they can easily accommodate a vast range of difficult boundary conditions. In most applications, nearly 75% of the resolvable wavenumbers own a resolution efficiency of at least 90%. This benefit lends compact finite differences to adequately address the spatial resolution demands of flow solution methodologies such as direct numerical simulation (DNS), large-eddy simulation (LES), and even detached eddy simulation (DES) in geometric topologies that are both simple and complex.

An alternate approach to quickly reaching a spectral-like compact stencil is parameter optimization. In this case, each coefficient of the stencil is not uniquely evaluated by a Taylor series expansion (TSE) of the participating constituents. Free parameters appear on the explicit and implicit sides of the compact stencil to simultaneously control the dispersive and dissipative errors, respectively. These parameters are evaluated using optimization techniques whose algebraic form appears through only partial application of TSE. Each free-parameter introduced into the stencil sacrifices one order of formal accuracy. For example, a three-point fourth-order compact stencil becomes second-order accurate when one free-parameter is introduced on the explicit and implicit sides.

Optimized compact finite differencing stencils are most commonly developed for approximating first-order derivatives. One of the first optimization strategies was presented by Lele [1] who attained a spectral-like resolution of a pentadiagonal system where a tenth-order stencil was reduced to fourth-order by introducing six free-parameters. Inasmuch as the stencil was symmetric, his technique need only optimize three. The process involved explicitly constraining the modified wavenumber of the new stencil to be spectral (exact) at three discrete points in Fourier space. Lele improved the spatial resolution efficiency of the fourth-order stencil by over 11% as compared to the tenth-order scheme. Recently, Kim [2] further optimized Lele's fourth-order compact stencil for aeroacoustic applications where the optimization procedure centered on minimizing the difference between the modified and exact wavenumber distributions in spectral space. Kim improved the resolution efficiency of the fourth-order three-parameter family to nearly 92%.

Besides optimizing the interior stencil, Lele [1] also tackled one-sided boundary stencils using an equivalent strategy. He focused on minimizing the well-known dissipative error inherent in all one-sided (or biased) standard schemes. In one example, the one-sided fourth-order expression of Rogallo and Moin [3] was condensed to a second-order stencil with near zero dissipative error while concurrently reducing dispersion. Jordan [4,5] also treated the compact stencil of Rogallo and Moin but his optimization strategy utilized a least-squares minimization technique of the spatial resolution errors by matching those of the one-sided boundary stencil to the adjacent interior scheme. He illustrated numerical superiority of the resultant template by lowering the predictive errors in solutions of the nonlinear Burgers equation as well as a two-dimensional acoustic scattering problem.

Tam and Webb [6] avoided the dispersive error of the one-sided finite difference expressions by introducing external ghost points that expanded the computational space to satisfy their optimized seven-point stencil everywhere within the physical domain. They implemented this tactic for building a dispersion-relation-preserving (DRP) scheme suitable for high-resolution aeroacoustic applications. The base stencil held seven points with adjustable coefficients whose final formal accuracy was dependent on the user demand for spectral-like resolution. Later, Ashcroft and Zhang [7] improved the DRP method by prefactoring the high-order compact stencils to reduce their size and boundary closure schemes while still maintaining low dispersive errors. Specifi-

Contributed by the Fluids Engineering Division of ASME for publication in the JOURNAL OF FLUIDS ENGINEERING. Manuscript received February 9, 2009; final manuscript received October 20, 2009; published online November 30, 2009. Editor: Joseph Katz.

cally, they prefactored central stencils into forward and backward upwind-biased forms whose coefficients were subsequently optimized to minimize the spatial resolution errors. Prefactorization was also utilized by Hixon and Turkel [8] and later by Hixon [9] for devising a MacCormack-type solution (MAC) technique. Their optimization technique reduced the stencil size of the high-order field operator such that only boundary point expressions were required for closure. Finally, Popescu et al. [10] recently extended the works of Tam and Webb [6] and Ashcroft and Zhang [7] to finite volume formulations tailored toward aeroacoustic problems.

Other notable works include the optimization strategy developed by Carpenter et al. [11] who operated on multiparameter fourth- and sixth-order families. They centered their success on achieving optimized templates that were asymptotically stable while simultaneously satisfying Gustafsson–Kreiss–Sundstrom (GKS) stability theory [12]. Asymptotic stability is guaranteed only when all roots from a stability analysis of the resultant compact operator lie inside the left-hand plane of the eigenvalue spectrum. Carpenter et al. [11] also treated explicit one-parameter first- and third-order boundary stencils after linked to fourth- and sixth-order operators, respectively. Demuren et al. [13]. showed the sixth-order template of Carpenter et al. [11] to possess strong pressure-velocity coupling for solving the general class of turbulent flow problems. Likewise, their sixth-order field scheme as coupled with optimized fifth-order stencils at the boundary and adjacent boundary points was tested by Cook and Riley [14] for resolving the fine-scale physics of a turbulent reactive plume. Finally, Sengupta et al. [15] developed a von Neumann spectral procedure to investigate and improve the stability characteristics of various compact finite differencing schemes including the destabilizing effects of the boundary closures.

The above citations illustrate the useful benefits one can expect by optimizing compact finite differencing schemes. But before their final forms can be accepted for practical purposes by the pertinent communities, the developers must properly treat the three intrinsic characteristics of accuracy, stability and resolution. While the analyses of optimized compact templates as reported by Carpenter et al. [11] provide suitable proof of their predictive accuracy and numerical stability, their true resolution errors still remain at large. Rather than treat the coupled form, the dispersive and dissipative errors are commonly given of the optimized stencils themselves. This approach gives a false impression of the expected gains in spatial resolution of the resultant composite template.

In the present paper, a simple process is proposed that optimizes compact finite differencing schemes for the purposes of attaining consistent low-resolution errors and guaranteed numerical stability. The process includes proper quantification of the dispersive and dissipative errors inherent in the final composite form. The numerical stability of these new optimized compact schemes is measured by eigenvalue analysis. We will assess a few of the previous compact templates in the above citations as well as new multiparameter stencils after optimized and joined together to form the final finite difference operator. Using several canonical test problems, we will also judge the predictive capability of these new compact schemes based on their spatial resolution of linear convection, the nonlinear Burger wave, flat plate turbulence, and the near-wall pressure of a circular cylinder.

2 Spatial Resolution

When attempting to properly resolve the smallest scales of the fluid motion, the advantages of optimizing the compact stencil become quite clear. This fact is easily quantified by differentiating the basic Fourier wave $q(x)=e^{ikx}$ and examining its approximation over the range of resolvable wavenumbers (up to the π wave). First, we will adopt the same nomenclature as Lele [1] where k and x are defined as the dimensionless wavenumbers and coordinates of the wave $q(x)$. The dependent variable k resides inside the periodic domain $[0,\pi]$. The exact differentiation of $q(x)$ with respect to x simply yields $q'(x)_{\text{ex}}=ikq(x)$, which ascribes spectral methods (except $k\neq\pi$). Conversely, finite difference schemes approximate the derivative as $q'(x)_{\text{fd}}=i\hat{k}q(x)$ where $\hat{k}$ becomes the modified wavenumber that may not necessarily be only real-valued. We will also implement the numerical limit of resolving efficiency $[e(\delta)]$ as coined by Lele [1] that depicts the fraction of *well-resolved* waves by a particular differencing stencil: $e(\delta)=(k\Delta)_{\delta}/\pi$. This measure essentially quantifies the dispersive and dissipative errors of the differencing stencil by evaluating the absolute disparity of the modified wavenumber from the exact one in spectral space. The variable δ is defined herein as the resolution expectancy that is specified by the user: $\delta_{r,i}=1-|1-(\hat{k}\Delta)_{r,i}/(k\Delta)_{\delta}|$ where $k\Delta$ denotes the dimensionless exact wavenumber and $\hat{k}=\hat{k}_r+i\hat{k}_i$, which are the real $(\hat{k}_r)$ and imaginary $(\hat{k}_i)$ components of the modified wavenumber. All resolution errors are less than the expectancy δ for resolved wavenumbers less than $(k\Delta)_{\delta}$.

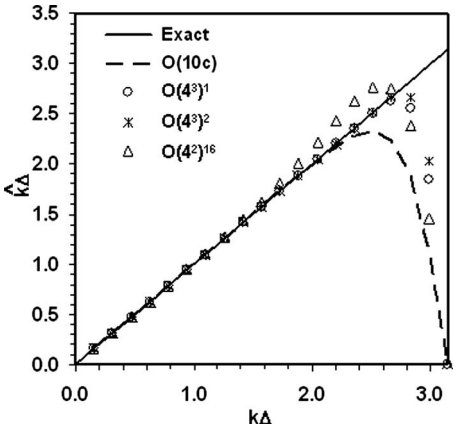

Fig. 1 Dispersive errors of the tenth-order standard compact stencil (10c) as compared to optimized two-parameter (4^2) and three-parameter (4^3) fourth-order families

2.1 Interior Operators. An illustrative example of stencil optimization to reduce the resolution errors is Lele's [1] operation on the compact fourth-order three-parameter family. The original stencil that approximates the first-order derivative at the ith point (q'_i) was a pentadiagonal tenth-order system that appeared as

$$b(q'_{i+2}+q'_{i-2})+a(q'_{i+1}+q'_{i-1})+q'_i = \alpha(q_{i+3}-q_{i-3})+\delta(q_{i+2}-q_{i-2})+\lambda(q_{i+1}-q_{i-1}) \quad (2.1)$$

where a TSE of each participant gives a unique set of coefficients defined as $b=1/20$, $a=1/2$, $\alpha=1/600$, $\delta=101/600$, and $\lambda=17/24$. This standard stencil marks 81% $[e(\delta_{90})\leq 0.81]$ of the resolvable wavenumbers as well-resolved when the resolution expectancy is 90% or better (see Fig. 1). If the off-diagonal coefficients (b, a, and α) are unconstrained for optimization, the stencil diminishes to a fourth-order three-parameter family with the additional expressions

$$3\lambda=2+b-8a+15\alpha \quad \text{and} \quad 12\delta=-1+4b+22a-48\alpha \quad (2.2a)$$

as derived from a partial application of TSE (only up to the fourth-order). By imposing three constraints on the modified wavenumber in the Fourier space ($\hat{k}_r^1=2.2$, $\hat{k}_r^2=2.3$, and $\hat{k}_r^3=2.4$), the free-parameters lock into the values [1]

$$b = 0.0896406, \quad a = 0.5771439, \quad \text{and} \quad \alpha = 0.006250408 \tag{2.2b}$$

that improves the spatial resolution efficiency to 90% $[e(\delta_{90}) \leq 0.90]$ as plotted in Fig. 1. By replacing these three discrete constraints with the minimization procedure by Kim [2], the resolution efficiency was raised to 92% $[e(\delta_{90}) \leq 0.915]$. As shown in Fig. 1, this seven-point stencil does indeed possess spectral-like characteristics.

A second look that further justifies parameter optimization of compact finite differences is treatment of the sixth-order Padé-type interior stencil. In this case, the solution system is tridiagonal (five-points) where $b = \alpha = 0$ in stencil (2.1). Ladeinde et al. [16] developed a minimization process similar to Kim [2] that evaluated the stencil coefficients as

$$a = 0.430816, \quad \lambda = 0.810272, \quad \text{and} \quad \delta = 0.060272 \tag{2.3}$$

where the resolution efficiency of this fourth-order interior operator was increased from 70% (standard scheme) to 88% for a 90% user expectancy $[e(\delta_{90}) \leq 0.88]$. This efficiency is nearly equivalent to the optimized fourth-order three-parameter stencil (see Fig. 1). Although the optimized scheme of Ladeinde et al. requires closure definitions at the boundary and adjacent interior points, its resolution efficiency is very attractive for solution strategies such as DNS and LES; especially when compared to the second-order explicit scheme $[e(\delta_{90}) \leq 0.25]$. Later, we will optimize several closure stencils as linked to this interior operator with the primary goal of maintaining consistent resolution errors throughout the entire computational domain.

2.2 Closure Stencils. Closure stencils are necessary for flow problems dealing with nonperiodic boundaries. Their optimized versions have appeared in both compact and explicit forms. Like the interior schemes, the stencil size, formal order and parameter optimization of the closure stencils is essentially limitless. The numerical molecules of the compact forms are always one-sided (or biased) that manifest high dissipative errors especially near the upper limit of resolvable wavenumbers. Moreover, these stencils must be no lower than one order in formal accuracy compared to the adjacent interior scheme. This requirement is necessary to preserve the predictive accuracy of the field operator [11,17,18]. One of the first compact versions came from Lele [1] who optimized a second-order two-parameter family using the same process of invoking parametric constraints in wavenumber space. The stencil approximates the first-order derivative at the boundary (q_1') as

$$aq_2' + q_1' = \alpha q_4 + \delta q_3 + \lambda q_2 + \beta q_1 \tag{2.4a}$$

where the coefficients (a, α) are considered as free-parameters. The quantities (q_i) are the explicit values given at the boundary and adjacent interior points. With focus on minimizing the dissipative error, Lele optimized this stencil to give the free-parameter values $a = 4$ and $\alpha = -0.5$ along with the expressions

$$\delta = \frac{-1 + a - 6\alpha}{2}, \quad \lambda = 2 + 3\alpha, \quad \beta = \frac{-3 - a - 2\alpha}{2} \tag{2.4b}$$

for the remaining coefficients. Although this optimized stencil owns attractive resolution properties by itself $[e(\delta_{90}) \leq 0.55]$, the actual dissipative and dispersive errors become quite unacceptable when coupled with a standard fourth-order Padé-type field scheme [5]. Notably, this optimized stencil will not preserve fourth-order accuracy at computational points near the boundary.

To remedy this deficit, we can easily increase the stencil size to realize higher accuracy at the boundary. For example, a fourth-order two-parameter (a, η) family has the form

$$aq_2' + q_1' = \eta q_6 + \xi q_5 + \alpha q_4 + \delta q_3 + \lambda q_2 + \beta q_1 \tag{2.5a}$$

with the expressions

$$\xi = \frac{-3 + a - 60\eta}{12}, \quad \alpha = \frac{8 - 3a + 60\eta}{6}, \quad \delta = \frac{-6 + 3a - 20\eta}{2}$$
$$\lambda = \frac{24 - 5a + 30\eta}{6}, \quad \beta = -\frac{25 + 3a + 12\eta}{12} \tag{2.5b}$$

for the remaining coefficients after applying TSE up to the fourth-order. According to Carpenter et al. [11], this stencil permits a field accuracy up to the fifth-order.

But when approximating the field derivatives by compact operators such as an upwind fifth-order or Padé's sixth-order or an optimized two-parameter fourth-order family, additional stencils are necessary at the adjacent boundary points to finalize the compact system. A suitable five-point stencil for approximating the adjacent boundary point derivative (q_2') that owns truncation errors up to the sixth-order is

$$aq_3' + q_2' + cq_1' = \alpha q_5 + \delta q_4 + \lambda q_3 + \beta q_2 + \gamma q_1 \tag{2.6a}$$

where the bias exists only on the explicit side. If employing TSE only up to the fourth-order and introducing the two free-parameters (a, α), one each on the implicit and explicit sides of the stencil, the expressions

$$c = \frac{1 - a - 12\alpha}{3}, \quad \delta = \frac{-1 + 4a - 96\alpha}{18}, \quad \lambda = \frac{1 + 2a + 24\alpha}{2}$$
$$\beta = \frac{1 - 4a - 32\alpha}{2}, \quad \gamma = \frac{-17 + 14a + 150\alpha}{18} \tag{2.6b}$$

arise for evaluating the remaining coefficients. Previous optimization strategies can generate appealing resolution characteristics of the compact stencil (2.6*a*) as well as the boundary expression (2.5*a*) by minimizing their dissipative errors. But observing the merits of these optimized families separately is actually meaningless because their individual resolution errors are not preserved once coupled together with the interior operator to form the composite template. In fact, the degraded spatial resolution errors of the closure stencils still permeate into the interior such that the expected resolving efficiency is not recovered until well beyond the boundary. In the next section, we will illustrate this deficiency and offer an alternate optimization procedure.

3 Optimization Strategy

The impetus for devising an optimization strategy of the free-parameters that are introduced into compact finite differencing stencils is the successful and substantial reduction in their spatial resolution errors. Several strategies are presently available but the operation treats the individual stencils rather than the single composite form. In particular, the improved spatial resolution characteristics are assessed only of the optimized stencils themselves. But one can not expect to retain the separate improvements of each stencil once they are joined together to form the final template. Consequently, these strategies lead to resolution characteristics of each optimized stencil that are largely dissimilar in the overall template. The resolution errors of the coupled scheme increase at the boundary and adjacent points and propagate well into the interior domain. Extent of this degradation depends on the participating stencil sizes, optimization, and formal orders. Herein, we develop a simple process that optimizes the composite template, ensures stability, and properly quantifies the spatial resolution properties. This process is applicable for all coupled systems but its ingredients will be restricted to mixing the two-parameter families at the boundary and adjacent interior points as given by the stencils (2.5*a*) and (2.6*a*), respectively. Comparisons will be made to previous templates to demonstrate the present optimization strategy as a favorable alternative for minimizing the resolution errors at and near the domain boundaries. Concurrently, we wish to approach consistent spatial resolution characteristics at all points (or cells) inside the computational space.

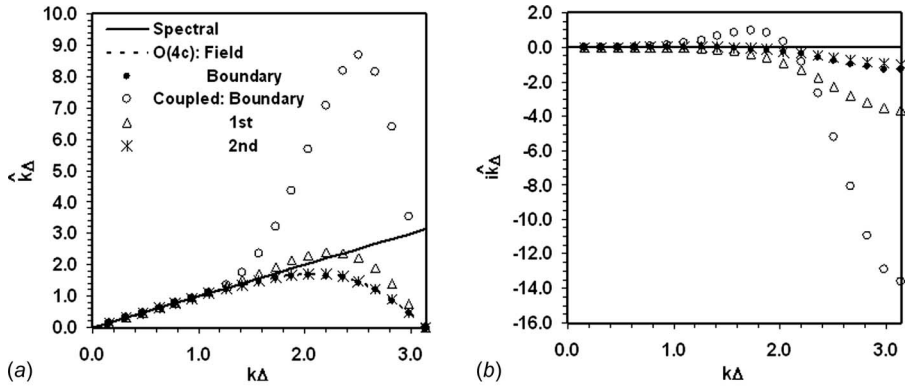

Fig. 2 Resolution errors of the fourth-order standard boundary stencil as coupled with a fourth-order Padé scheme: template notation 4-4-4. (*a*) Dispersive and (*b*) dissipative.

3.1 Spatial Resolution Properties. A composite template is defined herein as an equation system of at least two linked compact finite differencing stencils that approximate the first-order derivative along a single line inside the computational domain. Using the notations $[\cdot]$ and $\{\cdot\}$ to denote matrix and vector equation systems, the composite template can be represented as

$$[H]\{q'_{\text{fd}}\} = \frac{1}{\Delta}[G]\{q_{\text{fd}}\} \tag{3.1}$$

where $[H]$ is a $N \times N$ matrix that depicts the implicit coefficients of the approximated derivative $\{q'_{\text{fd}}\}$. The matrix $[G]$ in Eq. (3.1) constitutes the corresponding explicit elements. The integer $[N]$ denotes the total number of nodal points along a particular line. Reformulating this compact template in the Fourier space (via the substitution $q'(x)_{\text{fd}} = i\hat{k}q(x)$) becomes

$$i[P]\{\hat{k}\Delta\} = [S]\{k\Delta\} \tag{3.2}$$

where the matrices $[P]$ and $[S]$ house the spectral quantities. Each point along the line holds a unique modified wavenumber spectrum over an equivalent range of resolvable scales ($0 \le k\Delta \le \pi$).

Disparities between the separate stencil resolution errors and the composite scheme by solving Eq. (3.2) are illustrated in Fig. 2 for the example template 4-4-4. This approximation links standard fourth-order one-sided boundary stencils (4- and -4; stencil (2.4*a*) with no free-parameters) with a Padé interior scheme of similar accuracy (-4-). The matrix in Eq. (3.2) becomes

$$P(k\Delta) = \begin{bmatrix} 1 & 3e^{ik\Delta} & & & & & & \\ \frac{1}{4}e^{-ik\Delta} & 1 & \frac{1}{4}e^{ik\Delta} & & & & & \\ & \frac{1}{4}e^{-ik\Delta} & 1 & \frac{1}{4}e^{ik\Delta} & & & & \\ & & . & . & . & & & \\ & & & \frac{1}{4}e^{-ik\Delta} & 1 & \frac{1}{4}e^{ik\Delta} & & \\ & & & & \frac{1}{4}e^{-ik\Delta} & 1 & \frac{1}{4}e^{ik\Delta} & \\ & & & & & 3e^{-ik\Delta} & 1 & \end{bmatrix} \tag{3.3a}$$

with the corresponding explicit definitions at the forward boundary (s_{1+}) and interior (s_{diagonal}) points.

$$s_{1+} = \tfrac{1}{6}(-e^{3ik\Delta} + 9e^{2ik\Delta} + 9e^{ik\Delta} - 17) \tag{3.3b}$$

$$s_{\text{diagonal}} = \tfrac{3}{4}(e^{ik\Delta} - e^{-ik\Delta}) \tag{3.3c}$$

The solution of system (3.3) for $N=100$ computational points reveals that although this fourth-order closure stencil suggests favorable spatial resolution at the boundary, the actual dispersive, and the dissipative errors degrade to unacceptable levels for high efficiency templates. In particular, the resolution efficiency in terms of the dispersive error drops to 40% $[e_r(\delta_{90}) \le 0.40]$ and the dissipative error still damps nearly 1/2 of the resolvable wavenumbers at two computational points off the boundary $[e_i(\delta_{90}) \le 0.54]$. By substituting a third-order stencil at the boundary relaxes propagation of the boundary dissipative error $[e_i(\delta_{90}) \le 0.65]$ but this improvement costs a substantial degradation of the dispersive error efficiency $[e_r(\delta_{90}) \le 0.27]$. Thus, an optimization technique is suggested to remedy the poor resolution properties of this example template.

3.2 Boundary Stencil. Boundary stencils are always one-sided that require optimized free-parameters to control growth of the dispersive and dissipative errors. Herein, we propose reducing those errors by attempting to closely match the resolution properties of the adjacent interior scheme. This strategy imposes the general constraint $\hat{k}^b_{r,i} = \hat{k}^f_{r,i}$ on the boundary modified wavenumber ($\hat{k}^b_{r,i}$) over all resolvable scales ($0 \le k\Delta \le \pi$) in the spectral space. The modified wavenumber of the field (or interior) stencil is given the convenient notation ($\hat{k}^f_{r,i}$).

The fourth-order two-parameter (a, η) boundary stencil in Eq. (2.5*a*) has a complex form for the modified wavenumber in spectral space as follows:

$$i(\hat{k}\Delta)^b(1 + ae^{ik\Delta}) = \eta e^{5ik\Delta} + \xi e^{4ik\Delta} + \alpha e^{3ik\Delta} + \delta e^{24ik\Delta} + \lambda e^{ik\Delta} + \beta \tag{3.4}$$

By substituting the coefficient definitions (2.5*b*) and subsequently imposing the wavenumber constraint, two unique expressions arise that permit matching the boundary spatial resolution errors to the respective interior characteristics by appropriately adjusting the free-parameters. After expanding each term and collecting the respective real and imaginary components, the resultant expressions become (not completely simplified)

$$\begin{aligned}(&-12\hat{k}_r \sin k\Delta - 12\hat{k}_i \cos k\Delta - \cos 4k\Delta + 6\cos 3k\Delta - 18\cos 2k\Delta \\ &+ 10\cos k\Delta + 3)a \\ &= 12\hat{k}_i - 3\cos(4k\Delta) + 16\cos(3k\Delta) - 36\cos(2k\Delta) + 48\cos k\Delta \\ &- 25 + (12\cos(5k\Delta) - 60\cos(4k\Delta) + 120\cos(3k\Delta) \\ &- 120\cos(2k\Delta) + 60\cos k\Delta - 12)\eta \end{aligned} \tag{3.5a}$$

$$(12\hat{k}_r \cos k\Delta - 12\hat{k}_i \sin k\Delta - \sin 4k\Delta + 6 \sin 3k\Delta - 18 \sin 2k\Delta + 10 \sin k\Delta)a$$
$$= -12\hat{k}_r - 3 \sin(4k\Delta) + 16 \sin(3k\Delta) - 36 \sin(2k\Delta) + 48 \sin k\Delta + (12 \sin(5k\Delta) - 60 \sin(4k\Delta) + 120 \sin(3k\Delta) - 120 \sin(2k\Delta) + 60 \sin k\Delta)\eta \quad (3.5b)$$

where $(\hat{k}_{r,i})$ is the modified wavenumber of the interior operator.

3.3 Adjacent Boundary Stencil. First-point stencils are necessary for closure of field operators owning five-point molecules. The optimized variety is most often asymmetric, but only on the explicit side. This bias introduces dissipative errors that join with those introduced by the boundary stencil to further deteriorate the resolution character of the optimized field operator. Together, their standard versions permeate into the interior domain well beyond propagation of the boundary stencil itself. Like the boundary stencils, free-parameters are optimized in the adjacent scheme, but common practice examines only their local effect on reducing the resolution errors. In the following analyses, that approach will prove to be futile once the coupled version is properly assessed by the definition in Eq. (3.2).

Targeting fourth-order accuracy, we will employ the two-parameter (a, α) stencil in Eq. (2.6*a*). Its complex form for the modified wavenumber is

$$i(\hat{k}\Delta)^1(ae^{ik\Delta} + 1 + ce^{-ik\Delta}) = \alpha e^{3ik\Delta} + \delta e^{2ik\Delta} + \lambda e^{ik\Delta} + \beta + \gamma e^{-ik\Delta} \quad (3.6)$$

where the quantity $(\hat{k}\Delta)^1$ denotes the scaled modified wavenumber at the adjacent boundary point. After substituting the constraint $\hat{k}^1_{r,i} = \hat{k}^f_{r,i}$ and the explicit definitions for the remaining coefficients in Eq. (2.6*b*), the expressions

$$(-6\hat{k}_r \sin k\Delta - 12\hat{k}_i \cos k\Delta + 2 \cos 2k\Delta + 16 \cos k\Delta - 18)a$$
$$= +9\hat{k}_i + 3\hat{k}_i \cos k\Delta - 3\hat{k}_r \sin k\Delta + \tfrac{1}{2}(9 - \cos 2k\Delta) - 4 \cos k\Delta + (-36\hat{k}_i \cos k\Delta + 36\hat{k}_r \sin k\Delta - 144 + 9 \cos 3k\Delta - 48 \cos 2k\Delta + 183 \cos k\Delta)\alpha \quad (3.7a)$$

and

$$(12\hat{k}_r \cos k\Delta - 6\hat{k}_i \sin k\Delta + 2 \sin 2k\Delta + 16 \sin k\Delta)a$$
$$= -9\hat{k}_r - 3\hat{k}_r \cos k\Delta + 3\hat{k}_i \sin k\Delta - \tfrac{1}{2}\sin 2k\Delta + 13 \sin k\Delta + (36\hat{k}_r \cos k\Delta + 36\hat{k}_i \sin k\Delta + 9 \sin 3k\Delta - 48 \sin 2k\Delta + 33 \sin k\Delta)\alpha \quad (3.7b)$$

arise for evaluating the two free-parameters (a, α) once $\hat{k}_{r,i}$ is defined by the interior operator.

3.4 Parameter Evaluation. Again, evaluating the free-parameters of each compact stencil individually is a useless attempt to minimize the template resolution errors. The strategy must treat each parameter simultaneously to gain a realistic benefit. Like previous efforts, their evaluation should take place in wavenumber space. But picking discrete samples of the wavenumber profile is completely subjective and obviously a poor tactic towards representing the full spectrum. Given only two parameters per closing stencil, the compact system is highly overdeterminant.

A suitable alternative is a least-squares minimization of the resolution error. Unlike the approach of Kim [2], the present strategy minimizes the resolution errors $(\delta^c_{r,i})$ as defined by the difference between the scaled modified wavenumbers of the closure $(\hat{k}\Delta)^c_{r,i}$ and field $(\hat{k}\Delta)^f_{r,i}$ stencils: $\delta^c_{r,i} = 1 - |1 - (\hat{k}\Delta)^c_{r,i}/(\hat{k}\Delta)^f_{r,i}|$. This approach extends the original development by Jordan [4]. The strategy specifically targets consistent resolution characteristics over the whole computational domain, which is more readily attainable as oppose to optimizing towards the exact wavenumber [2] (zero error). This latter tactic is clearly unachievable for proposing a pragmatic optimization strategy.

Working with the expressions (3.5*a*) and (3.5*b*) (or similarly Eqs. (3.7*a*) and (3.7*b*) for parameters (a, α)), we can write the vector solutions

$$q_i a = b_i + r_i \eta \quad \text{and} \quad v_i a = d_i + t_i \eta \quad (3.8)$$

where examples of the quantity q_i at the boundary and adjacent points are

$$q_i = -12\hat{k}^i_r \sin(k\Delta)_i - 12\hat{k}^i_i \cos(k\Delta)_i - \cos 4(k\Delta)_i + 6 \cos 3(k\Delta)_i - 18 \cos 2(k\Delta)_i + 10 \cos(k\Delta)_i + 3 \quad \text{(boundary)} \quad (3.9a)$$

$$q_i = -6\hat{k}^i_r \sin(k\Delta)_i - 12\hat{k}^i_i \cos(k\Delta)_i + 2 \cos 2(k\Delta)_i + 16 \cos(k\Delta)_i - 18 \quad \text{(adjacent)} \quad (3.9b)$$

The quantity $(k\Delta)_i$ defines the number of discrete wavenumbers needed to replicate the spectrum $(0 \le (k\Delta)_i \le \pi)$ and $\hat{k}^i_{r,i}$ is the corresponding modified wavenumber of the adjacent interior operator. Combining the vector solutions in Eq. (3.8) as unique formulations for each scalar (a and η) gives

$$V_i a = R_i \quad \text{and} \quad T_i \eta = Q_i \quad (3.10a)$$

where the coefficient and source vectors become

$$V_i = q_i t_i - r_i v_i, \quad R_i = b_i t_i - d_i r_i, \quad T_i = r_i v_i - q_i t_i, \quad \text{and}$$
$$Q_i = v_i b_i - d_i q_i \quad (3.10b)$$

According to the least-squares minimizing approach for an overdeterminate system, we formulate the square of the errors E and F (summation implied) as

$$E = (R_i - V_i a)^2 \quad \text{and} \quad F = (Q_i - T_i \eta)^2 \quad (3.11)$$

that leads to the scalar evaluations ($\partial E/\partial a = 0$ and $\partial F/\partial \eta = 0$) as

$$a = (R_i V_i)/V_i^2 \quad \text{and} \quad \eta = -(Q_i T_i)/T_i^2 \quad (3.12)$$

Notice that both scalars are unique because the denominator and numerator of each formulation can only vanish simultaneously. After substituting a series of discrete wavenumbers $0 \le (k\Delta)_i \le \pi$ to evaluate the free-parameters (a, η), the expressions in Eq. (2.5*b*) are subsequently utilized to acquire the remaining coefficients (ξ, α, δ, λ, and β) in the fourth-order boundary stencil.

The evaluation of the free-parameters and accompanying coefficients for various optimized templates are listed in Table 1 (100 discrete wavenumbers). The example template 4-4-4 is also listed for comparison and clarification of the coefficient grid point locations as reference to the ith point. The sample notation -4^2- denotes a two-parameter fourth-order constituent of the respective template. Each template comprises optimized adjacent and/or boundary closing stencils as coupled with either standard or optimized field schemes. They require only a tridiagonal solver to examine their numerical properties. Good examples for comparing the resolution errors of the separate stencils to their corresponding templates are the fully and partially optimized schemes $4^2-4^2-4^2-4^2-4^2$ and $4^2-4^2-6-4^2-4^2$, respectively. These examples are illustrated in Fig. 3 with focus only on their relative dispersive errors.

Template $4^2-4^2-4^2-4^2-4^2$ (Fig. 3(*a*)) indicates a clear disparity between the coupled and decoupled versions. The most obvious difference occurs at the second computational point off the boundary. While the optimized stencil itself resembles the dispersive error of the field scheme, the actual modified wavenumber profile is similar to a Padé-type fourth-order approximation. As noted earlier, reduction in the dispersive error toward the field

Table 1 Coefficients of various optimized compact templates

Template	Stencil	$a(i+1)$	$c(i-1)$	$\eta(i+5)$	$\xi(i+4)$	$\alpha(i+3)$	$\delta(i+2)$	$\lambda(i+1)$	$\beta(i)$	$\gamma(i-1)$
4-4-4	Boundary	3.0	-	-	-	−0.166667	1.5	1.5	-2.833333	-
3^2-4-3^2	Boundary	3.5	-	-	0.048493	−0.443972	2.290958	1.056028	-2.951507	-
4^2-4-4^2	Boundary	3.649750	-	−0.005330	0.080796	−0.544842	2.527925	0.931892	-2.990441	-
$4^2-4-5-4-4^2$	Boundary	3.627836	-	−0.011855	0.111597	−0.599139	2.560308	0.917526	-2.978437	-
$4^2-4^2-4^2-4^2-4^2$	Boundary	3.861746	-	0.000912	0.067252	−0.588419	2.783498	0.786439	-3.049682	-
	Adjacent	0.404153	−0.080660	-	-	0.069819	−0.338112	1.741981	-1.425410	-0.048278
$4^2-4^2-5-4^2-4^2$	Boundary	−0.054967	-	0.438545	−2.447307	5.746269	−7.467903	6.238532	-2.508137	-
	Adjacent	0.024444	0.110468	-	-	0.053679	−0.336413	1.168595	-0.407756	-0.478105
$4^2-4^2-6-4^2-4^2$	Boundary	3.652111	-	0.000807	0.050308	−0.484652	2.470097	0.960609	-2.997168	-
	Adjacent	0.178418	0.109101	-	-	0.041190	−0.235587	1.172698	-0.515876	-0.462425

scheme resolution is only a gradual transition. For example, the resolution efficiency at the fourth point $[e_r(\delta_{90}) \leq 0.75]$ is still 15% below the interior optimum $[e_r(\delta_{90}) \leq 0.88]$. Likewise, the dissipative error behaves in a similar manner.

A simple correction that speeds transition toward the interior resolution is to relax the corresponding efficiency. Template $4^2-4^2-6-4^2-4^2$ (Fig. 3(*b*)) is an illustrative example where the standard six-order scheme well-resolves 70% of the resolvable waves 90% or better $[e(\delta_{90}) \leq 0.70]$. Interestingly, the resolution errors of this template exceed those of its constituents. For instance, the composite template owns a resolution efficiency $e_r(\delta_{90}) \leq 0.69$ at the adjacent boundary point as compared to the lower stencil value $e_r(\delta_{90}) \leq 0.62$. Clearly, the most attractive feature of this template is the near consistent spatial resolution at all computational points within the domain. This achieved characteristic is especially satisfying for high-resolution flow strategies such as DNS, LES, and DES.

4 Numerical Stability

Before testing the optimized templates in Table 1 for predictive accuracy, evidence must guarantee their intrinsic numerical stability. The customary method is a modal analysis. This method involves reformulating the linear convection equation into a system of ordinary differential equations (ODE) where the normal modes give a range of eigenvalues that denote the potential for unstable solutions. Accordingly, we first premultiplied the linear convection equation $q_t = -cq_x$ by the implicit coefficient matrix $[H]$. The matrix-matrix system in Eq. (3.1) is then substituted to give a similar ODE system as

$$[H]\{q_{\text{fd}}\}_t = -\frac{c}{\Delta}[G]\{q_{\text{fd}}\} \tag{4.1}$$

We find the normal modes of the ODE system by substituting the relationship $\{q_{\text{fd}}\} = e^{\omega_j t}\hat{q}$ where the quantity ω_j is a set of the complex eigenvalues with $\{\hat{q}\}$ as their respective eigenvectors. The subscript (j) denotes the number of computational points along a single line within the flow domain. The final system appears as

$$-\hat{\omega}_j[H]\{\hat{q}\} = [G]\{\hat{q}\} \tag{4.2}$$

where $\hat{\omega}_j$ are the dimensionless eigenvalues defined by $\hat{\omega}_j = \omega_j \Delta / c$. Each template owns a unique set of eigenvalues that depend on the number of computational points. All conjugate pairs of $\hat{\omega}_j$ must lie inside the left-half plane of the eigenvalue spectrum to guarantee numerical stability. We note that solving Eq. (4.2) requires direct treatment of the closing stencils because knowing q_j at the boundary makes its derivative redundant. Thus, the optimized boundary and adjacent stencils are combined to eliminate the first row in the final form of matrices $[H]$ and $[G]$.

Conjugate pairs of eigenvalues for both the standard (4-4-4) and optimized fourth-order templates 4^2-4-4^2 and 4^3-4-4^3 are plotted in Fig. 4. These values were determined using the MATLAB tool and 49 computational points. The three-parameter boundary family was optimized using the minimization procedure by Kim [2]. As noted by Carpenter et al. [11], the standard template 4-4-4 is inherently unstable as given by the eigenvalues appearing in the right-half plane of the spectrum. Stabilizing this template is possible through parameter optimization, but the procedure by Kim [2] improves its numerical stability to only a neutral state. Optimizing two free-parameters according to the present procedure provides real elements that fall strictly within the left-half plane of

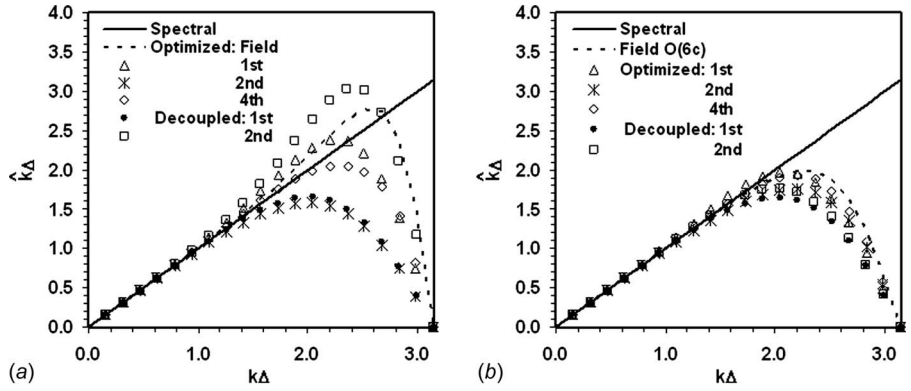

Fig. 3 Dispersive errors of optimized templates: notation -4^2- signifies fourth-order two-parameter family. (*a*) Template $4^2-4^2-4^2-4^2-4^2$ and (*b*) template $4^2-4^2-6-4^2-4^2$.

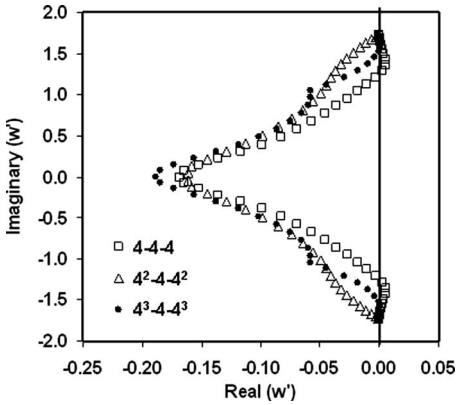

Fig. 4 Stability characteristics of the fourth-order standard (4-4-4) and optimized templates 4^2-4-4^2 and 4^3-4-4^3

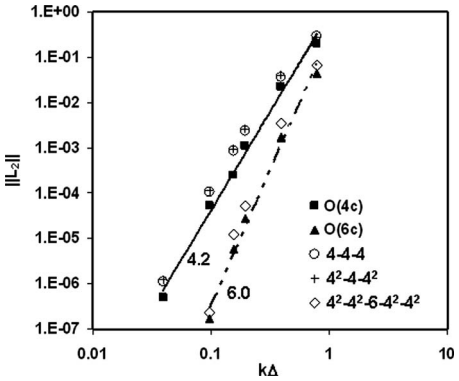

Fig. 6 Solutions of linear convection using fourth-order (4c) and sixth-order (6c) interior schemes as well as standard (4-4-4) and two optimized templates

the eigenvalue spectrum. This outcome indicates that the 4^2-4-4^2 template is asymptotically stable $|e^{\omega_j t}| \leq 1$ for all *CFL* values below the stability limit.

Strict stability of spectral-like templates is not guaranteed as illustrated in Fig. 5(*a*). These schemes were optimized by either the present technique or Kim's minimization method where each template achieved only neutral stability. The present strategy, in particular, introduces a substantial shift in the eigenvalue profile that suggests large differences among their relative rates of decay. But inserting the highly stable standard fifth-order compact stencil at the third interior point reestablishes strict stability as indicated in Fig. 5(*b*). Like the boundary and adjacent boundary stencils, this new stencil is asymmetric only on the explicit side and shares similar spatial resolution properties. In fact, the dispersive and dissipative error profiles of both new templates $4^2-4^2-5-6-5-4^2-4^2$ and $4^2-4^2-5-4^2-5-4^2-4^2$ displayed negligible change after inserting the fifth-order stencil. In the next section, we will use the former template for resolving the turbulent characteristics within the boundary layer of a flat plate as well as accurately predict the statistical fluctuating and mean pressures along a circular cylinder.

5 Applications

Employing optimized compact finite differencing templates for flow computations lies principally in the strong spatial resolution properties that contribute toward improving their overall predictive accuracy. In the following section, we will illustrate this predictive capability by selecting four benchmark problems that entail linear convection, the nonlinear viscous Burger equation, and LES results of a turbulent flat plate and flow past a circular cylinder. We intend to keep the interior operator manageably small (up to five-points) that demands boundary and adjacent boundary stencils to close the composite system. The interior operators are standard fourth-order (4c), fifth-order (5c), and sixth-order (6c) along with an optimized fourth-order (4^2) scheme. Coefficients for the optimized templates are listed in Table 1.

5.1 Linear Convection. The solutions of a propagating linear wave provide an initial measure of the predictive accuracy of the present optimized templates. The wave advances according to the one-dimensional equation

$$u_t + cu_x = 0 \tag{5.1}$$

with constant wave speed c. Initializing the wave as

$$u(x,t=0) = \tfrac{1}{2}e^{-\ln 2(x/n)^2} \tag{5.2a}$$

generates the exact wave for times $t \geq 0$

$$u(x,t) = \tfrac{1}{2}e^{-\ln 2(x'/n)^2} \tag{5.2b}$$

The local coordinate (x') is defined $x' = x - x_0 - t$ with x_0 being the origin. Given uniform grid spacing $\Delta = \Delta x$, the ratio Δ/n gauges the spatial resolution. A fictitious wall boundary is placed on the right side of the computational domain with spatial limits $-50 \leq x \leq 200$ where the predictive errors of the templates are assessed as compared to the exact wave.

Numerical solutions of the propagating linear wave using both standard and optimized templates over six grids are shown in Fig. 6. This figure also shows the convergence rates, as measured using the L_2 norm, of the fourth- and sixth-order interior operators ((4c) and (6c)) at the fifth point off the boundary. Five points (four

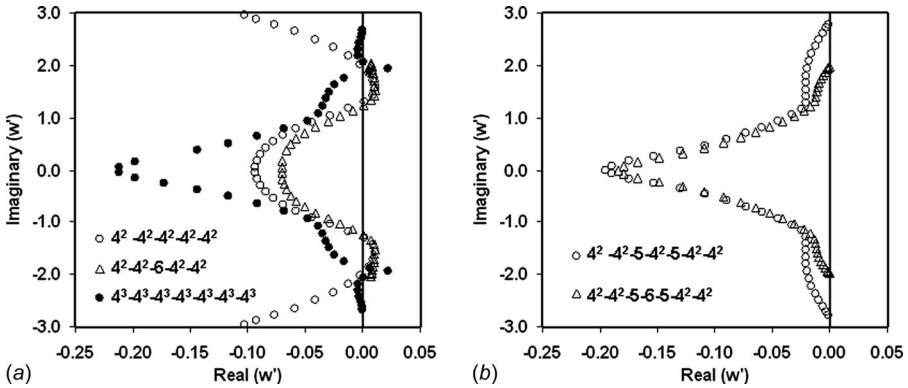

Fig. 5 Stability characteristics of various optimized templates: three-parameter fourth-order template $(4^3-4^3-4^3-4^3-4^3-4^3-4^3)^2$. (*a*) Neutrally stable and (*b*) strictly stable.

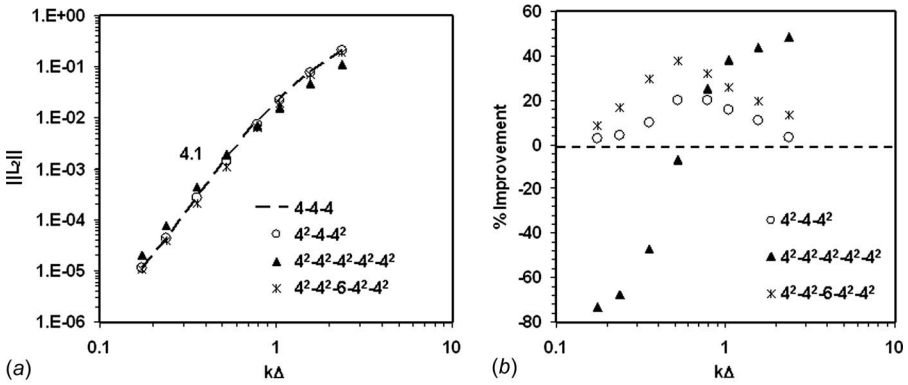

Fig. 7 Solution of burgers nonlinear viscous equation using standard fourth-order scheme (4-4-4) and various optimized templates. (*a*) Error norm and (*b*) percent improvement.

interior and one boundary) are used to quantify the L_2 norm of the composite templates. Each template was time-advanced by the MAC method with $CFL=0.001$. As predicted, the linear slopes in log-log space match the anticipated convergence rates for each interior scheme. Moreover, utilizing the optimized templates essentially maintains the same convergence rate as the field accuracy. This result should be expected because the predictive errors of optimized templates holding dissimilar resolution characteristics are only mildly affected by the linear wave solutions. Resolving propagation of the linear wave is a leading indicator of numerical convergence in view of verifying the template formal order but the benefits of the optimization strategy toward lowest resolution errors will not be readily apparent in the local predictive errors. The solutions of the nonlinear Burgers equation are better suited for this purpose.

5.2 Nonlinear Viscous Burgers Equation. This application also involves inserting a transparent fictitious wall far downstream from the initial wave position. Standard, partially optimized and fully optimized templates are evaluated in this particular problem. Specifically, the predictive accuracy of each composite template is assessed once the advancing wave is centered over the computational point adjacent to the fictitious wall. Inasmuch as each template owns unique resolution errors far into the interior, five points (four interior and one boundary) are used to quantify their predictive accuracy as compared to the exact solution. As before, all templates were time-advanced by the second-order MAC method with a small *CFL* value (0.001) to isolate the spatial resolution effects from any temporal errors. The predictive error of each template is gauged in terms of the L_2 norm. The grid spacing Δx was uniform in each simulation with the fictitious wall placed on the right side boundary of the domain $-100 \le x \le 100$.

Burgers nonlinear viscous equation for the velocity (u) is

$$u_t + uu_x = \mu u_{xx} \tag{5.3}$$

with the exact advancing wave solution at time (t) and position (x) as

$$u(x,t) = 1 - \tanh\left(\frac{x'}{2\mu}\right) \tag{5.4}$$

As before, the local coordinate is $x' = x - x_0 - t$, where $x' = 0$ at $t = 0$. With concentration on the nonlinear term, the exact form of the pseudoviscous term μu_{xx} was used in the computations.

$$\mu u_{xx} = \frac{1}{2\mu}\text{sech}^2(v')\tanh(v') \tag{5.5}$$

where $v' = x'/2\mu$.

Grid convergence of Burgers equation using the fourth-order template (4-4-4) and the two composite versions 4^2-4-4^2 and $4^2-4^2-4^2-4^2-4^2$ along with template $4^2-4^2-6-4^2-4^2$ are displayed in Fig. 7(*a*). Figure 7(*b*) shows the percent improvement in predictive accuracy by optimizing the base template 4-4-4 as well as raising the field scheme by two-orders. The convergence rate (4.1) was evaluated for the 4-4-4 template using the linear portion of the curve ($k\Delta \le 1.0$). Apart from the fully optimized template $4^2-4^2-4^2-4^2-4^2$, the L_2 norms over the coarsest grids are nearly indistinguishable with nonlinear convergence rates. This behavior is an artifact of the high-resolution errors shared by each template at the higher resolvable scales. Conversely, the strong resolution character of the $4^2-4^2-4^2-4^2-4^2$ template (Fig. 3(*a*)) over these coarse scales correlates well with the corresponding superior predictions of the nonlinear Burger wave. Exclusive of template $4^2-4^2-4^2-4^2-4^2$, the improved predictive accuracy reaches a maximum at the intermediate grid spacing as shown in Fig. 7(*b*). This result was not unexpected because the improved resolution efficiency of these composite templates (under an equivalent expectancy) actually measures a shift towards the upper resolvable scales at the intermediate level. Degradation of the predictive accuracy for the finest grids when using the fully optimized $4^2-4^2-4^2-4^2-4^2$ template can not be explained by its intrinsic resolution character.

5.3 Turbulent Flat Plate. Simulation conditions for this LES

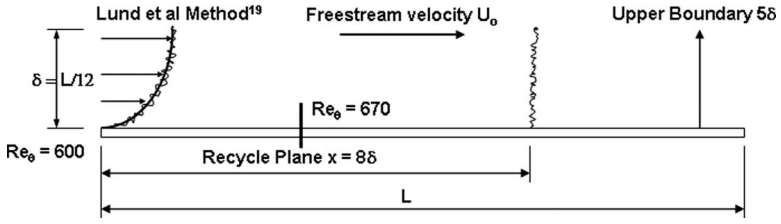

Fig. 8 Schematic of LES computations of the flat plate flow

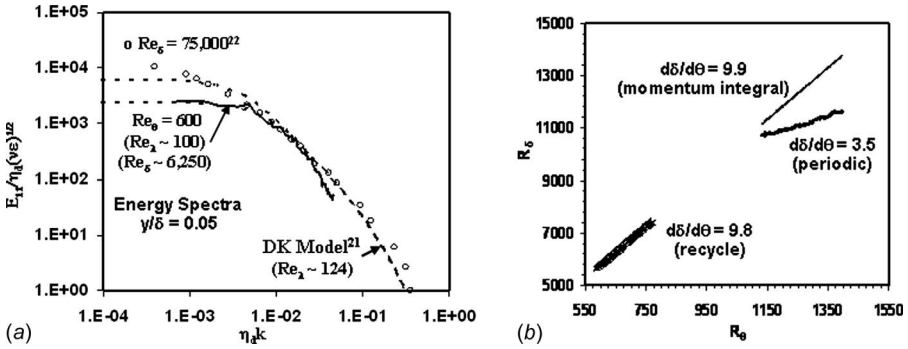

Fig. 9 Turbulent boundary layer growth and energy spectra using standard and optimized templates $4^2-4^2-5-6-5-4^2-4^2$ (streamwise), $4^2-4^2-5-4^2-4^2$ (normal) and -6- (spanwise periodic). (*a*) Stremwise growth and (*b*) energy spectra.

application are illustrated by the schematic in Fig. 8. For this canonical test case, the inflow boundary thickness (δ_o) is one-twelfth of the plate length. The "rescale-recycle" method of Lund et al. [19] applied at the downstream plane $\delta=8\delta_o$ was utilized to replenish the turbulent inflow time dependence. The flow conditions along the remaining boundaries also followed those used by Lund et al. [19]. At the inflow plane, the Reynolds number in terms of the momentum thickness (θ) was $\mathrm{Re}_\theta=600$ with the turbulent statistical data examined at plane $\mathrm{Re}_\theta=670$. The grid size was $192\times121\times48$ in the uniform streamwise (x), stretched wall-normal (y), and uniform spanwise periodic (z) directions, respectively. This gridding in wall units based on the inflow conditions was $\Delta x^+=20$, $\Delta y^+_{\mathrm{wall}}=3.1$, and $\Delta z^+=15$; $\Delta y^+_{\mathrm{wall}}=y(\nu/u_\tau)$ where the quantities ν and u_τ are the kinematic viscosity and wall-friction velocity, respectively. The near wall-normal gridding was purposely intermediate to evaluate the optimized templates. But a finer near-wall stretched spacing with $\Delta y^+_{\mathrm{wall}}=1.5$ and ten points inside the sublayer was ultimately utilized to test the convergence behavior of the best optimized template. Finally, this spatial resolution is in compliance with the LES simulations by Lund et al. [19] ($\Delta x^+=64$, $\Delta y^+_{\mathrm{wall}}=1.2$, and $\Delta z^+=15$ for $1400\leq\mathrm{Re}_\theta\leq1640$).

The overall LES solution methodology is described in detail by Jordan [20]. However, the present simulations depart from that strategy only in view of the approximation schemes tested for the nonconservative convective derivatives. Based on their favorable spatial resolution and stability characteristics, templates $4^2-4^2-5-6-5-4^2-4^2$ streamwise, $3,4^{0,2}-4^{0,2}-5-4^{0,2}-3,4^{0,2}$ wall-normal, and (6c) spanwise periodic were exercised for resolving the turbulent physics along a flat plate. Experience showed that the templates $3,4^{0,2}-4^{0,2}-5-4^{0,2}-3,4^{0,2}$ aided the subgrid scale (SGS) model in regions of intermediate grid spacing without over-damping (or dumping) the finest resolved scales near cut-off.

The streamwise growth of the boundary layer thickness (Re_δ) and decay of the dimensionless turbulent energy spectra ($E_{11}/\eta_d(\nu\varepsilon)^{1/2}$) at y-z plane $y/\delta_o=0.05$ as shown in Fig. 9 provide quality assurance of the selected spatial gridding. Turbulent quantities E_{11}, η_d, ε, and λ are the spanwise-averaged streamwise kinetic energy, Kolmorgorov scale, dissipation rate, and Taylor's microscale, respectively. Scales η_d, ε, and λ were evaluated using the Driscoll–Kennedy (DK) model procedure [21] for gauging numerical uncertainty where the experimental measurements given by Hinze [22] served as an adequate benchmark. Between the inflow and recycle planes, the boundary layer growth ($d\delta/d\theta=9.8$) agrees well with the value determined by the momentum integral method ($d\delta/d\theta=9.9$). For comparison, periodic boundary conditions were tested in lieu of the method by Lund et al. [19], which clearly produced an incorrect growth ($d\delta/d\theta=3.5$). A minor degree of energy damping is indicated near the finest resolvable scales when compared to the DK model. But this level is certainly inconsequential in view of properly resolving the respective turbulent intensity or Reynolds stresses by the simulation.

Figure 10(*a*) compares the predictive accuracy among the standard and optimized templates as varied only in the wall-normal direction. This accuracy centers on the LES predictions of the maximum streamwise turbulent intensity (u_{rms}/u_τ) as compared to the experimental measurements by Spalart [23] at the same Reynolds number $\mathrm{Re}_\theta=670$. As the boundary and adjacent stencils increase in formal orders and/or are optimized, predictions of the peak streamwise turbulent intensity improve as well as the wall-normal distribution. A peak error of 9% (wall-normal template $4^2-4^2-5-4^2-4^2$) is considered small in view of the few compu-

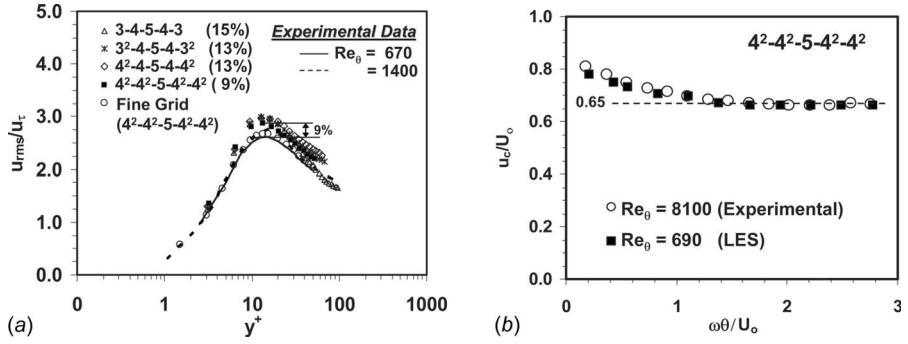

Fig. 10 Turbulent flat plate streamwise intensity and convective velocity using standard and various optimized templates: experimental data $\mathrm{Re}_\theta=670$ [23], $\mathrm{Re}_\theta=1400$ [24], and $\mathrm{Re}_\theta=8100$ [25]. (*a*) Stremwise intensity and (*b*) convective velocity.

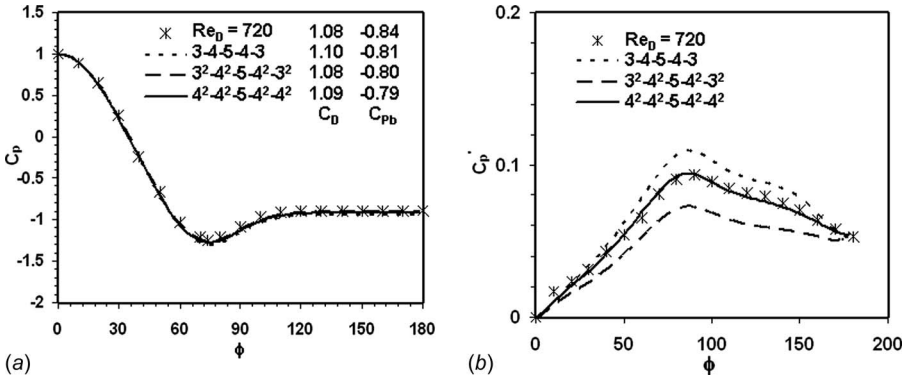

Fig. 11 Mean and fluctuating coefficients, drag, and base pressure of flow past a circular cylinder using standard and various optimized templates: experimental data Re_D =720 [26]. (*a*) Mean and (*b*) fluctuating.

tational points used to resolve the inner layer. This error became near negligible (<2%) over the finer grid spacing. The predicted dimensionless convective velocity (u_c/U_o) using this template as extracted along the convective ridge in a wavenumber-frequency spectrum closely agrees with the experimental measurement of Abraham and Keith [25] (see Fig. 10(*b*)). The convective velocity correctly decays to the constant value $u_c/U_o=0.65$ along the upper dimensionless frequencies ($\omega\theta/U_o$).

5.4 Circular Cylinder. This canonical test problem centers on the predictive capability of the optimized templates to accurately resolve the mean and fluctuating wall pressure. We chose $Re_D=720$ for the Reynolds number (based on the cylinder diameter D) because the experimental evidence [26] lies within the wide range of scale similarity in mean wall pressure, but comparatively higher surface fluctuations. In this case, the LES equations of Jordan [20] were recast into a cylindrical coordinate system with analogous exterior flow conditions. The O-type grid size was $161\times141\times33$ in the uniform circumferential periodic (φ), stretched wall-normal (r), and uniform spanwise periodic (z) directions, respectively. First-point interior spacing was $\Delta r \sim 0.007D$ with flow domain limits $r_{\max}=12D$. The spanwise spacing $\Delta z\sim 0.03\pi D$ provided eight points for resolving the formation of secondary structures in the separated shear layers according to the experimental measurements reported by Mansy et al. [27]. Exclusive of the wall-normal template $4^2-4-5-4-4^2$, numerical approximation of the convective derivative was similar to the turbulent flat plate problem (sixth-order (6c) circumferential periodic).

The resolved mean and fluctuating wall pressures for this test case are shown in Fig. 11. Although the mean profiles (C_p) of the three templates are nearly indistinguishable, the drag force (C_D), and base pressure (C_{Pb}) coefficients indicate otherwise. Composite template $3^2-4^2-5-4^2-3^2$ is most accurate for resolving C_D because its near-wall resolution efficiency is best among the three templates. Interestingly, C_{Pb} correlates poorly with increasing order and optimization. This prediction was not completely unforeseen because C_{Pb} is most sensitive to the three-dimensional grid spacing coupled with the template interactions within the wake formation zone. As an example, decreasing the spanwise spacing to $\Delta z\sim 0.02\pi D$ (48 points) improve the drag ($C_D=1.08$) and base pressure coefficients ($C_{\mathrm{Pb}}=-0.82$) toward the measured values ($C_D=1.08$ and $C_{\mathrm{Pb}}=-0.84$) using the wall-normal $4^2-4^2-5-4^2-4^2$ template. The most obvious advantage of using high-resolution templates is implied by their ability to accurately resolve the fluctuating wall pressure (C_p'). Like the flat plate, the optimized composite $4^2-4^2-5-4^2-4^2$ accurately resolved the fluctuating wall pressure with a L_2 norm less than 2%. Realistically, the surface distribution of C_p' is a better gauge for evaluating the predictive accuracy of each template because this turbulent statistic is strongly influenced by the resolution errors well beyond the wall boundary.

6 Final Remarks

Multiparameter optimization of finite differencing schemes is a guaranteed path towards high spatial resolution of fine-scale physics in complex topologies. But the optimization strategy should evaluate the free-parameters of each constituent simultaneously to quantify the true resolution errors of the new composite template. Otherwise, the benefits of the exercise will be misunderstood. Reaching consistent resolution characteristics throughout the computational domain is not routine for any optimized composite template due to the projected influence of the boundary and adjacent boundary errors far into the domain interior. Additionally, one must guarantee that the template is numerically stabile while validating its predictive accuracy.

Herein, an optimization procedure is offered that highlights a least-squares minimization approach to handle the highly over determinant system. The tactic optimizes each closing stencil simultaneously toward the resolution errors of the interior scheme. In particular, the $4^2-4^2-6-4^2-4^2$ (or $4^2-4^2-5-6-5-4^2-4^2$) template shows consistent resolution errors at all points with the computational domain. Each template is numerically stable with predictive field accuracies given by the formal truncation errors of the closing stencils. The test cases involved resolving the linear wave propagation, the nonlinear Burger wave, turbulence along a flat plate, and the wall pressure around a circular cylinder. The results show that raising the formal order of the closing stencils along with parameter optimization improved the predictive accuracy of the resultant template sufficient to justify their use.

Acknowledgment

The author gratefully acknowledges the support of the Office of Naval Research (Dr. Ronald D. Joslin, Program Officer) under Contract No. N0001408AF00002 and the Naval Undersea Warfare Center (Dr. Anthony A. Ruffa, ILIR Program Manager).

References

[1] Lele, S. K., 1992, "Compact Finite Difference Schemes With Spectral-Like Resolution," J. Comput. Phys., **103**, pp. 16–42.
[2] Kim, J. W., 2007, "Optimized Boundary Compact Finite Difference Schemes for Computational Aeroacoustics," J. Comput. Phys., **225**(1), pp. 995–1019.
[3] Rogallo, R., and Moin, P., 1984, "Numerical Simulation of Turbulent Flows," Annu. Rev. Fluid Mech., **16**, pp. 99–137.
[4] Jordan, S. A., 2007, "The Spatial Resolution Properties of Composite Compact Finite Differencing," J. Comput. Phys., **221**, pp. 558–576.
[5] Jordan, S. A., 2008, "Understanding the Boundary Stencil Effects on the Adjacent Field Resolution in Compact Finite Differences," ASME J. Fluids Eng., **130**, p. 074502.
[6] Tam, C. K. W., and Webb, J. C., 1993, "Dispersion-Relation-Preserving

Schemes for Computational Acoustics," J. Comput. Phys., **107**, pp. 262–281.
[7] Ashcroft, G., and Zhang, X., 2003, "Optimized Prefactored Compact Schemes," J. Comput. Phys., **190**(2), pp. 459–477.
[8] Hixon, R., and Turkel, E., 1998, "High-Accuracy Compact MacCormack-Type Schemes for Computational Aeroacoustics," Report No. NASA/CR-1998-208672.
[9] Hixon, R., 2000, "Prefactored Small Stencil Compact Schemes," J. Comput. Phys., **165**, pp. 522–541.
[10] Popescu, M., Wei, S., and Garbey, M., 2005, "Finite Volume Treatment of Dispersion-Relation-Preserving and Optimized Prefactored Compact Schemes for Wave Propagation," J. Comput. Phys., **210**(2), pp. 705–729.
[11] Carpenter, M. H., Gottlieb, D., and Abarbanel, S., 1993, "The Stability of Numerical Boundary Treatments for Compact High-Order Finite-Difference Schemes," J. Comput. Phys., **108**, pp. 272–295.
[12] Gustafsson, B., Kreiss, H.-O., and Sundstrom, A., 1972, "Stability Theory of Difference Approximations for Mixed Initial Boundary-Value Problems II," Math. Comput., **26**, pp. 649–686.
[13] Demuren, A. O., Wilson, R. V., and Carpenter, M., 2001, "Higher-Order Compact Schemes for Numerical Simulation of Incompressible Flows, Part 1: Theoretical Development," Numer. Heat Transfer, Part B, **103**, pp. 207–230.
[14] Cook, A. W., and Riley, J. J., 1996, "Direct Numerical Simulation of a Turbulent Reactive Plume on a Parallel Computer," J. Comput. Phys., **129**(2), pp. 263–283.
[15] Sengupta, T. K., Ganerlwal, G., and De, S., 2003, "Analysis of Central and Upwind Compact Schemes," J. Comput. Phys., **192**(2), pp. 677–694.
[16] Ladeinde, F., Xiaodan, C., Visbal, M. R., and Gaitonde, D. V., 2001, "Turbulence Spectra Characteristics of High Order Schemes for Direct and Large Eddy Simulations," Appl. Numer. Math., **36**, pp. 447–474.
[17] Gustafsson, B., 1975, "Highly Accurate Compact Implicit Methods and Boundary Conditions," Math. Comput., **29**(130), pp. 396–406.
[18] Abarbanel, S. S., and Chertock, A. E., 2000, "Strict Stability of High-Order Compact Implicit Finite-Difference Schemes: The Role of Boundary Conditions for Hyperbolic PDEs, I," J. Comput. Phys., **160**, pp. 42–66.
[19] Lund, T. S., Wu, X., and Squires, K. D., 1998, "Generation of Turbulent Inflow Data for Spatially-Developing Boundary Layer Simulations," J. Comput. Phys., **140**, pp. 233–258.
[20] Jordan, S. A., 2003, "Resolving Turbulent Wakes," ASME J. Fluids Eng., **125**, pp. 823–834.
[21] Jordan, S. A., 2005, "A Priori Assessments of Numerical Uncertainty in Large-Eddy Simulations," ASME J. Fluids Eng., **127**, pp. 1171–1182.
[22] Hinze, J. O., 1975, *Turbulence*, McGraw-Hill, New York.
[23] Spalart, P. R., 1988, "Direct Simulation of a Turbulent Boundary Layer Up To Re_θ=1410," J. Fluid Mech., **187**, pp. 61–98.
[24] De Graaff, D. B., and Eaton, J. K., 2000, "Reynolds Number Scaling of the Flat Plate Turbulent Boundary Layer," J. Fluid Mech., **422**, pp. 319–346.
[25] Abraham, B. M., and Keith, W. L., 1998, "Direct Measurements of Turbulent Boundary Layer Wall Pressure Wavenumber-Frequency Spectra," ASME J. Fluids Eng., **120**, pp. 29–39.
[26] Norberg, C., 1998, "LDV-Measurements in the Near Wake of a Circular Cylinder," ASME Paper No. FEDSM98-521.
[27] Mansy, H., Yang, P., and Williams, D. R., 1990, "Quantitative Measurements of Three-Dimensional Structures in the Wake of a Circular Cylinder," J. Fluid Mech., **270**, pp. 277–296.

Experimental Measurement of Laminar Axisymmetric Flow Through Confined Annular Geometries With Sudden Inward Expansion

Afshin Goharzadeh
e-mail: agoharzadeh@pi.ac.ae

Peter Rodgers

Department of Mechanical Engineering,
The Petroleum Institute,
P.O. Box 2533,
Abu Dhabi, United Arab Emirates

In this paper, separating and reattaching aqueous laminar flows produced by a sudden inward expansion within confined annular geometries are experimentally studied. The test geometries are based on a previous numerical study. The fluid flow structure at the expansion region is experimentally characterized using particle image velocimetry combined with refractive index matching. The detailed measurements of the velocity field, reattachment length, and relative eddy intensity are obtained for two different expansion ratios, 1.4 and 1.6. For both expansion ratios, the reattachment length is found to vary nonlinearly with the Reynolds number ($50<Re<600$), in line with numerical predictions. The eddy intensity is found to depend strongly on both the Reynolds number and expansion ratio with the relationship between the Reynolds number and the reattachment length being nonlinear. Overall, the corresponding numerical predictions are in good agreement with the measurements undertaken herein.
[DOI: 10.1115/1.4000482]

1 Introduction

Annular flows confined within coaxial cylinders have important industrial applications, such as in the petroleum industry for drilling operations and flow separation processes. The hydrodynamic properties of flows within coaxial cylinders have been extensively reported over the last two decades such as for rotating or fixed annuli applications with corresponding theoretical analyses well established [1]. In addition, extensive studies have been reported on the sudden expansion of flows inside pipes [2–5]. The primary results of such studies demonstrate a linear relationship between the Reynolds number and the reattachment length in laminar flow conditions for expansion ratios between 2:1 to 6:1.

However the structure of annular flows for the geometric case of when the diameter of the inner concentric tube varies suddenly in the axial direction has not been extensively assessed [6–8]. For such configurations, such as flow over a backward facing step, analysis has been focused primarily on planar expansion geometries [9,10], assessing the influence of Reynolds number, step aspect ratio, or reattachment length on the flow conditions. Nag and Datta [6] analyzed axisymmetric expansion in annular tubes numerically. Their findings showed a nonlinear relationship between the Reynolds number and the reattachment length for laminar flow ($Re<600$). However no experimental validation was presented. In the present study, the test geometries are based on those numerically investigated by Nag and Datta [6]. Laminar flow field measurements of flow expansion within concentric coaxial geometries are undertaken using particle image velocimetry (PIV) combined with refractive index matching (RIM). These measurements are performed for two different expansion ratios ($\varepsilon=1.4$ and 1.6) to investigate both the influence of the Reynolds number ($50<Re<600$) on the behavior of the recirculating eddy, characterized by the reattachment length (L_r), and the relative eddy intensity (ξ).

The paper is structure as follows. The theoretical solutions for the velocity profile in an annular flow and the relative eddy intensity are presented. The experimental setup and the flow visualization system employed are described. Measurements of the velocity field in the vicinity of the sudden backstep expansion are presented with discussion on the influence of Reynolds number on the characteristics of the recirculating eddy given.

2 Theoretical Background

2.1 Annular Flow Velocity Solution. For the geometry under analysis, shown in Fig. 1, a fully developed steady laminar flow is considered at the upstream end of the inlet annulus. The axisymmetric Navier–Stokes equations, combined with the continuity equation for incompressible flow, is used to determine the analytical solution of the velocity profile for annular flow. This solution is well described in classical fluid mechanics textbooks [11,12] and is given as

$$u(r)=\frac{2Q}{\pi}\left[\frac{r_1^2-r^2+\dfrac{r_1^2-r_2^2}{\ln(r_2/r_1)}\ln(r_1/r)}{r_1^4-r_2^4-\dfrac{(r_1^2-r_2^2)^2}{\ln(r_1/r_2)}}\right] \tag{1}$$

where $u(r)$ is the velocity in the radial coordinate (m/s), Q is the volumetric flow rate (m^3/s), and r_1 (m) and r_2 (m) are cylinder radii, Fig. 1.

Equation (1) shows that the maximum velocity does not occur at the midpoint of the annular tube, but rather nearer the inner cylinder. The position of this maximum depends on both r_1 and r_2.

2.2 Relative Eddy Intensity. Nag and Datta [6] defined relative eddy intensity as the ratio of the maximum backflow rate in the circulating eddy zone Ψ_{max} to the inflow rate into the system Ψ_{in}

$$\xi=\Psi_{max}/\Psi_{in} \tag{2}$$

where Ψ is the stream function, which in two-dimensional flow can be defined as

$$u=\frac{1}{r}\frac{\partial\Psi}{\partial r} \quad \text{and} \quad v=-\frac{1}{r}\frac{\partial\Psi}{\partial z} \tag{3}$$

where r and z are the radial and axial coordinates, respectively, with u and v the velocities with respect to the coordinates.

3 Experimental Setup

A schematic representation of the experimental setup used in this study is shown in Fig. 2(*a*) with the coaxial cylinder geometric detail given in Fig. 1. Two horizontal, 1 m long, coaxial transparent Plexiglas cylindrical tubes are used. The outer tube has a constant inner radius along the horizontal axis $r_1=20$ mm. The outer radius of the inner tube reduces suddenly at $L_e=580$ mm from the inlet forming an annular backstep perpendicular to the flow direction. The radius of the inner cylinder before the backstep r_2 is 11 mm and the outer radius r_3 is either 6.0 mm or 7.5 mm after the expansion. The inner to outer tube aspect ratio before the expansion is defined as $\kappa=r_2/r_1$. Downstream of the backstep, the expansion ratio is defined as $\varepsilon=(r_1\text{-}r_3)/(r_1\text{-}r_2)$. Flow field measurements are undertaken for a constant aspect ratio $\kappa=0.55$ and two expansion ratios $\varepsilon=1.39$ and 1.56. These expan-

Contributed by the Fluids Engineering Division of ASME for publication in the JOURNAL OF FLUIDS ENGINEERING. Manuscript received November 24, 2008; final manuscript received October 2, 2009; published online November 12, 2009. Editor: Joseph Katz.

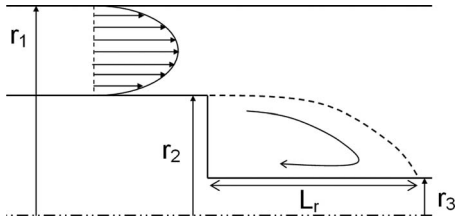

Fig. 1 Physical geometry of experimental setup

sion ratios were selected so as permit the experimental results to be compared with corresponding numerical predictions ($\varepsilon=1.4$ and 1.6) obtained by Nag and Datta [6]. Laminar flow is generated by a pump having a maximum flow capacity of $Q=15$ lpm with the flow rate controlled by a regulating valve and measured using a digital flow meter (GPI 09 series) having a measurement uncertainty of 6%.

The working fluid is water, maintained at a constant temperature of 20°C. A constant laminar flow is characterized by a Reynolds number $\mathrm{Re}=\bar{u}d_h/\nu$, where $\bar{u}$ is the average flow velocity, hydraulic diameter $d_h=2(r_1-r_2)=18$ mm, and ν the kinematic viscosity of water. In order to remove surface curvature effects of the cylinders, the outer tube was submerged inside a transparent rectangular box filled with silicon oil (Dow Corning 556) having a refractive index of $n=1.46$, which is close to that of Plexiglas $n=1.48$. Additionally, the inner tube contains stationary silicon oil in order to match the refractive index inside the system.

3.1 Flow Visualization System. Using PIV, all flow field measurements were taken in the central horizontal axial plane of the cylinder arrangement. To illuminate this measurement plane, a horizontal laser sheet was projected, with a charge coupled device (CCD) camera installed perpendicular to this plane to record particle motion, as illustrated in Fig. 2(*b*). The water is seeded with polyamide particles tracers with a diameter of 22 μm and density of 1.016 $\mathrm{g/cm^3}$ for flow visualization.

The PIV flow field measurements were undertaken at two different locations: (i) upstream region far from the sudden expansion zone and (ii) at the expansion plane. An example of a recorded PIV image is shown in Fig. 3(*a*) for the reattachment zone

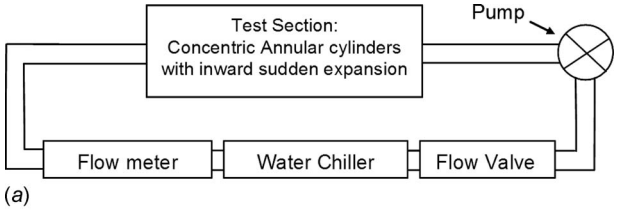

(*a*)

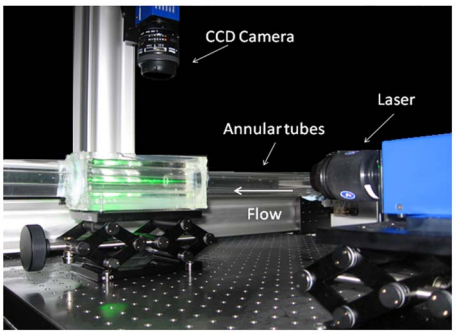

(*b*)

Fig. 2 Experimental setup: (*a*) schematic of experimental setup and (*b*) flow visualization system

in the expansion plane. The flow was observed with a field of view of 20×30 $\mathrm{mm^2}$. The tracers' density was 15–20 particles per interrogation area. A diode laser was used as the light source for PIV measurements having a maximum power output of 200 W at a wavelength $\lambda=532$ nm. A cylindrical lens ($f=28$ mm) was used to generate a light sheet of approximately 1 mm thickness. The synchronization between laser light pulses and the camera was accomplished by transistor-transistor logic pulses from the synchronizer. The time between each couple of images was 200 ms. The pulse separation time was adjusted between 5 ms to 20 ms depending on the Reynolds number. Full-frame images of 1024×1024 pixels were acquired and transferred to a computer via a frame grabber. Using the DAVIS FLOWMASTER software provided by the Lavision System (Germany), the 2D PIV image was divided into 16×16 pixels size subregions using a multigrid correlation process with 50% overlap. The average particle velocities was calculated using 100 images coupled with the cross correlation method. The spurious vectors calculated and based on the local median filtering were less than 3%. No smoothing data were used for the velocity calculation of the reattachment zone. In order to verify that no flow instability affected the measurements in terms of flow asymmetry, that could manifest itself in the form of an azimuthally varying reattachment length flow field, the velocity profiles between the horizontal and vertical planes were measured and compared. This was achieved by switching the position of the laser and CCD camera in order to measure the 2D velocity distribution. The velocity variation between both directions was found to be within the bound of measurement error discussed below. The third velocity component due to instabilities could therefore be neglected.

PIV measurement accuracy can be influenced by a range of error sources that include, for example, tracer density, particle displacement, velocity gradients in the interrogation windows, background noise of the recordings, and quantization level of the camera. In Raffle et al. [13], a detailed discussion of the influence of such error sources is given. Additionally, near wall measurements using PIV are often difficult and characterized by large errors and uncertainties due to potential difficulties encountered with light scattering from wall boundaries and lack of seed particles in the near wall region.

In the present study, error analysis assessment was based on comparing the mean velocity measured using PIV and the digital flow meter described in the previous section. Velocity measurement uncertainty was quantified to be less than 7% based on comparing the average velocity derived from PIV velocity distribution with corresponding measured flow rate.

4 Results and Discussions

To verify that the upstream flow conditions were fully developed, measured velocity profiles were compared with the exact analytical solution given in Eq. (1) with good agreement obtained as illustrated in Fig. 4. Additionally, the measured velocity profiles shown in Fig. 4 were found to be symmetrical on either side of the upstream inner annular tube. The good agreement between measured and predicted velocity profiles also served to estimate the accuracy of the PIV measurements with good qualitative agreement shown.

In Figs. 3(*b*)–3(*d*), sample velocity flow field measurements in the expansion plane region are presented with corresponding streamlines for Reynolds numbers of 100, 300, and 500. For each Reynolds number, the magnitude of particle velocities decreases at the expansion region. The flows are characterized as laminar with parallel streamlines. The recirculating regions are clearly developed downstream of the backstep with the flow two dimensional and nonoscillatory for $\mathrm{Re}<600$. Using the streamline patterns in Figs. 3(*b*)–3(*d*), the fundamental parameters of the recirculating region, namely, the reattachment length L_r and the relative eddy intensity ξ were derived and presented in Figs. 5 and 6.

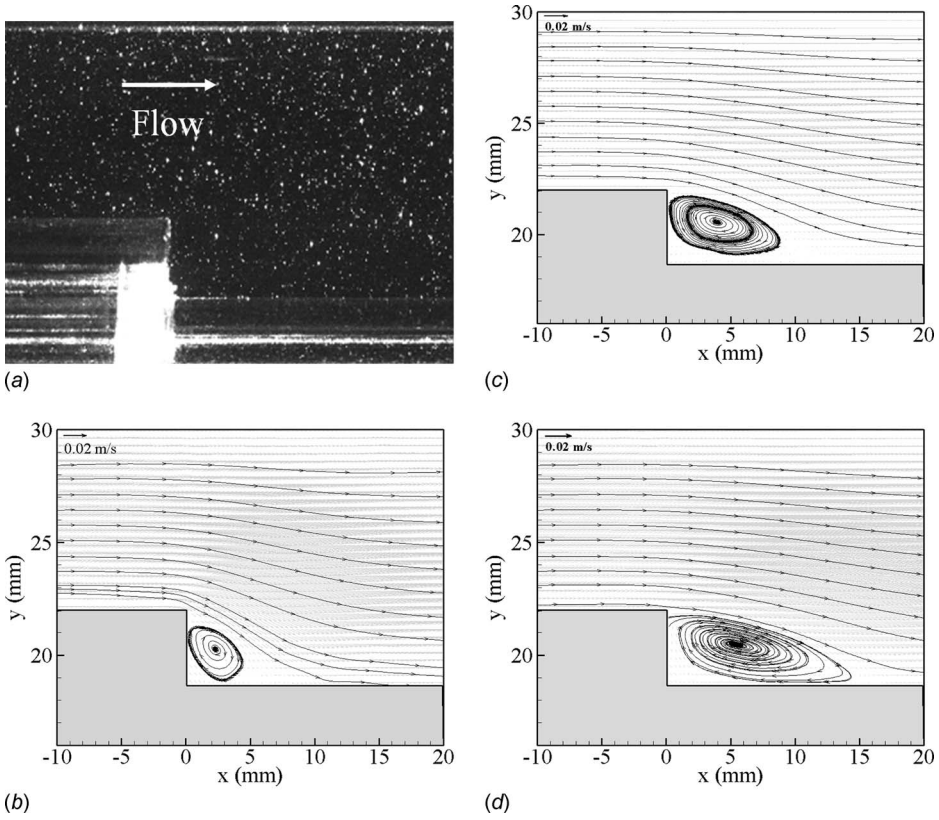

Fig. 3 Velocity flow field measurements: (*a*) typical PIV recorded image at expansion region, (*b*) flow field measurement Re=100, (*c*) flow field measurement Re=300, and (*d*) flow field measurement Re=500

In Fig. 5, a comparison between measured and numerically predicted reattachment lengths are given for the Reynolds number range of 50–600. As observed, good agreement exists between PIV measurements and corresponding numerical data published by Nag and Datta [6], for the similar geometric configurations. The present study shows that the variation in the reattachment length inside the annular tubes with sudden inward expansion (ε =1.39 and 1.56) does not follow the linear variation observed inside the axisymmetric sudden expansion pipe [4]. These experimental results confirm the numerical predictions obtained by Nag and Datta [6].

To analyze the influence of the Reynolds number on relative eddy intensity, the experimental results for expansion ratios are plotted in Fig. 6 and compared with corresponding numerical predictions of Nag and Datta [6]. It is found that the eddy intensity depends on both the Reynolds number and expansion ratio. An increase in the Reynolds number generates stronger eddy intensity with a nonlinear dependency. Above Re=300, the dependency becomes weaker and the eddy intensity approaches an asymptotic value.

Similar experimental results have been obtained using PIV for laminar flow inside a single pipe having axisymmetric sudden expansion [4]. The eddy intensity depends strongly on the expansion ratio. A 15% increase in the expansion ratio (from ε=1.39 to ε=1.56) leads to 50% increase in the eddy intensity. The strong dependency of the eddy intensity on the expansion ratio could be explained by the increase in the expansion region, which generates higher backflow velocity. It is important to highlight that the

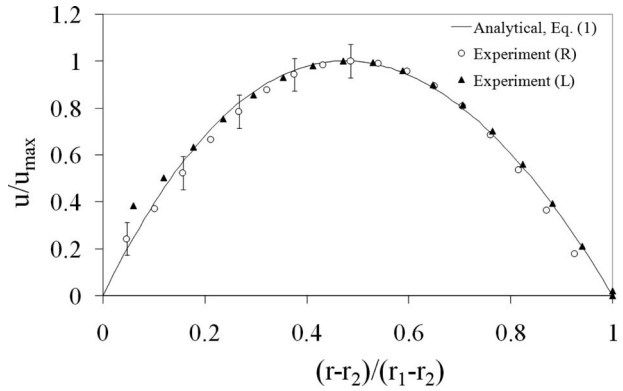

Fig. 4 Comparison of measured and analytically predicted velocity profile at the upstream end of the inlet annulus (*R* and *L* refer to right and left sides, respectively)

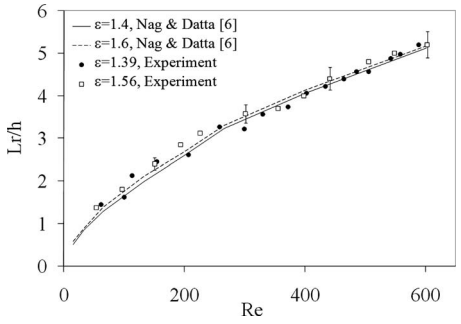

Fig. 5 Comparison of measured and numerically predicted reattachment lengths ($h=r_2-r_3$)

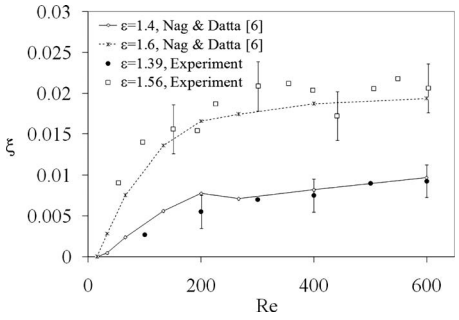

Fig. 6 Comparison of measured and predicted eddy intensity (ξ) as function of expansion ratio and Reynolds number

eddy intensity increases in the system with expansion ratio (Fig. 6) but the length of the recirculating region remains constant (Fig. 5) for a given Reynolds number.

The overall agreement between the present experimental results and the numerical predictions obtained by Nag and Datta [6] is very good and within the bounds of measurement uncertainty. This therefore validates their numerical predictions.

5 Conclusions

In this study, laminar axisymmetric water flows through confined annular geometries with sudden inward expansion were experimentally characterized using PIV combined with RIM. The numerical predictions previously obtained by Nag and Datta [6] for the same test configurations are in good agreement with the present experimental data. These measurements confirm the nonlinear dependency of the flow reattachment length with the Reynolds number ($50 < \mathrm{Re} < 600$). In addition, eddy intensity is found to strongly depend on both the Reynolds number and expansion ratio, with a nonlinear relationship with the Reynolds number.

References

[1] Frisch, B. R., Egbers, C., and Pfister, G., 2000, *Physics of Rotating Fluids*, Springer-Verlag, Berlin, Germany.
[2] Macagno, O. E., and Hung, T. K., 1967, "Computational and Experimental Study of Captive Annular Eddy," J. Fluid Mech., **28**(1), pp. 43–64.
[3] Badekas, D., and Knight, D. D., 1992, "Eddy Correlation for Laminar Axisymmetric Sudden Expansion Flows," ASME J. Fluids Eng., **114**(1), pp. 119–121.
[4] Hammad, K. J., Otungen, M. V., and Arik, E. B., 1999, "A PIV Study of the Laminar Axisymmetric Sudden Expansion Flow," Exp. Fluids, **26**, pp. 266–277.
[5] Hammad, K. J., Vradis, G. C., and Otungen, M. V., 2001, "Laminar Flow of a Herschel–Bulkley Fluid Over an Axisymmetric Sudden Expansion," ASME J. Fluids Eng., **123**, pp. 588–594.
[6] Nag, D., and Datta, A., 2007, "On the Eddy Characteristics of Laminar Axisymmetric Flows Through Confined Annular Geometries With Inward Expansion," Proc. Inst. Mech. Eng., Part C: J. Mech. Eng. Sci., **221**, pp. 213–226.
[7] Mohamed, A. G., Valentine, D. T., and Hassel, R. E., 1991, "Numerical Study of Laminar Separation Over an Annular Backstep," Comput. Fluids, **20**(2), pp. 121–143.
[8] Sheen, H. J., Chen, W. J., and Wu, J. S., 1997, "Flow Patterns for an Annular Flow Over an Axisymmetric Sudden Expansion," J. Fluid Mech., **350**, pp. 177–188.
[9] Durst, F., Pereira, J. C. F., and Tropea, C., 1993, "The Plane Symmetric Sudden-Expansion Flow at Low Reynolds Number," J. Fluid Mech., **248**, pp. 567–581.
[10] Piirto, M., Karvinen, A., Ahistedt, H., Saarenrinne, P., and Karvinen, R., 2007, "PIV Measurements in Square Backward-Facing Step," ASME J. Fluids Eng., **129**, pp. 984–990.
[11] White, F. M., 2003, *Fluid Mechanics*, McGraw-Hill, New York.
[12] Munson, B. R., Young, D. F., and Okiishi, T. H., 2002, *Fundamentals of Fluid Mechanics*, Wiley, New York.
[13] Raffle, M., Willert, C., Werely, S., and Kompenhans, J., 2007, *Particle Image Velocimetry—A Practical Guide*, Springer, Berlin, Germany.